

Mass Determinations of Cataclysmic Variables

Christopher D.J. Savoury

Department of Physics & Astronomy



The
University
Of
Sheffield.

*A dissertation submitted in candidature for the degree of
Doctor of Philosophy at the University of Sheffield*

February 2013

“Space is big. You just won’t believe how vastly, hugely, mind-bogglingly big it is. I mean, you may think it’s a long way down the road to the chemist’s, but that’s just peanuts to space.”

Douglas Adams, *The Hitchhiker’s Guide to the Galaxy*

Declaration

I declare that no part of this thesis has been accepted, or is currently being submitted, for any degree or diploma or certificate or any other qualification at this University or elsewhere.

This thesis is the result of my own work unless otherwise stated.

The following Chapters have been based on publications:

- Chapter 4 – Savoury et al. (2011)
- Chapter 5 – Savoury et al. (2011)
- Chapter 6 – Savoury et al. (2012)
- Chapter 7 – Savoury & Littlefair (2013)

Summary

Cataclysmic variables (CVs) are a class of closely interacting binary system that undergo mass transfer from a Roche lobe filling secondary star to a white dwarf primary star, usually via a gas stream and an accretion disc. A bright spot is formed where the gas stream meets the edge of the accretion disc. The light curves of CVs can be complex, with the accretion disc, white dwarf and bright spot all being eclipsed in rapid succession. When observed with time resolutions of the order of a few seconds, this eclipse structure allows the system parameters to be determined to a high degree of precision, with relatively few assumptions. In this thesis I present new, high-speed photometry of 20 eclipsing CVs. For 6 objects, I am able to determine the system parameters by fitting a parameterised model to the observed eclipse light curve (*the photometric method*). In addition, I perform an updated analysis of 11 CVs that were previously analysed by my group, bringing the total sample size of eclipsing CVs with precise mass determinations in this thesis to 17. I find the secondary stars in CVs are oversized in comparison to standard models. I show that this can be explained by either enhancing the mass-transfer rate, or by modifying the stellar physics of the secondary stars. Distinguishing between these two possibilities is not possible given the available data.

I perform an independent check of the photometric method by deriving system parameters for one object using well known spectroscopic methods. The parameters

derived are found to be consistent with the photometric method, thus supporting its accuracy and validity.

Finally, I look at the infrared spectra of a short period CV. I am able to make a direct detection of the secondary star and place some constraints on the spectral type of the secondary star.

Acknowledgements

There are many people I wish to thank, without whom the following work would not have been possible. In no particular order:

- My supervisor, Stuart Littlefair: Thank you for all of your patience and guidance over the last three and a half years, and thank you too for providing me with some great opportunities that have been both thoroughly enjoyable and educational.
- Vik Dhillon and Tom Marsh: If only more people took your attitude towards data acquisition and analysis, then astronomy would be a far richer place.
- Paul ‘Pablo’ Kerry: Your I.T skills are second to none. Thank you for all of your invaluable I.T support and advice, both inside the department and out.
- Marvin Rose, Darren White and Emile Doran: Legendary.
- Joanne Bibby, Richard Parker, Richard Allison, Krisada Rawiraswattana, Edgar Ramirez, Cristina Ramos Almeida, Patrica Bessiere, David Hubber, David Sahman, Chris Rosslowe, Pavel Lee; We’ve had plenty of laughs, some good of banter and many a great time. Thanks for all of your support, and good luck.
- David Maltby and Emma Bradshaw: It’s been an incredible journey, but we made it!

- Charlotte Angus: I don't know where to even start. Thank you for putting up with me, for being there everyday, and generally being so amazing. Love you.
- Mum & Dad: Thank you for all of your patience, support and encouragement over the years, no matter what. Without you, I would not have made it this far.

Contents

1	Introduction	1
1.1	Cataclysmic Variables	1
1.1.1	What is a CV?	1
1.1.2	Roche Lobe Geometry	2
1.2	Types of Cataclysmic Variable	5
1.2.1	Classical and Recurrent Novae	5
1.2.2	Dwarf Novae	7
1.2.3	Nova-Like Variables	8
1.2.4	Magnetic CVs	9
1.3	Disc Instability Model	9
1.4	Origins and Evolution	12
1.4.1	Progenitors of CVs	12
1.4.2	Common Envelope Phase	13
1.4.3	Pre-CV Evolution	14
1.4.4	Direct Formation from a White Dwarf-Brown Dwarf Binary	15
1.4.5	Response to Mass Loss	16
1.5	Angular Momentum Loss	20
1.5.1	Magnetic Braking of the Secondary Star	20
1.5.2	Gravitational Radiation	20

1.6	The Secondary Stars in CVs	21
1.7	The Distribution of Orbital Periods	22
1.7.1	The Long Period Cut-Off	23
1.7.2	The Period Gap	24
1.7.3	The Period Minimum	26
1.8	The Importance of Secondary Star Properties	28
1.8.1	Superhumps	29
1.8.2	Empirical Donor Sequences	31
1.9	This Thesis	31
2	Observations and Data Reduction	33
2.1	Observations	33
2.1.1	ULTRACAM Photometry	33
2.1.2	X-Shooter Spectroscopy	35
2.1.3	NIRI Spectroscopy	41
2.2	Data Reduction	42
2.2.1	Pipelines	42
2.2.2	Bias Subtraction	42
2.2.3	Flat Fielding	44
2.2.4	Dark Frames	47
2.2.5	NIRI Nodding	49
2.3	Aperture Photometry	50
2.4	Flux Calibration	53
2.4.1	Extinction	53
2.4.2	Instrumental Response	54
2.4.3	Absolute Flux Calibration	55
2.5	X-Shooter Extraction	55

2.5.1	Flexure Correction	57
2.5.2	Flux Calibration and Telluric Correction	58
2.6	NIRI Extraction	59
2.6.1	Wavelength Calibration	61
2.6.2	Flux Calibration and Telluric Correction	62
3	Techniques of Data Analysis	66
3.1	Data Phasing and Ephemerides	66
3.2	A Physical Model of the Binary System	68
3.2.1	White Dwarf Model Atmospheres	74
3.3	Markov Chain Monte Carlo	75
3.3.1	Bayes Theorem and MCMC	75
3.3.2	Conditions of MCMC	76
3.3.3	Metropolis-Hastings	76
3.3.4	MCMC in Practice	78
3.4	Photometric Mass Determinations	80
3.5	Radial Velocity Measurements	83
3.5.1	Cross-Correlation of the Secondary Star	83
3.5.2	Skew Mapping	85
3.6	Rotational Broadening and Spectral Type of the Secondary Star	86
3.7	Spectroscopic Mass Determinations	86
3.8	The K_2 Correction	87
3.9	Spectroscopic Distance Estimation	89
3.10	Doppler Tomography	89
3.10.1	Line Formation	90
3.10.2	Back Projections	91
3.10.3	Interpretation of Doppler Maps	93

3.10.4	Limitation of Doppler Tomography	95
4	Orbital Ephemerides and Light Curve Morphology	96
4.1	Introduction	96
4.2	Orbital Ephemerides	98
4.3	Light Curve Morphology and Variations	99
4.3.1	CTCV J1300-3052	99
4.3.2	CTCV J2354-4700	101
4.3.3	SDSS J1152+4049	102
4.3.4	CSS080623:140454-102702	102
4.3.5	SDSS J0901+4809	102
4.3.6	PHL 1445	103
4.3.7	SDSS J1325+2100	103
4.3.8	SDSS J0750+1411	104
4.3.9	SDSS J1524+2209	104
4.3.10	SDSS J1250+6655	104
4.3.11	SDSS J1555-0010	105
4.3.12	CSS080227:112634-100210	105
4.3.13	1RXS J1808+1010	106
4.3.14	SDSS J0920+0042	106
4.3.15	GAL0035	106
4.3.16	SDSS J1006+2337	107
4.3.17	SDSS J0924+0801	107
4.3.18	SDSS J0932+4725	108
4.3.19	SDSS J0935+1619	108
4.4	Systems for Modelling	108

5	Mass Determinations of 17 Eclipsing Systems	115
5.1	Introduction	115
5.2	Results	116
5.2.1	System Parameters	116
5.2.2	Notes on Individual Systems	128
5.3	Discussion	132
5.3.1	White Dwarf Masses	132
5.3.2	Period Bounce	135
5.3.3	SDSS J1507+5230	139
5.3.4	PHL 1445	140
5.3.5	Exploring the Standard Model of CV Evolution	140
6	A Radial Velocity Study of CTCV J1300-3052	143
6.1	Introduction	143
6.2	Results	145
6.2.1	Average Spectrum	145
6.2.2	Trailed Spectra	148
6.2.3	Doppler Tomography	151
6.2.4	Radial velocity of the Secondary Star	153
6.2.5	Irradiation of the Secondary Star	155
6.2.6	Rotational Velocity of the Secondary Star	157
6.2.7	System Parameters	158
6.2.8	Distance	162
6.3	Discussion	162
7	The Brown Dwarf Mass Secondary Star in SDSS J1433+1011	164
7.1	Introduction	164
7.2	Results	166

7.2.1	Average Spectrum	166
7.2.2	Skew Mapping	169
7.2.3	The Spectral Type of the Secondary Star	174
7.2.4	Secondary Star Contributions	174
7.3	Discussion	177
8	Conclusions and Future Work	179
8.1	Conclusions	179
8.2	Future Work	182
A	Model Fits	183
B	CTCV 1300 Double Solution	193
C	Calculating the Required Rate of Change of Orbital Period	195

List of Figures

1.1	A schematic diagram of a non-magnetic CV.	2
1.2	The Cartesian coordinate system used to define the Roche geometry.	3
1.3	The Roche potentials.	4
1.4	A schematic representation of the $\sum -T_{eff}$ relation.	10
1.5	The orbital period distribution.	23
2.1	An example master bias frame.	43
2.2	An example master flat frame.	46
2.3	The nodding process.	50
2.4	An example of aperture selection and profile fitting.	52
2.5	The highly curved orders of X-Shooter.	56
2.6	The telluric correction process for X-Shooter data.	60
2.7	The regpic routine in PAMELA.	61
2.8	The emission lines of the Argon arc.	63
2.9	The telluric correction process for NIRI data.	64
3.1	Gas stream trajectories computed for different mass ratios.	69
3.2	Bright spot beaming angles for the simple and complex bright spot models.	72
3.3	The bright spot intensity distribution.	73

3.4	An independent Gaussian distribution vs a multi-variate Gaussian distribution, for two correlated parameters.	80
3.5	Example MCMC chains.	81
3.6	A diagram showing how velocity co-ordinates relate to the binary system.	91
3.7	A model image and the equivalent profiles formed by projection along orbital phases.	92
3.8	A diagram showing the need for the filtering process.	93
3.9	The translation of velocity coordinates to position coordinates when interpreting a Doppler map.	94
4.1a	The phased-folded, g' band light curves of 20 eclipsing CVs.	109
4.1b	<i>continued</i>	110
4.1c	<i>continued</i>	111
4.1d	<i>continued</i>	112
4.2	The 2004, g' band light curve of SDSS 1501.	114
5.1a	The phased-folded $u'g'r'$ or $u'g'i'$ light curves of the CVs listed in Table 5.1a and 5.1b, together with model fits.	118
5.1b	<i>continued</i>	119
5.1c	<i>continued</i>	120
5.1d	<i>continued</i>	123
5.2a	The normalised probability density functions for each system.	124
5.2b	<i>continued</i>	125
5.3	The white dwarf colours derived from the model fitting, together with the white dwarf models of Bergeron et al. (1995).	126
5.4	The June 2010 g' band eclipse of CTCV 1300.	129
5.5	The g' band observations of CTCV 2354 from 2009.	130
5.6	The white dwarf mass as a function of orbital period.	136

5.7	The $M_2 - P_{orb}$ relationship.	142
6.1	The average spectra of CTCV 1300.	146
6.2	The average spectrum of CTCV 1300 between 4130-4330 Å, corrected to the rest frame of the white dwarf.	148
6.3	The trailed spectra of the most prominent hydrogen Balmer emission lines.	149
6.4	The trailed spectra of Na I, Ca II and He II.	150
6.5	The trailed spectra of Fe I, Fe II and Ca I.	151
6.6	Doppler maps of CTCV 1300 using a variety of different lines.	152
6.7	The radial velocity curves of CTCV 1300.	156
6.8	χ^2 vs $v \sin i$ from the optimal subtraction technique.	159
6.9	Monte Carlo determination of system parameters for CTCV 1300.	161
7.1	A model spectrum of SDSS 1433.	167
7.2	The average J-band spectrum of SDSS 1433.	170
7.3	Skew map for SDSS 1433 produced using an L2 template.	173
7.4	Reduced- χ^2 versus spectral type from the optimal subtraction technique.	175
7.5	The variation in Reduced- χ^2 versus spectral type when optimally sub- tracting from the L2 template.	175
7.6	The observed fractional contribution of each template versus the the- oretical contribution.	178

List of Tables

2.1a	Journal of observations.	36
2.1b	<i>continued</i>	37
2.1c	<i>continued</i>	38
2.1d	<i>continued</i>	39
4.1	Orbital ephemerides.	100
5.1a	System parameters derived using the probability density functions shown in Figure 5.2a and 5.2b.	121
5.1b	<i>continued</i>	122
6.1	Measured and corrected values of K_2 found using optically thick ($f=0.50$) and thin ($f=0.77$) corrections.	157
6.2	System parameters for CTCV 1300.	160
A.1a	The model parameters found for CTCV 1300.	184
A.1b	The model parameters found for CTCV 2354 and SDSS 1152.	185
A.1c	The model parameters found for OU Vir and DV UMa.	186
A.1d	The model parameters found for XZ Eri and SDSS 1433.	187
A.1e	The model parameters found for SDSS 1035 and SDSS 1507.	188
A.1f	The model parameters found for SDSS 1227 and SDSS 1502.	189
A.1g	The model parameters found for SDSS 1702 and SDSS 0903.	190

A.1h	The model parameters found for SDSS 1501 and CSS080623.	191
A.1i	The model parameters found for SDSS 0901 and PHL 1445.	192
B.1	The system parameters of CTCV 1300	194

Chapter 1

Introduction

1.1 Cataclysmic Variables

1.1.1 What is a CV?

Cataclysmic variables (CVs) are a type of semi-detached binary system with short (\lesssim 12 hour) orbital periods that undergo mass transfer. They usually consist of a white dwarf *primary star* (of mass M_1), that accretes matter from a red dwarf *secondary star* (of mass M_2).

In non-magnetic systems, mass transfer takes place via a *gas stream* and an *accretion disc*, through the *inner Lagrangian point* (see §1.1.2). Where the gas stream meets the edge of the accretion disc is often a shock-heated area of emission, referred to as the *bright-spot*. In some systems, this is the dominant source of luminosity. At the inner edge of the accretion disc is the *boundary layer*, where material in the accretion disc is decelerated to match the surface velocity of the white dwarf. A schematic view of a non-magnetic CV is shown in Figure 1.1.

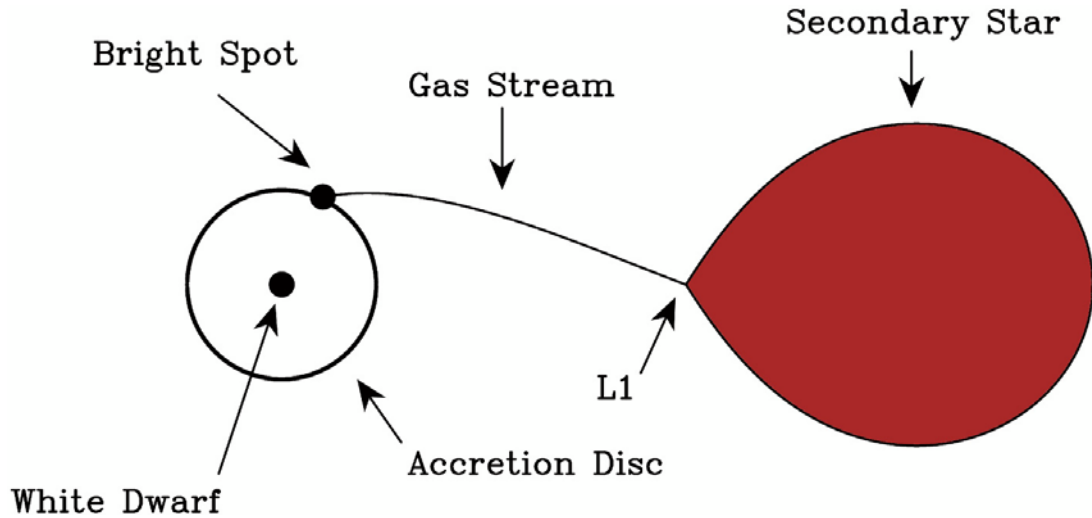


Figure 1.1: A schematic diagram of a non-magnetic CV. The white dwarf, secondary star, accretion disc, bright spot, inner Lagrangian point (L1) and gas stream are labelled.

1.1.2 Roche Lobe Geometry

The relationship between the CV component masses (M_1 , M_2), their separation (a) and the orbital period (P_{orb}) can be described by Kepler's third law,

$$a^3 = \frac{G(M_1 + M_2)P_{orb}^2}{4\pi^2}, \quad (1.1)$$

where G is the gravitational constant. For orbital periods of a few hours, and masses close to that of the Sun, Equation 1.1 implies orbital separations of the order of one solar radii. The short orbital periods and close proximity of the two components result in a strongly distorted secondary star that is tidally locked in synchronous rotation. This is due to a combination of tidal forces from the gravitation field of the primary star and centrifugal forces from the rotation. The synchronisation (and circularisation of the orbit) occurs on very short timescales in comparison to the lifetime of a CV (Zahn, 1977; Warner, 1995). The white dwarf remains unaffected by the tidal effects, due to its small radius.

The shape of the secondary star can be determined by the Roche approximation

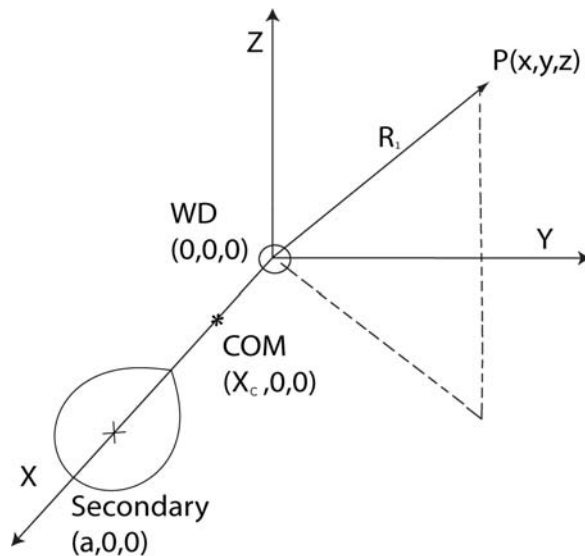


Figure 1.2: The Cartesian coordinate system used to define the Roche geometry. The frame is co-rotating with the binary with the primary star at the origin. The x-axis is the line between the centres of the two stars, and X increases towards the secondary star. The y-axis is perpendicular to the x-axis, in the plane of the binary (in the direction of the motion of the secondary) and the z-axis is perpendicular to the binary plane. X_c denotes the centre of mass of the binary, and R_1 is the length of the vector from the white dwarf, to a random point in the system, P .

(Kopal, 1959), which assumes that the gravitational field of each component is approximated as being due to a point mass, and thus neglects the influence of distortion on the gravitation field of the secondary star. To define the Roche geometry, a set of right-handed Cartesian coordinates as shown in Figure 1.2 is used. The total potential (Φ) at any point P is given by the sum of the gravitational potentials from each component plus the effective potential from the centrifugal force. From Figure 1.2, this is given by

$$\Phi = \frac{-GM_1}{\sqrt{(x^2 + y^2 + z^2)}} - \frac{-GM_2}{\sqrt{(x - a)^2 + y^2 + z^2}} - \frac{2\pi^2}{P_{orb}^2} \left[\left(x - \frac{M_2}{M_1 + M_2} \right)^2 + y^2 \right]. \quad (1.2)$$

Lines of equal potential are known as *Roche equipotentials*, and it can be shown that the scale of the equipotentials depends only upon the separation of the two stars. It can also be shown that the shape of the equipotentials depends only upon the ratio

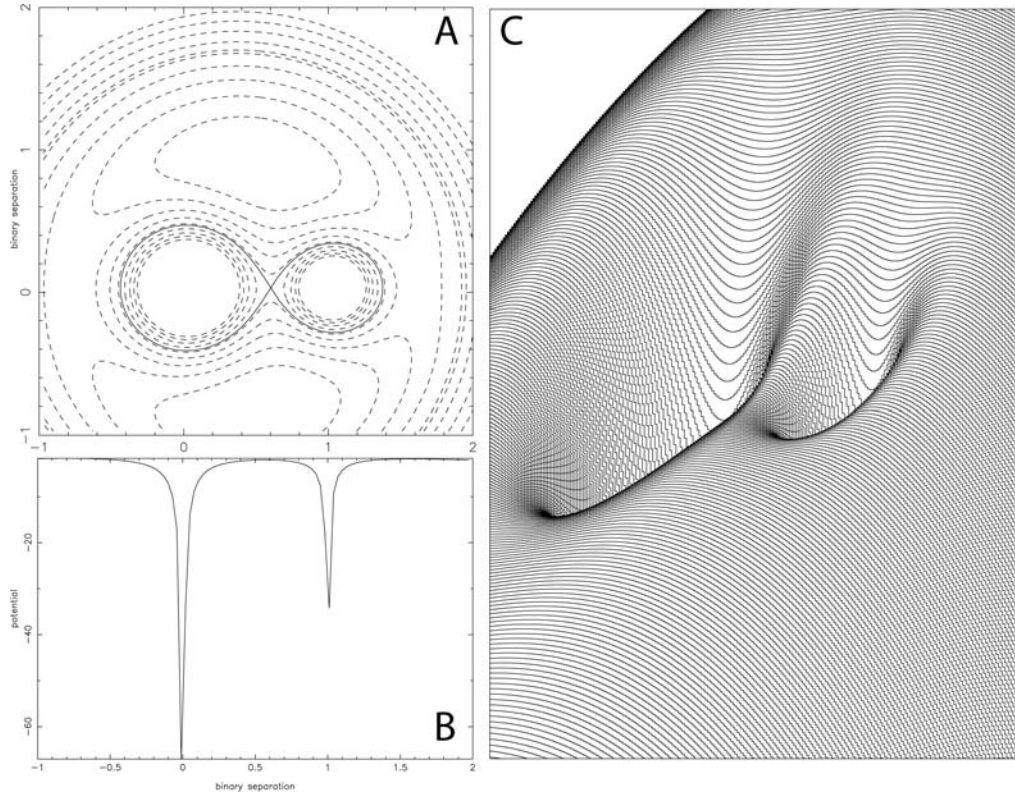


Figure 1.3: The Roche potentials. A: $q = 0.5$, in 2-dimensions, in the X-Y plane at $Z=0$. B: $q = 0.5$, in 1-dimension, cut in the x-axis along the line of centres. C: A pseudo 3-dimensional view of the Roche potential.

of masses between the two stars, q , that is defined as

$$q = \frac{M_2}{M_1} = \frac{K_1}{K_2}, \quad (1.3)$$

where K_1 and K_2 are the radial velocities of the primary and secondary stars, respectively.

Figure 1.3 shows the shape of the Roche potentials in 1, 2 and 3-dimensions. In Figure 1.3A, the potential defined by the figure of eight contour is the *critical potential*, which defines the *Roche lobes* of each star. The two Roche lobes meet at the inner Lagrangian point (L_1). For small stellar radii, a star lies well within its Roche lobe and is not distorted. In most CVs, this is the case for the white dwarf, but not the secondary star. In CVs, the secondary star fills its Roche lobe either by

expansion of the star through nuclear evolution, or by shrinking of the Roche lobe itself (see §1.4.3). If the Roche lobe is full, then matter ‘escapes’ the gravitational pull of the secondary star and flows between the two stars via the L_1 point (Paczynski, 1971).

In this thesis, the volume-equivalent radius of the Roche lobe, R_L , is used as a measure of the size of the secondary star. This is defined as the radius of the sphere that would have the same volume as the Roche-lobe, and is given by Eggleton’s formula (Eggleton, 1983), which is accurate to ~ 1 per cent:

$$\frac{R_L}{a} = \frac{0.49q^{2/3}}{0.6q^{2/3} + \ln(1 + q^{1/3})}, \quad 0 < q < \infty. \quad (1.4)$$

1.2 Types of Cataclysmic Variable

CVs derive their name from their *outbursts* - dramatic increases in the brightness of a system that can last from days to years with a wide range of amplitudes. Not all outbursts are caused by the same the physical process. These outbursts, although spectacular, are non-destructive. In some systems outbursts are frequently observed; in others they are rarely if at all seen. It is the range of outburst amplitudes, durations and recurrence times that lead to the definition of many classes and subclasses of CVs (Warner, 1995).

1.2.1 Classical and Recurrent Novae

Classical Novae (CN) were the first CVs to be observed. The increase in brightness in these systems may be anywhere between 6 and 19 magnitudes, and it exhibits a strong correlation with the nova decay time. The brightest eruptions tend to fade the fastest (days to weeks, *fast novae*), whilst the dimmer eruptions fade the slowest (months to years, *slow novae*). By definition, classical novae have been observed to

undergo one such outburst.

The mechanism responsible for CN is a *thermonuclear runaway explosion* (TNR) within a thin shell of hydrogen rich material accreted onto the surface of the white dwarf (see e.g. Shara, 1989; Warner, 1995, and references therein). As material is accreted into the shell, the pressure of the degenerate material rises to such a point where nuclear reactions begin. This increases the temperature of the material, which in turn increases the rate of reaction, leading to a runaway reaction within the hydrogen shell. This continues until the radiation pressure becomes great enough to blow the shell of material off the surface. The ejected material is often observed as a *nova* shell surrounding the CV. Spectroscopically this shell is observed as high-velocity, blue-shifted absorption lines accompanying each emission line. All CVs are expected to undergo many nova eruptions at some stage of their evolution with an expected recurrence time of approximately $10^4 - 10^6$ years (Shara et al., 1986; della Valle & Duerbeck, 1993). The discovery of a shell surrounding the dwarf nova Z Cam strongly supports this hypothesis (Shara et al., 2007).

Recurrent Novae (RN) are systems that have been observed to erupt more than once. The amplitudes, duration, decay time and recurrence time of RN often overlap those of *Dwarf Novae* (see §1.2.2), however the presence of the nova shell in their spectrum strongly suggests an outburst mechanism similar to that of CN. RN can be thought of as a special case of CN; the mass of the envelope required to trigger a TNR has been shown to fall rapidly with increasing white dwarf mass (e.g. Warner, 1995), and thus rapid accretion onto a high mass white dwarf would produce more frequent outbursts. Given that there is less material within the envelope compared to a CN, it follows that the amplitude, duration and decay time would also be smaller than those of CN. RN are therefore thought to be CVs in which accretion is occurring at a high rate onto a white dwarf that is close to the Chandrasekhar mass. Observational support of high mass white dwarfs in RN is provided by Thoroughgood et al. (2001),

who constrain the white dwarf in U Sco to be $M_1 > 1.31M_\odot$.

1.2.2 Dwarf Novae

Dwarf novae (DN) typically undergo outbursts with amplitudes between 2 and 6 magnitudes. Recurrence times are usually weeks to years, and are correlated with the duration of outburst (days to weeks). When a DN is not in outburst, or on the rise to outburst, it is said to be in *quiescence*. When it is in outburst, or on the rise to outburst, it is often described as being in a *high state*. Almost all of the objects studied in this thesis are DN in quiescence. The outburst mechanism for DN is very different from that of CN and RN. The favoured model is the *disc instability model* (Osaki, 1974). In the disc instability model (DIM), outbursts are caused by a sudden increase in mass transfer rate through the accretion disc. The DIM is discussed in detail in §1.3.

There are three distinct subtypes of DN based on the morphology of the long-term light curve. These include;

1. *SU UMa* stars. These systems exhibit occasional *super-outbursts* that are brighter (by ~ 0.7 magnitudes), and of longer duration (~ 5 times) than ordinary outbursts. In addition, they also exhibit *superhumps*. Superhumps are periodic humps that appear in the light curves of SU UMa stars as the star nears the maximum of its super-outburst. Superhumps have periods slightly longer than the orbital cycle, and there exists a unique relationship between the mass ratio, orbital period and superhump period (e.g. Patterson et al., 2005, §1.8.1).
2. *Z Cam* stars. These systems exhibit standstills around 0.7 magnitudes below the maximum brightness. During these standstills, regular outbursts cease for weeks to years. Z Cam stars are thought to have mass transfer rates very

close to the rate required to maintain a stable disc. Slight changes in the mass transfer rate are enough to drop the mass transfer rate below the rate required to maintain a stable disc and thus the disc becomes unstable and shows ‘normal’ DN outbursts.

3. *U Gem* stars. These are DN that do not exhibit standstills or super-outbursts, showing only ‘normal’ outburst behaviour.

1.2.3 Nova-Like Variables

The *nova-like variables* (NLs) generally include all CVs that follow the standard CV model outlined in §1.1.1, but have not shown any eruptive behaviour. This may be because the observational baseline of the system is too short, or the mass transfer rates are sufficiently high enough to suppress the disc instability mechanism (see §1.3). The majority of NL are thought to be because of the latter, and harbour steady state accretion discs. In this scenario the rate of mass transfer from the secondary star equals the accretion rate within the disc.

The NLs are divided into three main subgroups. These are the *UX UMa*, *RW Tri* and *AM CVn* stars. *UX UMa* stars show strong, broad absorption lines in their spectra, whilst the *RW Tri* stars show emission line spectra, occasionally with deep absorption cores. It is thought the differences in these two classes is due to inclination effects (with the *RW Tri* stars appearing more edge on). The *UM UMa* and *RW Tri* sub-classes can be broken down further into the *VY Scl* and *SW Sex* classes, that can belong to either the *UM UMa* or *RW Tri* classes. *VY Scl* systems exhibit periods of decreased brightness that last from weeks to years. *SW Sex* systems are eclipsing systems that show spectral peculiarities, such as single-peaked Hydrogen-Balmer and Helium emission (HeI) (see e.g. Dhillon et al., 2012, for recent developments). *AM CVn* stars are helium rich objects with ultra-short orbital periods (e.g. Nelemans,

2005). The secondary stars in these systems are thought to be a degenerate secondary star (e.g. another white dwarf). For a review of NLs, see e.g. Warner (1995), Dhillon (1996) and Hellier (2001).

1.2.4 Magnetic CVs

The magnetic CVs include *polars* (AM Her) and *intermediate-polars* (DQ Her). In magnetic systems, the magnetic field of the white dwarf is sufficiently strong enough to disrupt the formation of the accretion disc and boundary layer. This disruption may be partial (intermediate polars), and result in a truncated inner disc, or total (polars), where no disc forms and material flows directly onto the surface of the white dwarf via the magnetic field lines. In polars, the magnetic field strength of the white dwarf is so strong ($10^6 - 10^8$ Gauss) that the white dwarf is forced to rotate synchronously with its orbit. In intermediate polars the magnetic field strength is weaker, and the white dwarf rotates asynchronously with its orbit.

1.3 Disc Instability Model

As its name may suggest, outbursts in DN are the result of instability in the accretion disc. The source of this instability is *thermal instability* in the $\Sigma - T_{eff}$ plane, shown in Figure 1.4. The relationship between the surface density (Σ) and temperature (T_{eff}) describes an ‘S’-curve of thermal equilibrium where viscous heating is balanced by radiation from the surface of the disc. A system located off this line will heat or cool until thermal equilibrium is established. The relationship traces an S-shape due to variations in the opacity of disc material around the photo-ionisation point of hydrogen (see e.g. Lasota, 2001, for a review). The middle branch of the S-curve is thermally unstable and it is this instability that gives rise to DN outbursts. This can be understood by considering that the flux generated by viscosity must be

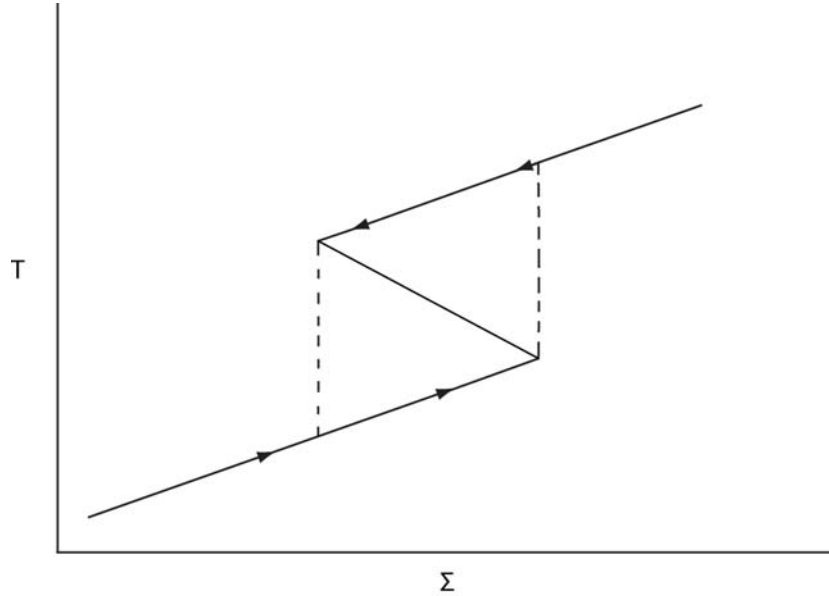


Figure 1.4: A schematic representation of the $\Sigma - T_{eff}$ relation. Dashed lines show the heating and cooling phases of the disc instability model. Arrows show the direction the disc moves through a DN outburst cycle.

proportional to the surface density of the disc. However, from the Stefan-Boltzmann law the emergent flux is proportional to T^4 . Therefore, for a given temperature, a system to the right of the curve in Figure 1.4 will produce more flux than can be radiated away and it will undergo rapid heating to return to thermal equilibrium. Likewise, a system to the left of the curve will undergo cooling. If the system is on the middle branch, a negative perturbation in temperature will move the system to the left of the S-curve and the system will experience rapid cooling moving to the lower branch. Likewise, a positive perturbation in temperature will produce rapid heating and move to the upper branch.

The overall outburst cycle of a DN can therefore be understood by considering an annulus of material in the disc. When the system is in quiescence, the rate of mass transfer to the annulus is greater than the rate of flow through the annulus (the local accretion rate). This results in a build up of material inside the annulus, increasing the surface density (Σ) and temperature (T_{eff}). The annulus thus moves along the

lower branch of Figure 1.4. When the annulus reaches the end of the lower branch, further increases in the surface density push the annulus out of thermal equilibrium and causes rapid, unstable heating until the annulus reaches the upper branch. At this point, a sudden rise in viscosity greatly increases the local accretion rate, leading to an outburst. The increase in viscosity can be understood by considering turbulence within the disc. Shakura & Sunyaev (1973) introduced the α -prescription, which characterises the viscosity of the disc in terms of turbulence, which in turn is described by a dimensionless parameter called the *alpha-viscosity*, α . This allows the viscosity of the disc, ν , to be quantified by

$$\nu = C_s H \alpha, \quad (1.5)$$

where C_s is the sound speed in the disc and H is the scale height of the disc. The sound speed is given by

$$C_s = \sqrt{\frac{3kT}{M_p}}, \quad (1.6)$$

where k is the Boltzmann constant, T is the temperature of the material and M_p is the mass of a typical particle. Therefore, for constant α , it follows that the viscosity of the disc will increase if the temperature of the disc increases. This increase in the viscosity of the disc therefore increases the local accretion rate, causing a reduction in the surface density and a cooling of the disc. The annulus now moves along the upper path of Figure 1.4. Eventually, the density and temperature drop to such a point where the annulus is on the left side of the S-curve, causing rapid cooling until thermal equilibrium is reached again on the lower path of Figure 1.4. The annulus is now back in quiescence and the cycle can begin again. The flow of material through one annulus naturally affects the flow of material to an adjacent annulus and so this cycle of heating and cooling in an unstable annulus triggers the same effect in neighbouring annuli, leading to most of the disc being in outburst or quiescence. This

mechanism also explains why DN outbursts are not seen in all systems; their mass transfer rates are high enough to maintain each annulus in the disc on the upper branch of Figure 1.4, or alternatively, the rates are too low and the system cannot leave the lower branch of Figure 1.4

Accretion disc models (e.g. Schreiber et al., 2003) suggest that for a DN in quiescence $\alpha \sim 0.01$, whilst in outburst $\alpha \sim 0.1$. The source of the viscosity is however still uncertain. Molecular viscosity is almost negligible ($\alpha \sim 10^{-11}$) and thus cannot account for the inferred α values. The most promising mechanism for accretion disc viscosity is the magnetic Balbus-Hawley (B–H) instability (Balbus & Hawley, 1991; Hawley & Balbus, 1998). Under the B-H instability, ionised material present within the disc couples to the magnetic field present in the disc. The exchange of angular momentum between coupled disc material results in material rotating at larger radii moving further out, material at smaller radii moving inwards and the magnetic field lines becoming stretched and amplified. As the magnetic field lines become more amplified, the process runs away, leading to magnetic turbulence throughout the disc. The large change in α between the high and low states of the accretion disc is evidence for the B-H instability because α increases as the disc becomes more ionised. At the same time, the B-H instability becomes more efficient as more ionised material is present. For a review of accretion discs, see e.g. Lasota (2001).

1.4 Origins and Evolution

1.4.1 Progenitors of CVs

White dwarfs (WDs) are the final stage in the evolution of low to intermediate mass stars, formed when a star sheds its hydrogen-rich envelope. Stellar theory tells us that the WD formed generally consists of either helium (He-WDs), carbon and oxygen

(CO-WDs), or oxygen and neon (ONe-WDs). The type of WD formed depends upon the initial mass of the star.

He-WDs ($0.15M_{\odot} \lesssim M_{wd} \lesssim 0.50M_{\odot}$) may form from low mass stars ($\lesssim 2.0M_{\odot}$) if the wind loss rate on the red giant branch is high enough (D’Cruz et al., 1996; Kalirai et al., 2007), or more likely via binary interactions (Marsh et al., 1995). CO-WDs ($0.50M_{\odot} \lesssim M_{wd} \lesssim 1.10M_{\odot}$) form from intermediate mass stars ($1.0M_{\odot} \lesssim M \lesssim 6 - 8M_{\odot}$ (e.g. Weidemann, 2000; Kalirai et al., 2008), whilst ONe-WDs ($1.10M_{\odot} \lesssim M_{wd} \lesssim 1.38M_{\odot}$) form from higher-mass intermediate stars ($8M_{\odot} \lesssim M \lesssim 9 - 10M_{\odot}$) (e.g. Prialnik, 2000; Salaris & Cassisi, 2005). The majority of CVs are found to contain WDs with masses around $\sim 0.75 - 0.77M_{\odot}$ (Smith & Dhillon, 1998; Knigge, 2006). This suggests a composition of carbon and oxygen, which in turn suggests the primary star was of intermediate mass. However, due to mass transfer, it is possible that the primary star was a low mass star that has subsequently accreted material.

WDs are formed following a giant phase of stellar evolution. During this phase, the stellar radii are typically around $10R_{\odot}$ (Hekker et al., 2011), but may extend as far as $\sim 200R_{\odot}$ (e.g. Prialnik, 2000; Schröder & Connon Smith, 2008). However, as discussed in §1.1.2, CVs have orbital separations of $\sim 1R_{\odot}$. This suggests that the system was initially a wide binary, and that significant orbital shrinkage must have taken place. The current explanation for this shrinkage is that the binary passes through a *common envelope phase* (Paczynski, 1976; Taam & Sandquist, 2000).

1.4.2 Common Envelope Phase

As a consequence of its higher mass, the primary star evolves to the giant phase of its evolution before the secondary star. During this giant phase, the primary star fills its Roche lobe and mass transfer commences from the primary star to the secondary star. As the secondary star is further from the centre of mass of the system, the orbital radius must decrease in order to conserve angular momentum. This causes

the Roche lobes to decrease in size, resulting in more matter being transferred. In this situation, mass transfer occurs on a timescale faster than the thermal timescale of the secondary star, and so the secondary star is unable to adjust its structure to accommodate this additional mass (see §1.4.5). The net result is unstable mass transfer that forms a common envelope surrounding both stars. The formation of this envelope is thought to be rapid and may only take a few orbital cycles (Paczynski, 1976).

The two stars continue to orbit within the common envelope, however they experience a drag force. This drag transfers angular momentum and energy from the binary to the envelope. This results in the binary separation shrinking dramatically and the luminosity of the envelope increasing rapidly (e.g. Meyer & Meyer-Hofmeister, 1979). If the energy released into the envelope is sufficient to exceed the binding energy of the envelope, then the envelope will be ejected as a planetary nebulae, leaving a *detached* binary system, consisting of a white dwarf primary and red dwarf secondary. If the energy released is insufficient, then the two stars are expected to merge and form a giant star. In either scenario, the common envelope phase is thought to be short, perhaps less than a few years (e.g. Passy et al., 2012; Ricker & Taam, 2012).

1.4.3 Pre-CV Evolution

The detached system that remains after the ejection of the common envelope, by definition, does not undergo mass transfer. In order to become a mass-transferring system once again, the secondary star must fill its Roche lobe. The mechanisms by which this can occur were briefly mentioned in §1.1.2; expansion of the secondary star through nuclear evolution, or by shrinking of the lobe.

The secondary stars in CVs are usually late-type, main-sequence like stars (e.g. Smith & Dhillon, 1998), that have a range of masses between $\sim 0.05 - 1.2M_{\odot}$. The lifetimes of these stars are long ($\tau_{ms} \gtrsim 10^9$ years) and so few will have been able

to expand to large enough radii to fill their Roche Lobe, given the current age of the universe. Therefore, a shrinking Roche lobe must be responsible for bringing the majority of systems into contact. This is possible through *angular momentum loss* (AML) from the binary: such AML shrinks the binary orbit and thus the size of the Roche lobe.

1.4.4 Direct Formation from a White Dwarf-Brown Dwarf Binary

Population synthesis models (Politano, 2004; Politano & Weiler, 2007) have shown that it is possible to form detached systems with secondary star masses in the substellar regime, provided the progenitor binary can survive the common envelope phase. Whether or not the system ejects the common envelope before a merger takes place, is dependent on the efficiency parameter, α_{ce} , of the envelope. Depending on the value of α_{ce} adopted, up to 15 per cent of the CV population could have formed in this way (Politano, 2004). Observations of the short period white dwarf-brown dwarf binary WD0137-349 (Maxted et al., 2006) have shown that progenitor systems do exist and can survive the common envelope phase. However, there is only one candidate CV that could have formed in this way: SDSS J1507+5230 (Littlefair et al., 2007), and even then, a far more plausible explanation is that this system is actually a member of the halo (Patterson et al., 2008; Uthas et al., 2011). It is likely that the lack of evidence for systems formed this way is a consequence of the so called ‘brown dwarf desert’ (e.g. Duquennoy & Mayor, 1991; Grether & Lineweaver, 2006), which is an observed lack of close ($\lesssim 5$ AU) brown dwarf companions to solar-type stars. Observations by Grether & Lineweaver (2006) have shown that brown dwarf-stellar binaries are ~ 10 times rarer than stellar-stellar binaries with orbital separations of $\lesssim 3$ AU. This therefore drastically reduces the number of systems that are able to,

or will be able to, enter a common envelope phase at some stage of their evolution.

1.4.5 Response to Mass Loss

The total angular momentum of the binary, J , can be written as

$$J = M_1 a_1 \frac{2\pi a_1}{P_{orb}} + M_2 a_2 \frac{2\pi a_2}{P_{orb}} = M_1 M_2 \left(\frac{Ga}{M} \right)^{\frac{1}{2}}, \quad (1.7)$$

where M is the total mass of the binary ($M = M_1 + M_2$) and a_1 and a_2 are the semi-major axis of each component ($a_1 + a_2 = a$). This can be logarithmically differentiated to give

$$\frac{\dot{J}}{J} = \frac{\dot{M}_1}{M_1} + \frac{\dot{M}_2}{M_2} + \frac{1}{2} \frac{\dot{a}}{a} - \frac{1}{2} \frac{\dot{M}}{M}. \quad (1.8)$$

Assuming that mass loss is conservative, that is $\dot{M}_1 = -\dot{M}_2$ and $\dot{M} = 0$, then

$$\frac{\dot{a}}{a} = 2 \frac{\dot{J}}{J} - 2(1 - q) \frac{\dot{M}_2}{M_2}. \quad (1.9)$$

Therefore, if the total angular momentum of the system is conserved ($\dot{J} = 0$), mass transfer from the secondary star to the primary star results in a increasing (provided $M_2 < M_1$). A similar expression for the response of the Roche lobe to mass loss can be derived using the relationship provided by Smith & Dhillon (1998) for the volume equivalent radius of the Roche lobe¹,

$$R_L = 0.47a \left(\frac{M_2}{M} \right)^{1/3}, \quad (1.10)$$

which may be logarithmically differentiated to give

$$\frac{\dot{R}_L}{R_L} = \frac{\dot{a}}{a} + \frac{1}{3} \frac{\dot{M}_2}{M_2} - \frac{1}{3} \frac{\dot{M}}{M}. \quad (1.11)$$

¹It is also possible to use Equation 1.4 or similar, however the mathematical manipulation is considerably more difficult and does not significantly increase the accuracy of the result.

By re-arranging Equation 1.11 for \dot{a}/a , and continuing the assumption that $\dot{M} = 0$, substituting into Equation 1.9 yields

$$\frac{\dot{R}_L}{R_L} = 2\frac{\dot{J}}{J} - \frac{\dot{M}_2}{M_2} \left(\frac{5}{3} - 2q \right). \quad (1.12)$$

From Equation 1.12, it can be seen that the response of the Roche lobe to mass loss is dependant on q . For the fully conservative case, $\dot{J} = 0$, and the Roche lobe will expand in response to mass loss whenever $q < 5/6$.

The stability of mass transfer depends on the relative change of the secondary star radius to its Roche lobe. For stable mass transfer, the secondary star must be able to adjust its radius quickly enough to remain within its Roche lobe; mass transfer is unstable if the radius of the secondary star expands relative to the radius of the Roche lobe. The criteria for stable mass transfer can be expressed as

$$\frac{\dot{R}_L}{R_L} \geq \frac{\dot{R}_2}{R_2}. \quad (1.13)$$

For the fully conservative case ($\dot{J} = 0$), combining Equations 1.12 and 1.13 with a mass-radius relationship in form of

$$R_2 \propto M^\xi, \quad (1.14)$$

gives rise to the following criteria for stable mass transfer

$$q \leq \frac{\xi}{2} + \frac{5}{6}. \quad (1.15)$$

The secondary star responds to mass loss on two timescales. The first is the *dynamical timescale*, T_{dyn} , which is the time taken to return to hydrostatic equilibrium,

and is given by

$$T_{dyn} = [G\bar{\rho}(R)]^{-1/2} \quad (1.16)$$

(e.g. Warner, 1995), where $\bar{\rho}$ is the mean density within a radius R . The second timescale is the *thermal timescale* of the secondary star (sometimes referred to as the *Kelvin-Helmholtz timescale*), which is the time taken for the secondary star to settle into a new thermal equilibrium configuration. This is given by

$$T_{KH} \sim \frac{GM_2^2}{R_2 L_2}, \quad (1.17)$$

where L_2 is the luminosity of the secondary star.

The initial response of the secondary star to mass loss is adiabatic and the secondary star will expand with mass loss. If the secondary star expands *relative* to the Roche lobe, mass transfer is said to be dynamically unstable and mass transfer will proceed on the dynamical timescale. To determine the condition for stable mass transfer to occur, the adiabatic response of the secondary is required. For low mass stars ($M_2 \lesssim 0.43$), this corresponds to $\xi = -1/3$ (Paczynski, 1965; Rappaport et al., 1982; Hjellming & Webbink, 1987; Politano, 1996). Using Equation 1.15, it can be seen that for dynamically stable mass transfer, $q \leq 2/3$. A system with $q > 2/3$ will therefore transfer mass on a dynamical timescale and rapidly form a common envelope. This system would by definition not be observed as a CV.

Whether the secondary star returns to thermal equilibrium depends how T_{KH} compares to the *mass-loss timescale* of the secondary star, T_{ML} , where

$$T_{ML} \sim \frac{M_2}{\dot{M}_2}. \quad (1.18)$$

If the mass-loss timescale is greater than the thermal timescale ($T_{ML} > T_{KH}$), the secondary star can respond to mass loss and maintain its thermal equilibrium. Under

this scenario, the secondary star will follow a mass-radius relationship similar to that of a main sequence star,

$$\frac{R_2}{R_\odot} = (0.91 \pm 0.09) \frac{M_2}{M_\odot}^{(0.75 \pm 0.04)} \quad (1.19)$$

(e.g. Smith & Dhillon, 1998), and therefore $\xi = 0.75$. Using Equation 1.15, it can be seen that for thermally stable mass transfer, $q \lesssim 1.21$. Systems not obeying this will be thermally unstable and transfer mass on a thermal timescale. These systems are thought to be one source of super-soft x-rays (SSSs, e.g. Kahabka & van den Heuvel, 1997; Schenker, 2001).

Mass transfer in CVs is both dynamically and thermally stable. Systems that are not stable will appear as other objects (e.g. SSSs). Most CVs also have $q < 5/6$ (Patterson et al., 2005), which from Equation 1.12, was shown to result in an expanding Roche lobe with mass loss. Therefore, in order for mass transfer to be sustained, angular momentum must be continuously lost from the binary orbit to keep the Roche lobe in contact with the surface of the secondary star. This is often described as a two stage process, where mass is first transferred from the secondary star to the primary star, which causes the orbital separation to increase, the Roche lobe to expand and the radius of the secondary star to decrease. The secondary star is now no longer in contact with the Roche lobe. In the next stage, the binary loses some angular momentum from its orbit, which decreases the orbital period and shrinks the Roche lobe back onto the surface of the secondary star. Mass transfer is then able to recommence. In practice, this is a continuous process and thus cataclysmic variables evolve to shorter orbital periods and the secondary stars to lower masses via AML from the binary orbit. There are thought to be two main mechanisms for AML in CVs; gravitational radiation and magnetic braking.

1.5 Angular Momentum Loss

1.5.1 Magnetic Braking of the Secondary Star

Magnetic braking (Verbunt & Zwaan, 1981; Rappaport et al., 1983) is a result of two components - an ionised stellar wind and a stellar magnetic field present in the secondary star. Under these conditions, the energetic, ionised particles present in the stellar wind of the secondary star are forced to co-rotate with the star due to coupling with the magnetic field lines of the secondary star. This co-rotation extracts angular momentum from the secondary star, and because the secondary star is locked in synchronous rotation, angular momentum is extracted from the binary as a whole. This causes the orbital separation to shrink.

Magnetic braking is still poorly understood in comparison to gravitational radiation and thus quantifying the AML and induced mass transfer for this mechanism is difficult (see e.g. Appendix A of Knigge et al., 2011, for a review). Whichever prescription of AML due to magnetic braking is adopted, it must be strong enough to drive mass-transfer rates in high accretion rate systems, which are observed to be $\sim 10^{-8} - 10^{-9} M_{\odot} \text{ yr}^{-1}$ (Townsend & Gänsicke, 2009).

1.5.2 Gravitational Radiation

General relativity states that matter causes space to curve. As a consequence of this, two stars orbiting in a close binary will cause a repeated disturbance in space curvature that results in waves propagating outwards from the source. These waves are known as *gravitational radiation*. The waves requires energy, which is consequently extracted from the binary orbit, causing the orbit to decay. The rate of angular momentum loss through gravitational radiation is given by

$$\frac{\dot{J}}{J} = \frac{-32G^3}{5c^5} \frac{M_1 M_2 (M_1 + M_2)}{a^4} \quad (1.20)$$

(e.g. Kraft et al., 1962; Paczyński, 1967; Webbink, 1976; Paczynski & Sienkiewicz, 1981; Rappaport et al., 1982). Warner (1995) show that for a main sequence secondary star, this leads to typical mass transfer rates of

$$\dot{M}_2 = 3.8 \times 10^{-11} \frac{M_1^{2/3} P_{orb}^{-\frac{1}{6}}(h)}{\left(1 - \frac{15q}{19}\right)(1+q)^{\frac{1}{3}}} M_{\odot} \text{yr}^{-1}. \quad (1.21)$$

For an orbital period of 2 hours, $M_1 = 0.75M_{\odot}$ and $M_2 = 0.15M_{\odot}$. Equation 1.21 suggests mass transfer rates of $\dot{M}_2 \sim 3.1 \times 10^{-11} M_{\odot} \text{yr}^{-1}$. AML through gravitational radiation therefore drives mass-loss at a rate of ~ 2 orders of magnitude less than that from magnetic braking.

1.6 The Secondary Stars in CVs

Combining Equations 1.1 and 1.10 yields a relationship between the orbital period, the mass of the secondary star, and radius of the secondary star,

$$P_{orb}^2(s^2) = 5.7 \times 10^{12} \left(\frac{R_2^3(m^3)}{M_2(kg)} \right). \quad (1.22)$$

Given that the mean density of the secondary star ($\bar{\rho}_2$) can be expressed as

$$\bar{\rho}_2 = \frac{3M_2}{4\pi R_2^3}, \quad (1.23)$$

and that the secondary star fills its Roche lobe, combining Equations 1.22 and 1.23 gives the *period density* relationship,

$$\bar{\rho}_2 (kg m^{-3}) = 1.361 \times 10^{12} P_{orb}^{-2}(s). \quad (1.24)$$

For orbital periods between 80 minutes and 11 hours, the mean density of the secondary star is $59000 \text{ kg m}^{-3} > \bar{\rho}_2 > 870 \text{ kg m}^{-3}$, which corresponds to the mean densities found in \sim F7V-M8V main sequence stars (Binney & Merrifield, 1998). Thus the majority of secondary stars in CVs should be similar to M, K, G, or late F main sequence stars.

The secondary stars in CVs can differ from main sequence stars due to the effects of mass loss, which can drive the secondary out of thermal equilibrium. As noted in §1.4.5, whether a system is thermal equilibrium depends how its thermal timescale compares to its mass loss timescale. If $T_{ML} > T_{KH}$, the secondary star can respond to mass loss and maintain thermal equilibrium. If the situation is reversed ($T_{ML} \leq T_{KH}$), the secondary star cannot respond to mass loss quickly enough to maintain thermal equilibrium, thus becoming oversized for a given mass.

1.7 The Distribution of Orbital Periods

The orbital period, P_{orb} , is by far the most commonly known parameter of CVs. Orbital periods are currently known for \sim 950 systems (Ritter & Kolb, 2003, Ritter 2012+). Because CVs evolve from longer periods to shorter periods (see §1.4.5), the distribution of orbital periods, as shown in Figure 1.5, offers strong clues to the detailed evolution of CVs. Considering Figure 1.5, there are three striking characteristics:

1. the number systems with orbital periods above \sim 6 hours decreases towards longer orbital periods, with few systems above \sim 11 hours (*the long period cut-off*),
2. there are a lack of systems with periods between \sim 2.2-3.2 hours (*the period gap*),

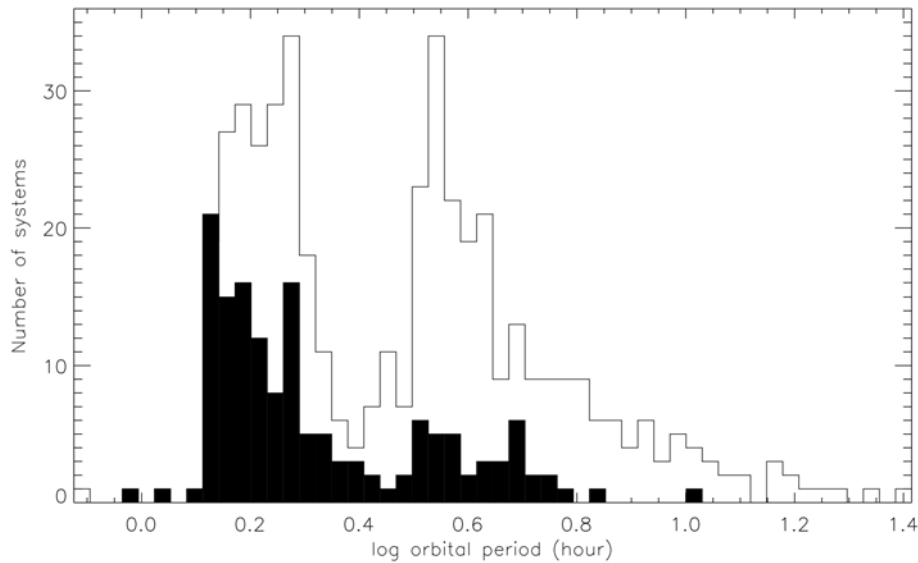


Figure 1.5: A histogram of the orbital period distribution, from Southworth et al. (2012). The systems marked in black are the systems discovered via the Sloan Digital Sky Survey (SDSS), whilst the systems in white are those catalogued by Ritter & Kolb (2003).

3. there is a sharp cut off of systems with periods below ~ 80 minutes (*the period minimum*).

Any theory of CV evolution must be able to account for these observations.

1.7.1 The Long Period Cut-Off

The lack of long period systems can be explained as a consequence of mass transfer stability. As the orbital period increases, so does the mass of the secondary star. It was shown in §1.4.5 that for thermally stable mass transfer, $q \lesssim 1.21$; given that the maximum possible mass of the primary star is $1.4 M_{\odot}$ (the Chandrasekhar limit), this limits the mass of the secondary star to $M_2 \lesssim 1.7M_{\odot}$. Note that this assumed $\dot{J} = 0$, which is not strictly true for CVs. If $\dot{J} < 0$, then from Equations 1.12 and 1.13, it can be shown that this upper limit of 1.21 decreases further.

Combining Equation 1.22 with a mass-radius relationship (e.g. Equation 1.19), a secondary star mass of $M_2 \lesssim 1.7M_{\odot}$ suggests a maximum orbital period of ~ 10

hours. Objects with orbital periods longer than ~ 10 hours are thought to possess evolved secondary stars. Evolved stars are larger than a main-sequence star of the same mass and are therefore able to fill their Roche lobes at a lower mass. Because there are few white dwarfs with masses close to the Chandrasekhar limit, the number of systems with orbital periods greater than 6 hours naturally begins to dwindle.

1.7.2 The Period Gap

The standard explanation for the observed period gap is the *disrupted magnetic braking* (DMB) scenario (Spruit & Ritter, 1983; Rappaport et al., 1983). In the DMB model CVs above the period gap experience AML through gravitational radiation (GR) and magnetic braking (MB), causing the orbital period and mass of the secondary star to decrease.

For CVs with periods around 5–6 hours, mass transfer rates are typically $10^8 - 10^9 M_\odot \text{ yr}^{-1}$. The secondary star masses are around $\sim 0.6 M_\odot$ with approximate radii of $\sim 0.6 R_\odot$ (e.g. Smith & Dhillon, 1998). Assuming the luminosity follows a similar relationship to that of a main sequence star ($L \propto M^{3.5}$), it can be seen from Equations 1.17 and 1.18 that $T_{ML} > T_{KH}$, and therefore the secondary star can respond quickly to mass loss and maintain a near-main sequence mass-radius relationship. However, as a system evolves to shorter periods and lower masses, T_{KH} increases faster than T_{ML} , and thus the secondary star is gradually driven out of thermal equilibrium (e.g. Patterson, 1984) becoming too large for its mass. As the orbital period of the secondary star approaches ~ 3 hours, the efficiency of magnetic braking is assumed to drop dramatically, possibly ceasing completely. This decrease in efficiency is thought to be caused by the mass of the secondary star crossing the convective boundary (Robinson et al., 1981), resulting in a dramatic loss of efficiency or cessation in its magnetic field (MacGregor & Charbonneau, 1997; Charbonneau & MacGregor, 1997). In single, isolated stars, this happens around $M_2 \sim 0.35 M_\odot$

(Chabrier & Baraffe, 1997), but in CVs it corresponds to secondary star masses around $0.20 - 0.30M_{\odot}$ (e.g. Smith & Dhillon, 1998; Patterson et al., 2005; Knigge, 2006). This sudden drop in mass transfer rate increases T_{ML} , such that it exceeds T_{KH} . This means the secondary star is able to relax back into thermal equilibrium and detach from its Roche lobe, thus terminating mass transfer. The loss of angular momentum from the binary orbit continues under the influence of GR until the Roche lobe comes into contact with the surface of the secondary star again at a period of ~ 2 hours, and mass transfer is able to commence, albeit at a lower rate. As a result, stars at the lower and upper edge of the period gap should have the same mass.

Despite the lack of plausible alternatives, this model has been challenged on the interpretation of rotation rates in open clusters. Andronov et al. (2003) argue that the observed spin down of rapid rotators implies AML rates that are too low to drive CVs out of thermal equilibrium, and that there is no evidence for a change in spin-down rates around $0.25M_{\odot}$. By contrast, Barnes (2003) argues that the open cluster data may be interpreted as two different magnetic field configurations for stars with a radiative/convective boundary, and that whilst radiative/convective stars can show either strong or weak MB, fully convective stars can only show weak braking. As a result, a transition would still be observed from strong to weak MB across the convective boundary. Likewise, observations by Reiners & Basri (2008) hint at a drop off in the efficiency of magnetic braking for stars below the convective boundary. Patterson et al. (2005) has shown that there is a discontinuity in secondary star masses between the upper and lower edges of the period gap, which adds further support to the DMB hypothesis.

Under the standard model of CV evolution, the small number of CVs that are present in the period gap are explained as either magnetic systems that do not show a period gap (e.g. Warner, 1995; Gänsicke et al., 2009), CVs that possess an evolved secondary star (e.g. Littlefair et al., 2006a), or are recently born systems that have

just exited the common envelope phase and commenced mass transfer (Davis et al., 2008).

1.7.3 The Period Minimum

The minimum period can be explained by considering Equation 1.22. The evolution to shorter orbital periods as M_2 decreases depends upon the response of the radius of the secondary star to mass-loss. For long period systems where the secondary stars are approximately main sequence, mass loss naturally drives the system to shorter periods. However, if the mass-radius relationship deviates significantly from that of a main sequence star, the evolution of the orbital period will also deviate. This can also be understood by considering Equation 1.22. If R_2^3/M_2 increases, so does the orbital period. Therefore by considering a mass-radius relationship in the form of $R_2 \propto M_2^x$, it can be seen that whenever $x < 1/3$, the orbital period will increase. Systems that have evolved past the period minimum are known as *post-period-bouncers*, or ‘period-bouncers’. This is thought to occur when the secondary star has lost enough mass to become a brown-dwarf like, partially degenerate object. Under this regime, hydrogen burning ceases and the mass-radius relationship begins to deviate significantly from that of a main sequence star. For example, a $0.05M_\odot$ brown dwarf is very similar in radius to Jupiter, but yet the mass is approximately 50 times greater.

The exact mass and orbital period at which the period minimum occurs depends on the thermal timescale of the secondary star (Equation 1.17) and the mass-loss timescale of the secondary star (Equation 1.18). As the system evolves towards shorter orbital periods, the secondary star evolves towards degenerate masses. At the same time, both timescales increase, however T_{KH} does so faster. When T_{ML} becomes shorter than T_{KH} , the secondary star is unable to respond rapidly enough to the mass loss and so is driven out of thermal equilibrium. Once out of thermal equilibrium, L_2 is reduced and so T_{KH} increases. Further mass loss thus drives the

star further from thermal equilibrium and so the star becomes progressively more oversized for its mass. Therefore the mass-radius index and the actual value of P_{min} is thus highly dependant on the point when the secondary star is driven out of thermal equilibrium, which is in turn highly sensitive to \dot{M}_2 , and therefore the AML rate from the binary orbit. The larger the AML rate, the shorter T_{ML} , and the sooner the star is driven out of thermal equilibrium, leading to higher P_{min} values.

In Figure 1.5, there are a large number of systems with periods immediately above the minimum period. This is known as the *period-spike*. The period spike arises because the time spent at a given orbital period is inversely proportional to the rate of change of orbital period (\dot{P}_{orb}), which is related to the AML rate and from Equation 1.22, the rate of change of radius of the secondary star. At the period minimum, $\dot{P}_{orb} = 0$, and so systems accumulate.

Standard evolutionary models predict that the minimum period should occur around $P_{min} \approx 65$ minutes (Kolb & Baraffe, 1999; Howell et al., 2001), and that up to ~ 70 per cent of the current CV population should have evolved past the period minimum (Kolb, 1993). This is in stark contrast to observations. The period spike has only recently been identified, and indicates that the period minimum is $P_{min} = 82.4 \pm 0.7$ minutes (Gänsicke et al., 2009). In addition, it is only recently that any post-period-bounce systems have been identified (Littlefair et al., 2006b, 2008). A longer than expected period minimum suggests that the secondary stars are larger than expected, which is supported by observations (e.g. Littlefair et al., 2008). This may be due to missing stellar physics, such as magnetic activity in the form of star spots (Chabrier et al., 2007), or an AML rate which is greater than expected. Given that AML through GR is well quantified, this suggests an additional form of AML may be present for CVs below the period (e.g. Willems et al., 2005).

One way to determine why the secondary stars appear oversized is to compare the shape of the observed secondary star mass-period relationship ($M_2 - P_{orb}$), and

by implication, mass-radius ($M_2 - R_2$) relationship, to the models of Kolb & Baraffe (1999), calculated with enhanced AML or modified stellar physics. Both of these models, in principle, make different predictions for the shape of the mass-radius relationship and position of the period minimum. If enhanced angular momentum loss is responsible for oversized CV secondaries, the systems immediately below the period gap would not be expected to be far from thermal equilibrium. In contrast, magnetic activity in the form of star spots would inhibit the convective processes in all the CV secondary stars below the period gap (assuming that spot properties are similar at all masses).

1.8 The Importance of Secondary Star Properties

The physical properties of the secondary stars in CVs are vital to understanding the evolution of CVs. In §1.4.5, it was shown that the secondary stars in CVs evolve towards lower masses and that CVs themselves (generally) evolve towards shorter orbital periods. Thus, the secondary star's mass serves as an indicator of the evolutionary status of a system. For example, systems with low masses can generally be considered older. However, the secondary star's mass *and* radius (and by analogy, P_{orb}), also tell us about the system's *long-term mass-transfer rate*, because the radius of a star is a measure of its state of thermal equilibrium. The long-term mass-transfer rate is responsible for the secular evolution of CVs, which is driven by AML from the binary orbit. Thus, an understanding of AML rates is crucial to understanding CV evolution.

AML rates are typically inferred by estimating the mass-transfer rate, \dot{M}_2 . However, it is thought that \dot{M}_2 may vary significantly on timescales of $\sim 10^4 - 10^9$ years (Knigge et al., 2011). Patterson (1984) show that \dot{M}_2 can be estimated using the luminosity of the accretion disc, however this technique is sensitive to a short ob-

servational baseline ($\sim 10 - 100$ years) and distance estimations, which are difficult to obtain. Alternatively, Townsley & Gänsicke (2009) use the effective temperature of the white dwarf to infer \dot{M}_2 . These are also difficult to obtain and average over $\sim 10^3 - 10^5$ years. Both of these methods are likely to provide a measure of the short term mass-transfer rate and therefore cannot be used to reliably trace the secular mass-transfer rate. The most reliable method for determining the long-term \dot{M}_2 is to use the radius of the secondary star. Stehle et al. (1996) and Knigge et al. (2011) show that the adjustment time of secondary star (T_{adj}) is given by

$$T_{adj} \sim 0.05T_{KH}, \quad (1.25)$$

which is longer the timescales discussed above and comparable to timescales on which mass transfer varies. Thus the mass-radius relationship for the secondary stars in CVs is crucial in understanding the evolutionary processes of CVs. To deduce the accurate mass-radius relationship, accurate and precise measurements of the masses and radii are required for a large sample of CVs, covering a wide range of orbital periods. Unfortunately, accurate and precise mass determinations are difficult to obtain. This is especially so for short period systems, whose secondary stars are often too faint to be visible in the spectrum (Friend et al., 1988; Littlefair, 2002; Littlefair et al., 2003), and have mass-transfer rates too low for clear bright spot ingress and egress features to be visible in their light curves (e.g. Chapter 4).

1.8.1 Superhumps

Although direct measurements of secondary star masses are difficult, there is an indirect method of measuring secondary star masses using a phenomena present in the light curves of many dwarf novae. As discussed in §1.2, SU UMa stars exhibit superhumps. These superhumps are caused by the precession of an elliptical disc

(Vogt, 1982; Osaki, 1985; Smith et al., 2007). The precession period, P_{pc} is longer than the orbital period, resulting in a ‘beat’, or *superhump period*, P_{sh} , between the orbital and precessional periods, which is given by

$$\frac{1}{P_{sh}} = \frac{1}{P_{orb}} - \frac{1}{P_{pc}}, \quad (1.26)$$

and so the fractional period excess (ϵ) of the superhump period can be given by

$$\epsilon = \frac{P_{sh} - P_{orb}}{P_{pc}}. \quad (1.27)$$

The elliptical disc forms through tidal interactions of the outer disc with the secondary star. These tidal forces result in material being pulled towards the secondary star, causing a slight bulge, which lies slightly ahead of the secondary star in orbital phase. However, the Keplerian orbit of the material at the edge of the disc is much faster than the orbital motion of the secondary star, and so provided $q \leq 0.35$ (e.g. Hellier, 2001; Patterson et al., 2005), it is possible for the disc material to achieve a 3:1 resonance with the secondary star. This resonance enhances the radial component of the disc material, elongating the orbital paths of the outer disc material. Because the ellipticity of the disc is formed through tidal interactions with the secondary star, the precession period, and therefore the superhump excess, depends upon the mass of the secondary star, and thus the mass ratio, q (Patterson, 1998). By measuring the superhump excess for CVs of known q , an empirical relationship between $\epsilon - q$ can be deduced. This is known as the *superhump excess-mass ratio* relationship. The secondary star mass of a superhumping CV can therefore be estimated by measuring ϵ , calculating q using the empirical relationship, and assuming a white dwarf mass.

1.8.2 Empirical Donor Sequences

In recent years several authors (Patterson et al., 2005; Pearson, 2006; Knigge, 2006) have derived $\epsilon-q$ relationships based on available mass estimates. These relationships have been used to derive secondary star masses and other physical properties for large numbers of CVs, which in turn have enabled the construction of a semi-empirical donor sequence against which CVs can be compared and other properties inferred (Knigge, 2006; Knigge et al., 2011). Knigge et al. (2011) also constructed a ‘self consistent’ CV evolutionary track, that implies the angular momentum rate loss below the period gap is around 2.5 times greater than the standard model of CV evolution and 1.5 times less for system above the period gap. These evolutionary tracks are important to our understanding of CVs, however they require accurate mass and radii determinations for calibration purposes.

1.9 This Thesis

In this thesis I present accurate mass determinations for 17 eclipsing CVs made using high-speed, three colour photometry, with the aim of using the masses and other system parameters, to test theories regarding the evolution of CVs. A detailed journal of observations, and the steps undertaken to reduce and calibrate the data used in this thesis are given in Chapter 2. In Chapter 3, I describe the analysis techniques used to derive the results of this thesis. In Chapter 4, I look at the light curve morphology of 20 eclipsing CVs, and identify systems that are suitable for light curve modelling and systems of interest for long term monitoring. In Chapter 5, I present the results of light curve modelling for 17 eclipsing CVs, and in Chapter 6, I test the validity of the light curve modelling technique by determining the mass of one eclipsing CVs using time-resolved spectroscopy. In Chapter 7, I investigate time-resolved spectra of a period-bouncing CV, and attempt to make the first direct

spectroscopic detection of a brown-dwarf like secondary star.

Chapter 2

Observations and Data Reduction

In this chapter I will outline the observations which form the basis of this thesis. Three forms of data are presented in this thesis; high-speed, multi-wavelength photometry; medium resolution, multi-wavelength spectroscopy; and low resolution J-band spectroscopy. First I discuss the observations, and then describe the steps undertaken to reduce and calibrate the data. The reduction of the data and the following text are my own work unless stated otherwise.

2.1 Observations

2.1.1 ULTRACAM Photometry

The photometry data presented in this thesis were obtained during six observing runs using the ULTRACAM (Dhillon et al., 2007) and ULTRASPEC (Dhillon et al., 2008) instruments on the following telescopes;

1. The 8.2-m Very Large Telescope (VLT), operated by the European Southern Observatory (ESO), at the Paranal observatory, Chile.
2. The 3.5-m New Technology Telescope (NTT) operated by ESO, at the La Silla

observatory, Chile.

3. The 4.2-m William Herschel Telescope (WHT) operated by the Isaac Newton Group of Telescopes (ING), on the island of La Palma, Spain.

ULTRACAM is an ultra-fast, triple-beam CCD camera that is capable of imaging in three different wave-bands simultaneously at speeds of up to 500 Hz. ULTRASPEC is the spectroscopic equivalent of ULTRACAM, although it is also equipped with an imager. For the data presented in this thesis, ULTRASPEC was used in imaging mode, making it near-identical to ULTRACAM, albeit with only single wave-band coverage. Consequently, the data reduction processes undertaken are the same as those for ULTRACAM, which are described in detail in this Chapter. Both instruments use the Sloan Digital Sky Survey (SDSS) $u'g'r'i'z'$ filter system (Fukugita et al., 1996; Smith et al., 2002). For further information, see Feline (2005), Dhillon et al. (2007) and Dhillon et al. (2008).

The initial target list consisted of CVs that were identified as eclipsing DN during the Sloan Digital Sky Survey (SDSS) follow-up (Szkody et al., 2002, 2003, 2004, 2005, 2007, 2009). This list was supplemented with all newly discovered eclipsing DN (e.g. Warner & Woudt, 2010). The targets that were eventually observed depended on scheduling constraints and target visibility. In Tables 2.1a, 2.1b, 2.1c and 2.1d I present details of all of the ULTRACAM/ULTRASPEC observations used in this thesis. Table 2.1a includes the objects CTCV 2354, CTCV 1300, SDSS 1152 and SDSS 1501, which form the main basis of Chapter 4, Chapter 5 and Savoury et al. (2011). In Table 2.1b, I present observations of the targets CSS080623, SDSS 0901 and PHL 1445. These systems are also included and analysed in Chapters 4 and 5, however, they are not published in Savoury et al. (2011). Tables 2.1c and 2.1d contain details of all remaining systems presented in Chapter 4 (SDSS 1250, SDSS 1555, SDSS 1524, SDSS 1325, SDSS 0750, CSS0806227, 1RXS J1808, SDSS 0920, GALEX0035,

SDSS 1006, SDSS 0924 and SDSS 0935) that were not used for photometric mass determinations or published in Savoury et al. (2011). This data was mostly used for determination of ephemerides. Full object names are provided in Chapter 4.

In addition, this thesis has also made use of a large amount of archival ULTRACAM data, which are not discussed here. The reduction of this data was carried out by William Feline and Stuart Littlefair in an identical manner to that described in §2.3. For details of these observations, the reader is referred to table 1 in the following publications: Feline et al. 2004a (OU Vir), Feline et al. 2004b (XZ Eri and DV UMa), Littlefair et al. 2006a (SDSS 1702), Littlefair et al. 2007 (SDSS 1507) and Littlefair et al. 2008 (SDSS 0903, SDSS 1227, SDSS 1433, SDSS 1501 and SDSS 1502).

Observations of the standard stars G162-66, G27-45, G93-48, G163-50 and Feige 22 were used to correct the magnitudes to the SDSS system (Smith et al., 2002), as described in §2.4.2. Due to time constraints and poor weather, no standard star could be observed to flux calibrate the data for SDSS 1152. Consequently, the Sloan magnitudes of the comparison stars were taken and corrected for the instrumental response of ULTRACAM. To do this, the measured response curves for the filters and dichroics used in ULTRACAM were used to create an overall ULTRACAM response curve. This was combined with curves of theoretical extinction (Hickman, 2011) and library spectra (Pickles, 1998) to obtain synthetic ULTRACAM colours. The same process was then repeated for the SDSS colour set, with the difference between the two sets being the correction applied.

2.1.2 X-Shooter Spectroscopy

CTCV 1300 was observed using the X-Shooter (Vernet et al., 2011) in service mode mounted on UT2 (Kueyon) on the VLT, at the Cassegrain focus on the nights beginning 9 February 2010 and 6 March 2010. CTCV 1300 was observed using the

Date	Object	Instr setup	T_{mid} (HMDJ)	Cycle	Phase Cov	Filters	T_{exp} (s)	N_{exp}	Seeing (")
2007 June 09	CTCV 2354	VLT+UCAM	54261.383926(25)	0	0.73-1.08	u'g'r'	2.22	821	0.6-1.0
2007 June 13	CTCV 2354	VLT+UCAM	54265.316786(61)	60	0.70-1.11	u'g'r'	4.92	473	0.8-1.2
2007 June 15	CTCV 2354	VLT+UCAM	54267.348921(21)	91	0.78-1.08	u'g'r'	2.22	779	0.6-0.7
2007 June 15	CTCV 2354	VLT+UCAM	54267.414476(20)	92	0.74-1.05	u'g'r'	2.22	757	0.6-0.7
2007 June 16	CTCV 2354	VLT+UCAM	54268.397717(20)	107	0.72-1.06	u'g'r'	2.22	845	0.6-1.1
2007 June 19	CTCV 2354	VLT+UCAM	54271.413077(21)	153	0.82-1.15	u'g'r'	2.22	826	0.6-1.0
2007 June 20	CTCV 2354	VLT+UCAM	54272.396368(29)	168	0.50-1.50	u'g'r'	2.32	2390	0.6-1.0
2007 June 21	CTCV 2354	VLT+UCAM	54273.314054(05)	182	0.86-1.20	u'g'r'	1.96	931	1.2-2.4
2007 June 21	CTCV 2354	VLT+UCAM	54273.379579(03)	183	0.77-1.09	u'g'r'	1.96	916	0.9-1.5
2009 June 12	CTCV 2354	NTT+USPEC	54995.350263(06)	11197	0.65-1.35	g'	9.87	482	1.4-2.6
2009 June 12	CTCV 2354	NTT+USPEC	54995.415961(06)	11198	0.35-1.17	g'	9.87	482	1.0-2.2
2009 June 23	CTCV 2354	NTT+USPEC	55006.428224(02)	11366	0.66-1.16	g'	3.36	817	1.4-2.2
2009 June 25	CTCV 2354	NTT+USPEC	55008.394766(01)	11396	0.70-1.22	g'	3.36	855	1.2-2.0
2009 June 29	CTCV 2354	NTT+USPEC	55012.393334(01)	11457	0.55-1.37	g'	2.98	1593	0.8-2.4
2009 June 30	CTCV 2354	NTT+USPEC	55013.376588(01)	11472	0.30-1.55	g'	1.96	3592	1.2-2.0
2010 May 03	CTCV 2354	NTT+UCAM	55320.414(2)*	16156	0.43-1.21	u'g'r'	8.23	526	1.4-1.8
2010 June 06	CTCV 2354	NTT+UCAM	55354.434846(24)	16676	0.47-1.19	u'g'r'	3.84	1048	1.0-1.2
2007 June 10	CTCV 1300	VLT+UCAM	54262.099145(03)	0	0.72-1.20	u'g'r'	1.00	3462	0.6-1.2
2007 June 13	CTCV 1300	VLT+UCAM	54262.123093(08)	34	0.74-1.15	u'g'i'	1.95	1573	0.6-1.1
2010 June 06	CTCV 1300	NTT+UCAM	55355.002677(01)	12288	0.85-1.12	u'g'r'	2.70	511	0.8-1.1
2010 Jan 07	SDSS 1152	WHT+UCAM	55204.101282(09)	0	0.16-1.13	u'g'r'	3.80	1492	2.0-3.8
2010 Jan 07	SDSS 1152	WHT+UCAM	55204.169031(08)	1	0.72-1.12	u'g'r'	3.80	600	1.4-2.5
2010 Jan 07	SDSS 1152	WHT+UCAM	55204.236742(07)	2	0.85-1.12	u'g'r'	3.80	415	1.2-3.2
2004 May 17	SDSS 1501	WHT+UCAM	53142.921635(06)	-11546	0.80-1.21	u'g'r'	6.11	335	1.0-1.6
2010 Jan 07	SDSS 1501	WHT+UCAM	55204.213149(03)	24718	0.78-1.12	u'g'r'	3.97	435	1.4-4.0
2010 Jan 07	SDSS 1501	WHT+UCAM	55204.270000(03)	24719	0.88-1.13	u'g'r'	3.97	321	1.4-3.0

Table 2.1a: Journal of observations. Table reproduced from Savoury et al. (2011). *Instr setup* denotes the telescope (WHT, NTT or VLT) and instrument used for each observation, where UCAM and USPEC represent ULTRACAM and ULTRASPEC, respectively. The mid-eclipse times, T_{mid} , are determined using the method outlined in Chapter 3. The mid-eclipse times marked with a '*' were estimated by a visual inspection of the light curve. *Cycle* is the cycle number as defined by the ephemerides in Chapter 4. *Phase Cov* corresponds to the phase coverage of the eclipse, taking the eclipse of the white dwarf as phase 1. T_{exp} and N_{exp} denote the exposure time and number of exposures, respectively.

Date	Object	Instr setup	T_{mid} (HMDJ)	Cycle	Phase Cov	Filters	T_{exp} (s)	N_{exp}	Seeing (")
2010 May 12	CSS080623	NTT+UCAM	55329.234670(45)	0	0.70-1.17	$u'g'r'$	3.30	504	1.3-1.7
2010 May 17	CSS080623	NTT+UCAM	55334.120147(47)	82	0.68-1.35	$u'g'r'$	4.92	712	1.2-2.2
2010 May 17	CSS080623	NTT+UCAM	55334.179709(30)	83	0.75-1.45	$u'g'r'$	3.92	909	1.2-1.6
2010 May 17	CSS080623	NTT+UCAM	55334.239263(30)	84	0.45-1.27	$u'g'r'$	3.92	1021	1.2-2.1
2010 June 07	CSS080623	NTT+UCAM	55355.032314(30)	433	0.74-1.24	$u'g'r'$	3.82	644	1.1-1.4
2010 June 07	CSS080623	NTT+UCAM	55355.151499(30)	435	0.68-1.25	$u'g'r'$	3.82	764	1.2-1.7
2011 May 27	CSS080623	NTT+UCAM	55709.050551(22)	6375	0.90-1.14	$u'g'r'$	2.89	427	1.0-1.3
2011 May 30	CSS080623	NTT+UCAM	55711.969940(24)	6424	0.82-1.15	$u'g'r'$	3.94	440	1.2-1.5
2011 May 30	CSS080623	NTT+UCAM	55712.029510(24)	6425	0.52-1.14	$u'g'r'$	3.94	798	1.2-1.5
2011 May 30	CSS080623	NTT+UCAM	55712.148668(22)	6427	0.50-1.28	$u'g'r'$	3.94	1023	1.1-1.3
2006 March 09	SDSS 0901	WHT+UCAM	53803.906320(14)	-13	0.22-1.17	$u'g'r'$	4.97	1374	1.1-2.5
2006 March 10	SDSS 0901	WHT+UCAM	53804.996713(12)	1	0.86-1.09	$u'g'r'$	4.97	775	1.0-1.5
2006 March 10	SDSS 0901	WHT+UCAM	53805.152462(11)	3	0.76-1.18	$u'g'r'$	4.97	591	1.2-2.0
2010 Jan 07	SDSS 0901	WHT+UCAM	55203.964448(39)	17964	0.71-1.14	$u'g'r'$	1.68	1685	1.5-3.0
2012 Jan 15	SDSS 0901	WHT+UCAM	55942.116392(04)	27442	0.64-1.15	$u'g'r'$	4.48	752	0.8-1.0
2012 Jan 15	SDSS 0901	WHT+UCAM	55942.194238(04)	27443	0.58-1.24	$u'g'r'$	4.48	987	0.9-1.2
2012 Jan 16	SDSS 0901	WHT+UCAM	55942.973078(05)	27453	0.88-1.15	$u'g'r'$	4.48	417	1.0-1.7
2012 Jan 16	SDSS 0901	WHT+UCAM	55943.050939(04)	27454	0.62-1.13	$u'g'r'$	4.48	752	1.0-2.0
2012 Jan 16	SDSS 0901	WHT+UCAM	55943.206691(04)	27456	0.88-1.18	$u'g'r'$	4.48	456	1.0-1.7
2012 Jan 16	SDSS 0901	WHT+UCAM	55943.284584(05)	27457	0.76-1.22	$u'g'r'$	4.48	678	1.0-2.2
2011 Aug 26	PHL 1445	WHT+UCAM	55800.151040(01)	11288	0.65-1.90	$u'g'i'$	2.68	2098	0.8-1.5
2011 Nov 01	PHL 1445	WHT+UCAM	55867.123998(01)	12552	0.60-1.13	$u'g'r'$	2.14	1119	1.0-2.0
2012 Jan 14	PHL 1445	WHT+UCAM	55940.878971(01)	13944	0.60-1.22	$u'g'r'$	1.98	1405	1.4-2.5
2012 Jan 14	PHL 1445	WHT+UCAM	55940.984899(01)	13946	0.70-1.18	$u'g'r'$	1.98	1102	1.5-2.7
2012 Jan 15	PHL 1445	WHT+UCAM	55941.991630(01)	13965	0.68-1.12	$u'g'r'$	1.98	1108	1.2-1.7
2012 Jan 16	PHL 1445	WHT+UCAM	55942.892369(01)	13982	0.80-1.50	$u'g'r'$	1.98	1600	1.5-3.0
2012 Jan 16	PHL 1445	WHT+UCAM	55942.945333(01)	13983	0.50-1.18	$u'g'r'$	1.98	1580	1.3-2.5

Table 2.1b: *continued*

Date	Object	Instr setup	T_{mid} (HMDJ)	Cycle	Phase Cov	Filters	T_{exp} (s)	N_{exp}	Seeing (")
2006 March 04	SDSS 1250	WHT+UCAM	53799.002620(02)	0	0.80-1.18	u'g'r'	3.97	488	1.2-3.0
2006 March 04	SDSS 1250	WHT+UCAM	53799.237595(01)	4	0.80-1.17	u'g'r'	3.97	370	1.3-2.5
2006 March 05	SDSS 1250	WHT+UCAM	53799.942363(01)	16	0.86-1.14	u'g'r'	3.97	362	1.5-3.5
2006 March 08	SDSS 1250	WHT+UCAM	53802.937970(02)	67	0.75-1.20	u'g'r'	3.97	572	1.1-1.8
2006 March 08	SDSS 1250	WHT+UCAM	53802.996574(02)	68	0.64-1.13	u'g'r'	3.97	615	1.2-2.3
2006 March 08	SDSS 1250	WHT+UCAM	53803.114174(01)	70	0.86-1.12	u'g'r'	3.21	385	1.0-1.5
2006 March 08	SDSS 1250	WHT+UCAM	53803.172882(01)	71	0.72-1.21	u'g'r'	2.98	827	1.0-1.5
2006 March 08	SDSS 1250	WHT+UCAM	53803.231610(01)	72	0.70-1.14	u'g'r'	3.97	557	0.8-1.2
2010 Jan 05	SDSS 1250	WHT+UCAM	55202.256923(01)	23892	0.76-1.48	u'g'r'	2.24	1611	1.4-2.2
2010 Jan 07	SDSS 1250	WHT+UCAM	55204.136408(01)	23924	0.59-1.20	u'g'r'	3.97	814	1.4-3.5
2010 Jan 07	SDSS 1250	WHT+UCAM	55204.195122(02)	23925	0.70-1.10	u'g'r'	3.97	544	1.2-2.0
2010 Jan 07	SDSS 1250	WHT+UCAM	55204.253881(02)	23926	0.88-1.16	u'g'r'	3.80	359	1.1-2.0
2007 June 08	SDSS 1555	VLT+UCAM	54260.226210(05)	0	0.84-1.06	u'g'r'	2.01	747	0.6-0.9
2007 June 08	SDSS 1555	VLT+UCAM	54260.305063(05)	1	0.73-1.24	u'g'r'	2.01	1700	0.8-1.3
2007 June 21	SDSS 1555	VLT+UCAM	54272.999190(05)	162	0.84-1.08	u'g'r'	1.96	821	1.0-4.0
2009 June 29	SDSS 1555	NTT+USPEC	55012.097338(01)	9536	0.85-1.26	g'	2.27	1216	1.4-3.4
2009 June 29	SDSS 1555	NTT+USPEC	55012.176209(01)	9537	0.80-1.20	g'	2.27	1277	1.8-3.0
2009 June 30	SDSS 1555	NTT+USPEC	55012.964609(03)	9547	0.84-1.15	g'	2.93	638	1.6-3.2
2010 May 17	SDSS 1555	NTT+UCAM	55334.339081(21)	13623	0.20-1.25	u'g'r'	4.87	1512	1.4-2.2
2011 April 21	SDSS 1555	NTT+UCAM	55673.374997(26)	17923	0.47-1.65	u'g'r'	3.69	2151	1.1-2.5
2011 May 30	SDSS 1555	NTT+UCAM	55712.245823(12)	18416	0.53-1.16	u'g'r'	3.50	1214	1.2-1.6
2011 May 30	SDSS 1325	NTT+UCAM	55711.984511(05)	7360	0.95-1.17	u'g'r'	4.89	238	1.5-2.5
2011 May 30	SDSS 1325	NTT+UCAM	55712.047047(04)	7361	0.87-1.16	u'g'r'	4.89	320	1.3-1.8
2011 June 01	SDSS 1325	NTT+UCAM	55714.043325(04)	7393	0.60-1.34	u'g'r'	4.89	850	1.3-2.0
2011 June 01	SDSS 1325	NTT+UCAM	55714.105729(04)	7394	0.34-1.10	u'g'r'	4.89	828	1.2-2.0
2012 Jan 16	SDSS 1325	WHT+UCAM	55943.12072(29)	11065	0.74-1.30	u'g'r'	5.98	505	2.0-4.0
2012 Jan 16	SDSS 1325	WHT+UCAM	55943.24543(24)	11067	0.61-1.23	u'g'r'	5.98	554	1.0-2.0

Table 2.1c: *continued*

Date	Object	Instr setup	T_{mid} (HMDJ)	Cycle	Phase Cov	Filters	T_{exp} (s)	N_{exp}	Seeing ($''$)
2011 May 27	SDSS 1524	NTT+UCAM	55709.098365(03)	0	0.48-1.33	$u'g'r'$	4.88	986	1.2-1.9
2011 May 27	SDSS 1524	NTT+UCAM	55709.163617(03)	1	0.77-1.14	$u'g'r'$	4.88	430	1.1-1.4
2011 May 30	SDSS 1524	NTT+UCAM	55712.102938(01)	46	0.75-1.16	$u'g'r'$	3.03	775	1.3-2.0
2011 June 01	SDSS 1524	NTT+UCAM	55714.127861(01)	77	0.84-1.15	$u'g'r'$	3.03	517	1.2-1.7
2011 June 01	SDSS 1524	NTT+UCAM	55714.1930(5)*	78	0.74-1.11	$u'g'r'$	3.94	547	1.3-1.9
2012 Jan 14	SDSS 0751	WHT+UCAM	55940.928983(42)	11399	0.70-1.14	$u'g'r'$	3.98	866	1.2-1.7
2012 Jan 14	SDSS 0751	WHT+UCAM	55941.022020(34)	11400	0.78-1.29	$u'g'r'$	3.98	991	1.0-1.7
2012 Jan 15	SDSS 0751	WHT+UCAM	55942.140282(56)	11412	0.91-1.23	$u'g'r'$	3.98	613	1.0-1.3
2012 Jan 16	SDSS 0751	WHT+UCAM	55943.071805(33)	11422	0.92-1.15	$u'g'r'$	3.98	447	1.0-2.0
2010 May 17	CSS0806227	NTT+UCAM	55333.986154(01)	0	0.88-1.63	$u'g'r'$	2.89	1767	0.9-1.5
2010 May 17	CSS0806227	NTT+UCAM	55334.063646(01)	1	0.63-1.24	$u'g'r'$	2.89	1393	1.0-1.4
2011 May 29	CSS0806227	NTT+UCAM	55711.029552(01)	4866	0.82-1.18	$u'g'r'$	3.96	614	1.1-1.8
2010 April 29	1RXS J1808	NTT+UCAM	55316.36030(05)*	0	0.70-1.40	$u'g'r'$	2.01	2180	1.5-2.2
2010 May 17	1RXS J1808	NTT+UCAM	55316.43030(05)*	1	1.40-1.08	$u'g'r'$	2.01	1976	1.5-2.5
2010 May 17	1RXS J1808	NTT+UCAM	55334.42900(05)*	260	0.23-1.24	$u'g'r'$	1.93	3113	1.5-2.5
2010 May 18	SDSS 0920	NTT+UCAM	55700.10500(10)*	1	0.60-1.12	$u'g'r'$	2.88	2349	1.4-2.8
2010 May 27	SDSS 0920	NTT+UCAM	55708.97750(10)*	60	0.88-1.14	$u'g'r'$	2.79	1216	1.0-1.5
2012 Jan 14	GALEX0035	WHT+UCAM	55940.824606(09)	26920	0.93-1.15	$u'g'r'$	1.85	1673	1.2-2.5
2012 Jan 15	GALEX0035	WHT+UCAM	55941.85844(28)*	26980	0.83-1.09	$u'g'r'$	1.85	2083	0.8-1.7
2012 Jan 15	SDSS 1006	WHT+UCAM	55942.052418(59)	7541	0.88-1.18	$u'g'r'$	3.98	1187	0.9-1.3
2011 May 27	SDSS 0924	NTT+UCAM	55709.023613(04)	9107	0.78-1.10	$u'g'r'$	4.89	515	1.2-1.6
2011 May 29	SDSS 0935	NTT+UCAM	55710.98250(10)*	7180	0.40-1.40	$u'g'r'$	4.88	1085	1.0-2.5

Table 2.1d: *continued*

1.0" x 11" slit in the ultra-violet blue arm (UVB), the 1.2" x 11" slit in the visible-red arm (VIS), and the 0.9" x 11" slit in the near-infrared arm (NIR). This corresponded to dispersions of $\sim 0.133 \text{ \AA pixel}^{-1}$ in the UVB (at 4500 \AA), $\sim 0.148 \text{ \AA pixel}^{-1}$ in the VIS (at 7850 \AA) and $\sim 0.544 \text{ \AA pixel}^{-1}$ in the NIR (at 17500 \AA). This setup provided a total resolving power, as measured by the width of the night sky lines, of $R = 5020 \pm 180$ ($60 \pm 2 \text{ km s}^{-1}$) in the UVB, $R = 6770 \pm 360$ ($44 \pm 2 \text{ km s}^{-1}$) in the VIS, and $R = 4550 \pm 350$ ($66 \pm 5 \text{ km s}^{-1}$) in the NIR-arm. These values are in excellent agreement with those published in the X-Shooter user manual. Seeing conditions on both nights were fair, varying between 0.5 and 1.5 arc-seconds, but with flares of up to 2.0 arc-seconds.

In total, 48 spectra were obtained (24 on each night), covering a total of 1.5 orbital cycles and a wavelength range of 3000-24800 \AA . Exposure times were 235 seconds in the UVB-arm, 210 seconds in the VIS-arm and 255 seconds in the NIR-arm, with dead times between exposures of approximately 8, 9 and 1 seconds, respectively.

Observations of the standard star GD-153 (Bohlin et al., 1995) were used to flux calibrate the data and correct for telluric absorption as described in §2.5.2. Due to an error in the Phase 2 preparation, the data were obtained in ‘stare’ mode rather than nodding along the slit as is normal for long slit infrared spectroscopy. Consequently, the sky subtraction on the NIR-arm is significantly worse than is normally possible with X-Shooter. Spectra of the spectral type templates GJ2066 (M2V) and GJ1156 (M5V) were also obtained. These data were taken on the nights of the 11 Dec 2009 and 28 Jan 2010, respectively.

No arc spectra were provided with the data set. An arc was obtained from the ESO data archive.

2.1.3 NIRI Spectroscopy

SDSS 1433 was observed using Gemini’s Near Infra-Red Imager and Spectrometer (NIRI) (Hodapp et al., 2003) in service mode on the 8.1-m Frederick C. Gillett Gemini North Telescope, on Mauna Kea, Hawaii. The setup comprised of the NIRI spectrograph + f/6 camera, an Aladdin In-Sb 1024x1024 pixel array, a 0.75x110” slit and a J-grism disperser with a dispersion of $\sim 0.133 \text{ \AA pixel}^{-1}$ (at 12500 \AA). The resolving power, as measured by the width of the night sky lines, was found to be $R = 454 \pm 16$ ($661 \pm 24 \text{ km s}^{-1}$).

The data were obtained on nights beginning 2 July 2009, 7 May 2010, 26 May 2010, 27 May 2010, 15 June 2010 and 16 June 2010. In total 389 spectra covering a wavelength range of 10353.8-13959.1 \AA (the *J-band*) were obtained. For each spectrum exposure times were 59 seconds. The data was observed using a ‘nodding’ technique, where the target object is first observed at a given position on the slit (e.g. position ‘A’) and then over subsequent frames this position is varied (e.g. A-B-B-A). This procedure is standard for infrared observations and improves sky subtraction. Nodding is described in greater detail in §2.2.5.

Observations of the standard star HIP 73593 (Monet et al., 2003) were taken at the start of each night and again after every hour of science data. Exposure times were 3 seconds. These observations were used to flux calibrate the spectra and correct for telluric absorption, as described in §2.6.2. Arc spectra were taken after every hour of science data using an argon lamp.

Seeing conditions on each night were good, typically varying between 0.4 and 1.2 arc-seconds.

2.2 Data Reduction

In this section I describe the steps necessary to reduce and calibrate the data. Both photometric and spectroscopic observations may be affected in similar ways by instrumental variations. As such, many of the methods used to reduce and calibrate the data are common across different instruments.

2.2.1 Pipelines

The steps undertaken to reduce and calibrate the data are described in detail in the text below. All data in this thesis was reduced using data reduction pipeline software. For ULTRACAM and ULTRASPEC, the ULTRACAM pipeline was used (e.g. Feline, 2005). For X-Shooter, the European Southern Observatory's reduction extraction tool (ESOREX), equipped with the X-Shooter pipeline version 1.2.2 (Modigliani et al., 2010) was used. For the NIRI data, the Image Reduction and Analysis Facility (IRAF²) was used to reduce and combine the data, whilst Tom Marsh's PAMELA software was used to extract the spectra.

All data analysis was carried out using Stuart Littlefair and Will Feline's LFIT programme (described in detail in Chapter 3) and Tom Marsh's PONTO and MOLLY software³.

2.2.2 Bias Subtraction

A bias is added to every pixel on the CCD before the image is read out. An analogue-digital converter cannot read out negative counts, and so the bias is added to keep the counts on each pixel positive, thus preventing a systematic error that would otherwise result when reading out low counts. The added bias is roughly constant, but due to

²Available at <http://iraf.noao.edu/>

³Freely available at <http://www2.warwick.ac.uk/fac/sci/physics/research/astro/people/marsh/software/>

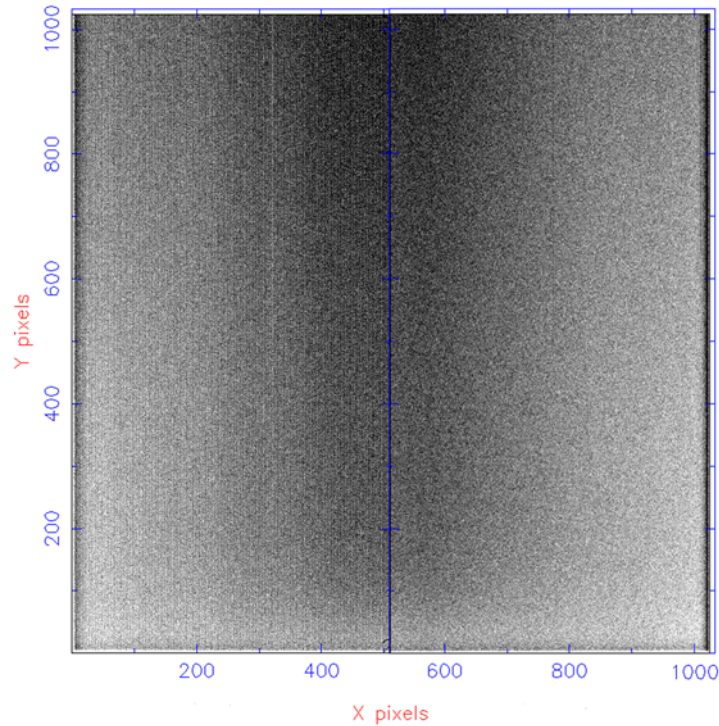


Figure 2.1: An example g-band master bias frame, created using the ULTRACAM pipeline software. Colours are inverted for ease of viewing.

imperfections on the CCD, the value of the bias can vary from pixel-to-pixel.

Bias can be corrected for by constructing and then subtracting a master bias frame from each individual science frame. To reduce the read-noise, the master bias frame is usually an average of a series of individual bias frames. Individual bias frames can be obtained by taking a zero second exposure when the CCD is not exposed to any light. Because no photons are detected, the resulting image is only that of the bias.

Ultracam Photometry

A master bias frame was created for each entry in Table 2.1a, 2.1b, 2.1c and 2.1d by taking a series of bias frames (usually 51 or 101) and then combining them using a clipped mean, rejecting outliers at the $3\text{-}\sigma$ level. An example master bias frame is shown in Figure 2.1.

X-Shooter Spectroscopy

With X-Shooter, a master bias frame was produced for the UVB and VIS arms. It was not required for the NIR arm, because it is accounted for when subtracting a dark frame (see §2.2.4). The master bias frame was created from five individual bias frames, which were combined using a median-stack. Contributions from outlying counts were removed at the $5\text{-}\sigma$ level.

NIRI Spectroscopy

A master bias frame was not required for reducing NIRI data. This is because when the frames taken at different sky positions are subtracted from each other (see §2.2.5), any additive background is removed.

2.2.3 Flat Fielding

The sensitivity of a CCD varies across its surface. This may be due to manufacturing imperfections, geometric variations between pixels or mechanical stress. Consequently, two pixels on the same CCD that are exposed to the same level of light may produce a different number of counts. These variations can occur on small scale (pixel to pixel) or large scale (gradients across the chip). Large scale variations may include dust on the chip, or vignetting, where the brightness of an image is reduced as one traverses further from the centre of the image. This can be seen clearly towards the left side of Figure 2.2. This is usually the result of off centre light rays being partially blocked by elements within the telescope or instrument.

Sensitivity variations can be corrected for by dividing the science frame by a normalised flat field. The flat field is normalised to unity to measure the response of each pixel relative to each other. A flat field can be created by taking an exposure of a uniformly illuminated field, usually during twilight. The response of the CCD is

also dependent on wavelength, and so the exposures must be taken using the same filters as the data. A master flat field is usually constructed from a series of individual flats that have been bias subtracted. For photometric flats, normalisation is carried out by dividing by the mean or median pixel value. For spectroscopic flat fields, additional care must be taken, as the raw flat field frame will be sensitive to not only the pixel to pixel variations, but also the spectral response of the instrument and the spectral energy distribution of the illumination source. In this thesis, the spectroscopic flat fields were normalised by fitting a spline or polynomial fit to the flat field spectrum in the spatial direction and then dividing by this fit. This removes the spatial variation, but not the pixel to pixel variations or spectral shape.

When the science frames are divided by the resulting, normalised flat field, the pixel to pixel variations are removed from the science frame. The spectral shape is removed during the flux calibration process (see §2.5.2 and §2.6.2).

Ultracam Photometry

A flat field was created by observing a blank area of the sky at twilight. This was done over many exposures, typically 30-40 per filter. To mitigate against the presence of very faint stars, the telescope was stepped in a spiral pattern around the sky. This is so that any faint stars that are present will appear at different positions on the CCD on each frame and thus when the frames are combined, they will be rejected from the average as outlying points.

The individual frames were combined in a similar way to when constructing the master bias, that is using a clipped mean with outliers removed at the $3\text{-}\sigma$ level. The resulting frame was then normalised by its mean pixel value to produce a master flat. During the combination process, frames with counts above or below a threshold value ($\sim 30,000$ and $5,000$, respectively) were automatically rejected. This is because frames with counts below the lower limit are likely to introduce noise into the master flat,

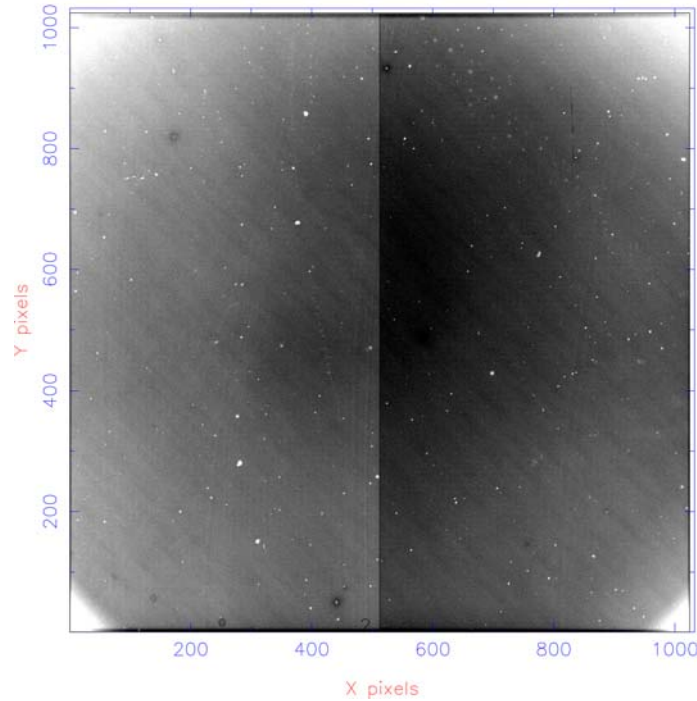


Figure 2.2: An example g-band master flat frame, created using the ULTRACAM pipeline software. Colours are inverted for ease of viewing.

whilst those above the threshold are likely to be saturated or suffer from ‘peppering’ (Hickman, 2011). The cause of peppering is currently unknown, but the effects are easy to identify. Adjacent pixels appear to have massively differing count levels, resulting in a ‘salt and pepper’ like appearance on the CCD. An example master flat frame is shown in Figure 2.2.

X-Shooter Spectroscopy

X-Shooter flat frames are taken in groups of five and stacked in the same way as the master bias frame, but then each order is normalised by the median pixel value for that order. The flat frames were taken using a halogen lamp within the spectrograph’s internal calibration unit. For the UVB arm, an additional set of flats must be taken using a deuterium (^2D) lamp. This is to provide good counts across all orders.

NIRI Spectroscopy

NIRI flat frames were taken with the Gemini Facility Calibration Unit (GCAL) Quartz-halogen lamp (Ramsay-Howat et al., 1997). Nine flat frames were provided with the data release per hour of science data. The normalised flat field was created using the IRAF ‘nsflat’ command. Here, the master flat field was constructed by first combining the individual frames (average) and then by dividing the exposure data by a smoothed version of the same data. The smoothed data was generated by fitting a spline to the collapsed flat field spectrum in the spatial direction. This process also produced a bad pixel map by flagging normalised pixels that fall above or below a user defined threshold. For the data presented in this thesis, thresholds of 0.8 and 1.2 were adopted.

2.2.4 Dark Frames

In the absence of any light falling on a detector, a signal greater than that of the bias is still registered. This signal arises because of thermal excitation in the semiconductor layer of the CCD. This excitation can cause electrons to randomly jump into the conduction bands of a CCD, which are then subsequently stored in the CCD’s potential wells and registered as an additional signal, known as the dark current. These electrons are indistinguishable from photo-electrons.

Dark current can be removed by subtracting a dark frame. A master dark is created by exposing the CCD for a significant period of time in the absence of light over a number of frames and then combining these frames (correcting for the exposure time).

Ultracam Photometry

Dark subtraction is not normally necessary when using ULTRACAM. The CCDs are Peltier cooled to -40°C , resulting in a dark current usually less than 0.1 electrons/pixel/sec. Given the read noise of the instrument is typically $\sim 3.5e^{-}$ (Dhillon et al., 2007), exposure times would need to be 35 seconds for the dark current to match the read-noise. For all the data presented in Tables 2.1a, 2.1b, 2.1c and 2.1d, the exposure times are considerably shorter than this, usually between 2 and 5 seconds (with a maximum of 9.88 seconds) and so dark current can be neglected. The ULTRACAM data presented in this thesis was not corrected for dark current.

X-Shooter Spectroscopy

Dark frames are not necessary for the UVB and VIS arms as the contribution is negligible ($\lesssim 0.02$ electrons/pixel/sec). In the NIR arm, dark current is much higher at approximately 0.35 electrons/pixel/sec. Three dark frames were provided, taken with the shutter closed with exposure times equal to that of the science observations (255 seconds in the NIR arm). The mean level of each dark frame was calculated (with outliers rejected at the $9\text{-}\sigma$ level) and then subtracted from each frame. A master dark frame was created by combining the resulting frames with a median stack and then adding the average of the individual means back. This improves the rejection of outliers. Remaining bad/noisy pixels were then removed at the $9\text{-}\sigma$ level and stored in an additional bad pixel map. Because the exposure times are equal to the exposure times of the science frames, the dark frames do not require correction for exposure times. These dark frames also remove the bias because both dark current and bias are additive.

NIRI Spectroscopy

As with the master bias frame, a master dark frame is not required for reducing NIRI data. This is because the dark current is removed during the ‘nodding’ procedure (see §2.2.5).

2.2.5 NIRI Nodding

At infrared wavelengths, the sky and telescope make significant contributions to the background. In addition, these contributions are often highly variable over short timescales. The standard method of dealing with this is to employ a technique called ‘nodding’. Here, the position of the telescope is moved slightly (~ 2 arc-seconds) between observations so that the target spectrum switches between two different spatial positions on the detector. Subtracting adjacent observations (that are flat-fielded) during the data reduction phase removes the emission from the sky and telescope from the resulting frame, as shown in Figure 2.3. In addition, it also removes bias and dark current. The subtraction of frames was carried out using the ‘nsreduce’ command in IRAF.

Each complete batch of NIRI observations were taken in groups of 54 spectra. These 54 spectra were averaged in groups of four, with one remaining group of two, using the ‘nscombine’ command in IRAF. This was done in an effort to improve the signal-to-noise of the data. Groups of four were chosen as they improved the signal-to-noise of the data, without significantly degrading the time resolution. The nscombine command shifts and combines frames that are taken at different positions on the detector (e.g. as a result of nodding). These shifts are calculated using the World Coordinate System (WCS) information stored in the fits headers of each file. The frames were combined using a clipped mean, with outlying points rejected at the $5\text{-}\sigma$ level.

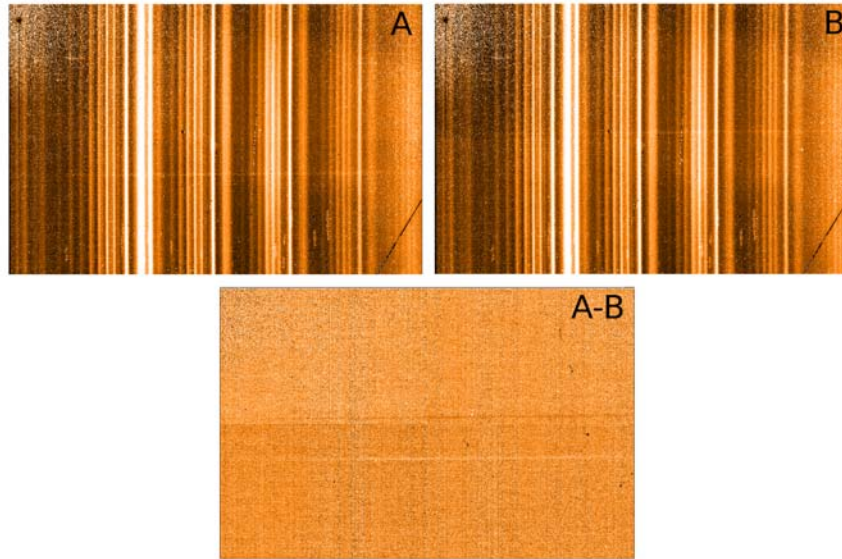


Figure 2.3: The nodding process. On the top left is a single J-band science frame, on the top right the next observation in the sequence. The position of the target spectrum has moved between spectra. The bottom image is the result of subtracting the second image from the first.

2.3 Aperture Photometry

The ULTRACAM data presented in this thesis were extracted using standard, differential aperture photometry. The counts from within a user defined aperture were summed to obtain the number of counts from a target object. Two further apertures surround the target, which are used to define an area of the sky (the sky annulus). The average brightness of the sky was estimated using a clipped mean of the counts from the sky annulus and then subtracted from each pixel within the star aperture. The sky error was estimated using the variance in sky photons within the sky annulus. The counts of a nearby (within the same field of view), bright comparison star were also measured using the same aperture sizes. This way, the ratio of counts of the target to the comparison are obtained. Assuming that the point-spread function (PSF) is constant across the field, then the same fraction of counts are recorded for each object. If the conditions are less than optimal or are changeable (e.g. cloud cover,

seeing variations, airmass), then both stars are affected by the same amount and thus the ratio of counts should remain the same. This is invaluable when studying the variability of an object.

The size of the apertures are crucial to the quality of the final data output. If the aperture is too large, then additional noise from the sky and additional read-out noise is included, whilst the counts from the target remains the same. This will lower the signal-to-noise ratio. If the aperture is too small, then fewer counts from the target will be recorded. When using differential photometry, this is not fatal, as the same ratio of counts are also lost from the comparison star. However, the signal-to-noise will be lower because the total number of counts is lower. The best aperture size is one that maximises the object counts, without adding additional noise. Such an aperture will therefore scale with the size of the FWHM of the stellar profile. However, the variation of the seeing across a set of observations (see e.g. Tables 2.1a, 2.1b, 2.1c and 2.1d) means that the size of the FWHM, and therefore the size of the ideal aperture, will also vary with the seeing. Therefore, to maximise the signal-to-noise ratio, variable aperture sizes were used; that is the aperture size is different for each individual frame taken. The size of these apertures were defined by fitting a PSF to the bright comparison star and scaling both apertures by a set amount of the resulting full-width at half maximum (FWHM). A Moffat profile (Moffat, 1969) was used, as this produced a better fit than a Gaussian. For fainter targets where the noise is sky-limited, Naylor (1998) recommends using an aperture radii around 1.5 times the FWHM. The targets presented in this thesis were reasonably bright, so 1.5 was usually an underestimate. A ratio of 1.7 was adopted for all data in this thesis. An example aperture selection with profile fit is shown in Figure 2.4.

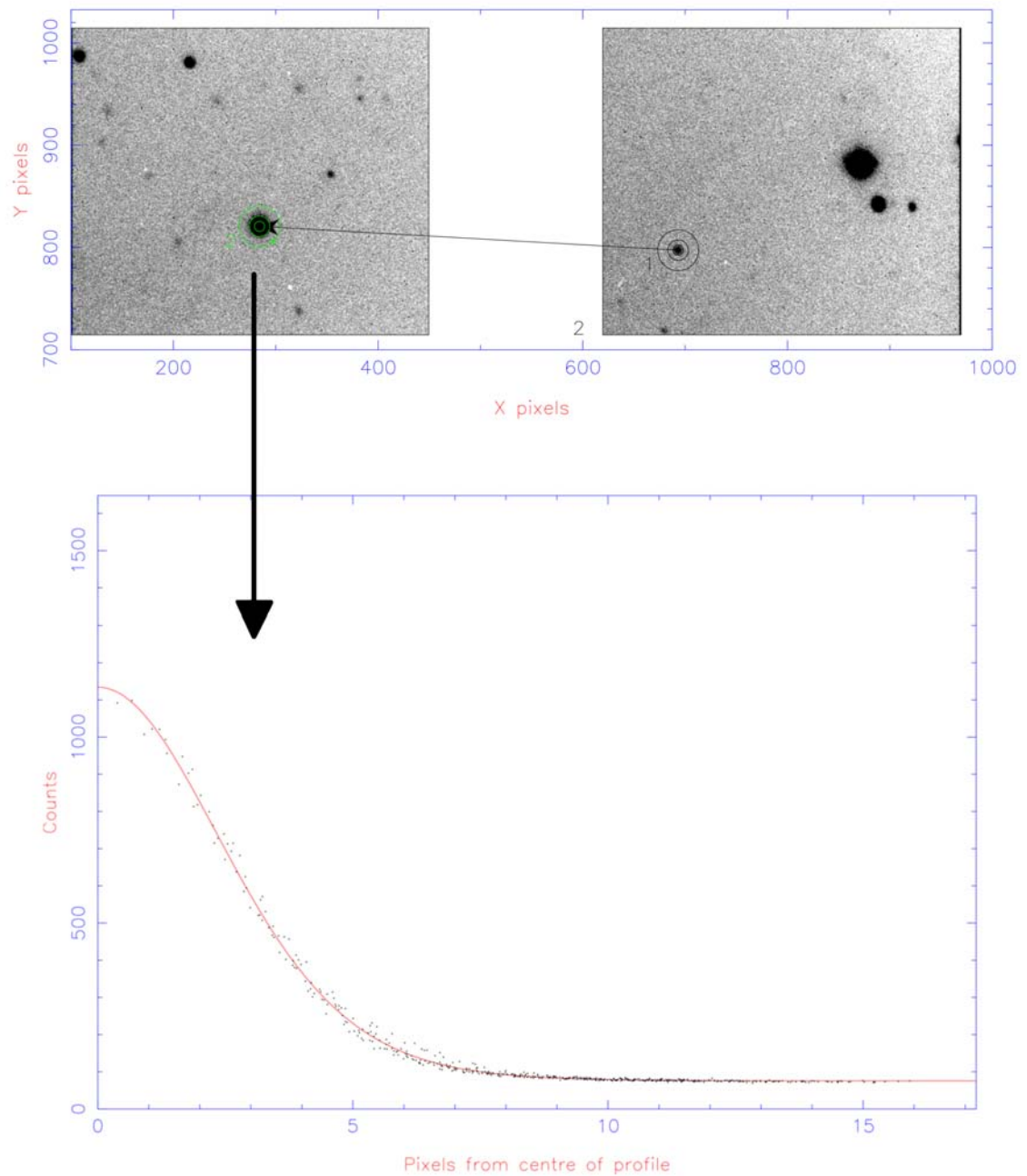


Figure 2.4: The aperture selection process for ULTRACAM data reduction complete with profile fit for object 2, the comparison star.

2.4 Flux Calibration

The process of aperture photometry described in the previous section gives the ratio of counts from the target to the comparison star, which can be used to derive a light curve for the target. It does not give the total number of counts, as some fraction of the total counts lie outside the aperture. In order to correctly calibrate the counts into fluxes a three stage process is carried out;

1. Correction for extinction;
2. Correction for instrumental response;
3. Conversion of calibrated magnitudes into flux units.

2.4.1 Extinction

Extinction is the absorption and scattering of light in the Earth's atmosphere, which can drastically reduce the amount of flux received from a star. The data in this thesis was corrected for first order extinction effects only, as the secondary effects are typically small in comparison (e.g. Smith et al., 2002). The correction varies depending on atmospheric conditions, the bandpass of observation, and the position of the target on the sky. The position of the target provides the *airmass*, which is the length of the column of air that the light has passed through relative to that at the zenith.

The flux received was converted to an instrumental magnitude, which was then corrected to the instrumental magnitude above the Earth's atmosphere. This conversion is given by

$$m_{instr,0} = -2.5 \log_{10} \frac{C}{T_{exp}} - k_{\lambda} \sec Z, \quad (2.1)$$

where $m_{instr,0}$ is the instrumental magnitude in a given filter corrected to above the Earth's atmosphere, C is the number of counts received in a given filter, T_{exp} is the

exposure time, k_λ is the extinction coefficient for a given filter and $\sec Z$ is the airmass of an object. For all data sets, only the r' -band extinction coefficient was required. The remaining coefficients (g' and u') were derived from the r' -band coefficient using theoretical ULTRACAM extinction curves (Hickman, 2011). For observations taken using the WHT, the nightly extinction coefficients measured by the Carlsberg Meridian Telescope on La Palma were used to correct the data. For observations using the VLT and NTT, no nightly extinction coefficients were measured or provided, and so estimated extinction coefficients⁴ were used. A study of the extinction above Paranal (Patat et al., 2011) found that atmospheric extinction varied over the course of a year varied by around 0.04 magnitudes, except for wavelengths shorter than 4000 Å, where the variability was typically 0.07 magnitudes. Therefore, the estimated coefficients can be considered a reasonable approximation.

2.4.2 Instrumental Response

The extinction-corrected, instrumental magnitude needs to be converted to a standard magnitude system. This is because the response of every instrument and telescope is different. For example, two separate instruments observing the same target at the same time may record a different number of counts and thus different instrumental magnitudes. This may be due to differences in filter response, CCD response, or differences in the telescope optics. To prevent ambiguity, these magnitudes are converted to a standard magnitude system by defining a zero point, or offset, for each filter.

ULTRACAM uses the SDSS photometric system, and so the zero point can be determined by observing SDSS standard stars (Fukugita et al., 1996; Smith et al., 2002). The zero point, ZP , is given by the difference in observed instrumental magnitude of the flux standard, corrected to zero airmass, and the expected (defined)

⁴See <http://www.lis.eso.org/lasilla/Telescopes/2p2/D1p5M/misc/Extinction.html>

magnitude of the flux standard. Combining this zero point with Equation 2.1 yields

$$m = ZP - 2.5 \log_{10} \frac{C}{T_{exp}} - k_{\lambda} \sec Z, \quad (2.2)$$

where m is the calibrated magnitude of a star in a given filter. In practice, the magnitude of the comparison star is found first, and then the magnitude of the target star by

$$m_{target} = m_{comparison} - 2.5 \log_{10} \frac{C_{target}}{C_{comparison}}. \quad (2.3)$$

2.4.3 Absolute Flux Calibration

The method outlined above converts the observations onto the AB magnitude system (Oke & Gunn, 1983). The flux per unit frequency and magnitude are related by

$$F_{\nu}(mJy) = 3.631 \times 10^6 \times 10^{-0.4m}. \quad (2.4)$$

2.5 X-Shooter Extraction

The X-Shooter data format is complex, with highly curved orders that require straightening and merging before extracting (see Figure 2.5). The X-Shooter data in this thesis were reduced using a physical model of the X-Shooter instrument as described by Bristow et al. (2008) and Modigliani et al. (2010). In practice, the X-Shooter physical model is a set of matrix transformations, each of which represent an optical surface within the spectrograph. The matrices describe physical quantities, such as temperature, angles and distances between optical surfaces, that affect and describe the passage of a photon of known wavelength through the spectrograph. The data reduction cascade involves calibrating this physical model.

A first order guess is made of the spectral format of the instrument by locating

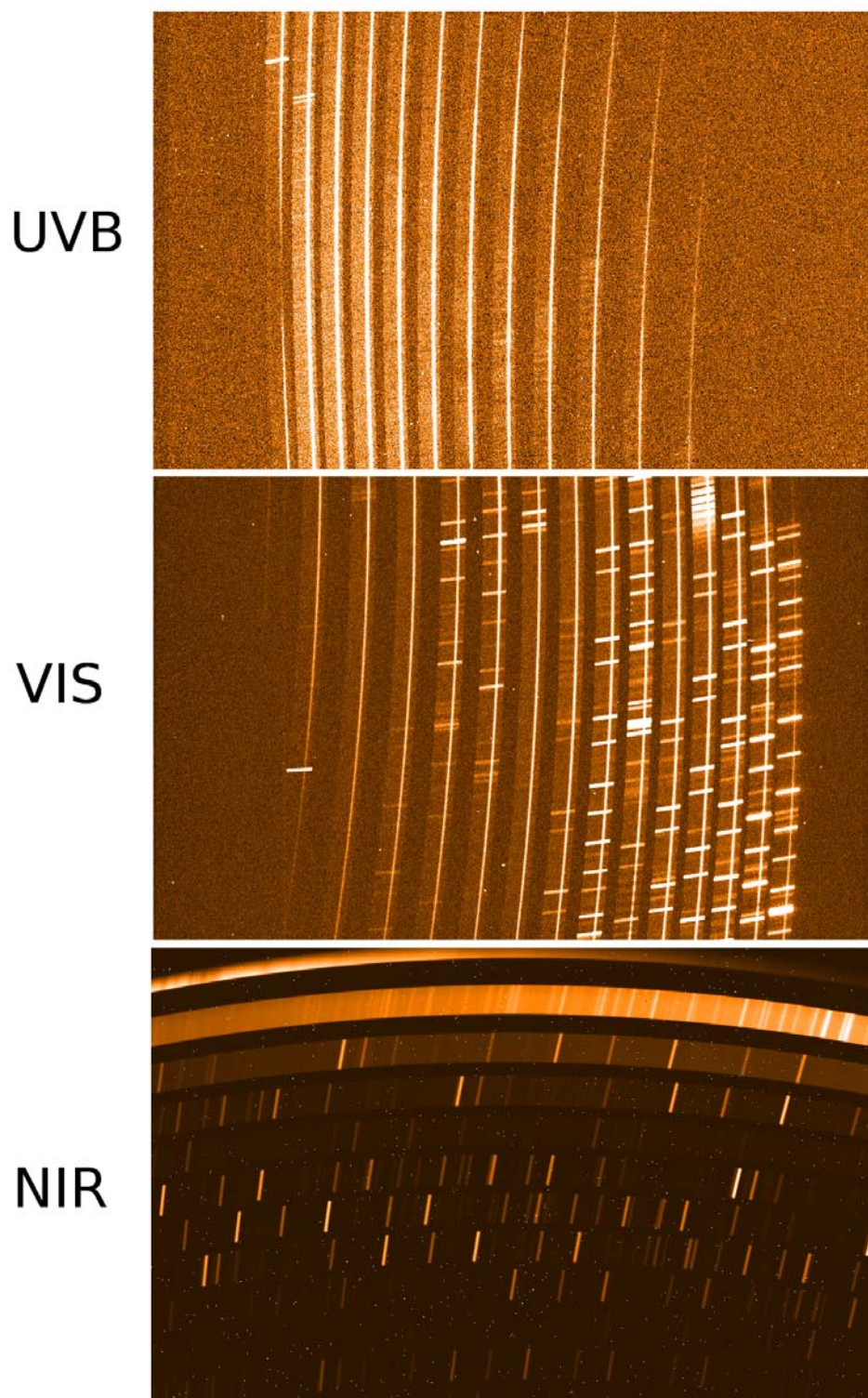


Figure 2.5: The highly curved orders of X-Shooter. From Top to bottom, they are the UVB, VIS and NIR arms.

the positions of emission lines from a single pinhole arc via a 2D Gaussian fit. This first guess solution takes into account information such as instrument temperature, that is available in the fits headers of each frame. These positions are then used to locate the centroids of each spectral pixel bin on a single pinhole flat (continuum). This allows for an accurate determination of the order tracing. The full, physical model of the instrument was then produced using a multi-pinhole arc frame by fitting 2D Gaussians to the positions of these lines. This allows the determination of pixel position (X, Y) for any traced order number (m) , wavelength (λ) and position along the slit (s) . The wavelength solution was tweaked further through use of arc line spectrum taken from the ESO archive. From residuals to the line fitting, this wavelength calibration has a relative accuracy of $\sim 1 \text{ km s}^{-1}$.

The data were extracted in the standard manner for ‘stare’ mode observations; that is each frame were reduced and extracted individually, rather than using nodded frames. To extract the data, the individual frames were first bias (UVB and VIS) or dark (NIR) subtracted and then an inter-order background fit was subtracted. This fit was obtained using a spline fit to the positions of the order edges, which were located whilst creating the master flat field. The data were then divided by the master flat. Cosmic ray removal was carried out using Laplacian edge detection as described by van Dokkum (2001). The sky background was then subtracted using the method described by Kelson (2003). The frame was then rectified from pixel-space (X, Y) , to a merged 2D spectrum (λ, s) . A final, 1D spectrum was then extracted using an optimal extraction technique (Horne, 1986; Marsh, 1989).

2.5.1 Flexure Correction

The orientation of the X-Shooter instrument varies with zenith distance (i.e. airmass of target). Flexure can cause slight deviations in the position of the object along the slit of the X-Shooter spectrograph. It may also result in small movements of the opti-

cal elements within the instrument. These small movements alter the spectral format and thus also the wavelength solution. It is estimated that for airmasses between 1 and 2, the resulting movement may be up to 1.2 pixels ($\sim 20 \text{ kms}^{-1}$ in the VIS arm). These shifts, if present, may severely distort any radial velocity measurements, which are required to be accurate and precise.

Flexure can be corrected for by using flexure compensation frames, which measure the shift of a small set of emission lines compared to the physical model derived in the previous section. Unfortunately, these frames were not provided as a standard at the time of observation and were not available. Instead, the flexure was found by measuring the shift of the observed sky lines relative to their positions measured by Hanuschik (2003). The individual spectra were then moved by these shifts, which for the VIS arm was typically between 10 and 35 kms^{-1} . This was only attempted for VIS arm observations, as precise radial velocity measurements were not required in other wavebands.

2.5.2 Flux Calibration and Telluric Correction

In order to calibrate the received counts onto an absolute flux scale, the spectrum of a spectroscopic flux standard is required. These stars have published values of flux as a function of wavelength. If the star has very few intrinsic features, such as rapidly rotating B stars, F stars, or white dwarfs, they can also be used to remove atmospheric absorption features. These features, known as telluric lines, are the result of the Earth's atmosphere absorbing light at different wavelengths.

Flux calibration was achieved using standard star flux tables provided by Hamuy et al. (1994) and Vernet et al. (2010), which list the defined flux of the star as a function of wavelength. The flux as a function of wavelength were fit with a 10th order polynomial to interpolate between values. Using this fit, and the observed spectrum of the standard star, it was then possible to obtain a unique relationship

between the observed counts, wavelength and absolute flux. This relationship was then applied to the observed counts from the target star, to obtain the absolute flux. This flux was not corrected for differential slit losses between the target and standard star.

To correct for telluric absorption, a copy of the flux-calibrated standard star spectrum was divided by the above fit to the tabulated flux values for this standard. The result was a spectrum normalised to one, containing only the telluric features. A constant was then subtracted from this spectrum, and all regions that were not affected by telluric absorption were set to zero, as shown in Figure 2.6. The resulting telluric spectrum was then subtracted from the target spectrum. Because the strength of the telluric lines vary depending on the airmass at which the telluric star is observed, the telluric features on the standard must be scaled, because the standard and target are rarely observed at the same airmass. This was done via an optimal subtraction routine (see §3.6), optimising the region around the Na I doublet at 8190 Å. The resulting VIS arm average spectrum, before and after telluric correction, is also shown in Figure 2.6.

2.6 NIRI Extraction

The NIRI data were extracted using PAMELA. The object was first tracked across the CCD, using the TRACK command. The x position of the spectrum was fit as a function of y using a 2nd or 3rd order spline fit. The target extraction aperture was chosen using the *regpic* routine. Regions were also selected that defined the background. These background regions were fit with a low order polynomial (usually 3rd order) using the *skyfit* command. This was done in order to estimate the background level under the target profile, which was then subtracted. The selection process is shown in Figure 2.7.

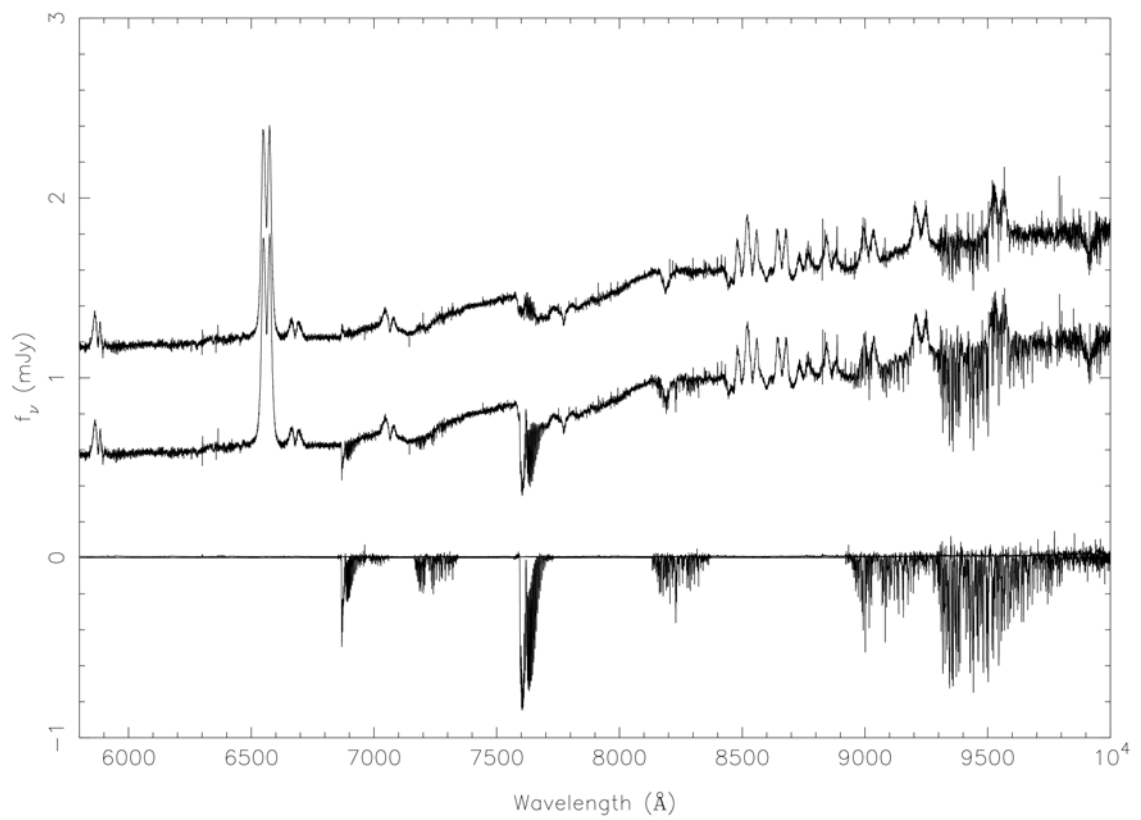


Figure 2.6: The telluric correction process for X-Shooter data. From bottom to top, the telluric spectrum, the uncorrected target spectrum and the target spectrum after telluric correction. Spectra are offset by 0.6 mJy.

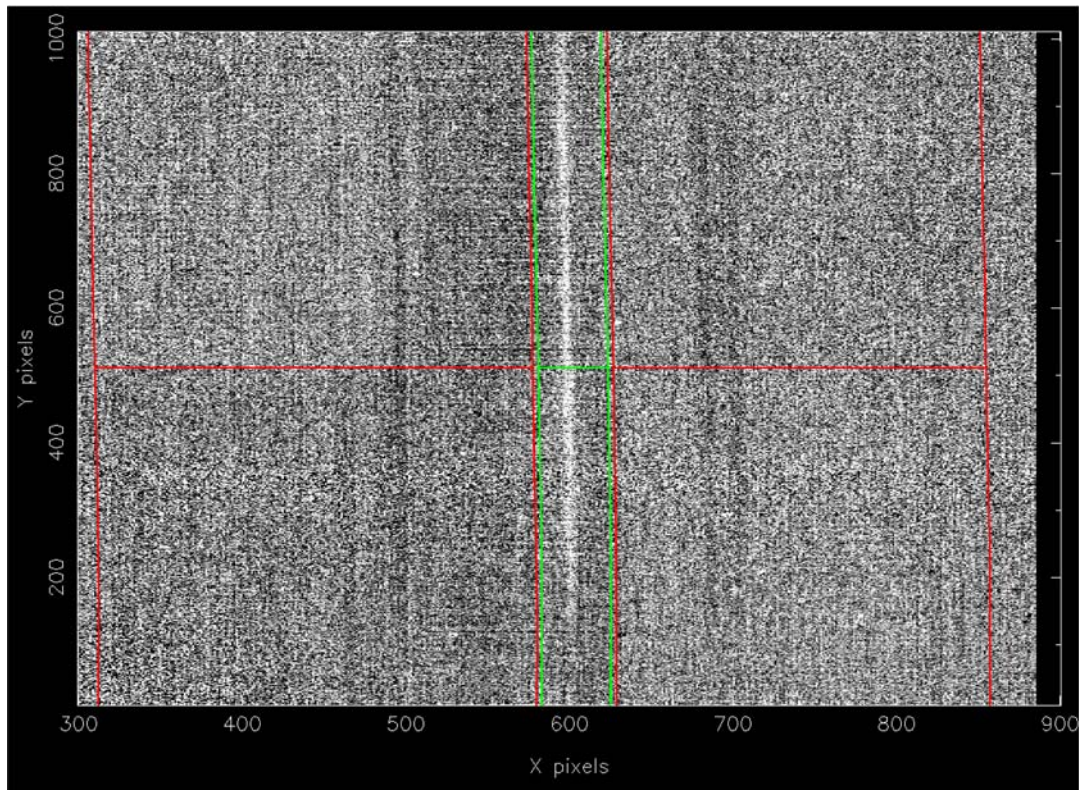


Figure 2.7: The regpic routine in PAMELA. The regions marked in red are user defined as background regions, whilst the green region is marked as target regions.

The data were extracted using an optimal extraction technique in PAMELA as described by Marsh (1989). This technique adapts that described by Horne (1986) for use with spectra that are curved or tilted across the CCD. In optimal extraction, each column on the CCD is weighted according to the inverse variance in order to maximise the signal-to-noise ratio (see e.g. Marsh, 1989, for a full mathematical treatment). This results in a reduction of statistical noise, whilst maximising the target flux. This is particularly useful for low signal-to-noise data. The optimal extraction algorithm is implemented into the *profit* and *optext* routines within PAMELA.

2.6.1 Wavelength Calibration

Arc spectra taken with an argon lamp were used to wavelength calibrate the data. The arc spectrum has a series of sharp, discrete emission lines with known wave-

lengths, superimposed on a weak continuum, as shown in Figure 2.8. By observing the positions of these lines, a relationship between pixel number and wavelength can be obtained via a polynomial fit. This relationship can then be applied to the relevant science frames using the ‘acal’ command in MOLLY. For the data presented in this thesis, 4th order polynomials were used, resulting in an RMS scatter of $\sim 0.3 \text{ \AA}$ for all NIRI spectra.

2.6.2 Flux Calibration and Telluric Correction

Observations of the standard star HIP 73593 (G2V) were used to flux calibrate the target spectra and correct for telluric absorption. In general, tabulated flux values are not available infra-red data, and so the method used to flux calibrate the target spectra and correct for telluric absorption is different to that used for the X-Shooter data. Because the standard star is the same spectral type as the Sun, a solar spectrum was used derive the telluric spectrum and flux calibrate the standard spectrum. This process is described below.

The observed standard star spectrum was first normalised to 1 by dividing by a 7th order polynomial fit. A solar spectrum, corrected for telluric absorption (data provided by Kitt Peak Observatory⁵) was broadened to match the resolution of the NIRI data and then normalised to 1 by dividing by a 7th order polynomial fit. The solar spectrum was then subtracted from the standard star via optimal subtraction, leaving only the telluric features, as shown in Figure 2.9. The telluric spectrum was then re-multiplied by the polynomial fit, to reproduce the original standard star spectrum, minus any stellar absorption lines.

The standard star is the same spectral type as the Sun, and so to a good approximation the standard star spectrum can be considered a black body spectrum with an

⁵Data from Kitt Peak Observatory available on ESO website. NSO/Kitt Peak FTS data used here were produced by NSF/NOAO

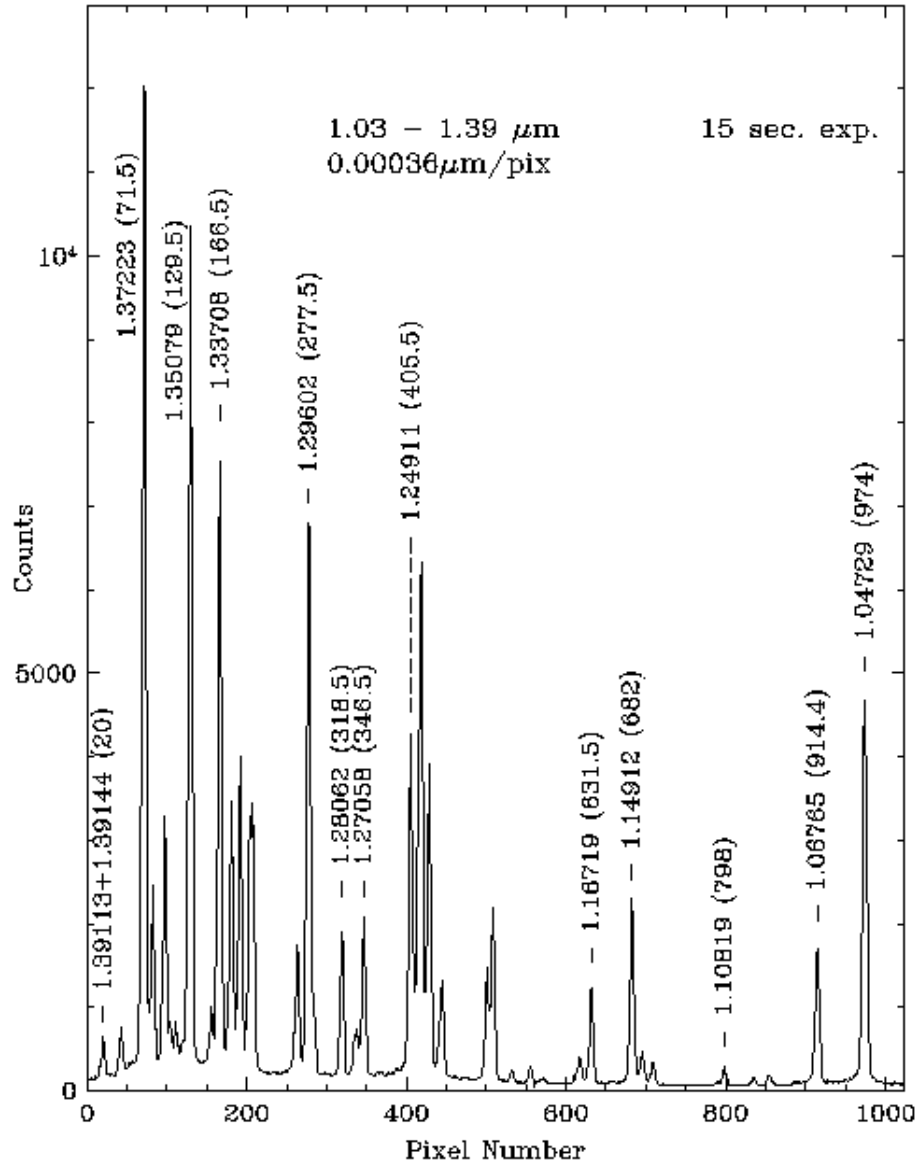


Figure 2.8: The emission lines of the Argon arc. The positions of these lines were fit via a 4th order polynomial. Plot reproduced from <http://www.gemini.edu/sciops/instruments/niri/>.

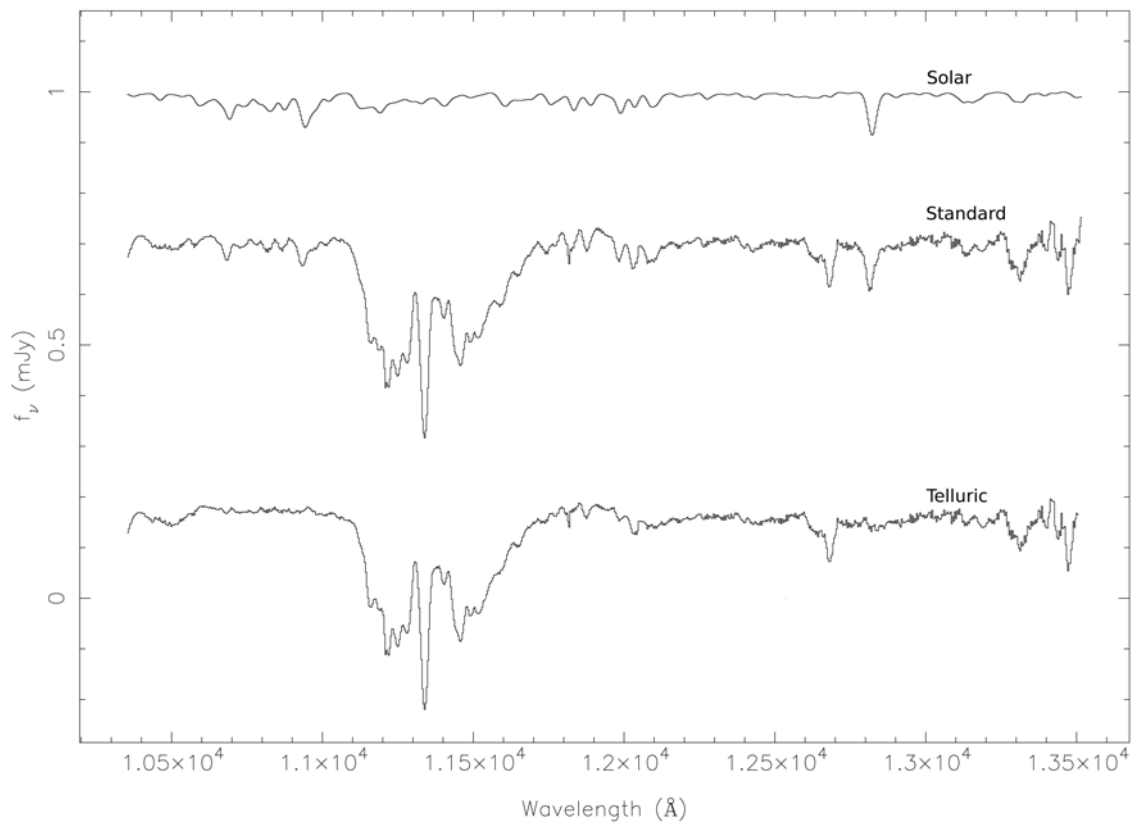


Figure 2.9: The telluric correction process for NIRI data. The normalised Kitt Peak solar spectrum (top) is subtracted from the normalised standard star spectrum (middle). The result is the telluric spectrum (bottom) that may then be used for correcting individual spectra. Spectra have been vertically offset for clarity.

effective temperature of 5778 K (B) (e.g. Carroll & Ostlie, 1996), scaled to match the reference flux of the standard star. Such a black body curve was created using the ‘black body’ command in MOLLY and the magnitude/flux tables provided by Cutri et al. (2003) and Tokunaga & Vacca (2005). In practice, the observed standard star spectrum (T), is affected by telluric absorption and the response of the instrument. It therefore follows that the overall spectral response is given by

$$R = \frac{T}{B}, \quad (2.5)$$

which is related to the observed target spectrum ($C^{observed}$) by

$$C_{\lambda}^{observed} = R_{\lambda} \times C_{\lambda}^{flux,telluric}, \quad (2.6)$$

where $C^{flux,telluric}$ is the flux calibrated and telluric corrected spectrum that is required. Therefore, to obtain a final, flux calibrated and telluric corrected spectrum, the individual object spectrum was multiplied by the black body curve and divided by the telluric spectrum.

Chapter 3

Techniques of Data Analysis

3.1 Data Phasing and Ephemerides

When analysing the light curves of an eclipsing binary, the first step that should be undertaken is to convert the x-axis from units of time, to a unit that defines the point at which the star is in its orbit. This is the ‘orbital phase’, and it runs from 0 to 1 over a cycle. Subsequent integers denote later cycles. Phase zero or one is usually defined as the mid-point of the white dwarf eclipse. Assuming a symmetrical white dwarf eclipse, this equivalent to the superior conjunction of the white dwarf. In some literature (e.g. Tappert et al., 2004) phase zero is defined as the point of minimum light. For systems with prominent bright spots, this can lead to a systematic disagreement of mid-eclipse times by up to a few minutes between the two definitions of phase zero (see §4.2).

The times of white dwarf mid-ingress, T_{wi} , and mid-egress, T_{we} , were determined by locating the minimum and maximum times, respectively, of the smoothed light-curve derivative (e.g. Wood et al., 1985). A median filter was used to smooth the data, and then the derivative was calculated. A box-car filter was then applied to the derivative. Gaussians were fit to the resulting light curve derivative to locate the

the minimum and maximum values. These points correspond to the mid-points of white dwarf ingress (T_{wi}) and white dwarf egress (T_{we}). If a prominent bright spot was visible in the light curve, the ingress and egress times were inspected to ensure that the bright spot ingress and egress times had not been detected instead. The times of mid-eclipse, T_{mid} , were determined by assuming the white dwarf eclipse to be symmetric around phase one, and taking $T_{mid} = (T_{wi} + T_{we})/2$. The accuracy of this technique is comparable to the time resolution of the data. The orbital ephemeris for a given system was found via a linear least-square fit to the eclipse times and cycle numbers listed in Tables 2.1a, 2.1b, 2.1c and 2.1d, in addition to eclipse times published in the literature (see Table 4.1 and references therein). The orbital ephemerides were of the form

$$T_{mid}(HJD) = T_0(HJD) + P_{orb}E, \quad (3.1)$$

where T_{mid} is the mid-eclipse time for cycle E , P_{orb} is the orbital period and T_0 is the mid-eclipse time of cycle 0. In most cases there was no evidence of any O-C variations (see §4.2 and §7.2.2 for details of exceptions). All eclipse times presented in this thesis are co-ordinated universal time (UTC), corrected to the heliocentre.

The errors on the eclipse times in Table 2.1a, 2.1b, 2.1c and 2.1d are set by the accuracy of determining the maximum and minimum times of mid-ingress T_{wi} and mid-egress T_{we} . These errors were then adjusted when calculating the ephemerides to give $\chi^2 = 1$ with respect to a linear fit. The errors on the eclipse times in the literature, where not explicitly stated, are estimated by giving $\chi^2 = 1$ with respect to a linear fit to those times only.

3.2 A Physical Model of the Binary System

The geometry of an eclipsing binary system allows for the determination of the system parameters by measuring the timings of the white dwarf and bright spot eclipse. It is possible because there exists a unique relationship between the width of the white dwarf eclipse ($\Delta\phi$), the inclination (i) and the mass ratio (q) (Bailey, 1979). This can be seen by considering an eclipse at a high inclination and low inclination; for the low inclination case, the radius of the secondary star must be larger to reproduce the same eclipse width as in the high inclination case. From §1.1.2, the radius of a Roche lobe filling secondary star depends only upon q , and so $\Delta\phi = f(q, i)$. By assuming that the bright spot lies on the ballistic trajectory from the secondary star, the path of the gas stream also depends only upon q (e.g. Hellier, 2001), as shown in Figure 3.1. Therefore the timings of the bright spot ingress and egress also depend upon q and i . Measuring $\Delta\phi$ and the timings of the bright spot ingress and egress therefore provides three constraints for which q and i can be solved.

In practice, to determine the system parameters a physical model of the binary system is used to calculate eclipse light curves for the white dwarf, bright spot, accretion disc and secondary star. Feline et al. (2004b) showed that this method gives a more robust determination of the system parameters in the presence of flickering than the derivative method of Wood et al. (1986). The model itself is based on the techniques developed by Bailey (1979), Smak (1979), Cook & Warner (1984), Wood et al. (1985), Wood et al. (1986), Horne et al. (1994), Littlefair et al. (2008) and Copperwheat et al. (2010) and relies on just four assumptions: the bright spot lies on the ballistic trajectory from the secondary star; the secondary star fills its Roche lobe; the white dwarf is accurately described by a theoretical mass-radius relation; and the whole of the white dwarf is visible with an unmodified surface brightness. These assumptions cannot be tested directly, but it has been shown that the masses

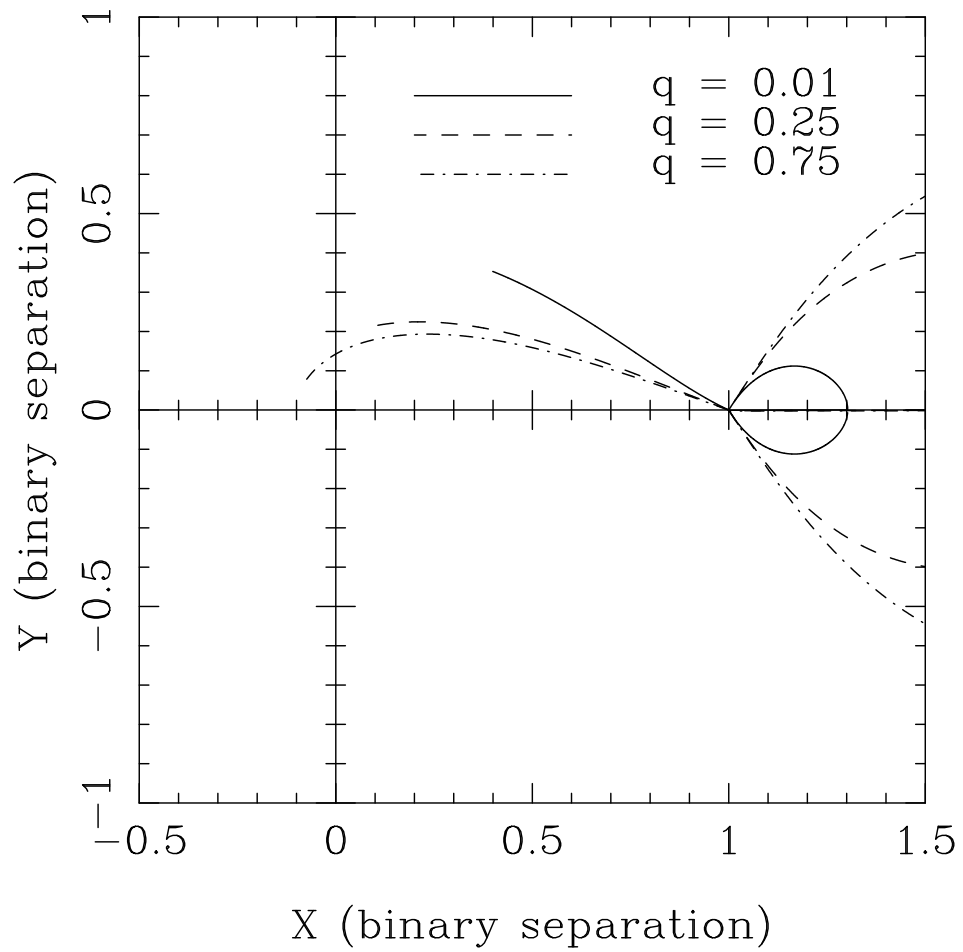


Figure 3.1: Gas stream trajectories computed for different mass ratios.

derived with this model are consistent with other methods commonly employed in CVs over a range of orbital periods (e.g. Feline et al., 2004; Tulloch et al., 2009; Copperwheat et al., 2010, 2012, Chapters 6 and 7 of this thesis).

The model used by Littlefair et al. (2008) had to be adapted due to the prominent bright spot observed in CTCV J1300-3052 (see Chapters 4 and 5). The old (simple) model fails to correctly model the bright spot ingress and egress features in this system satisfactorily and results in a poor fit. Following Copperwheat et al. (2012), four new parameters were added to the model to account for a more complex variety of bright spot shapes. This brings the total number of variables to 18. These are:

1. The mass ratio, $q = M_2/M_w$.
2. The white dwarf eclipse phase full-width at half-depth, $\Delta\phi$.
3. The outer disc radius, R_d/a , where a is the binary separation.
4. The white dwarf limb-darkening coefficient, U_w . This is defined by $I_l/I_0 = 1 - U_w(1 - \cos\beta)$, where I_l/I_0 is the ratio of the intensity at the limb of the star compared to the intensity at the centre, and β is the angle between a line normal to the stellar surface and the line of sight of the observer.
5. The white dwarf radius, R_w/a .
6. The bright spot scale, S/a . The bright spot is modelled as two linear strips passing through the intersection of the gas stream and disc. One strip emits isotropically, while the other beams in a given direction. Both strips occupy the same physical space. The intensity distribution is given by $(X/S)^Y e^{-(X/S)^Z}$, where X is the distance along the strips. The non-isotropic strip does not beam perpendicular to its surface. Instead the beaming direction is defined by two angles, θ_{tilt} and θ_{yaw} .

7. The first exponent, Y , of the bright spot intensity distribution.
8. The second exponent, Z , of the bright spot intensity distribution.
9. The bright spot angle, θ_{az} , measured relative to the line joining the white dwarf and the secondary star. This angle defines the direction of the two strips, and allows for adjustment of the phase of the orbital hump.
10. The tilt angle, θ_{tilt} , that defines the beaming direction of the non-isotropic strip. All emission from the non-isotropic strip is beamed in this direction. This angle is measured out of the plane of the disc, such that $\theta_{tilt} = 0$ would beam light perpendicular to the plane of the disc.
11. The yaw angle, θ_{yaw} . This angle also defines the beaming direction of the non-isotropic strip, but in the plane of the disc and with respect to the first strip.
12. The fraction of bright spot light that is isotropic, f_{iso} .
13. The disc exponent, b , describing the power law of the radial intensity distribution of the disc.
14. A phase offset, ϕ_0 .
15. The flux contribution of the white dwarf.
16. The flux contribution of the secondary star.
17. The flux contribution of the accretion disc.
18. The flux contribution of the bright spot.

The goodness of fit for a given model was found by calculating χ^2 . The uncertainties for each parameter are expected to follow a normal distribution.

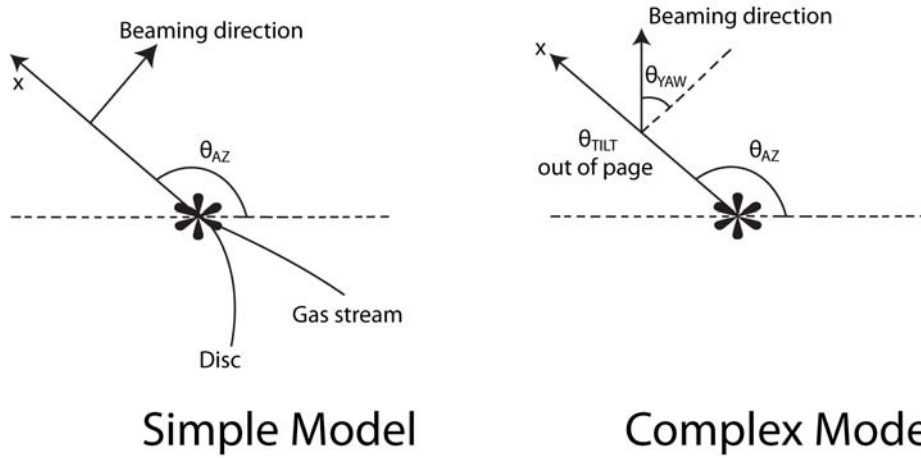


Figure 3.2: Bright spot beaming angles for the simple and complex bright spot models. The bright spot is located on the dotted line, which is parallel to the line of centres of each star.

In the simple model used by Littlefair et al. (2008), the beaming angle of the second bright spot strip was fixed perpendicular to the surface of the first strip, as shown in Figure 3.2. The complex model allows for a larger variety of beaming orientations. In Littlefair et al. (2008), the bright spot intensity distribution followed the same form of $(X/S)^Y e^{-(X/S)^Z}$, but the exponents Y and Z were fixed at 2 and 1, respectively. Altering these exponents result in a different intensity distribution along the strip, as shown in Figure 3.3. Together, the additional angles and variable exponents allow for more complex bright spot ingress and egress shapes. The bright spot model itself is not physically motivated. The aim of the bright spot model is to reproduce a range of bright spot ingress and egress shapes in such a manner that q is not affected by the shape of ingress and egress, only their positions. In this bright spot model the brightest part of the bright spot is always at the intersection of the gas stream and accretion disc and so provided this is not violated, the mass ratios provided by this model should be reliable. Because the bright spot model is not physically motivated, the parameters obtained through the fitting process should be treated with caution.

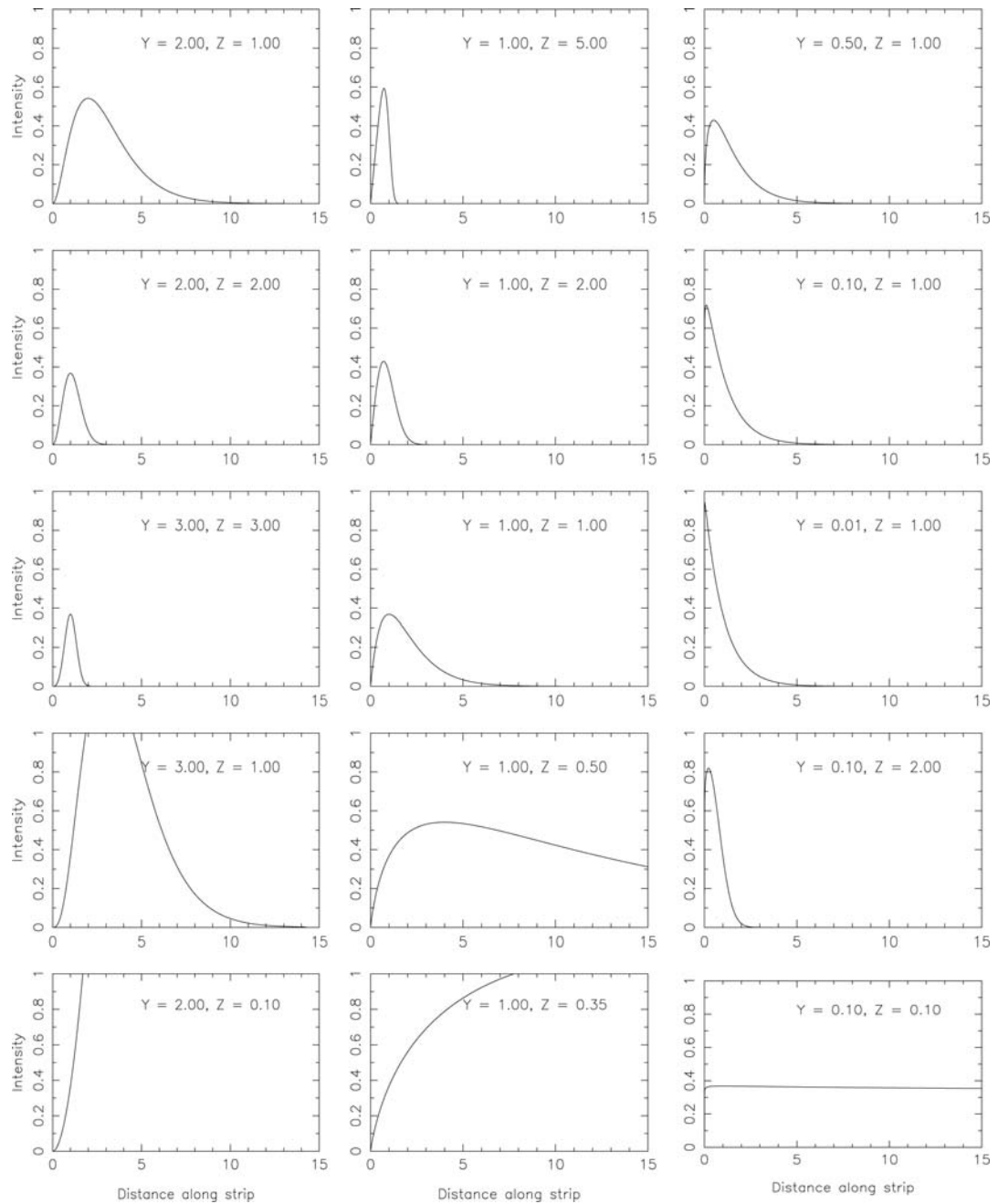


Figure 3.3: The bright spot intensity distribution, as defined by $I = (X/S)^Y e^{-(X/S)^Z}$, for a range of different X and Y values. The X-axis is the distance along the strip, X .

In this thesis, a Markov chain Monte Carlo (MCMC) analysis was used to adjust all parameters bar U_w and the flux contributions. MCMC analysis is an ideal tool as not only does it provide a robust method for quantifying the uncertainties in the various system parameters, it is more likely to converge on the global minimum rather than a local minimum. MCMC is described in detail in §3.3. Once the model parameters were optimised, the system parameters were calculated following the method outlined in §3.4.

3.2.1 White Dwarf Model Atmospheres

The white dwarf temperature and distance were found by fitting the three-colour white dwarf fluxes from the model fit to the predictions of the hydrogen rich, white dwarf model atmospheres of Bergeron et al. (1995). The white dwarf temperature was used to correct the white dwarf mass-radius relationships, which were in turn used to calculate the final system parameters (see §3.4).

An estimate of the white dwarf limb-darkening coefficient was obtained by using the white dwarf effective temperature and an estimate of $\log g$, in conjunction with the stellar atmosphere codes of Gänsicke et al. (1995). The model spectra were folded through ULTRACAM response curves (Hickman, 2011) in order to convert the spectra to fluxes. These fluxes were then fit as a function of the limb position in order to derive limb-darkening parameters appropriate for each band (e.g. Littlefair et al., 2006b, 2007).

3.3 Markov Chain Monte Carlo

3.3.1 Bayes Theorem and MCMC

MCMC is a stochastic approximation used to carry out Bayesian inference, which is a statistical approach of expressing all forms of uncertainty in terms of probability. Bayesian inference derives a quantity known as the *posterior distribution*, which in this thesis, is the probability distribution of a set of parameters, M , assuming some model, and given the available data (D). It is a probability distribution function (PDF), often expressed as $P(M|D)$. From Bayes rule, the posterior distribution of a set of parameters is given by

$$P(M|D) = \frac{P(D|M) \times P(M)}{P(D)}, \quad (3.2)$$

where $P(D|M)$ is the *likelihood function*, $P(M)$ is the set of *prior distributions*, and $P(D)$ is the marginal likelihood function, which is used for normalisation. $P(D)$ is very difficult to determine when a model contains a large number of dimensions. However, it is not required for parameter estimation, because it is only the shape of the distribution that is of interest, and a direct comparison between two models is not required (e.g. Gregory, 2007). The prior distribution, $P(M)$, expresses the knowledge of a given parameter before taking into account the data. Often, it is a subjective assessment based upon reasonable expectation. The likelihood function is a measure of how likely the data is to be observed, given a particular model configuration.

In principle, the aim is to solve Bayes formula for $P(M|D)$; the probability distribution of the model parameters given the available data and prior knowledge. The most probable parameter set is wanted, along with the fully quantified uncertainties that arise with it. However, solving Bayes formula for a complex model with many parameters such as the one described in §3.2, is not analytically feasible. MCMC is

an approach to estimating the posterior probability distribution, $P(M|D)$. Although $P(M|D)$ is unknown, if random samples can be drawn from $P(M|D)$, then $P(M|D)$ can be inferred using those samples. The larger the number of samples drawn, the more accurate the inferences of the total sample are. This is a Monte Carlo analysis, and is used to great effect in Chapter 6. By constructing a *Markov chain* which has parameter space M as its *state space* and $P(M|D)$ as its limiting, stationary distribution, it is possible to sample from $P(M|D)$, and then make Monte Carlo inferences about M .

3.3.2 Conditions of MCMC

An Markov chain will only converge on $P(M|D)$ if it is aperiodic, irreducible and reversible (e.g. Smith & Roberts, 1993). An aperiodic chain is a Markov chain which does not switch between two particular states in a regular periodic way. An irreducible chain means that it is possible for the chain to reach every state with a non-zero probability from any another state with a non-zero probability, in a finite number of steps. If a chain is reversible, then there is a finite possibility that a particular state may be revisited at some later point in the chain.

3.3.3 Metropolis-Hastings

A Markov chain can be produced by starting from an initial parameter set, M_N , and proposing the next step in the chain, via a transition probability (or *transitional kernel*), $q(M_{N+1}|M_N)$, where M_{N+1} is the parameter set at the next step in the chain. The transition kernel, $q(M_{N+1}|M_N)$, depends only on the current state, M_N , and no other state. This proposed step M_{N+1} , is then accepted with a probability $\alpha(M_{N+1}|M_N)$, such that the probability distribution of M_{n+1} , $P(M_{N+1}|M_N)$ is given

by

$$P(M_{N+1}|M_N) = q(M_{N+1}|M_N)\alpha(M_{N+1}|M_N). \quad (3.3)$$

If the step is accepted, the next state is set to the trial state. If the step is rejected, the next state is set to the current state, $M_{N+1} = M_N$, and a new trial state is drawn from $q(M_{N+1}|M_N)$.

There are several possibilities for the choice of $\alpha(M_{N+1}|M_N)$, the majority of which are generalisations of either the Metropolis-Hastings (M-H) algorithm (Metropolis et al., 1953; Hastings, 1970) or the Gibbs sampler (e.g. Casella & George, 1992). In this thesis, the M-H algorithm is used to describe $\alpha(M_{N+1}|M_N)$, which is given by

$$\alpha(M_{N+1}|M_N) = \min\left[\frac{P(M_{N+1}|D)q(M_N|M_{N+1})}{P(M_N|D)q(M_{N+1}|M_N)}, 1\right] \quad (3.4)$$

(e.g. Gilks et al., 1995; Ford, 2005, 2006; Gregory, 2007). $q(M_{N+1}|M_N)$ can take any form, but for the chain to be reversible, the transition kernel must satisfy the following criteria

$$q(M_{N+1}|M_N) = q(M_N|M_{N+1}). \quad (3.5)$$

Gilks et al. (1995) show that if the above criteria are satisfied, then the *detailed balance equation* can be reproduced, which must be satisfied in order to obtain a true Markov chain (e.g. Smith & Roberts, 1993). From the detailed balance equation, Gilks et al. (1995) go onto show that if M_N is drawn from $P(M|D)$, then M_{N+1} will also be from $P(M|D)$, and that once one sample from $P(M|D)$ is drawn, all subsequent samples will also be drawn from $P(M|D)$. Thus, after a sufficiently long period of initial random sampling (*the burn-in*), samples will eventually be drawn from $P(M|D)$, provided that Equation 3.5 is satisfied.

3.3.4 MCMC in Practice

Provided Equation 3.5 is satisfied, and the prior, $P(M)$, is ‘flat’ ($P(M) \sim 1$), then the transition probability, $\alpha(M_{N+1}|M_N)$, may be written as

$$\alpha(M_{N+1}|M_N) = \min\left[\frac{P(D|M_{N+1})}{P(D|M_N)}, 1\right]. \quad (3.6)$$

Because the likelihood function $P(D|M) \approx e^{[-\chi^2/2]}$, the Metropolis-Hastings algorithm was implemented according to Ford (2005), and is described as follows:

1. Start the chain with an initial state, M_0 , and step number N .
2. Generate a trial state, M_T , according to the transition kernel, $q(M_{N+1}|M_N)$.
3. Calculate $\chi^2(M)$ for the trial state *and* the current state.
4. Calculate $\alpha(M_{N+1}|M_N) = e^{-0.5[-\chi^2(M_T) - \chi^2(M_0)]}$.
5. Draw a random number, k , from a uniform distribution between 0 and 1.
6. If $k \leq \alpha(M_{N+1}|M_N)$, set $M_{N+1} = M_T$, otherwise set $M_{N+1} = M_N$.
7. Set $N = N+1$.
8. Go to step 2.

The choice of $q(M_{N+1}|M_N)$ is crucial to the practical implementation of MCMC. Provided that $q(M_{N+1}|M_N)$ satisfies Equation 3.5, it can take any form. A common choice for $q(M_{N+1}|M_N)$ is a Gaussian distribution centred around M_N , with an initial estimate of the scale parameters (e.g. Ford, 2005, 2006). However, care must be taken, as a poor choice of $q(M_{N+1}|M_N)$ may lead to poor sampling (e.g. sampling far from $P(M|D)$), and a very slow rate of convergence towards $P(M|D)$. The scale of $q(M_{N+1}|M_N)$ is vital, as if there is a large variation between trial states (i.e. a

large dispersion), then a large number of states will be rejected, and the chain will take a long time to converge. Likewise, if the chain accepts too many steps, then the chain will behave like a random walk and also converge very slowly (e.g. Gilks et al., 1995; Ford, 2005). The ‘mixing’ of a chain is also a crucial factor. A chain is said to ‘mix poorly’ when large numbers of steps are rejected. A chain may mix poorly even after convergence. A well mixed chain accepts enough steps to sample efficiently around $P(M|D)$. To aid the mixing of a chain, it is common practice to introduce a scale factor. The scale factor scales the variance of the Gaussians used to generate $q(M_{N+1}|M_N)$, and is tuned to keep the acceptance rate near 0.23. This was found by Roberts et al. (1997) to be the optimal value. This improves the mixing of the chain, and enables convergence towards $P(M|D)$ on an acceptable time scale. In this thesis, the scale factor was only varied during the initial stages of the MCMC, as altering it throughout would violate Equation 3.5, making the chain non-Markovian. This would result in not sampling from the true $P(M|D)$.

For models with several parameters or where parameters exhibit strong correlations, independent Gaussian distributions are an inefficient choice of $q(M_{N+1}|M_N)$, regardless of the scale factor, as shown in Figure 3.4. Therefore, in this thesis, multivariate Gaussian distributions are used. These are defined by a covariance matrix, which describes how each of the various parameters are related. For the MCMC simulations described in this thesis, an initial estimate of $q(M_{N+1}|M_N)$ was obtained using a Levenberg–Marquardt (LM) algorithm (Press et al., 1992). The resulting parameters obtained from the LM fit were used as a starting point for the MCMC simulation. A typical MCMC was split into two sections; the burn-in phase, which was used to converge towards $P(M|D)$; and the production phase, which samples from $P(M|D)$. During the burn-in phase, the covariance matrix and scale factor were updated every 5,000 steps. A typical burn-in phase included a total of 350,000 steps. After the burn-in phase, if the chain was judged through a by-eye inspection to

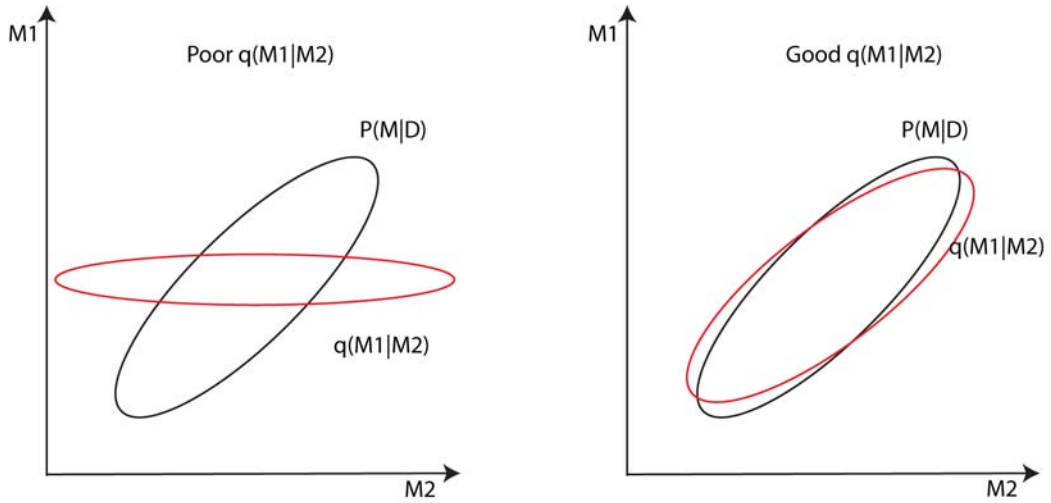


Figure 3.4: Left: Two parameters with strong correlations are poorly described by independent Gaussian distributions. This choice of $q(M1|M2)$ would lead to poor sampling. Right: A multi-variate Gaussian distribution is a better approximation to the desired distribution, and will sample far more efficiently.

have converged and mixed well, the production phase was initiated. The production phase, also typically 350,000 steps, was started from the parameters obtained at the final stage of the burn-in phase, with the covariance matrix and scale factor defined using the final 5,000 steps of the burn-in phase. Example burn-in and production chains are shown in Figure 3.5

3.4 Photometric Mass Determinations

The LFIT procedure provides optimised values of the mass ratio (q), the eclipse full half maximum ($\Delta\phi_{1/2}$), and the white dwarf radius as a fraction of binary separation (R_w/a). The inclination (i) is determined from q and $\Delta\phi_{1/2}$, via a binary chop search using an accurate model of the Roche Lobe. When combined with the orbital period, P_{orb} , the remaining system parameters are solved by starting from Equation 1.1 and

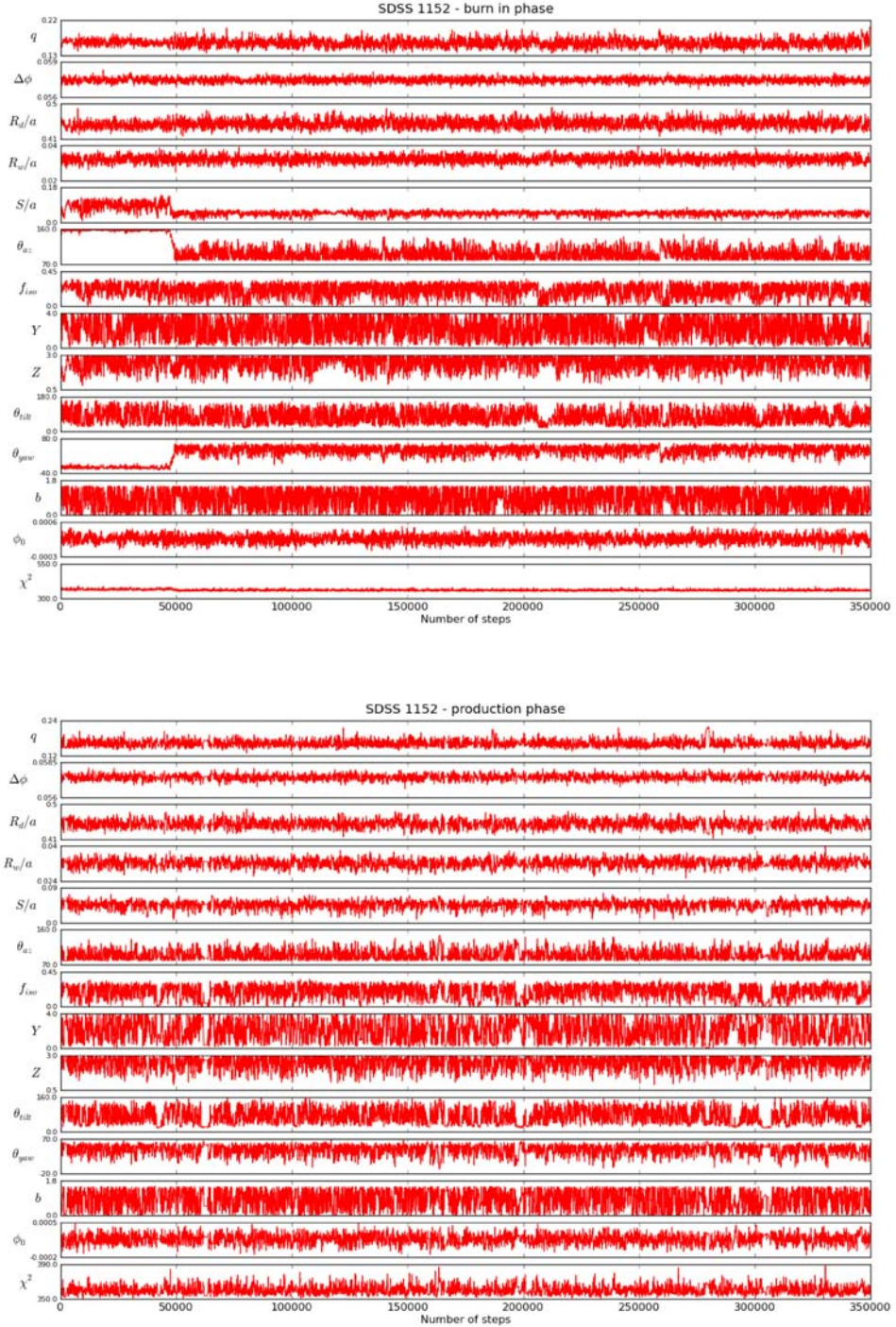


Figure 3.5: A plot of the MCMC burn-in chain (top) and MCMC production chain (bottom) for the g' band eclipses of SDSS 1152. Each chain corresponds to the variables in our model, outlined in §3.2. The limb darkening coefficient of the white dwarf, U_w , and the flux contributions of each component, were not modelled. The flatness of each chain indicates the chain has converged to a solution, whilst the scatter of the chain indicates that it is well mixed.

substituting $y = R_w/a$ and $q = M_2/M_w$ to obtain

$$R_w = y \left(\frac{GM_w(1+q)P_{orb}^2}{4\pi^2} \right)^{1/3}. \quad (3.7)$$

Equation 3.7 can then be combined with a series of white dwarf mass-radius relationships (Wood, 1995; Panei et al., 2000; Hamada & Salpeter, 1961), that are corrected for the temperature of the white dwarf (see §3.2.1). This can then be solved for for R_w , M_w and a . The relationships of Wood (1995) are favoured, because they have thicker hydrogen layers which may be more appropriate for CVs. However, they do not reach high enough masses for some of the systems presented in this thesis. Above $M_w = 1.0M_\odot$, the mass-radius relationships of Panei et al. (2000) are adopted. In turn, these models do not extend beyond $M_w = 1.2M_\odot$; above this mass the Hamada & Salpeter (1961) relationship is applied. No attempt is made to remove discontinuities from the resulting mass-radius relationship.

The mass of the secondary star, M_2 , is found using Equation 1.3 and M_w , whilst the radius of the secondary star, R_2/a , can be found using Equation 1.4. The radial velocity of the secondary star, K_2 , can be found using the velocity form of Kepler's 3rd law,

$$\frac{K_2^3 P_{orb}}{2\pi G} = \frac{M_w \sin^3 i}{(1+q)^2}, \quad (3.8)$$

which in turn can be used to obtain K_w using Equation 1.3.

At each step in the MCMC chain the model values of q , i and R_w/a are used to calculate the white dwarf mass M_w/M_\odot , white dwarf radius (R_w/R_\odot), secondary star mass (M_2/M_\odot), secondary star radius (R_2/R_\odot), binary separation (a/R_\odot) and the radial velocities of the white dwarf and secondary star (K_w and K_2 , respectively). Because each step of the MCMC has already been accepted or rejected based upon the Metropolis-Hastings rule, the distribution function for each parameter gives an estimate of the probability density function (PDF) of that parameter, given the

constraints of our eclipse data. The PDFs obtained in each band fit by the model can then be combined into the total PDF for each system, as shown in Chapter 5.

3.5 Radial Velocity Measurements

3.5.1 Cross-Correlation of the Secondary Star

In Chapter 6 the radial velocity of the secondary star, K_2 , is one of four components used to measure the system parameters for the eclipsing CV CTCV J1300-3052. If the spectral features of the secondary star are easily visible in the spectrum, then the easiest way to determine K_2 is via cross-correlation (Tonry & Davis, 1979). This requires time-series CV spectra. The positions of a given absorption/emission line are measured relative to the same feature on a template star at different phases of an orbital cycle.

The template star is usually a star with similar spectral features to the secondary star. If possible it should be the same spectral type, although often this is initially unknown. Templates are usually bright, isolated stars with a known radial velocity which should be removed before cross-correlating. The CV and the template spectra should both be normalised by dividing by a constant and subtracting fits to the continuum. The template star should also be broadened to match the smearing of the CV spectra over the exposure time. The most accurate method to do this would be to calculate the smearing in small time steps and sum the result. At each step, the velocity shift of secondary star can be estimated from a first guess/estimate of K_2 , and the brightness of features in the template scaled according to the estimated brightness of the secondary star at a given point in its orbit. In practice, this is too complicated to do and so the effect may be approximated by convolving the template

spectrum with a Gaussian of width given by

$$V_{smear} = \frac{2\pi t_{exp} K_2}{P_{orb}}, \quad (3.9)$$

where V_{smear} is the orbital smearing, t_{exp} is the exposure time, P_{orb} is the orbital period and K_2 is the radial velocity of the secondary star (e.g. Watson & Dhillon, 2001). K_2 is usually the aim of the study, so a first guess/estimate is still required. The template star also needs to be broadened by the rotational velocity of the secondary star, $v \sin i$ (see §3.6). However, in order to determine $v \sin i$, K_2 is required, and so in practice finding K_2 and $v \sin i$ requires an iterative technique. Although this method of calculating the orbital smearing is not strictly correct, the values of $v \sin i$ derived in Chapter 6 using this technique were found to vary only slightly ($\pm 3 \text{ km s}^{-1}$) when the amount of orbital smearing applied was varied between the minimum (0 km s^{-1} at quadrature) and maximum amounts (65 km s^{-1} at conjunction). Given that the amount of smearing makes such a small difference to the final result, it is unlikely that changing the method used to apply the smearing will alter the result significantly, and thus convolving the spectrum with a Gaussian can be considered a reasonable approximation.

Once the CV and template have been normalised and the template broadened by the appropriate amount, the CV and template spectra are re-binned onto a constant velocity scale and then cross-correlated to find the difference in position ($\Delta\lambda$) between the CV spectrum and template spectrum at a given orbital phase. Whilst cross-correlating, a cross-correlation-function (CCF) is produced for each spectrum over the wavelength range that was cross-correlated. The CCF is effectively the probability function, $P(v)$, where P is the probability that the radial velocity is v . The shift between the CV spectrum and template spectrum, $\Delta\lambda$, can be converted to a velocity

shift according to

$$V = \frac{c(\lambda_{cv} - \lambda_{template})}{\lambda_{template}}, \quad (3.10)$$

where V is the velocity shift, λ_{cv} is the position of the line in the CV spectrum, $\lambda_{template}$ is the position of the line in the template star spectrum, and c is the speed of light, $3 \times 10^8 \text{ ms}^{-1}$. The velocity shifts as a function of orbital phase may then be fit with a sine function according to

$$V = \gamma - K_2 \sin[2\pi(\phi - \phi_0)], \quad (3.11)$$

where V is the velocity shift, γ is the systemic velocity of the system, K_2 is the radial velocity of secondary star, ϕ is the orbital phase, and ϕ_0 is the phase offset. K_2 is thus given by the amplitude of the sinusoid.

3.5.2 Skew Mapping

The secondary star features in CV spectra are often very weak, and the CCFs produced using the method outlined in §3.5.1 can produce weak, broad CCFs with many spurious peaks caused by noise. In this situation, a technique known as skew mapping (Smith et al., 1993) can be used. Skew mapping relies on the fact that the true peak in the CCFs follows the radial velocity curve of the secondary star, which moves sinusoidally with orbital phase. By computing the line integrals for many different sine curves (i.e. back-projecting the CCFs, see §3.10.2) the line integral with the maximum contribution from the CCF provides the sinusoidal solution to the radial velocity curve (Vande Putte et al., 2003). Skew mapping essentially co-adds the absorption features from the secondary star, strengthening the true CCF peak while smearing out the noise peaks.

A detected secondary star would present itself as a peak in the skew map at K_x

$= 0$, $K_y = K_2$, assuming a systemic velocity (γ) of zero. If the peak lies off the $K_x = 0$ axis, then γ can be estimated by applying different systemic velocities in the back-projection until the peak is shifted onto the $K_x = 0$. By repeating the process with a number of different spectral types, the one that shows the strongest peak in the skew map provides an estimate of the spectral type of the secondary star.

3.6 Rotational Broadening and Spectral Type of the Secondary Star

The value of $v \sin i$ and the spectral type of the secondary star can be estimated via an optimal subtraction routine, which subtracts a constant times the normalised, broadened template spectrum from the normalised, orbitally corrected CV spectrum. The match between the template and CV spectra is measured by carrying out the subtraction and then computing χ^2 between the residual spectrum and a smoothed version of itself. This method is used as it reduces the effect of the continuum shape, so that the spectral type estimate is only a function of the relative absorption line strengths. Because the templates are normalised, the multiplicative constant gives the fraction of the light of the secondary star to the total light of the system. By finding the value of rotational broadening and/or spectral type template that minimises χ^2 , a value of $v \sin i$ and the spectral type of the secondary star (Dhillon & Marsh, 1993; Marsh et al., 1994) can be deduced. This value of $v \sin i$ should then be corrected for the intrinsic rotational velocity of the template star.

3.7 Spectroscopic Mass Determinations

Following the techniques outlined §3.5.1 and §3.6 yields values of the radial velocity of the secondary star, K_2 , and the rotational velocity of the secondary star, $v \sin i$.

For an eclipsing binary system with measurements of K_2 , $v \sin i$, P_{orb} and $\Delta\phi_{1/2}$, the system parameters can be calculated as follows.

The secondary star rotates synchronously with the orbital motion, so K_2 and $v \sin i$ can be combined to get

$$\frac{R_2}{a}(1 + q) = \frac{v \sin i}{K_2} \quad (3.12)$$

(e.g. Horne et al., 1993; Warner, 1995). Combining Equation 3.12 with Equation 1.4 gives two simultaneous equations that can be solved for q and R_2/a . The orbital inclination, i , is fixed by q and $\Delta\phi_{1/2}$, using geometrical arguments, (e.g. Bailey, 1979, §3.2). In this thesis, the inclination is determined from q and $\Delta\phi_{1/2}$ via a binary chop search using an accurate model of the Roche Lobe. Using Equation 3.8, the previously calculated values of q and i can be used to find the mass of the primary star, M_w . From this, the mass of the secondary star, M_2 and radial velocity of the primary star, K_w can be found using Equation 1.3. The radius of the secondary star can be calculated using the observed rotational velocity of the secondary star, $v \sin i$, according to

$$\frac{v \sin i}{R_2} = \frac{2\pi \sin i}{P_{orb}} \quad (3.13)$$

(e.g. Warner, 1995). The final parameter, the binary separation, a , can be calculated using by substituting the values derived in the steps above into Equations 3.12 and 3.13.

3.8 The K_2 Correction

In order to calculate accurate component masses, the centre of mass radial velocity amplitude of the secondary star is required. However, the irradiation of the secondary stars in CVs by the emission regions around the white dwarf and bright spot have

been shown to influence the measured K_2 (e.g. Wade & Horne, 1988). If absorption lines are suppressed on the irradiated side of the secondary star, the centre of light will be shifted towards the back of the star. Likewise, if emission is enhanced on the inner face, the centre of light will be shifted towards the front of the star. The measured value of K_2 will either be larger (absorption) or smaller (emission) than the true value.

It is possible to correct the measured K_2 value if the distribution of absorption or emission can be estimated. This can be done using the formula

$$K_2 = \frac{K_{meas}}{1 - f(1 + q)(R_2/a)} \quad (3.14)$$

(Wade & Horne, 1988; Parsons et al., 2012a,b), where f is a constant between -1 and 1 that describes the distribution of absorption or emission across the stellar surface, K_{meas} is the measured radial velocity of the secondary star, q is the mass ratio and R_2/a is the radius of the secondary star in units of binary separation. For $f=0$, the emission is distributed uniformly across the surface of the secondary star, while for $f=1$ all of the flux is assumed to come from the sub-stellar point. A negative value of f implies that the light originates from the back of the secondary star. Parsons et al. (2010) show that if the emissivity is proportional to the incident flux, then the correction factor is typically $f=0.77$ for optically-thin emission and $f=0.50$ for optically-thick emission. Parsons et al. (2010) found that for the highly irradiated M-star in the close binary NN Ser, most of the emission lines were somewhere between optically thin and thick, rather than either extreme; thus it is likely the true value will lie somewhere inbetween and thus a range of expected K_2 values can be calculated using Equation 3.14.

3.9 Spectroscopic Distance Estimation

By finding the apparent magnitude (m) of the secondary star from its contribution to the total light during eclipse, and by estimating the absolute magnitude (M), the distance (d) in parsecs to the system can be calculated using the equation

$$5 \log(d/10) = m - M - A_\lambda, \quad (3.15)$$

where A_λ is the interstellar extinction along the line of sight in magnitudes and λ is a given wave-band. For all observations in this thesis, A_λ was not known and there was no way to estimate it. However, the objects studied in this these are close (< 1 kpc), and so the effects of extinction should be relatively small. For this reason, A_λ is assumed to be zero throughout.

The largest source of uncertainty using this method is the absolute magnitude (M_λ) of the secondary star. This can be estimated using empirical relationships such as those of Knigge et al. (2011). For a recent review of distance estimations in CVs, see Gariety & Ringwald (2012).

3.10 Doppler Tomography

A CV typically subtends $< 10^{-4}$ arc-seconds at Earth and so it is not possible to resolve the individual components by direct imaging. It is therefore necessary to use indirect methods. Doppler tomography is an indirect imaging technique developed by Marsh & Horne (1988), which uses the velocity information contained in emission line profiles at different orbital phases to determine the velocity-space distribution of the emission in CVs. For a comprehensive review of Doppler tomography, see Marsh (2001).

3.10.1 Line Formation

If one considers a single particle at some point in the binary that is moving parallel to the orbital plane, then the emission will trace a sinusoid around the mean velocity of the system. This sinusoid can be associated with a velocity within the binary system if the phase and amplitude are known. In practice, the emission lines in CVs are formed from many particles (often in different regions), and thus the profiles are the sum of many sinusoids which are blended together. As there are many lines and regions, interpretation is often difficult. Doppler tomography aims to separate these profiles and recover a map of the emission regions.

By considering Figure 3.6, each point in the binary system can be represented in velocity coordinates, (V_X, V_Y) . The radial velocity of any point in the system at phase ϕ is given by

$$V_R = \gamma - V_X \cos 2\pi\phi + V_Y \sin 2\pi\phi. \quad (3.16)$$

The binary can then be represented as an image in velocity space, where the emission line strength is a function of velocity, $I(V_X, V_Y)$. The strength of the line profile between any radial velocities V and $V + \delta V$ is given by the integration of all emission sites with appropriate radial velocities, that is

$$f(V, \phi) = \int_{-\infty}^{\infty} \int_{-\infty}^{\infty} I(V_x, V_y) g(V - V_R) \delta V_x \delta V_y, \quad (3.17)$$

where $g(V - V_R)$ is a function representing the line profile at each point of emission. It includes all effects such as instrumental broadening and is assumed to be identical at each point. This function is a narrow function and thus the shape of the line profile between V and $V + \delta V$ is given by the summation of all points $I(V_X, V_Y)$ which satisfy $V_R \sim V$. The shape of the line profile at a certain radial velocity is therefore obtained by summing emission from all points with the relevant radial velocity. This

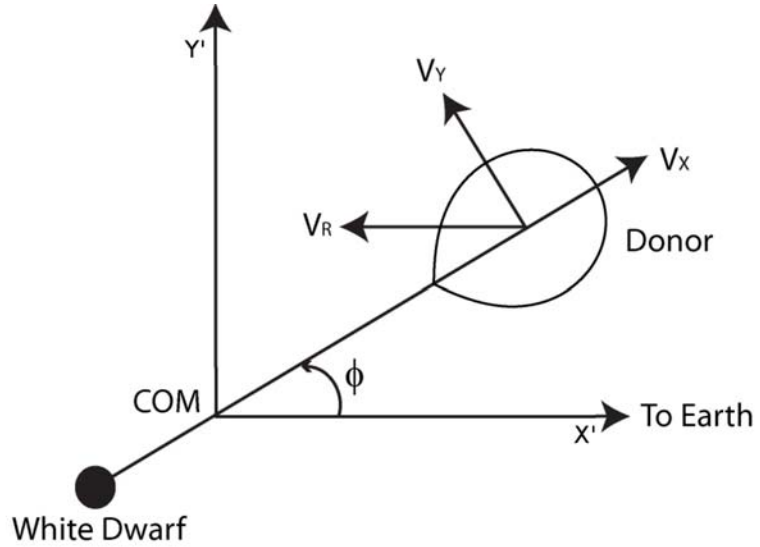


Figure 3.6: A diagram showing how velocity co-ordinates relate to the binary system. COM denotes the centre of mass of the binary.

is equivalent to summing along the straight lines defined by Equation 3.16. The line profile at any given orbital phase can therefore be thought of as a projection of the velocity space image along the direction determined by the orbital phase. This is shown in Figure 3.7.

3.10.2 Back Projections

If the line profiles ($f(V, \phi)$) are known, as they usually are, it is possible to transform them to obtain the velocity space image $I(V_x, V_y)$ via Fourier transform and *back-projection*. The process is described in detail in Marsh (2001) and summarised below.

The Fourier transform of $f(V, \phi)$ is multiplied by $|s|/G(s)$, where $G(s)$ is the Fourier transform of $g(V)$ over V and s is the frequency in inverse velocity units. The inverse Fourier transform of this product is then taken to produce filtered, modified line profiles $\tilde{f}(V, \phi)$. These modified line profiles are then back-projected to obtain

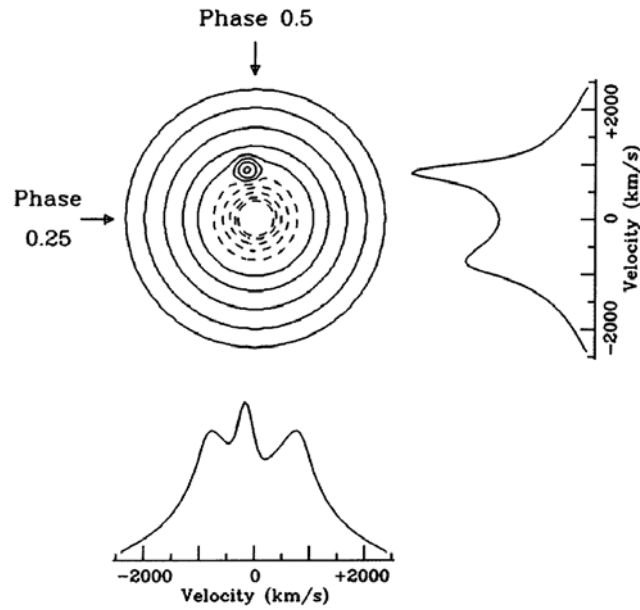


Figure 3.7: A model image and the equivalent profiles formed by projection along orbital phases 0.25 (right) and 0.5 (bottom). Figure taken from Marsh (2001).

the image $I(V_X, V_Y)$, which is given by

$$I(V_x, V_Y) = \int_0^{0.5} \tilde{f}(V_R = \gamma - V_X \cos 2\pi\phi + V_Y \sin 2\pi\phi, \phi) \delta\phi. \quad (3.18)$$

This means that each point in the image $I(V_X, V_Y)$ is the result of the integration along a sinusoidal path defined by the values of V_X and V_Y in the line profile. The need for the filtering process can be understood by considering the following situation; a single point of emission in a real image from a point $(0, K_y)$, as shown in the left panel of Figure 3.8, has a resulting trail consisting of a well defined sinusoid (the black line in the centre panel of Figure 3.8). Back projecting this sinusoid leads to a bright peak at $(0, K_y)$, but sinusoidal paths with slightly lower or higher K_y values (blue line in the centre panel of Figure 3.8) have non-zero line integrals. The bright peak is therefore a convolution of the true image with a point spread function as shown in the right panel of Figure 3.8. By filtering, this point spread function can be deconvolved and the true disc image recovered. In practice, $G(s)$ is Gaussian, and



Figure 3.8: Left: An emission site in a real image $(0, K_y)$. Centre: The resulting trail from a point in the emission site (black), together with a sinusoid of similar velocity (blue). Right: A back projection of the trail without filtering. The image is blurred due to contamination with similar sinusoids.

so the filtering process often amplifies high frequencies as $G(s)$ drops to zero at large s , which introduces noise into the image. However, this problem can be overcome by applying a Gaussian window filter, $W(s)$, which cuts off the higher frequencies and limits the noise propagation in the final image. However, by applying this filter the final image obtained is a blurred version of the true image, and thus the filtering process is a trade-off between resolution and noise.

3.10.3 Interpretation of Doppler Maps

Doppler tomography produces images of emission distribution in velocity space. The relationship between velocity coordinates and positional coordinates are shown in Figure 3.9. Figure 3.9 shows that the white dwarf and secondary star are centred on $(0, -K_W)$ and $(0, K_2)$, respectively, while the accretion disc appears as a ring centred on the white dwarf, but inverted such that the inner disc shows higher velocities.

In practice, this transformation is rarely made outright because such a transformation depends on the system parameters, which are generally not known or uncertain. In addition, one velocity can correspond to emission at several different spatial locations.

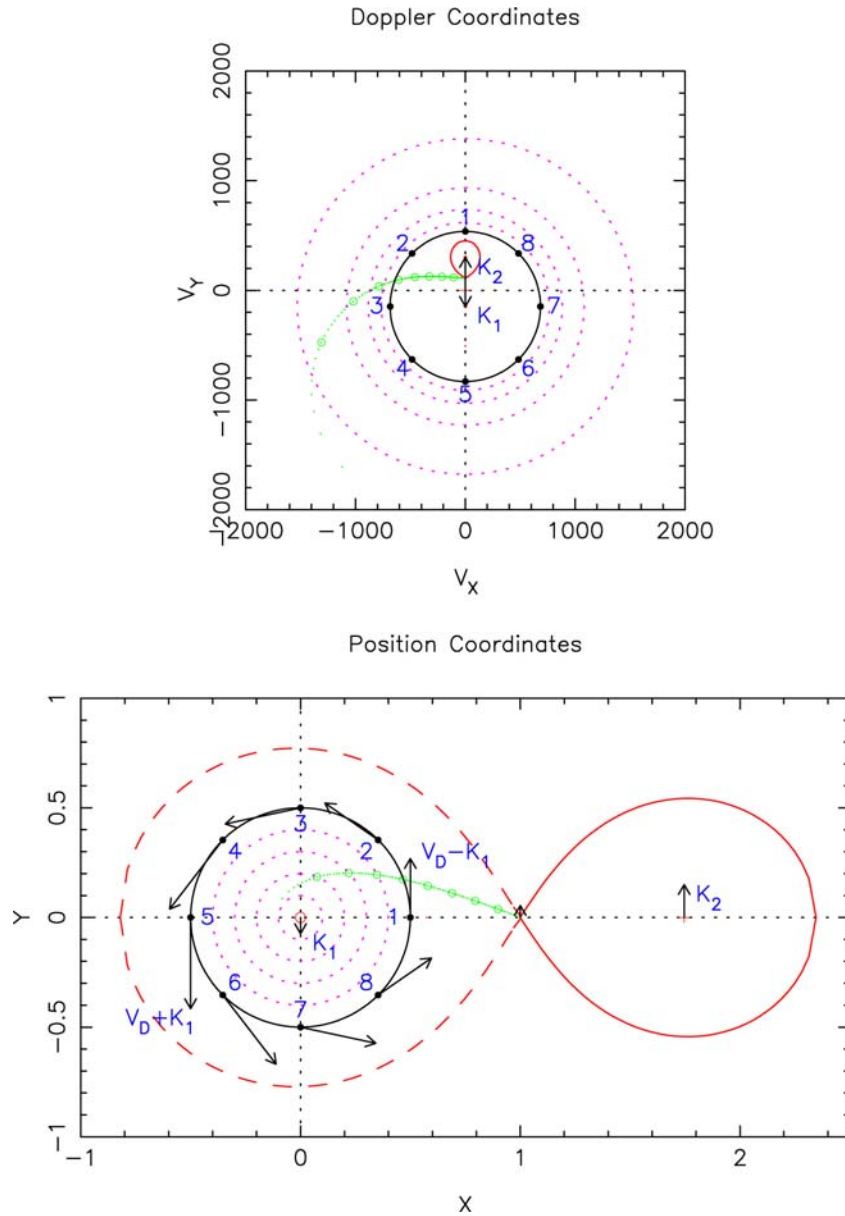


Figure 3.9: The translation of velocity coordinates to position coordinates when interpreting a Doppler map. K_2 and K_w represent the radial velocities and centre of mass of the secondary and primary stars, respectively. Diagram reproduced from Steeghs (1999).

3.10.4 Limitation of Doppler Tomography

Doppler tomography relies on five key assumptions. They are;

1. All points are equally visible at all times.
2. The flux from any point is constant.
3. The intrinsic width of the profile from any point is negligible.
4. All vectors rotate with the binary star.
5. All motion is parallel to the orbital plane.

Assumption one is violated by the eclipsing nature of the systems studied in this thesis. The inner, irradiated face of the secondary stars are self-eclipsed around phase 0 and again by the white dwarf and disc around phase 0.5. The white dwarf and accretion disc are likewise eclipsed around phase 0. Assumption two is violated by flares and flickering, which are especially prevalent in CTCV J1300-3052 (see Chapters 4, 5 and 6). Assumptions four and five are frequently violated by the bright spot, where in-falling material collides with the accretion disc and emission occurs non-parallel to the orbit, and Marsh & Dhillon (1997) showed that assumption three may not always hold true.

Despite the clear limitations of Doppler tomography, the information obtained from the Doppler maps can be incredibly useful. It should however, always be treated with a degree of caution.

Chapter 4

Orbital Ephemerides and Light Curve Morphology

The contents of this Chapter regarding the targets CTCV 1300, CTCV 2354, SDSS 1152 and SDSS 1501 have been published in the Monthly Notices of the Royal Astronomical Society, **415**, 2025-2041 in a manuscript entitled '*Cataclysmic variables below the period gap: mass determinations of 14 eclipsing systems*', by Savoury, Littlefair, Dhillon, Marsh, Gänsicke, Copperwheat, Hickman and Parsons (Savoury et al., 2011). The analysis of the data and the following text are my own work.

4.1 Introduction

Over the last eight years the ULTRACAM group has used the high-speed, three-colour camera ULTRACAM (Dhillon et al., 2007) to obtain high time-resolution data for CVs. The ability to image in three different wave-bands simultaneously allows for determination of the white dwarf temperature, and thus allows the white dwarf mass-radius relationships to be corrected for white dwarf temperature as described in

§3.2.1. This makes ULTRACAM the ideal tool to study the complex and highly variable light curves of CVs.

Using ULTRACAM data, system parameters have been obtained for several short period systems (Feline et al. 2004a, 2004b; Littlefair et al. 2006a, 2007, 2008), including the first system in which accretion occurs from a sub-stellar secondary star (Littlefair et al. 2006b). In order to further enhance this sample of CVs, a number of eclipsing CVs were identified for which no high-time resolution data was known (with the exception of SDSS J1006+2337) for investigation with ULTRACAM. In total, eclipses of twenty CVs were observed, of which seventeen were below the period gap.

CTCV J2354-4700 and CTCV J1300-3052 (CTCV 2354 and CTCV 1300 hereafter) were discovered as part of the Calán-Tololo Survey follow up by Tappert et al. (2004), who found both systems to be eclipsing with orbital periods of 94.4 and 128.1 minutes, respectively.

SDSS J0750+1411 (SDSS 0751), SDSS J0901+4809 (SDSS 0901), SDSS J0920+0042 (SDSS 0920), SDSS J0924+0801 (SDSS 0924), SDSS J0932+4725 (SDSS 0932), SDSS J0935+1619 (SDSS 0935), SDSS J1006+2337 (SDSS 1006), SDSS J1152+4749 (SDSS 1152), SDSS J1250+6655 (SDSS 1250), SDSS J1524+2209 (SDSS 1524) and SDSS J1555-0010 (SDSS 1555) were identified as eclipsing CVs as part of the Sloan Digital Sky Survey (SDSS) follow up by Szkody et al. (2002, 2003, 2004, 2005, 2007, 2009) via analysis of their spectra. The spectra of the majority of systems showed strong, double-peaked emission from their Balmer emission lines, which is characteristic of a high inclination accreting binary. Follow up work by Southworth et al. (2007, 2010), Southworth (priv. comm., 2010) and Dillon et al. (2008) confirmed the systems to be eclipsing, with all but SDSS 0920 and SDSS 1006 below the period gap (see also Southworth et al., 2009). SDSS 0924 was identified as a possible polar due to the presence of strong HeII lines, but polarimetric observations revealed no polarisation. Photometry by Southworth et al. (2010) indicated a lack of accretion disc, supporting

the possibility of the system being magnetic.

SDSS J1325+2100 (SDSS 1325), CSS080227:112634-100210 (CSS0806277) and CSS080623:140454-102702 (CSS080623) were identified as eclipsing CVs as part of the Catalina Real-Time Transient Survey (CRTS) by Drake et al. (2009). Follow up observations by Southworth (priv. comm., 2010) confirmed SDSS 1325 and CSS080227 to be eclipsing, with orbital periods of 89.8 and 111.5 minutes, respectively. Similar follow up photometry by Warner & Woudt (2010) confirmed CSS080623 to be eclipsing with an orbital period of 85.6 minutes.

1RXS J180834.7+101041 (1RXS J1808) was identified as an eclipsing CV by Denisenko et al. (2008), who noted deep (1.3 mag) eclipses with an orbital period of 100.8 minutes. Denisenko et al. (2008) also noted that this system may be a AM Her type system due to the large scale variability between eclipses.

PHL 1445 was identified as an eclipsing CV by Wils (2009). Follow up observations by Wils et al. (2011) confirmed the system to have deep eclipses with an unusually short orbital period of 76.3 minutes. Wils et al. (2011) also presented follow up observations of a long period system, GALEX J0035+4623 (GAL0035), that was originally identified as a variable by Martin et al. (2005). This system was also confirmed to be eclipsing, with an orbital period of 248.1 minutes.

In this Chapter I present orbital ephemerides for each of the systems mentioned above and briefly discuss the light curve morphology for each system. Systems that are suitable for light curve modelling are identified.

4.2 Orbital Ephemerides

Orbital ephemerides were determined by fitting a second order polynomial to the eclipse times presented in Table 2.1a, 2.1b, 2.1c and 2.1d as described in §3.1. In each case there was no cycle ambiguity. However, a significant O-C offset was observed

between the data presented in this thesis and the times published by Tappert et al. (2004) for the targets CTCV 1300 and CTCV 2354. For CTCV 1300, the average O-C difference is 165.9 seconds, while for CTCV 2354 it is 148.0 seconds. This is thought to be due to the differing methods of calculating T_{mid} ; Tappert et al. (2004) calculated T_{mid} by fitting a parabola to the overall eclipse structure, whereas in this thesis T_{mid} is determined from the white dwarf eclipse. The average offsets were therefore subtracted from the published literature values and the resulting O-C difference used as the error for that mid eclipse time. In most cases, the mid-eclipse times were measured using only the g' band light curve, although for CTCV 1300, CTCV 2354, SDSS 1152 and SDSS 1501 the mid-eclipse times are an average of the time obtained using both the g' and r' band light curves. The ephemerides found are shown in Table 4.1.

4.3 Light Curve Morphology and Variations

Figure 4.1a, 4.1b, 4.1c and 4.1d shows the light curves for each system discussed in §4.1. Where relevant, the stacked (left) and average (right) light curves are shown. Each light curve is folded on orbital phase in the g' band. The g' band was chosen as they were generally the best quality light curves. In order to carry out the light curve modelling technique described in §3.2, the light curves are required to show clear white dwarf and bright spot ingress and egress features. Systems that fulfil this criteria are identified in the text below.

4.3.1 CTCV J1300-3052

Figure 4.1a shows the two eclipses of CTCV 1300 from the 2007 data set. The white dwarf ingress and egress features are clearly visible in both eclipses, as are the bright spot features. These features dominate the light curves, which follow a

Table 4.1: Orbital ephemerides.

Object	T_0 (HJD)	P_{orb} (d)	Additional Times
CTCV 1300	2454262.599146 (8)	0.088940717 (1)	Tappert et al. (2004)
CTCV 2354	2454261.883885 (5)	0.065550270 (1)	Tappert et al. (2004)
SDSS 1152	2455204.601298 (6)	0.067721356 (3)	Southworth et al. (2010)
SDSS 1501	2453799.710832 (3)	0.0568412623(2)	Littlefair et al. (2008)
SDSS 0901	2453773.487484(44)	0.077880543 (2)	Dillon et al. (2008)
CSS080623	2455329.734645(14)	0.059578967 (3)	–
PHL 1445	2455202.557859(41)	0.052984874 (3)	Wils et al. (2011)
SDSS 1325	2455253.332859(60)	0.062384797 (6)	Southworth, priv. comm., 2010
SDSS 0751	2454879.435969(64)	0.093165453 (7)	Southworth et al. (2010)
SDSS 0920	2455700.6050 (1)	0.147875 (1)	–
SDSS 0924	2454879.504552(93)	0.09114078 (10)	Southworth et al. (2010)
SDSS 0932	2453106.618386(76)	0.066161317 (4)	Homer et al. (2006)
SDSS 0935	2455251.56671 (17)	0.06405513 (28)	Southworth, priv. comm., 2010
SDSS 1006	2454540.57957 (14)	0.18591337 (21)	Southworth et al. (2009)
SDSS 1250	2453799.502725(12)	0.0587356841(8)	Dhillon et al. (2008)
SDSS 1524	2455709.598309(17)	0.065318662 (8)	Southworth et al. (2010)
SDSS 1555	2454260.726212 (3)	0.0788455473(7)	Southworth et al. (2010)
CSS080227	2455334.408756 (5)	0.077421637 (3)	Southworth, priv. comm., 2010
GAL 0035	2455477.56149 (12)	0.172274978(55)	Wils et al. (2011)
1RXS J1808	2455316.860552(35)	0.06949403 (24)	–

typical dwarf nova eclipse shape (e.g. Wood et al., 1986). The depth of the bright spot eclipse indicates that the bright spot is the dominant source of light in this system, while the eclipse of the accretion disc is difficult to discern by eye, indicating that the accretion disc contributes little light to this system. Closer inspection of the two eclipses reveals a noticeable difference in the shape of the bright spot ingress feature. This is caused by heavy pre-eclipse flickering. The flickering is reduced between phases corresponding to the white dwarf ingress and bright spot egress, indicating the source of the flickering is the inner disc and/or bright spot. The 2010 observations are discussed in §5.2.2. The clear white dwarf and bright spot features make this system ideal for modelling.

4.3.2 CTCV J2354-4700

Figure 4.1a shows all of the eclipses from the 2007 data set. The white dwarf ingress and egress features are clearly visible and along with the accretion disc dominate the shape of the light curve. A weak bright spot ingress feature is visible at an orbital phase of 0.995, however the system suffers from heavy flickering, making it difficult to identify the bright spot egress. The shape of the average light curve indicates possible egress features at phases 1.060 and 1.080. However, given the scatter there is some doubt as to whether these represent genuine egress features or merely heavy flickering. The flickering is reduced between phases corresponding to the white dwarf ingress and egress, indicating the source of the flickering is the inner disc. The observations from 2009 and 2010 are discussed in §5.2.2. The clear white dwarf ingress and egress features and the presence of some bright spot features means that this system is suitable for attempted modelling.

4.3.3 SDSS J1152+4049

Figure 4.1a shows all of the eclipses from the 2010 data set. The signal-to-noise ratio of this data is low in comparison to other systems, but a clear bright spot ingress feature at phase 0.975 is visible in addition to a clear bright spot egress feature at phase 1.075. The white dwarf features are clear, and dominate the overall shape of the light curve. Like CTCV 1300, the eclipse of the accretion disc is difficult to discern by eye, which again suggests that the accretion disc contributes little light to this system. The clear white dwarf and bright spot features make this system ideal for modelling.

4.3.4 CSS080623:140454-102702

Figure 4.1a shows all of the eclipses from the 2010 and 2011 data sets. The eclipse of CSS080623 follows a typical dwarf novae shape. The white dwarf and bright spot ingress and egress are clear, and dominate the shape of the light curve. An orbital hump is clearly visible, whilst there appears to be little contribution from the accretion disc. The clear white dwarf and bright spot features make this system ideal for modelling.

4.3.5 SDSS J0901+4809

Figure 4.1a shows the eclipses from the 2012 data set. The average light curve of SDSS 0901 is similar in shape to CTCV 1300 and SDSS 1152, and follows the ‘typical’ dwarf novae eclipse shape. The white dwarf and bright spot ingress and egress features are clearly visible, as is an orbital hump. These features dominate the shape of the light curve. The 2006 and 2010 eclipses (not shown) are very different; they show clear white dwarf ingress and egress features, and a clear orbital hump, but lack any obvious bright spot ingress or egress features. The clear white dwarf and

bright spot features visible in the 2012 data make this system ideal for modelling.

4.3.6 PHL 1445

Figure 4.1b shows the eclipses from the 2012 data set. The white dwarf ingress and egress features are clearly visible, as is the bright spot ingress. The bright spot egress is much more difficult to identify in the individual light curves, although the average light curve indicates a possible egress feature around phase 1.070. The individual light curves show heavy flickering that is reduced between phases corresponding to the white dwarf ingress and egress, which indicates the source of the flickering is the inner disc. This flickering is unusual, and unexpected given the very short orbital period of the system. There is a considerable drop in brightness outside of eclipse between the observations taken on the 14th January 2012 and those taken on the 15th and 16th of January 2012 that can be attributed to changes in the accretion disc. This rapid change in disc brightness over such short timescales suggests the accretion disc is highly unstable. The eclipse dated November 2011 (not shown) was found to be in outburst, further highlighting the active nature of this system. Although the flickering of individual eclipses is high, the clear features present in the average light curve means this system is suitable for modelling.

4.3.7 SDSS J1325+2100

Figure 4.1b shows the eclipses from the 2011 and 2012 data sets. The shape of the eclipse is similar to that of SDSS 1152. The white dwarf and bright spot features are clearly visible, although the signal-to-noise of the data is poor in comparison to other systems. The out of eclipse brightness of the 2012 data set is considerably fainter than the 2011 data set, and the bright spot ingress is less well defined. This is likely to be the result of changes in the accretion disc. Although the average eclipse

looks promising, the low signal-to-noise means that it is not possible to constrain a full MCMC model using these light curves. Further observations of this system are required for accurate and precise mass determinations to be made.

4.3.8 SDSS J0750+1411

Figure 4.1b shows all of the eclipses from the 2012 data set. The light curves are dominated by heavy flickering. The white dwarf ingress and egress features are clearly visible, as is the accretion disc. The bright spot features appear lost in the flickering of the individual light curves, although the bright spot ingress feature is visible in the average light curve around phase 0.975. The bright spot egress feature is not obvious, and so these light curves are not suitable for modelling. Further observations of this system are required.

4.3.9 SDSS J1524+2209

Figure 4.1b shows all of the eclipses from the 2011 data set. The average light curve of SDSS 1524 is similar in shape to CTCV 2354. The eclipse shows clear white dwarf ingress and egress features in addition to a clear bright spot egress feature. The bright spot ingress feature is much more difficult to resolve. The asymmetric shape of the eclipse bottom indicates the bright spot ingress feature is present between phase 0.975 and 0.990. The weakness of the bright spot features and low signal-to-noise mean that these light curves are not suitable for modelling at present. Further observations of this system are required.

4.3.10 SDSS J1250+6655

Figure 4.1b shows all of the eclipses from the 2006 and 2010 data sets. This system is highly variable and suffers from heavy flickering. There are clear white dwarf ingress

and egress features and in some individual light curves what appears to be bright spot ingress and egress features. However, when averaged together, these features disappear, indicating they are artifacts of flickering. As a result of the uncertainty in bright spot position, this system is not suitable for modelling at present. Further monitoring is desirable.

4.3.11 SDSS J1555-0010

Figure 4.1c shows all of the eclipses from the 2007, 2009, 2010 and 2011 data sets. Eclipse cycle 162 has been omitted from the plot due to low signal-to-noise, caused by a combination of poor seeing and cloud. The eclipse of SDSS 1555 shows a distinct ‘U’-shape that is dominated by the white dwarf ingress and egress features. There does not appear to be any obvious bright spot ingress or egress features, and so these light curves are not suitable for modelling. The white dwarf ingress and egress features appear short, although are of similar duration to systems containing high mass white dwarfs (e.g. CTCV 2354). These light curves are not suitable for modelling, however further monitoring is desirable.

4.3.12 CSS080227:112634-100210

Figure 4.1c shows all of the eclipses from the 2010 and 2011 data sets. The light curves are highly variable and are dominated by flickering and the accretion disc. The white dwarf ingress and egress features are clear, but there are no obvious bright spot features. These light curves are not suitable for modelling, however further monitoring is desirable.

4.3.13 1RXS J1808+1010

Figure 4.1c shows all of the eclipses from the 2010 data set. The light curve of J1808 is dominated by heavy flickering and the accretion disc. The object varies in brightness by ~ 0.6 magnitudes between observations, while the depth of the eclipse also varies. There are no obvious white dwarf ingress or egress features, which combined with the shape and depth of the eclipse, indicates that this system is only partially eclipsing. The high variability supports the observations by Denisenko et al. (2008) that is system could be magnetic. Recent eclipse studies by Southworth & Copperwheat (2011) and Yakin et al. (2011) also support a partially eclipsing system, indicating an inclination of $\sim 77-78^\circ$. This system is not suitable for modelling.

4.3.14 SDSS J0920+0042

Figure 4.1c shows all of the eclipses from the 2011 data set. The overall shape of the light curve is dominated by the accretion disc, although comparison of the photometry presented in this thesis to that of Szkody et al. (2003) does not indicate that the system was in outburst at the time of observation. There are no obvious white dwarf or bright features and so these light curves are not suitable for modelling.

4.3.15 GAL0035

Figure 4.1d shows the eclipse of the long period system GAL0035 dated 14th January 2012 (cycle 26920). The white dwarf ingress and egress features are clearly visible, although the ingress feature appears blended with the bright spot ingress. The bright spot egress feature is questionable, with possible features around 1.04 and 1.08. The eclipse observed on the 15th January 2012 (cycle 26980, not shown) was found to be in outburst, showing a ‘V’-shaped eclipse approximately one magnitude brighter than cycle 26920. This indicates that cycle 26920 may have been on the rise to outburst

at the time of observation. This eclipse is not suitable for modelling, however further monitoring, with better phase coverage, is desirable.

4.3.16 SDSS J1006+2337

Figure 4.1d shows the single eclipse of the long period system SDSS 1006. The light curve of SDSS 1006 is similar in shape to CTCV 1300, however the white dwarf ingress and bright spot ingress features are unresolved. This eclipse is very different to that of Southworth et al. (2009), who observed a clear bright spot ingress but had poor phase coverage of the bright spot egress. The eclipse in Figure 4.1d eclipse has a ‘u’-shaped bottom, which is again different from Southworth et al. (2009). Comparison of photometry to that of Southworth et al. (2009) does not suggest that the object was in outburst or the rise/decline from outburst at the time of observation. This single eclipse is not suitable for modelling, however further monitoring is desirable.

4.3.17 SDSS J0924+0801

Figure 4.1d shows the single eclipse of SDSS 0924. The light curve shows clear white dwarf ingress and egress features but no evidence of the type of bright spot ingress or egress features seen previously. A flare or jump in the light curve is visible immediately after the white dwarf egress, which could be attributed to the bright spot egress. Like Southworth et al. (2010), there are no obvious accretion disc features visible. Southworth et al. (2010) suggest that the object might be a polar, however the signal-to-noise of the data is too low to be conclusive. This light curve is not suitable for modelling, however further monitoring is desirable.

4.3.18 SDSS J0932+4725

Figure 4.1d shows the single eclipse of SDSS 0932. There is clear contribution from the accretion disc, and what appears to be a clear white dwarf ingress. The system shows a very gradual increase in light, characteristic of an accretion disc coming out of eclipse. The overall shape of the light curve suggests a highly asymmetric disc. Homer et al. (2006) suggests that this system may be an intermediate polar, but x-ray spectra is inconclusive. This system is not suitable for modelling, but further monitoring is desirable.

4.3.19 SDSS J0935+1619

Figure 4.1d shows the single eclipse of SDSS 0935. There appears to be a faint ingress and egress feature followed immediately by a large rise, similar in shape to an orbital hump. A similar feature appears present in three of the five eclipses presented by Southworth (priv. comm., 2010), but the feature is much smaller in comparison to the eclipse. A similar feature, but not as smooth as the one observed here, is also visible in the light curves of HU Aqr (e.g. Schwarz et al., 2009), suggesting that this object may be a polar. Szkody et al. (2009) noted broad, but weak emission lines with strong continuum, suggesting the system may be an old nova. The eclipse feature visible in Figure 4.1d is shallow, indicating that the eclipse is only partial. This system is not suitable for modelling.

4.4 Systems for Modelling

Based on the light curve morphologies discussed above, CTCV 1300, CTCV 2354, SDSS 1152, CSS080623, SDSS 0901 and PHL 1445 have been identified as suitable for modelling. These systems all show clear white dwarf and bright spot ingress and

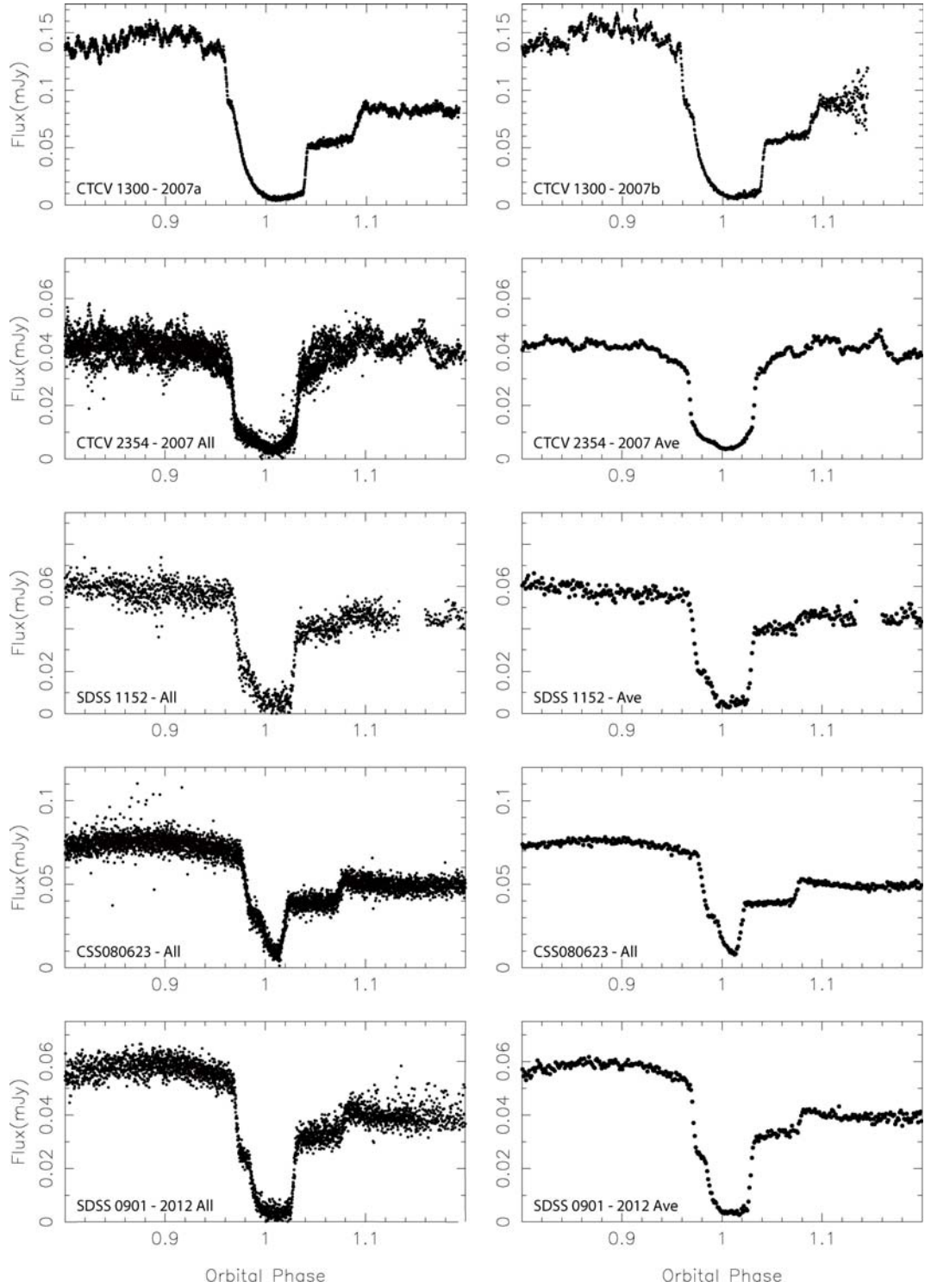
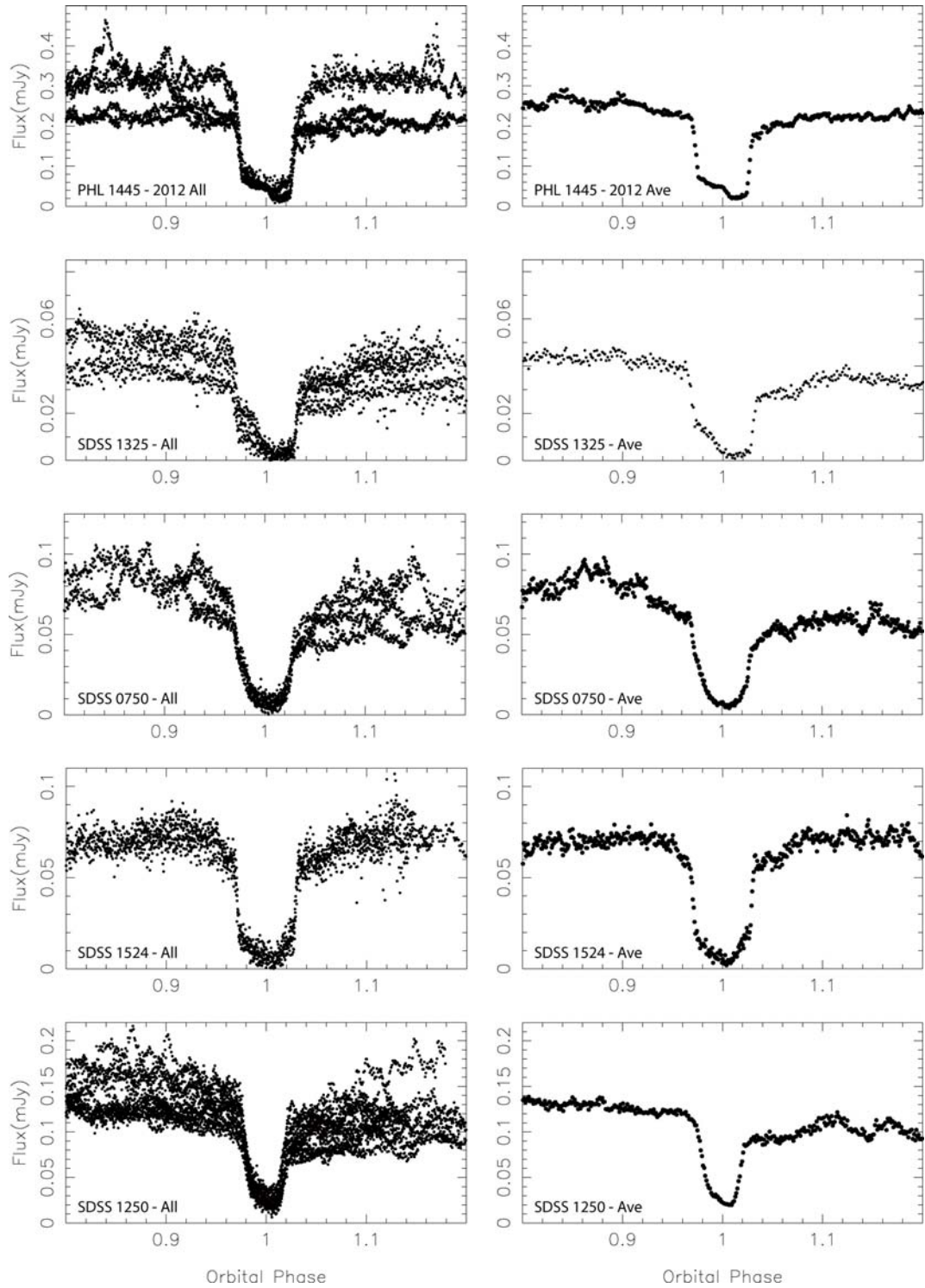
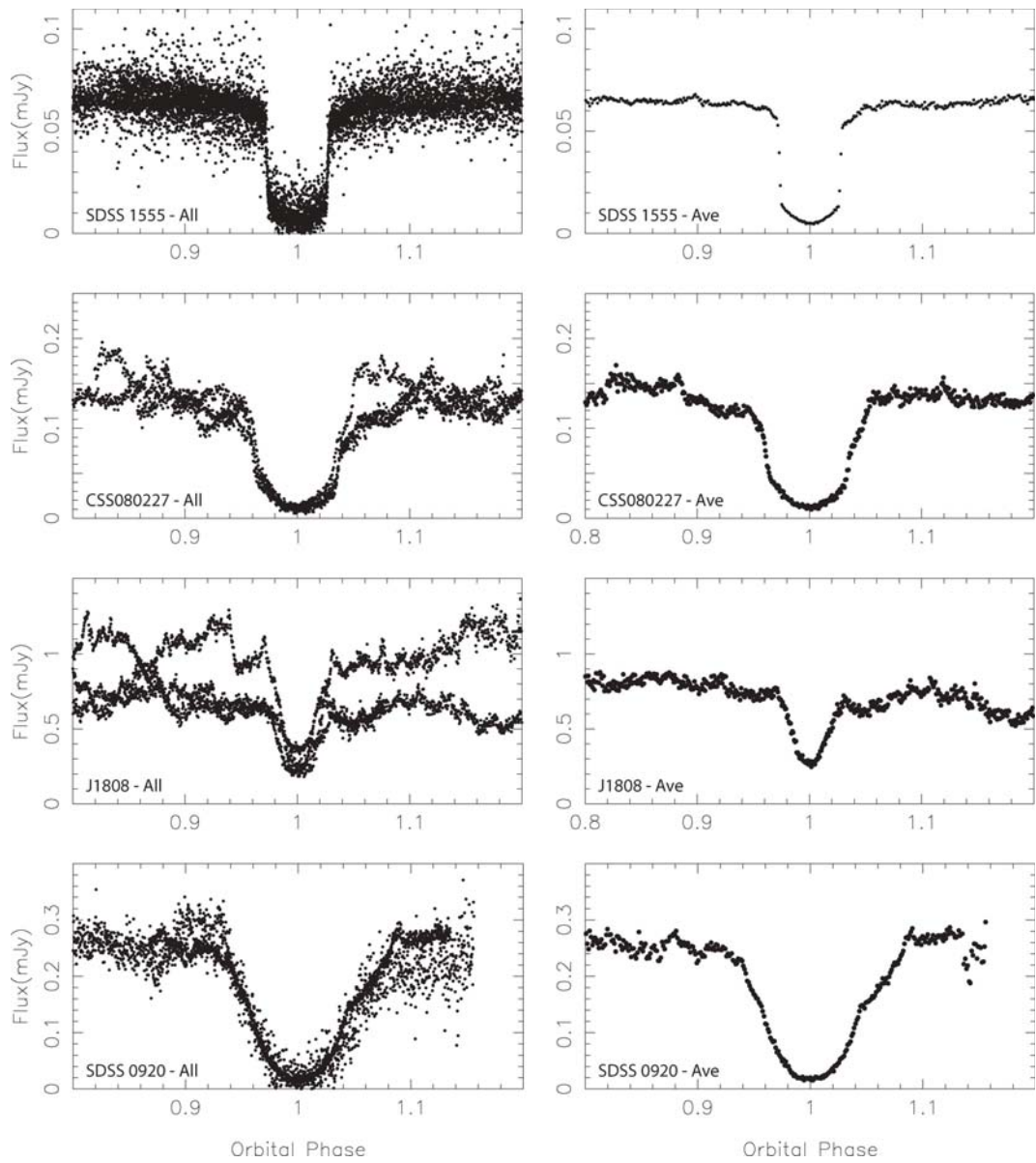
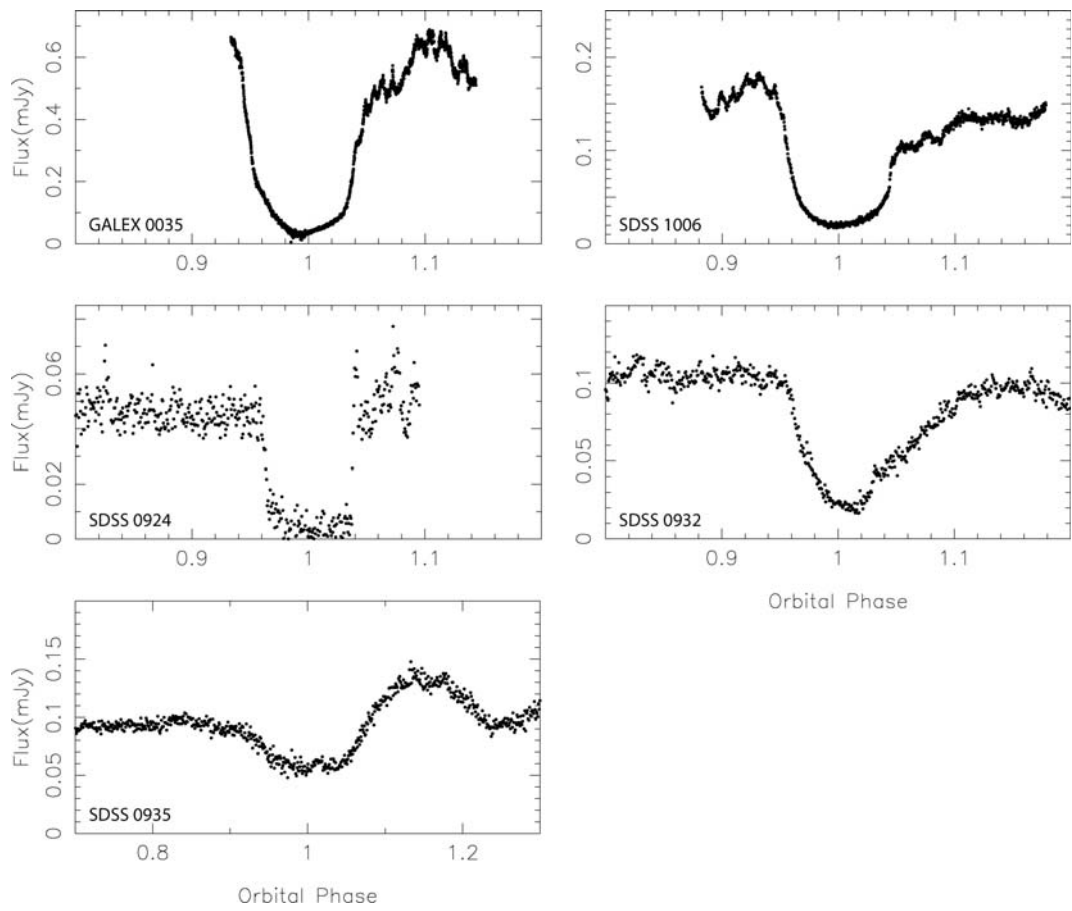


Figure 4.1a: The phased-folded, g' band light curves of 20 eclipsing CVs.

Figure 4.1b: *continued*

Figure 4.1c: *continued*

Figure 4.1d: *continued*

egress features in their average light curves.

Due to the heavy flickering in CTCV 1300, each night was fit individually, rather than a single fit to a phase-folded average. This was in order to provide a more robust estimation of the uncertainties. In general, the errors induced by flickering dominate over any photometric errors. Ideally, the same procedure would have been carried out with CTCV 2354, however the weak bright spot features and poor phase coverage of individual observations meant this was not possible.

Not all of the eclipses listed in Table 2.1a and 2.1b were used for determining system parameters. This is because some of the eclipses have poor signal-to-noise, or lack clear bright spot features. However, the eclipses not used for determining system parameters were still used to refine the orbital ephemerides presented in Table 4.1. These eclipses include CTCV 2354 cycles 11197, 11198, 11366, 11396, 11457, 11472, SDSS 1501 cycles 24718, 24719, SDSS 0901 cycles -13, 1, 2, 17964 and PHL 1445 cycles 11288 and 12552. CTCV 2354 cycle numbers 16156, 16676 and CTCV 1300 cycle number 12888 are analysed separately at the end of Chapter 5 because the shape of the eclipse changed significantly in comparison to the 2007 data.

While implementing the MCMC code described in §3.2, Stuart Littlefair discovered a bug in the original lfit code. The re-binning code used to average several light curves together mistreated the widths of the bins, which in turn affected the trapezoidal integration of the model over these bins. The direct result was that in cases of heavy binning, such as systems with heavy flickering or where several light curves had been averaged together, the white dwarf radius, R_w/a , was underestimated. The exact amount depended on the level of binning used. This consequently resulted in an overestimate of the white dwarf mass. Because the mass of the secondary star, M_r , is related to the white dwarf mass M_w by $M_r = qM_w$, this also resulted in an overestimate of the secondary star mass. This problem affects all of the eclipsing-CV papers published by the ULTRACAM group (Feline et al. 2004a, 2004b; Littlefair et

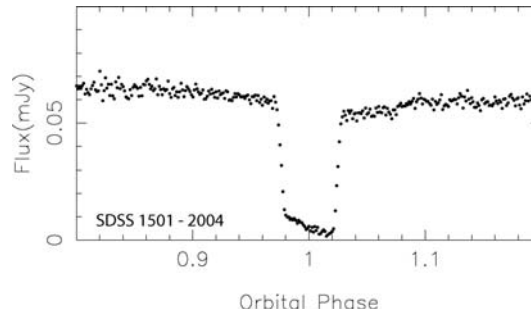


Figure 4.2: The 2004, g' band light curve of SDSS 1501.

al. 2006a, 2006b, 2007, 2008) by differing amounts. In this thesis, I therefore perform a re-analysis of the following systems: OU Vir, DV UMa, XZ Eri, SDSS J1702+3229 (SDSS 1702), SDSS J1035+0551 (SDSS 1035), SDSS J1507+5230 (SDSS 1507), SDSS J0903+3300 (SDSS 0903), SDSS J1227+5139 (SDSS 1227), SDSS J1433+1011 (SDSS 1433), SDSS J1502+3334 (SDSS 1502) and SDSS J1501+5501 (SDSS 1501).

The SDSS 1501 data listed in Littlefair et al. (2008) was not used in the new analysis. Instead, a single eclipse observed in 2004 (see Table 2.1a) was modelled. This single light curve is shown in Figure 4.2. This 2004 data was not fit by Littlefair et al. (2008) because the simplex methods used gave a seemingly good fit to the 2006 data. Despite appearing to have converged to a good fit, the MCMC analysis revealed that the 2006 data does not constrain the model, most likely due to the very weak bright spot features. The 2004 data shows much clearer and well-defined bright spot features than the 2006 data (see Fig. 1 of Littlefair et al. 2008), and so despite only having one eclipse (and thus lower signal-to-noise) it is favoured for the fitting process.

Chapter 5

Mass Determinations of 17

Eclipsing Systems

The contents of this Chapter have been published in the Monthly Notices of the Royal Astronomical Society, **415**, 2025-2041 in a manuscript entitled *Cataclysmic variables below the period gap: mass determinations of 14 eclipsing systems*, by Savoury, Littlefair, Dhillon, Marsh, Gänsicke, Copperwheat, Hickman and Parsons (Savoury et al., 2011). The reduction and analysis of the data and the following text are my own work unless stated otherwise.

5.1 Introduction

In this Chapter I present ULTRACAM light curves of CTCV 1300 ($u'g'r'i'$), CTCV 2354 ($u'g'r'$), SDSS 1152 ($u'g'r'$), CSS080623 ($u'g'r'$), SDSS 0901 ($u'g'r'$) and PHL 1445 ($u'g'r'$), and derive the system parameters via light curve modelling as described in Chapter 3. These targets are described in Chapter 4. In addition, I present an updated analysis of all eclipsing systems previously published by the ULTRACAM

group: OU Vir (Feline et al. 2004a), XZ Eri and DV UMa (Feline et al. 2004b), SDSS J1702+3229 (Littlefair et al. 2006a), SDSS J1035+0551 (Littlefair et al. 2006b, 2008), SDSS J150722+523039 (Littlefair et al., 2007, 2008), SDSS J0903+3300, SDSS J1227+5139, SDSS J1433+1011, SDSS J1501+5501 and SDSS J1502+3334 (Littlefair et al., 2008).

5.2 Results

5.2.1 System Parameters

For each system an MCMC analysis was performed on each phase-folded u' , g' , r' or i' light curve from an arbitrary starting position. Exceptions include CTCV 1300, where each night of observations were fit individually, and SDSS 1152, SDSS 1501, PHL 1445, for which fits were only calculated in the g' and r' bands due to u' -band data of insufficient quality to constrain the model. Bad data points, areas of the light curve with poor phase coverage or heavy flickering and parts of the light curve that the model is unable to fit, possibly due some additional physics not included in the model (e.g. accretion disc opacity), were excluded from the fitting process (shown as red data points in Figure 5.1) in order to optimise the fits around the white dwarf and bright spot ingress and egress. In most cases, phases 0.95 – 1.10 are fit without masking. Where no u' band MCMC fit could be obtained, the g' band model was fit and scaled to the u' band light curves without χ^2 optimisation. This allows for estimation of the white dwarf flux in the u' band, and determination of the white dwarf temperature. The white dwarf temperature (T_w) was estimated using an iterative process. A first estimate of T_w was derived from the white dwarf mass and radius found from a first iteration of the light curve modelling, assuming a white dwarf temperature of 10,000K and a limb-darkening coefficient of 0.345. The

white dwarf colours were then fit to the white dwarf models of Bergeron et al. (1995) (see §3.2.1). The value of $\log g$ implied from the white dwarf mass and radius was used to place an additional constraint on the fit, and thus the derived T_w . However, allowing both $\log g$ and T_w to vary whilst fitting the white dwarf colours was not found to have a significant effect; temperatures derived with the constraint were within 1000K (and so within errors) of those derived without. The data were not good enough to determine the white dwarf limb-darkening coefficient, U_w , accurately and so the procedure outlined in §3.2.1 was repeated in order to find an appropriate limb-darkening coefficient. Littlefair et al. (2007) show that the typical uncertainties in U_w using this technique are ~ 5 per cent, which leads to uncertainties in R_w/a of ~ 1 per cent. These errors have negligible impact on the final system parameters. Once an estimate of U_w and T_w were made, the fitting process was repeated using these values of U_w and T_w . A final estimate of T_w was derived from the final iteration of the fits. In general, the fits to each system are in excellent agreement with the light curves, as shown in Figures 5.1a, 5.1b, 5.1c and 5.1d. The model parameters found via the fitting process are shown in Appendix A. Overall, these model parameters are found to be in good agreement for each system across each band fit.

The PDFs obtained from each band fit were combined into the total PDF for each system, as shown in Figures 5.2a and 5.2b. Most systems have system parameters with a Gaussian distribution with very little asymmetry. The adopted value for a given parameter is taken from the peak of the PDF. Upper and lower error bounds were derived from the 67% confidence levels. For simplicity, and because the distributions are mostly symmetrical, an average is taken of the upper and lower error bounds. The final adopted system parameters, derived from the fits as described in §3.4, are shown in Tables 5.1a and 5.1b. Figures 5.6 and 5.7 show the true 67% confidence levels for the white dwarf mass and secondary star mass, respectively, for each system.

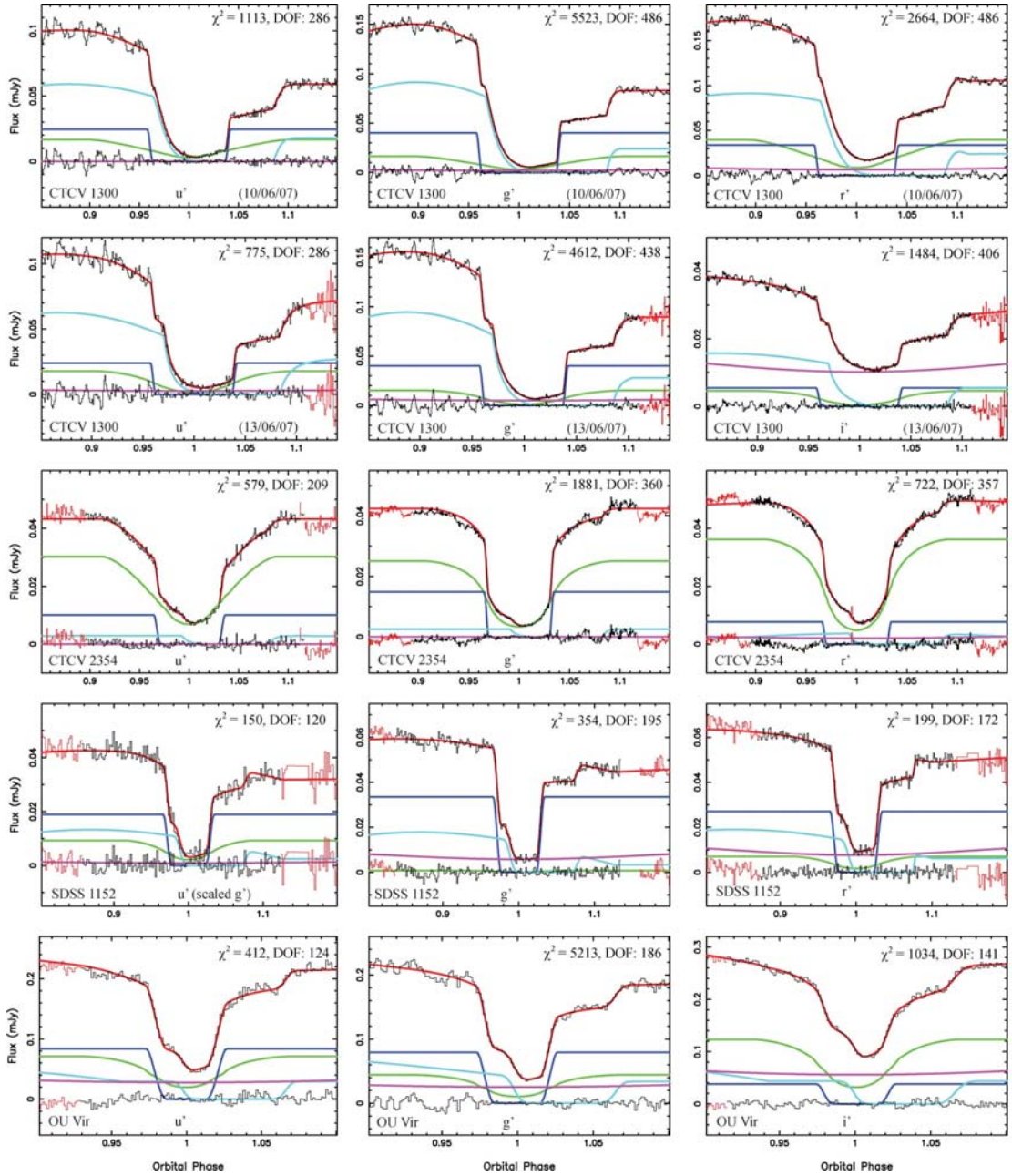
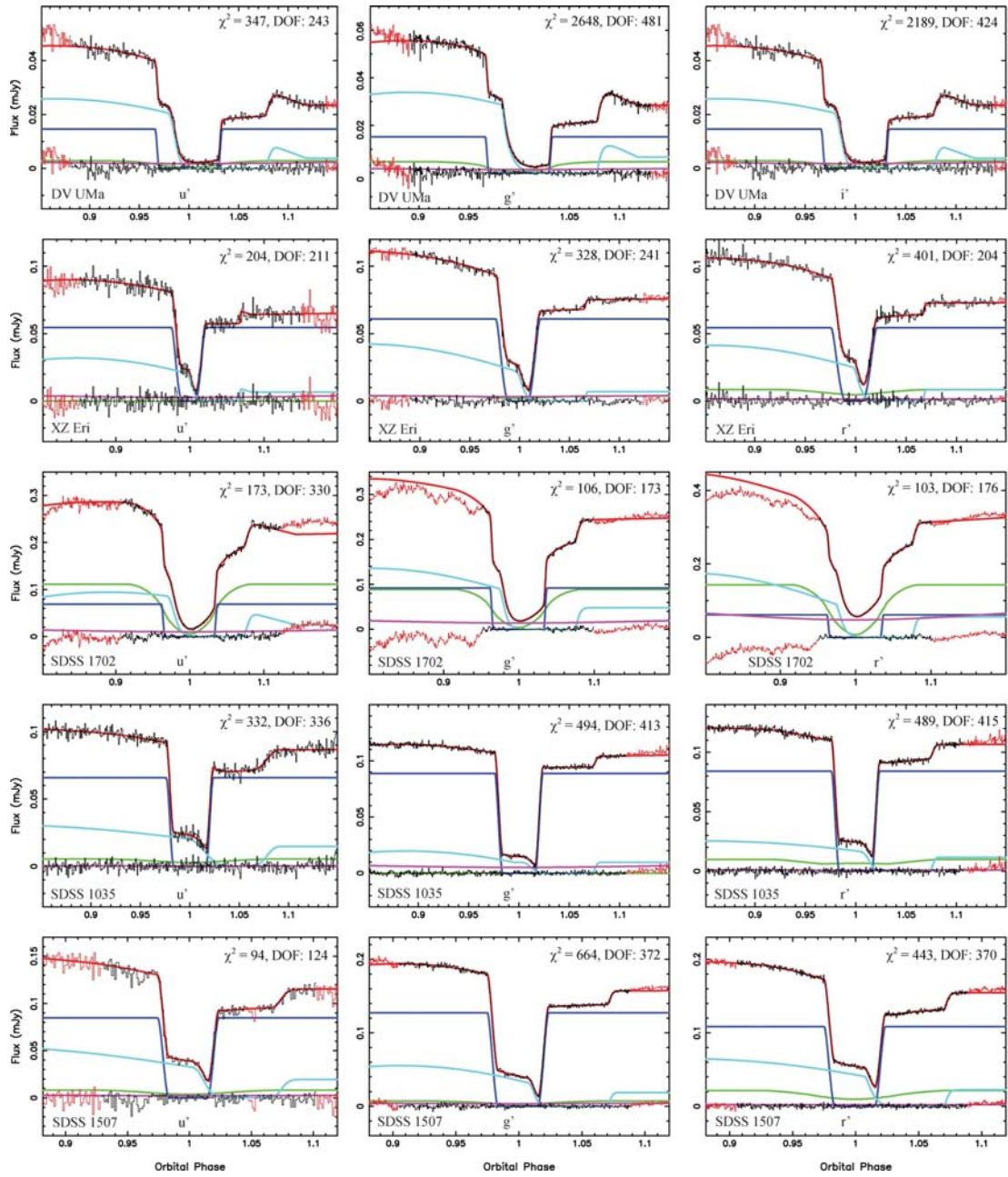
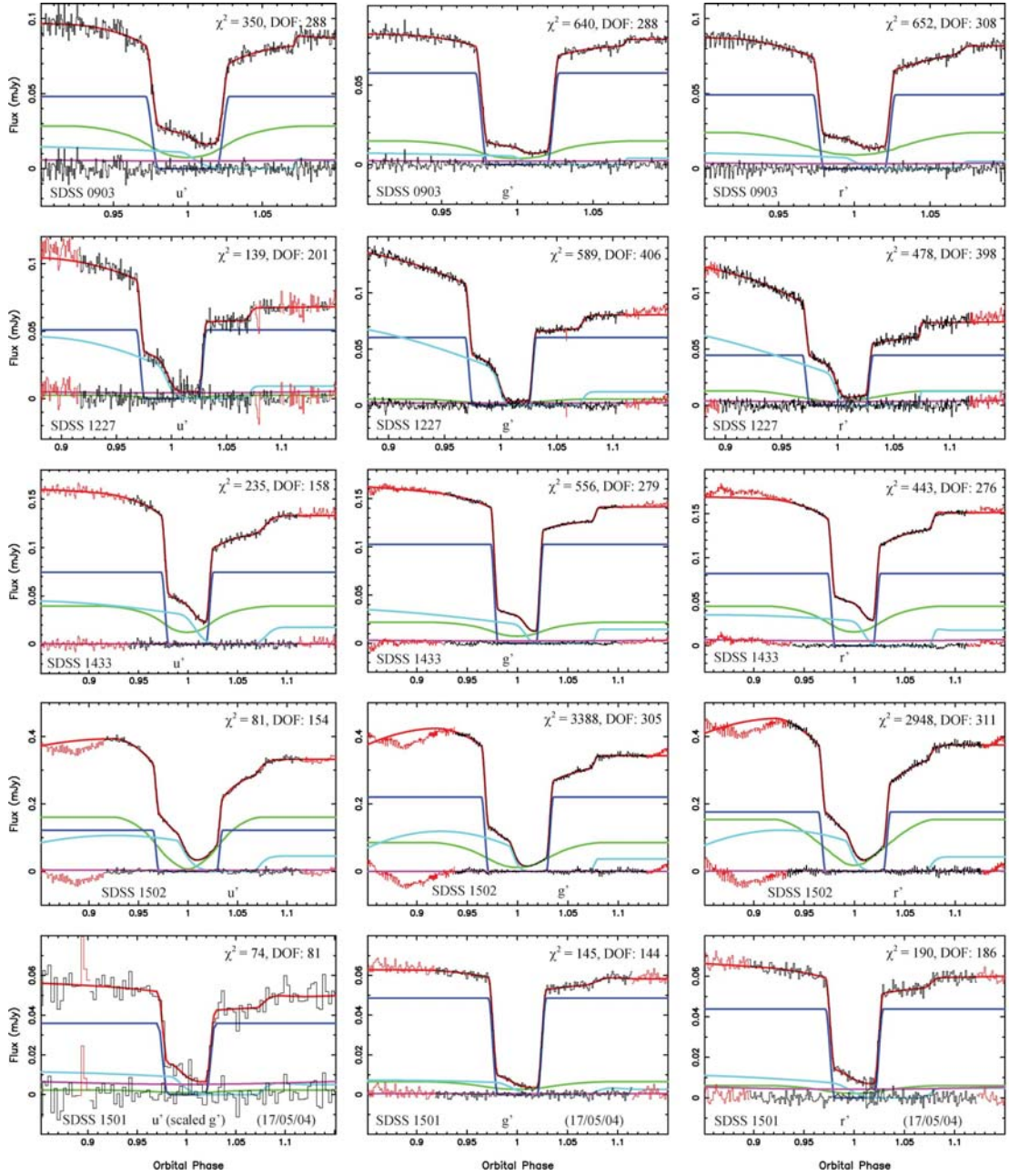


Figure 5.1a: The phased-folded $u'g'r'$ or $u'g'i'$ light curves of the CVs listed in Table 5.1a and 5.1b, fit using the model outlined in §3.2. The data (black) are shown with the fit (red) overlaid and the residuals plotted below (black). Below are the separate light curves of the white dwarf (dark blue), bright spot (light blue), accretion disc (green) and the secondary star (purple). Data points omitted from the fit are shown in red. χ^2 values for each fit, together with the number of degrees of freedom (DOF) are also shown.

Figure 5.1b: *continued*

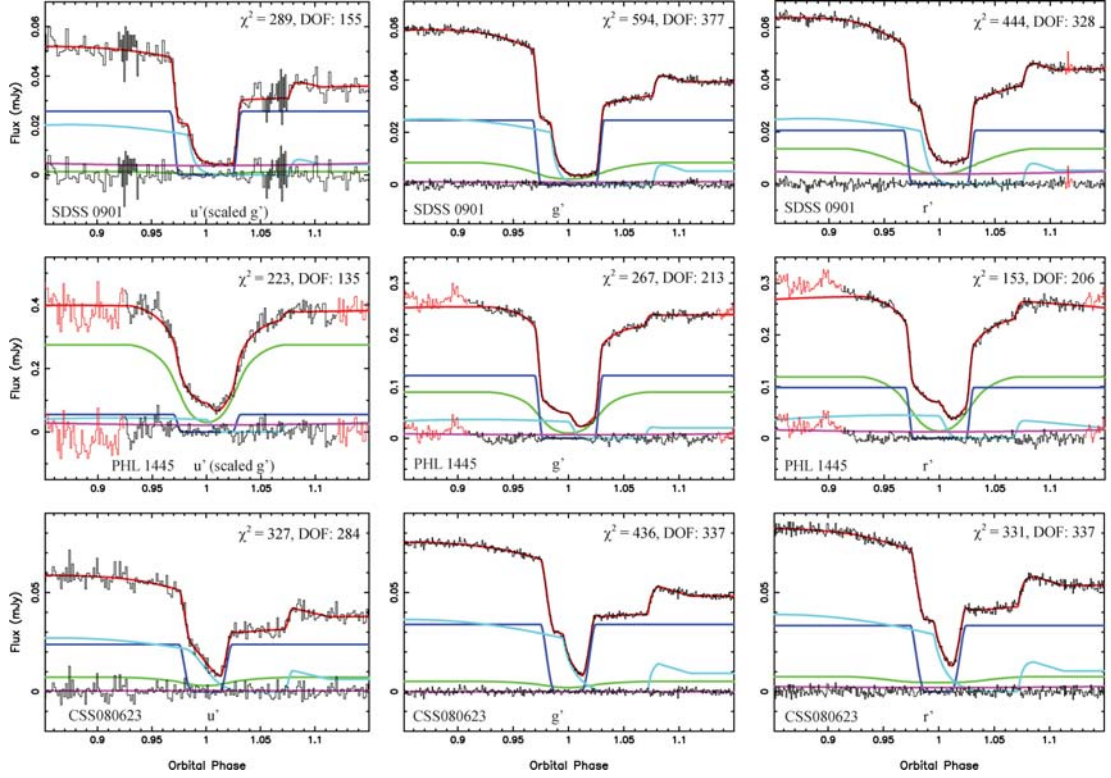
Figure 5.1c: *continued*

	CTCV J1300-3052	CTCV J2354-4700	SDSS J1152+4049	OU Vir	DV UMa
q	0.240 ± 0.021	0.1097 ± 0.0008	0.155 ± 0.006	0.1641 ± 0.0013	0.1778 ± 0.0022
M_w/M_\odot	0.736 ± 0.014	0.935 ± 0.031	0.560 ± 0.028	0.703 ± 0.012	1.098 ± 0.024
R_w/R_\odot	0.01111 ± 0.00018	0.0089 ± 0.0003	0.0135 ± 0.0004	0.01191 ± 0.00017	0.00703 ± 0.00028
$\log g$	8.21 ± 0.02	8.51 ± 0.04	7.93 ± 0.05	8.13 ± 0.02	8.78 ± 0.04
$T_w(K)$	11100 ± 800	14800 ± 700	12400 ± 1400	22300 ± 2100	15500 ± 2400
M_2/M_\odot	0.177 ± 0.021	0.101 ± 0.003	0.087 ± 0.006	0.1157 ± 0.0022	0.196 ± 0.005
R_2/R_\odot	0.215 ± 0.008	0.1463 ± 0.0016	0.142 ± 0.003	0.1634 ± 0.0010	0.2176 ± 0.0018
a/R_\odot	0.813 ± 0.011	0.692 ± 0.008	0.606 ± 0.010	0.686 ± 0.004	0.892 ± 0.006
K_w (kms $^{-1}$)	90 ± 8	51.9 ± 0.6	60 ± 3	66.4 ± 0.6	78.9 ± 1.0
K_2 (kms $^{-1}$)	372.2 ± 2.5	482 ± 6	387 ± 6	403.0 ± 2.3	443 ± 3
i°	86.3 ± 1.1	89.26 ± 0.28	82.38 ± 0.23	79.60 ± 0.04	82.93 ± 0.10
d (pc)	375 ± 13	674 ± 19	543 ± 21	570 ± 70	504 ± 30
P_{orb} (mins)	$128.0746325(14)^*$	$94.3923889(14)^*$	$97.518753(4)^*$	$104.696803(7)^1$	$123.6278190(20)^2$
	SDSS 1035	SDSS 1507	SDSS 0903	SDSS 1227	SDSS 1433
q	0.0571 ± 0.0010	0.0647 ± 0.0018	0.113 ± 0.004	0.1115 ± 0.0016	0.0661 ± 0.0007
M_w/M_\odot	0.835 ± 0.009	0.892 ± 0.008	0.872 ± 0.011	0.796 ± 0.018	0.865 ± 0.005
R_w/R_\odot	0.00991 ± 0.00010	0.00956 ± 0.00013	0.00947 ± 0.00019	0.01052 ± 0.00022	0.00962 ± 0.00006
$\log g$	8.37 ± 0.01	8.45 ± 0.01	8.42 ± 0.02	8.29 ± 0.02	8.41 ± 0.01
$T_w(K)$	10000 ± 1100	11300 ± 1000	13300 ± 1700	15900 ± 1400	12700 ± 1500
M_2/M_\odot	0.0475 ± 0.0012	0.0575 ± 0.0020	0.099 ± 0.004	0.0889 ± 0.0025	0.0571 ± 0.0007
R_2/R_\odot	0.1047 ± 0.0008	0.0969 ± 0.0011	0.1358 ± 0.0020	0.1365 ± 0.0013	0.1074 ± 0.0004
a/R_\odot	0.5977 ± 0.0022	0.5329 ± 0.0019	0.632 ± 0.003	0.640 ± 0.005	0.5869 ± 0.0012
K_w (kms $^{-1}$)	28.5 ± 0.6	35.1 ± 1.0	54.6 ± 2.0	51.3 ± 0.8	33.8 ± 0.3
K_2 (kms $^{-1}$)	499.3 ± 1.5	543.7 ± 1.2	481.7 ± 1.9	460 ± 3	511.1 ± 0.9
i°	83.98 ± 0.08	83.47 ± 0.12	82.09 ± 0.19	84.29 ± 0.10	84.36 ± 0.05
d (pc)	174 ± 12	168 ± 12	299 ± 14	400 ± 13	226 ± 12
P_{orb} (mins)	$82.08965(29)^{4,6}$	$66.61192(6)^{5,6}$	$85.065902(13)^6$	$90.661019(10)^6$	$78.106657(3)^6$

Table 5.1a: System parameters derived using the probability density functions shown in Figure 5.2a and 5.2b. R_r is the volume radius of the secondary's Roche lobe Eggleton (1983). The errors quoted are statistical errors of the fitting process and do not include systematic effects. The orbital periods are from the following works; *Chapter 4 of this thesis; ¹Feline et al. 2004a; ²Feline et al. 2004b; ³Littlefair et al. 2006a; ⁴Littlefair et al. 2006b; ⁵Littlefair et al. 2007; ⁶Littlefair et al. 2008.

	XZ Eri	SDSS 1702	CSS080623	SDSS 0901
q	0.118 ± 0.003	0.248 ± 0.005	0.140 ± 0.003	0.201 ± 0.005
M_w/M_\odot	0.769 ± 0.017	0.91 ± 0.03	0.699 ± 0.016	0.800 ± 0.025
R_w/R_\odot	0.01081 ± 0.00022	0.0092 ± 0.0004	0.01149 ± 0.00020	0.01055 ± 0.00031
$\log g$	8.26 ± 0.03	8.47 ± 0.05	8.16 ± 0.03	8.29 ± 0.04
$T_w(K)$	15300 ± 1900	15200 ± 1200	9400 ± 1100	18800 ± 2400
M_2/M_\odot	0.091 ± 0.004	0.223 ± 0.010	0.098 ± 0.003	0.161 ± 0.007
R_2/R_\odot	0.1350 ± 0.0018	0.252 ± 0.004	0.1357 ± 0.001	0.1911 ± 0.0028
a/R_\odot	0.621 ± 0.005	0.945 ± 0.012	0.595 ± 0.005	0.758 ± 0.008
K_w (kms $^{-1}$)	53.6 ± 1.5	94.0 ± 2.2	61.2 ± 1.3	81.4 ± 2.1
K_2 (kms $^{-1}$)	452 ± 3	380 ± 4	437 ± 3	404 ± 4
i°	80.02 ± 0.12	82.55 ± 0.17	79.82 ± 0.09	80.80 ± 0.15
d (pc)	371 ± 19	270 ± 16	309 ± 4	726 ± 23
P_{orb} (mins)	$88.069667(7)^2$	$144.11821(13)^3$	$85.793712(4)^*$	$112.147982(3)^*$
	SDSS 1502	SDSS 1501	PHL 1445	
q	0.1099 ± 0.0007	0.101 ± 0.010	0.086 ± 0.003	
M_w/M_\odot	0.709 ± 0.004	0.767 ± 0.027	0.81 ± 0.05	
R_w/R_\odot	0.01145 ± 0.00005	0.0107 ± 0.0003	0.0101 ± 0.0006	
$\log g$	8.17 ± 0.01	8.26 ± 0.04	8.34 ± 0.08	
$T_w(K)$	11800 ± 1200	10800 ± 1500	12600 ± 1900	
M_2/M_\odot	0.0781 ± 0.0008	0.077 ± 0.010	0.071 ± 0.005	
R_2/R_\odot	0.1241 ± 0.0003	0.122 ± 0.005	0.113 ± 0.003	
a/R_\odot	0.5844 ± 0.0013	0.588 ± 0.008	0.571 ± 0.012	
K_w (kms $^{-1}$)	50.4 ± 0.4	48 ± 5	42.9 ± 1.8	
K_2 (kms $^{-1}$)	456.5 ± 0.8	470.5 ± 3.2	500 ± 10	
i°	88.35 ± 0.17	82.8 ± 0.5	85.40 ± 0.26	
d (pc)	175 ± 11	306 ± 21		
P_{orb} (mins)	$84.82984(7)^6$	$81.85141771(28)^*$	$76.298219(4)^*$	

Table 5.1b: *continued*

Figure 5.1d: *continued*

With the exception of CTCV 2354, all of the systems analysed in this study lie near, or within, the range of white dwarf colours allowed by the atmosphere models of Bergeron et al. (1995), as shown in Figure 5.3. However, the systems do not always lie near the track for the appropriate mass and radius of the white dwarf. Littlefair et al. (2008) compare the temperatures derived using light curve fits to those found using SDSS spectra and GALEX (Galaxy Evolution Explorer) fluxes for a small number of systems and conclude their white dwarf temperatures are accurate to $\sim 1000\text{K}$. The systems examined by Littlefair et al. (2008) are all found to lie close to the Bergeron tracks; it is likely that systems that lie far from the tracks are less accurate. The white dwarf temperatures in this thesis have larger uncertainties than those of Littlefair et al. (2008). This is because the temperatures in Table 5.1a and 5.1b take into account the uncertainty in white dwarf mass when comparing the white dwarf fluxes to the models of Bergeron et al. (1995).

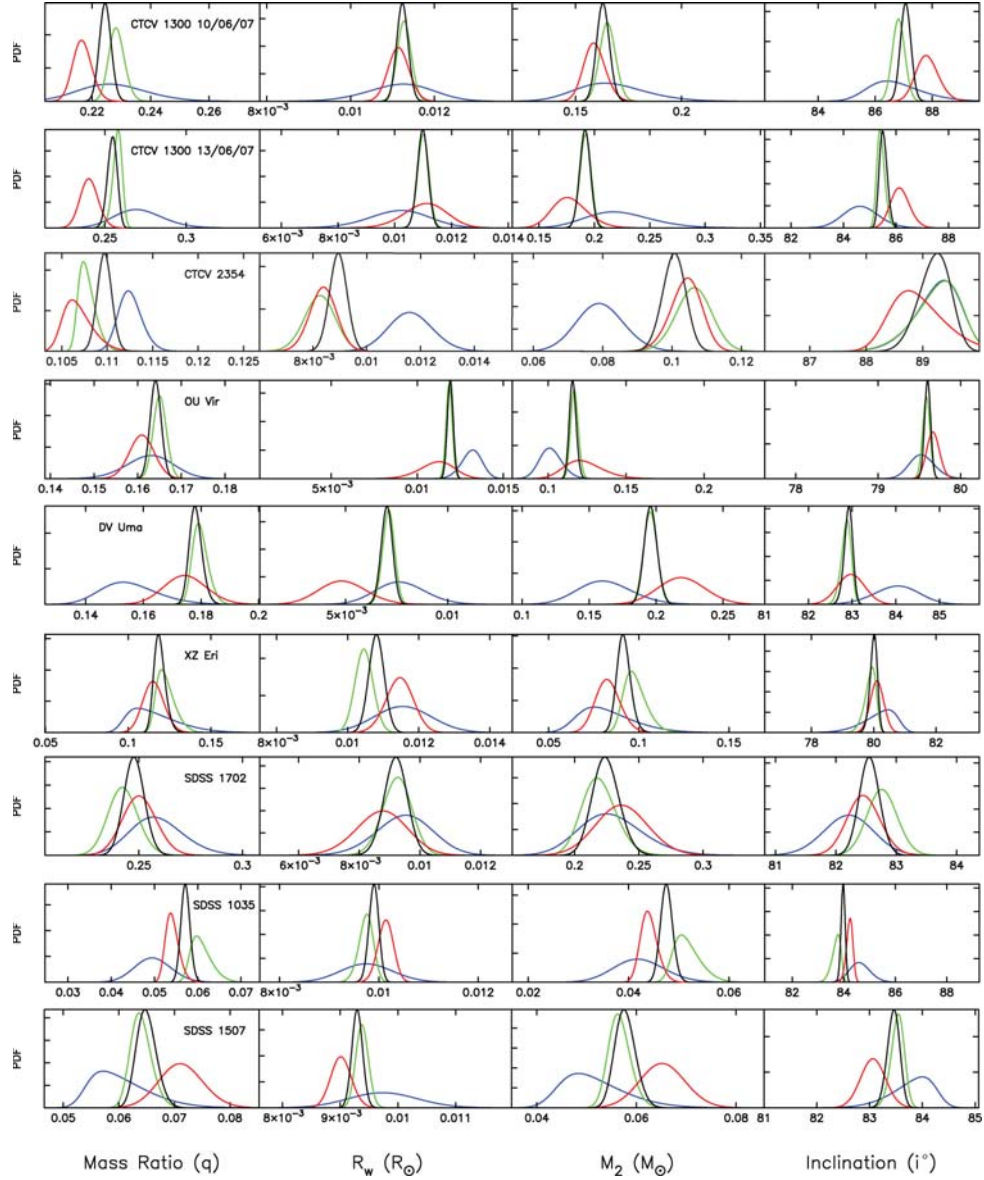
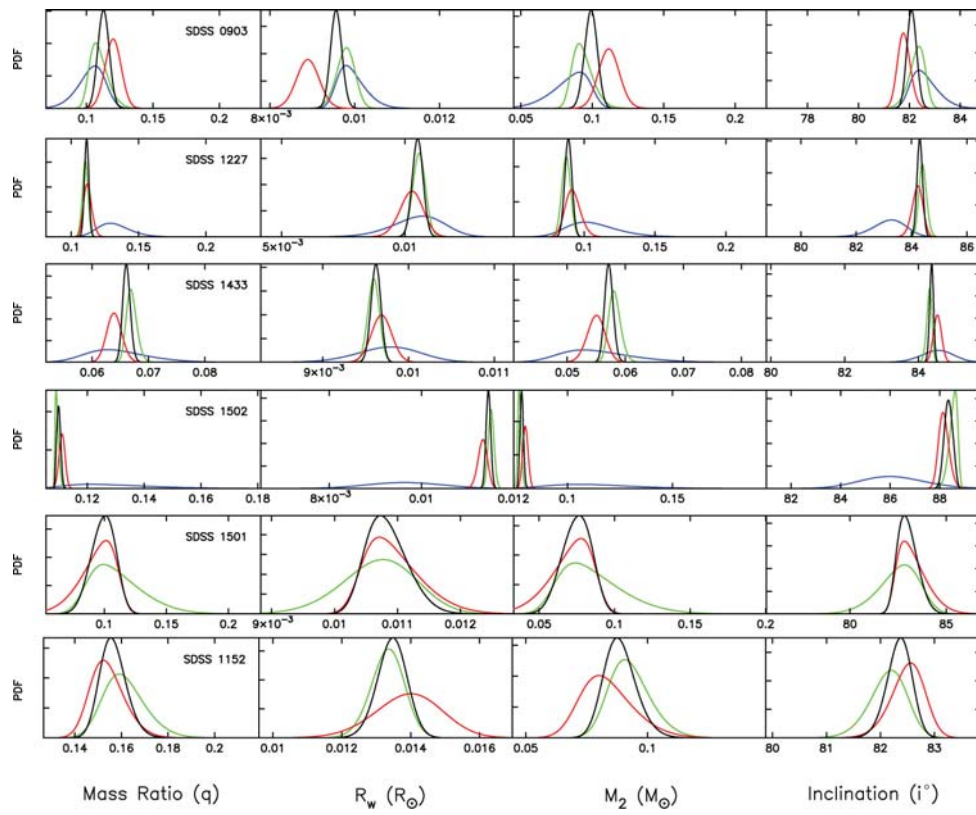


Figure 5.2a: The normalised probability density functions for each system, derived using the MCMC chains, orbital period and the mass–radius relationships of Wood (1995), Panei et al. (2000) and Hamada & Salpeter (1961), at the appropriate white dwarf temperature. The red curve represents the r' or i' band fit, the green represents the g' band, and blue curve (where present) represents the u' band. The black represents the total, combined PDF. Shown are the PDFs for mass ratio q , white dwarf radius R_w/R_\odot , secondary star mass M_2/M_\odot , and inclination i° .

Figure 5.2b: *continued*

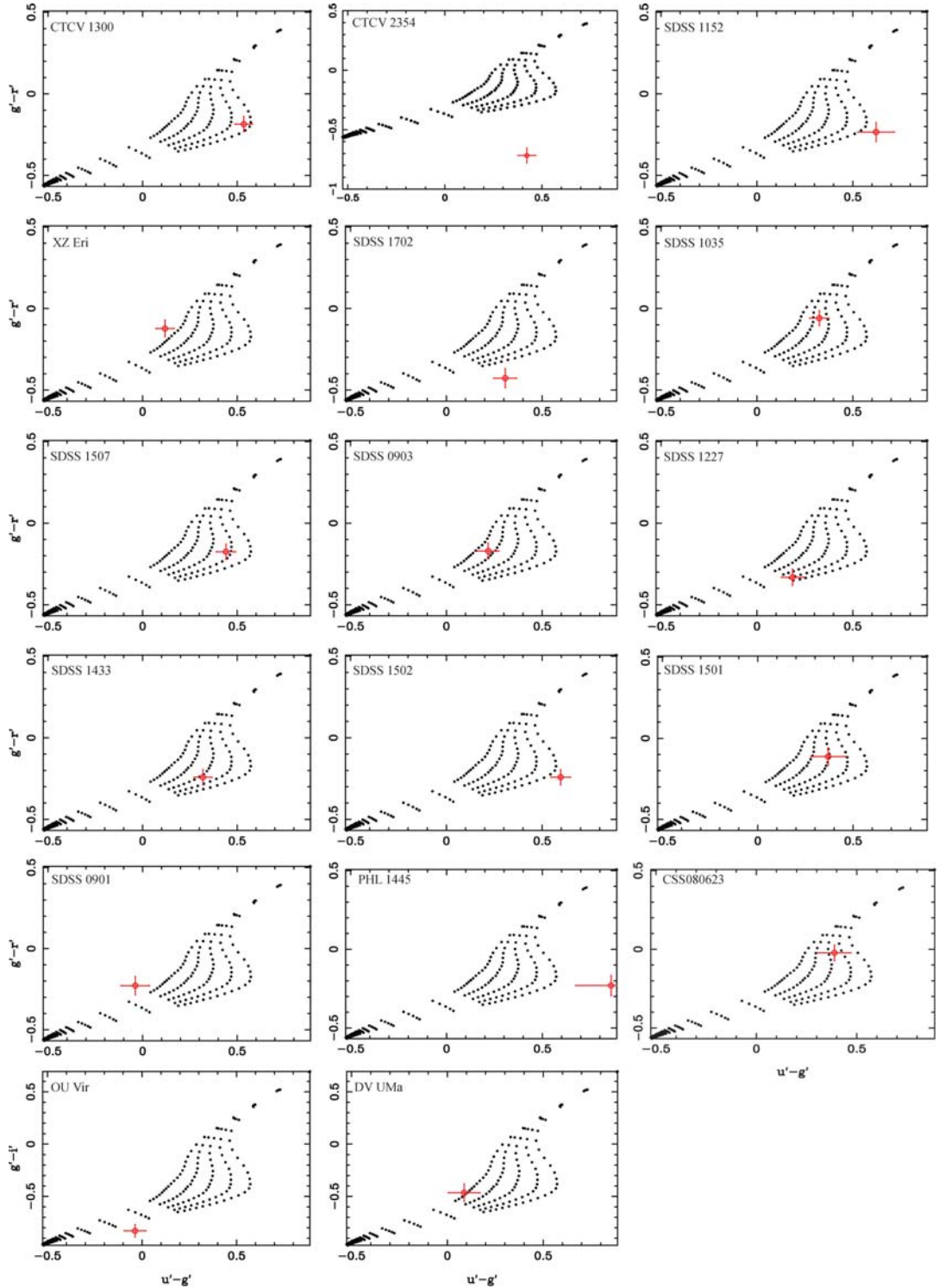


Figure 5.3: The white dwarf colours derived from the model fitting, together with the white dwarf models of Bergeron et al. (1995). From top to bottom, each curve represents $\log g = 9.0, 8.5, 8.0, 7.5$ and 7.0 respectively. The measured white dwarf colours are shown here in red, and are used to derive the white dwarf temperature, which in turn is used to correct the white dwarf mass-radius relationships used later to obtain the final system parameters.

It is possible that the white dwarf colours obtained from the modelling process are affected by contamination from the accretion disc, bright spot, or an unmodelled light source such as a boundary layer. If the white dwarf colours are incorrect, then the derived white dwarf temperatures will be affected. The affect on the final system parameters can be understood by considering the following.

1. Changing the white dwarf temperature will alter U_w .
2. The model fitting measures R_w/a and uses a mass-radius relationship to infer M_w , which is then used to find the mass of the secondary star. However, U_w and R_w are partially degenerate, so U_w therefore affects R_w and M_w .
3. M_w is affected by temperature changes because the white dwarf mass-radius relationship is temperature dependent.
4. The white dwarf temperature also affects the luminosity of the system, and hence distance estimate.

It is therefore important to quantify the effect that incorrect white dwarf temperatures may have on distance estimates and the final derived system parameters. To do this, the white dwarf temperature of the best quality, white-dwarf dominated systems were altered and by 2000K and the fitting procedure repeated. For lower quality data, the random errors dominate over any systematic errors, and thus changes to the best quality data represent a worst case scenario. It was found that changing the white dwarf temperature by 2000K changed R_w/a by less than 1σ . The white dwarf distance estimates changed by 10-20pc. Therefore, any error in white dwarf temperature that may occur does not affect the final system parameters by a significant amount. However, a caveat to this is that the modelling procedure does not include treatment of any boundary layer around the white dwarf, and assumes all of

the white dwarf's surface is visible. Either effect could lead to systematic uncertainty in the white dwarf radii (Wood et al., 1986).

5.2.2 Notes on Individual Systems

CTCV 1300

As noted in Chapter 4, the two eclipses of CTCV 1300 were modelled individually due to the heavy pre-eclipse flickering present in each light curve. The $u'g'r'$ eclipses from the night of 2007 June 10 gave consistent results, as did the $u'g'i'$ eclipses from the night of 2007 June 13. However, results from the individual nights were not consistent with each other and thus there exists two distinct solutions that are the result of heavy pre-eclipse flickering altering the shape of the bright spot ingress feature. This in turn gives two very different values for the mass ratio, q . Encouragingly, the white dwarf mass and radii are consistent between nights. To derive the final system parameters, the PDFs were combined as outlined in §5.2.1, and then an average was taken of the two solutions. The error is taken as the standard deviation between the two solutions. Both solutions are shown in Appendix B.

Figure 5.4 shows the g' -band eclipse from June 2010 together with a modified version of the model obtained from the 2007 dataset. This new model was found by starting from an average of the two 2007 fits and using a downhill simplex algorithm to vary all parameters bar q , $\Delta\phi$, R_w/a and U_w . These parameters should not change with time, and so the simplex fit will confirm if the bright spot positions and white dwarf radius are correct, and thus if the system parameters are reliable. A simplex algorithm was used for two reasons; firstly, because only a consistency check was required, and no system parameters were extracted from the fitting process, a full MCMC analysis was not required; secondly, the bright spot flux appears to have reduced significantly between data sets, and the strength of the bright spot ingress

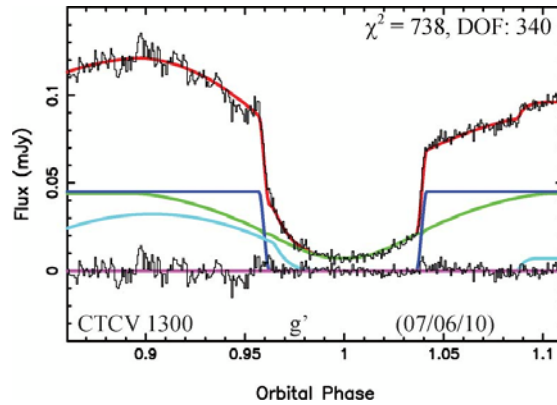


Figure 5.4: The June 2010 g' band eclipse of CTCV 1300, together with a modified model found using the 2007 data. Starting from an average of the two 2007 models, a downhill simplex fit was performed varying all parameters bar q , $\Delta\phi$, R_w/a and U_w .

feature means that a full fit could not be constrained using MCMC. The model confirms the bright spot flux has decreased considerably, although an orbital hump is still visible. The white dwarf flux remains almost unchanged, although the accretion disc appears brighter. The fit to the data is good, indicating that the models derived from the 2007 data (and used to derive the system parameters) are reliable.

CTCV 2354

In Chapter 4 it was noted that the shape of the light curve of CTCV 2354 indicated possible bright spot egress features around phases 1.060 and 1.080. Figure 5.1a shows that the model has fit the bright spot egress feature at phase 1.080. Given the strength and shape of the bright spot features and general scatter present in the light curve there is some uncertainty over whether the bright spot positions have been correctly identified by the model, and thus there is some element of doubt as to the value obtained for the mass ratio and thus the secondary star mass. It is at this point the readers is referred to the 2010 data, shown in Figure 5.5. The eclipse dated 2010 May 3 (centre panel) shows clear bright spot ingress and egress features, with a clear orbital hump visible from phases 0.70–0.95. The system is much brighter in

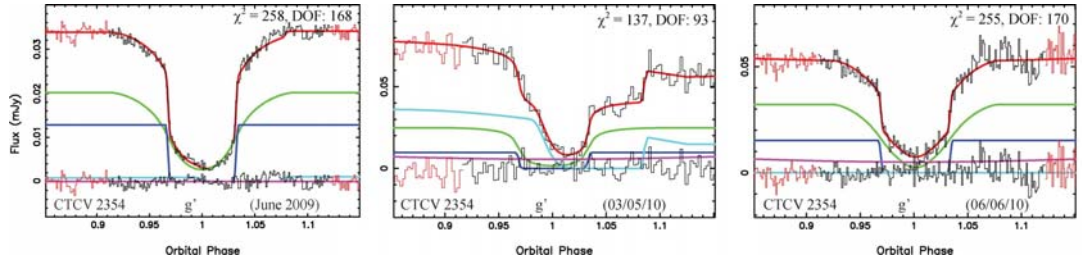


Figure 5.5: The g' band observations of CTCV 2354 from 2009 (left), 2010 May 3 (centre) and 2010 June 6 (right), fit with a modified version of the model obtained from the 2007 data as described in §5.2.2.

this state than the 2007 data previously modelled, in part due to a dramatic increase in bright spot flux. As with CTCV 1300 a downhill simplex method was used to vary all parameters bar q , $\Delta\phi$, R_w/a and U_w . The fit to the eclipse of May 3 is especially pleasing, as its excellent agreement with the light curve confirms that the 2007 model correctly identified the bright spot egress feature and thus the mass ratio obtained is reliable.

Figure 5.5 also shows a single eclipse observed just one month later (June 2010, right panel), and six eclipses averaged together from June 2009 (left panel). Both of these datasets are fit with a downhill simplex model as above. The June 2009 and June 2010 datasets are in stark contrast to the May 2010 data, with the bright spot features appearing extremely faint (2009), or seemingly non-existent (June 2010). The accretion disc flux in the June 2010 data appears to have increased significantly, giving rise to a distinct “u” shape. The rapid change in bright spot and accretion disc light curves over such short (1 month - 1 year) time scales suggests that the disc is highly unstable.

DV UMa

The secondary star mass derived for DV UMa has increased by 6.1σ ($\Delta M = 0.039 M_\odot$) from that published by Feline et al. (2004b). Close inspection of the original fit reveals that the bright spot features were fit poorly by the old bright spot model.

This arose because the old bright spot model could not describe the complex bright spot profile present and an inaccurate value of the mass ratio was found as a result. The new bright spot model is much better in this respect, and is able to take into account a wider variety of geometric effects and orientations. Given that the white dwarf radius is consistent with that of Feline et al. (2004b), this seems the most likely cause of such a large change. It is worth noting that the new secondary star masses for both DV UMa and XZ Eri, are both consistent with the masses obtained by Feline et al. (2004b) using the derivative method, which, unlike the parameterised model, does not make any attempt to recreate the bright spot eclipse profile (e.g. Wood et al. 1986; Horne et al. 1994; Feline et al. 2004a; Feline et al. 2004b).

SDSS 1502

The new fits to SDSS 1502 decrease the secondary star mass by 2.9σ ($\Delta M_2 = 0.012M_\odot$) from that of Littlefair et al. (2008). The mass ratio and inclination are consistent with those of Littlefair et al. (2008), however the white dwarf radius, R_w , has increased by 13 percent (3.4σ). It is thought that the primary reason for this change was that the original fit was heavily binned, and thus more susceptible to the bug outlined in §4.4.

SDSS 1501

The most important change of all of the re-modelled systems is for that of SDSS 1501. Whilst the secondary star mass has only increased by 1.9σ from that of Littlefair et al. (2008), it should be noted that the uncertainties are large ($\sigma M_2 = 0.010M_\odot$) and the mass difference is large enough to take this system from being a post-period-bounce system, to a pre-period-bounce system. Although the errors do not formally rule out the possibility of SDSS 1501 being post-period-bounce, the secondary star's position with respect to the evolutionary tracks shown in Figure 5.7 strongly favours

that of a pre-period-bounce system. Such a change arises from a difference in bright spot positions between the model presented in this thesis and that of Littlefair et al. (2008), which in turn affects the mass ratio obtained. The data used by Littlefair et al. (2008) shows a very weak bright spot ingress feature. With the improvements made to the modelling process resulting from the introduction of MCMC, it is clear that the 2006 data used by Littlefair et al. (2008) does not constrain the mass ratio, q , tightly enough. In contrast, the 2004 data shows much clearer bright spot features, and is therefore favoured over the 2006 data as discussed in §4.4.

5.3 Discussion

5.3.1 White Dwarf Masses

Population studies by Willems et al. (2005) predict that between 40 and 80 percent of CVs are born with He-core white dwarfs ($M_w \lesssim 0.50M_\odot$) and therefore He-core white dwarfs (He-WDs) are expected to be common amongst CV primaries. It is surprising then that out of the sample of 17 systems presented in §5.2.1, there no He-WDs. Of all of the systems, SDSS 1152 is found to have to the lowest white dwarf mass with $M_w = 0.560 \pm 0.028$. The mass distribution of Kepler et al. (2007) for SDSS white dwarfs suggests He-WDs have a typical mass of $\sim 0.38M_\odot$. The most massive He-WDs may form from single RGB stars, which due to extreme mass loss are able to avoid the Helium flash; D’Cruz et al. (1996) consider models with a range of mass loss rates on the RGB and manage to produce He-WDs with masses up to $\sim 0.48M_\odot$. It is likely that this represents an upper limit to the mass of He-WDs and hence SDSS 1152 is still too massive to be a viable candidate for a He-core white dwarf.

The white dwarf masses presented in thesis are found to not only be massive

to be He-WDs, but are also well in excess of the average mass for single DA white dwarfs. Using the same method as Knigge (2006), the average white dwarf mass of the entire sample of systems in §5.2.1 is found to be $M_w = 0.81 \pm 0.03M_\odot$, with an intrinsic scatter of $0.12M_\odot$. In comparison, Liebert et al. (2005) find the mean mass of DA white dwarfs to be $M_w \sim 0.603 M_\odot$, while Kepler et al. (2007) find a mean mass of $M_w = 0.593 \pm 0.016M_\odot$. This study thus supports previous findings (e.g. Warner, 1973, 1976; Ritter, 1976, 1985; Robinson, 1976; Smith & Dhillon, 1998; Knigge, 2006) that white dwarfs in CVs are on average higher in mass than single field stars. Like Littlefair et al. (2008), the white dwarf masses derived here are compared to the average mass of $M_w = 0.73 \pm 0.05M_\odot$ for white dwarfs in CVs below the period gap (Knigge, 2006). It was found the white dwarf masses in this study are generally higher. This is especially so for systems $P_{orb} \leq 95$ mins, where a mean white dwarf mass of $M_w = 0.82 \pm 0.02M_\odot$ was found, with an intrinsic scatter of $0.07M_\odot$. Some of the white dwarf masses are revised, and have accordingly moved downwards in mass compared to Littlefair et al. (2008), but as Figure 5.6 shows, for $P_{orb} \leq 95$ mins, 9 out of 11 systems are more massive than the average found by Knigge (2006), with SDSS 1502 and CSS080623 the only exceptions. On the same plot, the dispersion of masses as found by Knigge (2006) and the mean mass of single SDSS white dwarfs found by Kepler et al. (2007) are shown. It should be noted that the Knigge (2006) sample contains three systems also included in this study: OU Vir, DV UMa and XZ Eri, using the old mass determinations of Feline et al. (2004a, 2004b). Most of the new white dwarf masses are within the dispersion found, indicating that no individual white dwarf mass is unusual. However 9 out of 11 systems above average does seem anomalously high, considering that if the white dwarf masses are modelled as a binomial distribution, the probability of such an occurrence is less than 3.5 percent (independent of the actual mean or variance). Such difference between this sample and that of Knigge (2006) is concerning, and it

is therefore desirable to consider the selection effects, considering the majority of the short period systems are SDSS objects (Szkody et al., 2004, 2005, 2006, 2007).

The majority of SDSS CVs found are generally rejected quasar candidates with a limiting magnitude of $g' = 19 - 20$, and are initially selected for follow up on the basis of $u'-g'$ colour cuts (see Gänsicke et al. (2009) for a more in depth description). Littlefair et al. (2008) show that systems with $M_w \geq 0.50M_\odot$ are blue enough to pass the SDSS colour cuts and conclude that selection effects such as these are unlikely to explain the high mass bias of our white dwarf sample. However, the majority of the systems studied in this thesis are close ($g' \sim 17.5 - 19.5$) to the $g' = 19$ limit of the SDSS survey. This raises the possibility that the SDSS sample only finds the brightest of the short period CVs. Ritter & Burkert (1986) have shown that CVs with high mass white dwarfs are brighter than their low mass counterparts. This suggests there maybe some bias towards high mass dwarfs. However, this conclusion is not appropriate to the systems studied here: Ritter & Burkert (1986) only consider the effects of accretion luminosity whereas in most of our systems the white dwarf considerably outshines the accretion disc.

Zorotovic et al. (2011) consider selection effects in white dwarf dominated SDSS systems with a variety of different mass transfer rates and conclude there is actually bias *against* high mass white dwarfs. They find a $0.90M_\odot$ white dwarf is approximately 0.15 magnitudes fainter than a $0.75M_\odot$ white dwarf, which corresponds to a decreased detection efficiency of $\sim 20\%$. This suggests that the finding of high mass white dwarfs at short orbital periods within the sample of objects studied here may not be due to selection effects, and could in fact be a true representation of the intrinsic mass distribution of CVs. However, this analysis only considers white dwarf luminosity; in some of the systems studied here the bright spot features are prominent, and contribute significantly to the overall flux of the system. It remains possible that the finding of very high white dwarf masses for short period CVs is due

to selection effects. However, a full and thorough quantification of any bias would require detailed calculations of the luminosity of white-dwarf dominated systems (including bright spot emission), plus an investigation of the selection effects in the SDSS sample. Such an analysis is beyond the scope of this study.

The results presented in this thesis have important consequences for the modelling of nova outbursts and their impact on the long-term evolution on CVs. Typical calculations show that the mass of the white dwarf decreases by between 1 and 5 percent per 1000 nova cycles (e.g. Yaron et al., 2005; Epelstain et al., 2007). The dominance of high-mass white dwarfs in the sample of short period systems presented in this Chapter suggests that any white dwarf erosion due to nova explosions must be minimal, or that not all of the accreted matter is ejected during nova ignition, resulting in the white dwarf mass *increasing* over time. This could, in principle enable the white dwarfs in cataclysmic variables to grow in mass until they reach the Chandrasekhar limit.

5.3.2 Period Bounce

Population synthesis models for cataclysmic variables (e.g. Kolb, 1993; Willems et al., 2005) all predict that large numbers of the CV population ($\sim 15 - 70$ percent) have evolved past the period minimum. This has always been in stark contrast to observations, possibly in part due to selection effects (e.g. Littlefair et al., 2003).

Littlefair et al. (2006b, 2007, 2008) identified four systems (SDSS 1035, SDSS 1507, SDSS 1433, SDSS 1501) with secondary stars below the sub-stellar limit, three of which are likely to be post-period-bounce CVs (SDSS 1035, SDSS 1501 and SDSS 1433). The subsequent re-analysis gives three systems (SDSS 1035, SDSS 1507, SDSS 1433) with secondaries below the sub-stellar limit, two of which (for reasons outlined below) are thought to be post-period-bounce CVs (SDSS 1035 and SDSS 1433). SDSS 1501, which no longer features as a post-period-bounce system, is discussed in

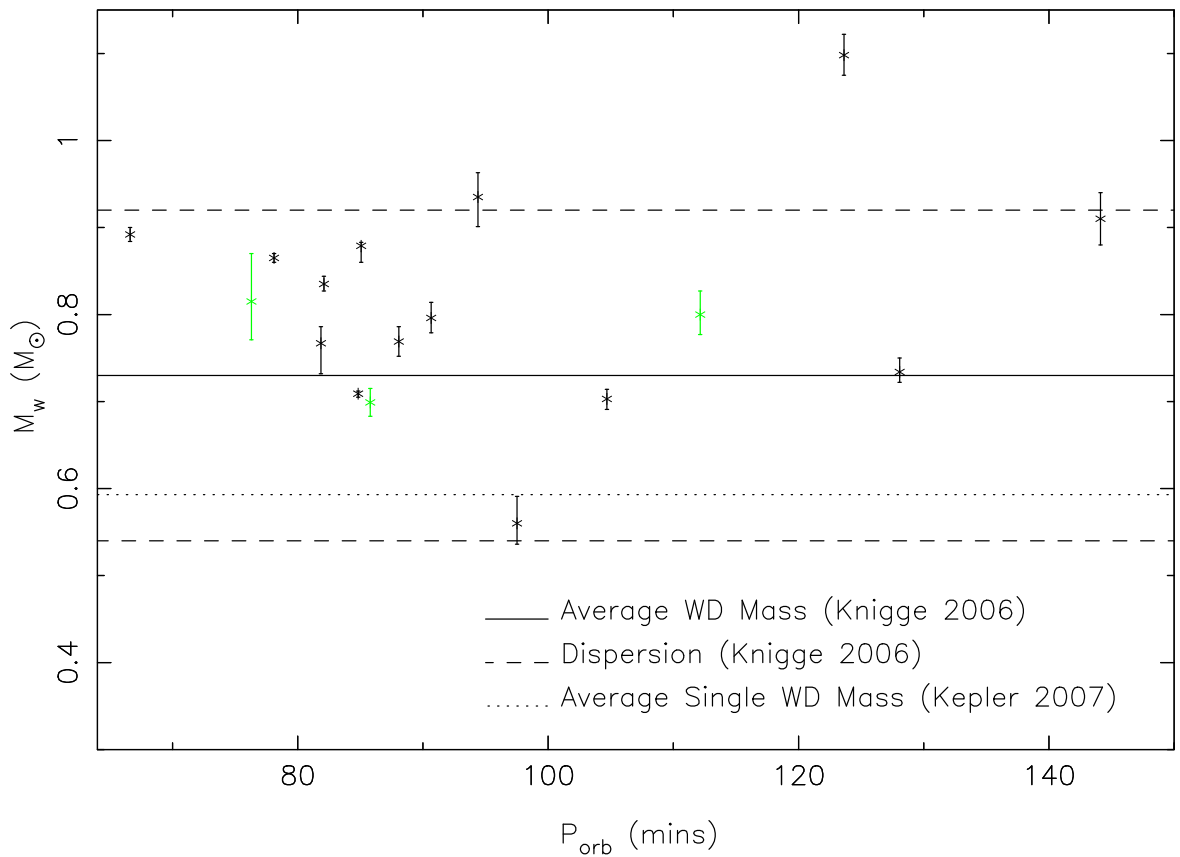


Figure 5.6: The white dwarf mass as a function of orbital period. The mean white dwarf mass for systems below the period gap, as found by Knigge (2006) is shown with a solid line, along with the associated intrinsic scatter (dashed line). The mean white dwarf mass in single stars as found by Kepler et al. (2007) is shown by a dotted line. The objects marked with green are systems not included in Savoury et al. (2011).

greater detail in §5.2.2.

Sirotkin & Kim (2010) claim that SDSS 1433 cannot be considered a post-period-bounce object because the mass transfer rates and secondary star temperatures implied are too high. The mass transfer rate was found using an estimate of the white dwarf temperature (Townesley & Gänsicke, 2009), while the secondary star temperature was inferred using a semi-empirical relationship that is also dependent on the white dwarf temperature. The white dwarf temperature used by Sirotkin & Kim (2010) was that derived by Littlefair et al. (2008) from model fitting. In this case, using \dot{M} and T_2 is an unreliable test of the evolutionary status of CVs secondary stars, because accurate determinations of the white dwarf temperature are difficult to obtain. Of all the system parameters derived through model fitting, the white dwarf temperatures are the least well constrained, and do not take into account systematic errors. Because the white dwarf temperature is found using the flux from just three colours, and the model does not include all possible sources of luminosity (e.g. a boundary layer), there is a good chance that the white dwarf temperatures are affected by systematic errors at some level, as discussed in §5.2.1. Instead, the secondary stars are favoured as indicators of evolutionary status (see Chapter 1).

If the angular momentum loss rate is similar for systems with identical system parameters, then all CVs are expected to follow very similar evolutionary tracks with a single locus in the mass-period relationship (and by analogy, mass-radius relationship) for CV secondary stars, as shown in Figure 5.7. The empirical donor star mass-radius relationship derived by Knigge (2006) shows that a single evolutionary track does very well at describing the observed $M_2 - P_{orb}$ relationship, although the shape of that relationship is loosely constrained at low masses. A single evolutionary path also explains the presence of the “period spike”, a long sought after feature in the orbital period distribution recently identified by Gänsicke et al. (2009). It is therefore expected that there exists a unique secondary star mass corresponding

to the minimum orbital period, below which an object becomes a period-bouncer. The exact mass at which this occurs is very uncertain, and does not necessarily correspond to the sub-stellar limit (e.g. Patterson, 2011). From the empirical work of Knigge (2006), the best estimate for M_{bounce} is $M_2 = 0.063 \pm 0.009 M_{\odot}$. Three of the systems studied here (SDSS 1035, SDSS 1433 and SDSS 1507) fall well below this value and PHL 1445 is found to be consistent with this mass. PHL 1445 and SDSS 1507 are unusual systems and are discussed in the following sections. They are not included in the sample of post-period minimum CVs. Therefore, there are two strong candidates for post-period minimum CVs (SDSS 1035 and SDSS 1433) from the total sample of 17 CVs (nine of which are SDSS systems). From this, it is estimated that ~ 12 per cent of all CVs below the period gap and ~ 18 per cent of all short period CVs ($P_{orb} \leq 95$ mins) have evolved past the period minimum. This crude estimate neglects selection effects; there is of course some natural bias against period bouncers, as they tend to be extremely faint objects and thus more difficult to observe (Littlefair et al., 2003; Pretorius et al., 2007). Because the majority of the short period systems studied are SDSS CVs, other selection effects cannot be ruled out. However, Gänsicke et al. (2009) have shown that the number of period minimum CVs found within the SDSS is broadly consistent with other surveys, allowing for normalisation of survey volumes. The target selection for the objects presented in this thesis (see §2.1.1) is not thought to contribute any additional bias towards or against period bouncers as all objects with orbital periods below the gap were targeted equally; the limiting factor was object visibility at the time of observation. Selection effects aside, these findings are consistent with current population synthesis models, albeit to a very crude approximation given the small sample of objects.

5.3.3 SDSS J1507+5230

The orbital period of SDSS 1507 is far below the well-defined period minimum and thus the nature of this system is of great interest to theorists and observers. It is possible that this system represents the true orbital period minimum as predicted by Kolb & Baraffe (1999). However, if this is indeed the case, a large number of systems would be expected between orbital periods of 67 minutes and 83 minutes, where the period spike is observed (Gänsicke et al., 2009). These systems are not observed, and hence it is likely that some other mechanism is responsible. Littlefair et al. (2007) speculate that this system was either formed directly from a white dwarf/brown dwarf binary, while Patterson et al. (2008) argue that the system could be a member of the halo. Both derive system parameters, and both obtain distance estimates to the system.

The system parameters derived in this study are consistent with those of Littlefair et al. (2007) and Patterson et al. (2008), within uncertainties. The new distance estimate is in excellent agreement with Littlefair et al. (2007), which is not surprising because both distances are calculated using the same methods and dataset. However, the new distance estimate still places the system nearer than that of Patterson et al. (2008). Patterson et al. (2008) obtain a lower limit to the distance using parallax. The parallax value implies a distance $d > 175$ pc, which taken alone, is consistent with that found in this study of $d = 168 \pm 12$ pc. Patterson combines his parallax with a range of other observational constraints using Bayesian methods to yield a final distance estimate of $d = 230 \pm 40$ pc. If the distance of $d = 168 \pm 12$ pc is nearer the true distance, then combining with Patterson's proper motion measurement of $0.16''/yr$ yields a transverse velocity of $d = 128 \pm 9$ kms⁻¹. This lower transverse velocity is still very much an outlier in the distribution of 354 CVs shown in Fig. 1 of Patterson et al. (2008). Therefore, regardless of which distance is correct, the proper

motion of SDSS 1507 still supports halo membership. Halo membership is further supported by Uthas et al. (2011), who use UV spectroscopy to obtain an estimate of the metallicity. Their value is found to be significantly sub-solar, and comparable to halo stars of a similar space velocity.

5.3.4 PHL 1445

PHL 1445 is an unusually active system given that its orbital period is close to the period minimum. The white dwarf mass is comparable to other systems at similar orbital periods, although the mass of the secondary star is slightly higher than expected. This could be because the system formed from an evolved donor, or because the bright spot egress has been incorrectly identified as a result of the heavy flickering, giving an incorrect mass ratio. Given the scatter present in the data, the latter cannot be ruled out. This system remains of high interest and follow up photometry and spectroscopy is desired.

5.3.5 Exploring the Standard Model of CV Evolution

Figure 5.7 shows the evolutionary models of Kolb & Baraffe (1999) calculated with enhanced mass-transfer rates. Also shown is a model with 50 percent star spot coverage on the surface of the secondary star. In both cases, the effects of distortion of the secondary star due to tidal and rotational forces (Renoizé et al., 2002) are included. The positions of the period minimum, and period gap, as found by Knigge (2006) are also shown. Mass determinations for all systems presented in this study are included. From Figure 5.7, it is clear that the standard theoretical models are a poor fit to the data. For a given mass, the models of Kolb & Baraffe (1999) significantly underestimate the orbital period, and thus the secondary star radii.

Models with enhanced mass transfer rates and star spot coverage do rather better

at reproducing the observed secondary star masses, although the general scatter of short period systems makes choosing between these difficult. This is in line with the conclusions of Littlefair et al. (2008). The models begin to diverge significantly at orbital periods greater than 100 minutes; unfortunately, in this regime there are few systems with precisely known secondary masses. Clearly, more mass determinations for systems with orbital periods between 100 and 130 minutes are required.

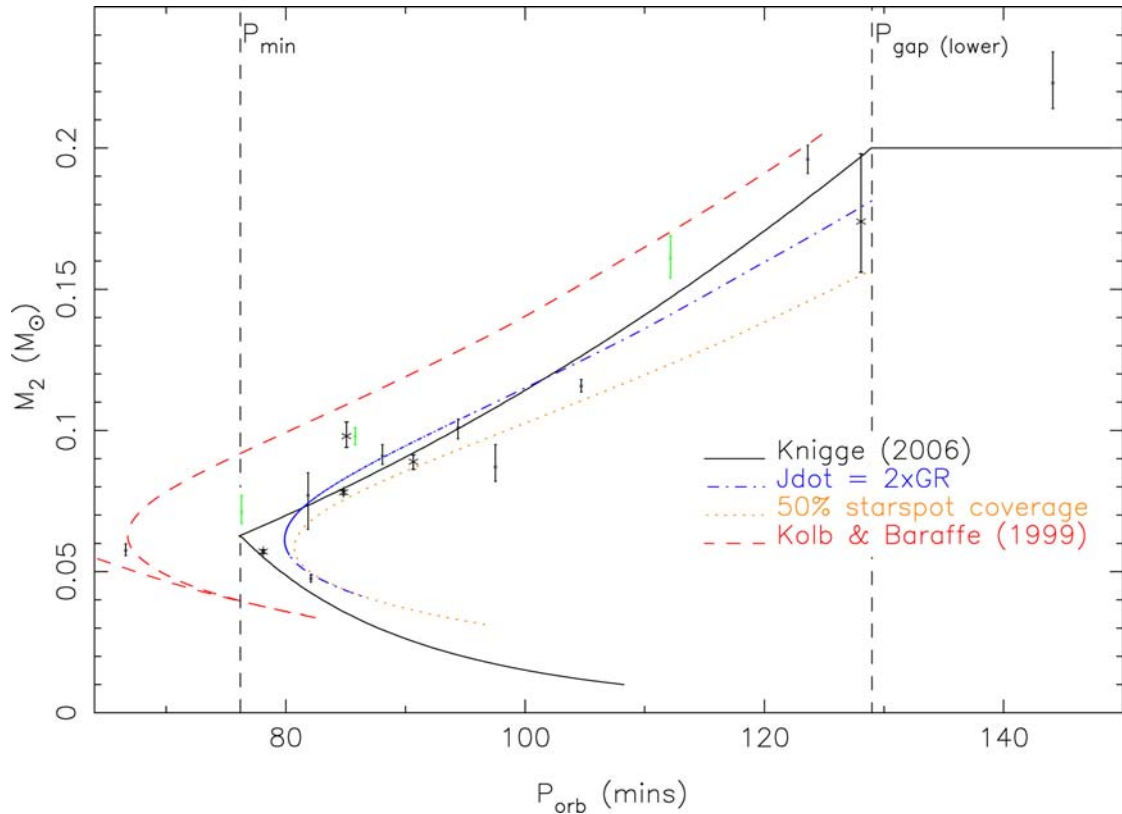


Figure 5.7: The $M_2 - P_{orb}$ relationship. Mass determinations for all systems using ULTRACAM data are included. The objects marked with in green are the systems not included in Savoury et al. (2011). The evolutionary models of Kolb & Baraffe (1999) calculated with different mass-transfer rates are shown with red (dashed) and blue (dot-dashed) lines. A model with 50 percent star spot coverage on the surface of the secondary star is shown with an orange (dotted) line. In the modified models, the effects of distortion of the secondary star due to tidal and rotational forces (Renvoizé et al., 2002) are taken into account. The solid (black) line shows the empirical mass-radius relationship as found by Knigge (2006). The position of the period minimum and period gap, as found by Knigge (2006), are also shown.

Chapter 6

A Radial Velocity Study of CTCV J1300-3052

The contents of this Chapter have been published by Savoury, Littlefair, Marsh, Dhillon, Parsons, Copperwheat and Steeghs in the Monthly Notices of the Royal Astronomical Society, 2012, **422**, 469-477, in a manuscript entitled ‘*A radial velocity study of CTCV J1300-3052*’. The work was carried out in collaboration with Stuart Littlefair, Tom Marsh, Vik Dhillon, Steven Parsons, Chris Copperwheat and Danny Steeghs (Savoury et al., 2012). The reduction and analysis of the data and the following text are my own work unless stated otherwise.

6.1 Introduction

In Chapter 5 I carried out a photometric study of eclipsing CVs and found the masses and radii for both the white dwarf and secondary star in 17 systems. These masses were found by fitting a parameterised model to the eclipse light curves. Photometric mass determinations such as these are based on a number of assumptions which,

whilst reasonable, remain untested across a wide range of orbital periods. It is photometric mass and radii determinations such as these that are used to calibrate the ϵ - q (superhump excess-mass ratio) relations of Patterson et al. (2005), Knigge (2006) and Pearson (2006), which can then be used to derive secondary star mass estimates for large samples of CVs. It is therefore important to check the validity of photometric mass determinations.

For objects with orbital periods above the period gap, the photometric fitting technique appears robust, with the secondary star radial velocities predicted by photometry in agreement with those found by other techniques (Watson et al., 2003; Feline, 2005; Copperwheat et al., 2010). However, for objects below the period gap, independent tests of the photometric technique are rare. Tulloch et al. (2009) found the radial velocity of the white dwarf (K_w) in SDSS J143317.78+101123.3 ($P_{orb} = 78.1$ mins), as measured from disc emission lines, to be in excellent agreement with the photometric value predicted by Littlefair et al. (2008). The agreement is encouraging, but the motion of the inner disc does not necessarily follow the motion of the white dwarf, and so K_w estimates from disc emission should be treated with caution (e.g. Marsh, 1988). More recently, Copperwheat et al. (2012) found the radial velocity and rotational broadening of the secondary star in OY Car ($P_{orb} = 90.9$ mins) to be in good agreement with those predicted by photometric methods (Wood & Horne, 1990; Littlefair et al., 2008). However, it is possible that the assumptions made in the modelling process may break down at certain orbital periods; for example, the assumption of a ballistic trajectory for the gas stream may not be valid in instances where the accretion flow is very low (e.g. short period); the surface of the white dwarf may be partially covered when the accretion flow is high (e.g. long period); or the white dwarf mass-radius relationship used may not be appropriate for the given mass and temperature of the white dwarf. Such is the importance of mass determinations in CVs, additional verification across a range of orbital periods is highly desirable.

One of the systems analysed in Chapter 5 was CTCV J1300-3052 (hereafter CTCV 1300). Its orbital period is 128.1 minutes, placing it immediately below the period gap. The average spectrum obtained by Tappert et al. (2004) showed clear emission lines from the accretion disc and absorption lines from the secondary star. It is through absorption lines such as these that the radial velocity and rotational broadening of the secondary star can be found, which can in turn be used to derive an independent measure of the masses and radii of the component stars (e.g. Horne et al., 1993; Smith et al., 1998; Thoroughgood et al., 2001, 2004).

In this Chapter I present time resolved-spectroscopy of CTCV 1300 and determine the system parameters. The parameters derived using spectroscopy will provide an independent test of the photometric methods used in Chapter 5.

6.2 Results

6.2.1 Average Spectrum

The average spectrum of CTCV 1300 is shown in Figure 6.1. The upper panel shows the wavelength range 3200-5500 Å (from the UVB-arm), the centre panel shows 5750-10000 Å (from the VIS-arm), and the lower panel 10000-13500 Å (from the NIR-arm). Note that the scales differ between panels. Each spectrum is flux calibrated, and correction for telluric absorption has been attempted. The redder bands from the NIR-arm (H and K) are not shown; this is because the only features visible are telluric or sky lines that have not been completely removed.

Throughout the spectrum, strong, broad, double-peaked Balmer lines and several double-peaked He I lines (4471, 4922, 5015, 5875, 6678, 7065 and 10830 Å) are visible. Broad double-peaked lines such as these are typical of a high-inclination accreting binary (e.g. Horne & Marsh, 1986).

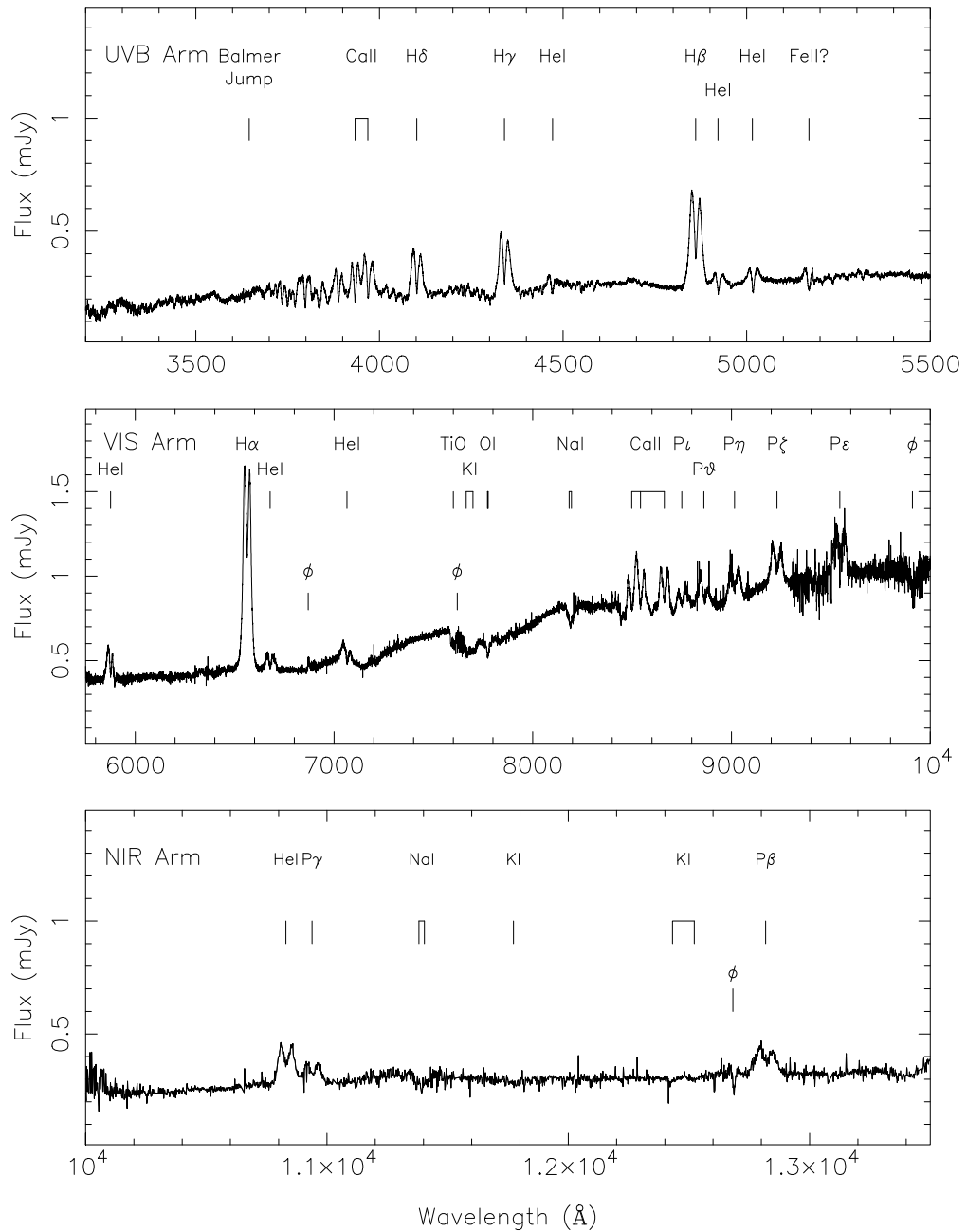


Figure 6.1: The average spectra of CTCV 1300, in the rest frame of the binary. The upper panel shows the UVB-arm, the centre panel the VIS-arm, and the lower panel the NIR-arm. The most prominent features are labelled.

The high ionisation line He II 4686 Å appears absent in the average spectrum, but is visible in the trailed spectra (see §6.2.2 and §6.2.3). Several absorption lines are present between 4000-4800 Å, as shown in Figure 6.2, which appear to trace the motion of the disc (see §6.2.2). The most likely cause of these absorption lines is thought to be a veil of disc material along the line of sight. The majority of these lines appear to be Fe I, Fe II and Ca I. Similar features have been observed in the spectrum of OY Car by Horne et al. (1994) and Copperwheat et al. (2012) (the ‘iron curtain’).

The helium lines at 4922, 5015 Å appear to show strong, narrow absorption cores that dip below the continuum, as do the higher-order Balmer lines between 3600-4000 Å. The O I triplet at 7773 Å is clearly visible, and also appears to drop below the continuum. Features such as these are observed in a number of CVs (e.g Marsh, 1987; Wade & Horne, 1988; Friend et al., 1988). The deep absorption cores are believed to originate through self-absorption in the accretion disc.

The Ca II triplet at 8498, 8542 and 8662 Å (hereafter 8567 Å) is clearly present and originates from the disc, although there is evidence of emission from the irradiated side of the secondary star (see §6.2.2 and §6.2.3). Similar features have been observed in the spectrum of GW Lib (van Spaandonk et al., 2010). The higher orders of the Paschen series are also visible from ~ 8800 Å onwards, and are possibly blended with the Ca II emission.

Absorption features from the secondary star are clearly visible in the form of TiO bands around 7100 Å and 7600 Å, and weak K I absorption doublet at 7664, 7699 (hereafter 7682 Å), 11773, 12432 and 12522 Å. However, these regions are heavily affected by telluric absorption. The clearest features from the secondary star are the Na I doublets at 8183, 8194 Å (hereafter 8189 Å) and 11381, 11404 Å (hereafter 11393 Å), although the feature at 11393 Å is heavily affected by telluric absorption.

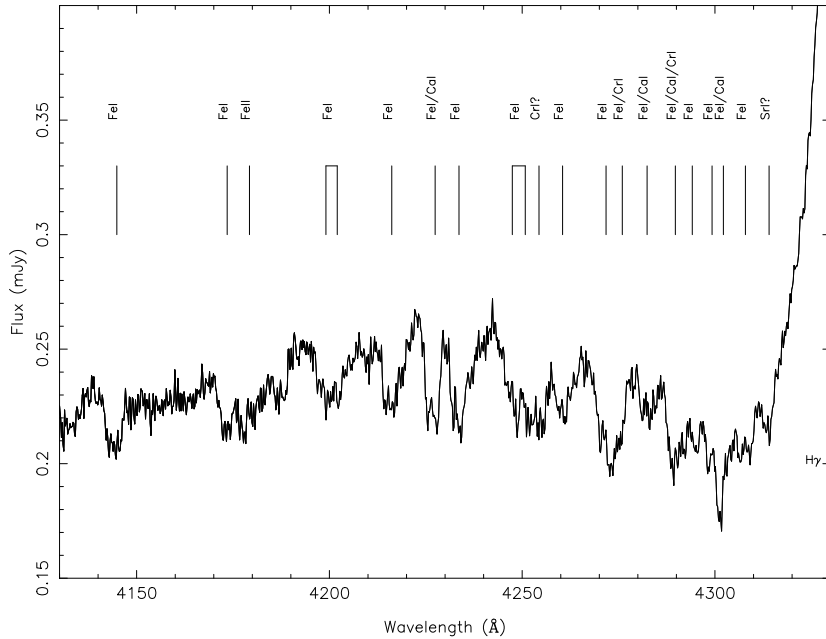


Figure 6.2: The average spectrum of CTCV 1300 between 4130-4330 Å, corrected to the rest frame of the white dwarf. Spectra taken during eclipse are not included in this average.

6.2.2 Trailed Spectra

The data were phase binned into 30 bins, according to the ephemeris presented in §4.2. The UVB-arm has complete phase coverage, although due to the differing exposure times (see §2.1.2), one of these bins is empty in both the VIS and NIR-arms.

The continuum was divided by a polynomial fit and spectra re-binned onto a constant velocity-interval scale centred on the rest wavelength of the lines. Figure 6.3 shows the trailed spectra of the H α , H β , H γ and H δ lines in CTCV 1300. Each line shows two clear peaks that vary sinusoidally with phase, in addition to the characteristic s-wave between phases 0.1–0.4 from the bright spot.

Figure 6.4 shows the trailed spectra of two Na I doublets (8189 and 11393 Å), the Ca II triplet (8567 Å), the 7682 Å K I doublet and He II (4686 Å) lines. The phases at which the Na I and K I lines show maximum red-shift ($\phi = 0.25$) and blue-shift ($\phi = 0.75$) suggests that they originate from the secondary star. There is evidence

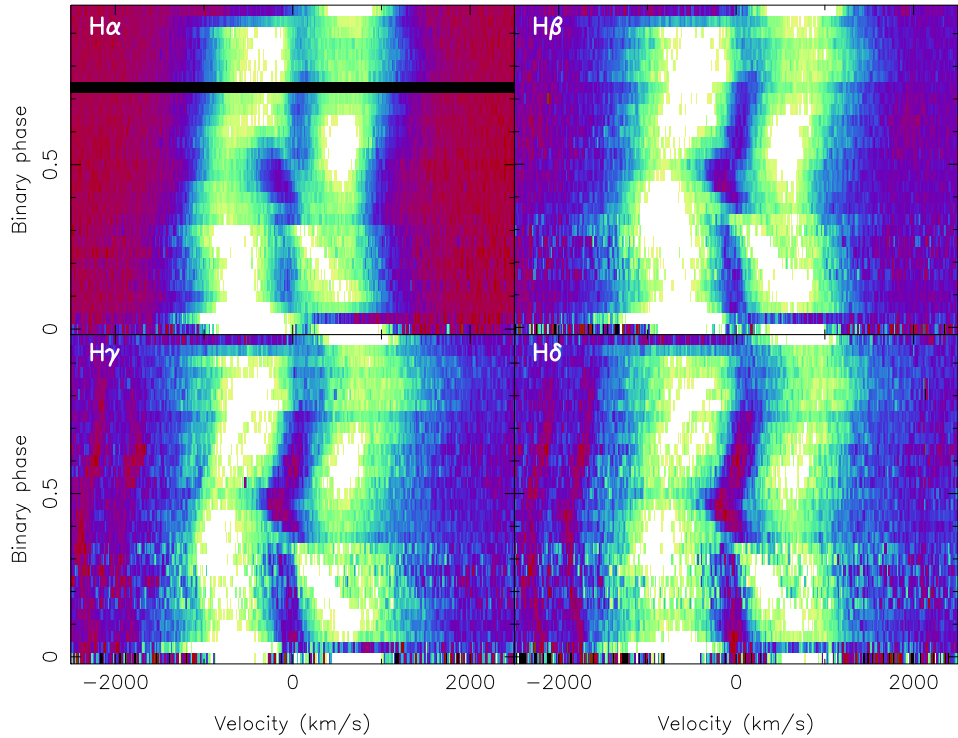


Figure 6.3: The trailed spectra of the $H\alpha$ (top left), $H\beta$ (top right), $H\gamma$ (bottom left) and $H\delta$ (bottom right) lines in CTCV 1300.

for emission from the secondary star in the Ca II lines through a component in the trail that is in phase with the Na I lines. However, this component is only visible during phases ~ 0.25 - 0.75 , which indicates that it arises from the irradiated side of the secondary star (see §6.2.5). The He II line appears to follow the motion of the bright spot, as defined by the s-wave in the Balmer trails.

Figure 6.5 shows the trailed spectra of the absorption line forest between 4130-4300 Å. The lines all appear to move together, suggesting a common place of origin. Using the same method outlined in §6.2.4, the velocity of these lines was found to be $K_{abs} = 116 \pm 4 \text{ km s}^{-1}$, with a phase offset of $\Delta\phi = 0.072 \pm 0.006$. The high velocity, (compared to the expected motion of the white dwarf, $\sim 90 \text{ km s}^{-1}$, see §5.2.1) and significant phase offset suggests that these lines originate in the disc.

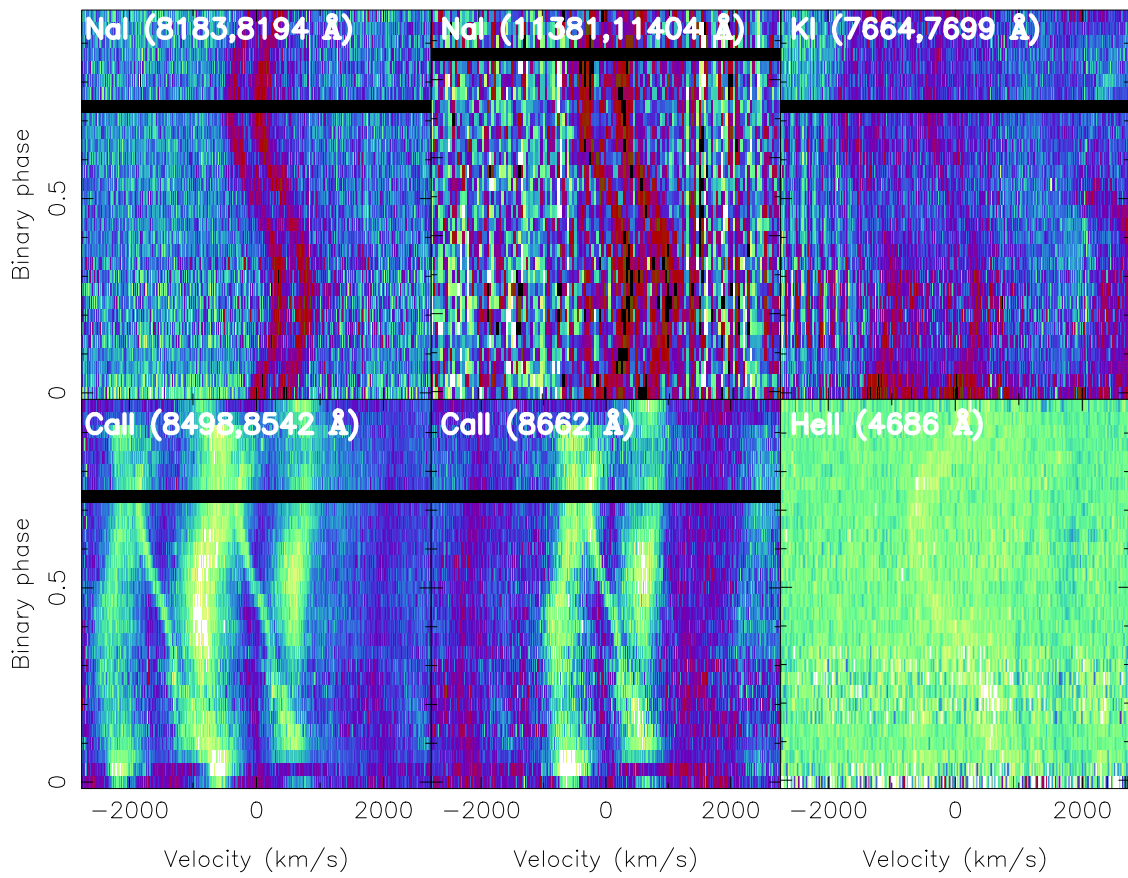


Figure 6.4: The trailed spectra of the 8189 and 11393 Å Na I doublets (upper left and upper centre, respectively), the 7682 Å K I doublet (top right), the Ca II triplet (8498, 8542 Å bottom left, 8662 Å bottom centre) and He II (4686 Å, bottom right) in CTCV 1300. Black and white lines represent absorption and emission, respectively.

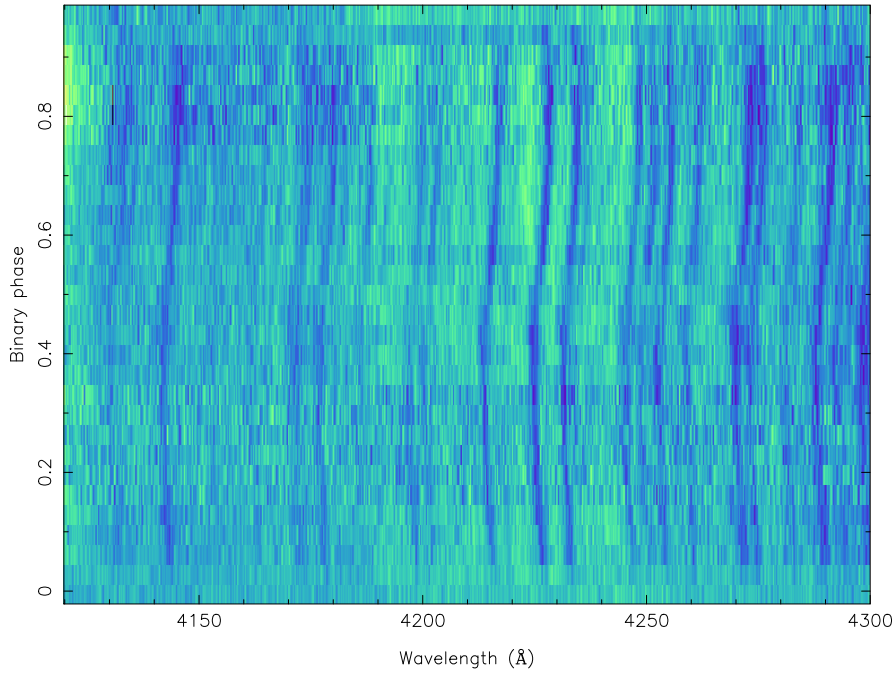


Figure 6.5: Trailed spectra of the forest of Fe I, Fe II and Ca I absorption lines between 4130-4300 Å.

6.2.3 Doppler Tomography

Figure 6.6 shows Doppler maps for Ca II (8498, 8542 & 8662 Å), H α , H β and He II (4686 Å). Eclipse data (between phases 0.95 and 1.05) were removed. A systemic velocity of $\gamma = -20 \text{ km s}^{-1}$ was applied to shift the maps onto the $K_x = 0 \text{ km s}^{-1}$ axis (see §6.2.4).

In each map there is a ring-like distribution of emission centred on the white dwarf, which is characteristic of an accretion disc. In the Ca II maps, an enhanced area of emission is present at velocities intermediate to the free-fall velocity of the gas stream (lower stream) and the velocity of the disc along the gas stream (Keplerian velocity, upper stream). This emission is attributed to the bright spot. The three Ca II maps all show clear emission from the secondary star, which appears to be concentrated towards the inner hemisphere, indicating that irradiation is significant. The H α map shows weak emission from the secondary star, a feature uncommon in short period CVs. The H β map shows weak bright spot emission. The He II

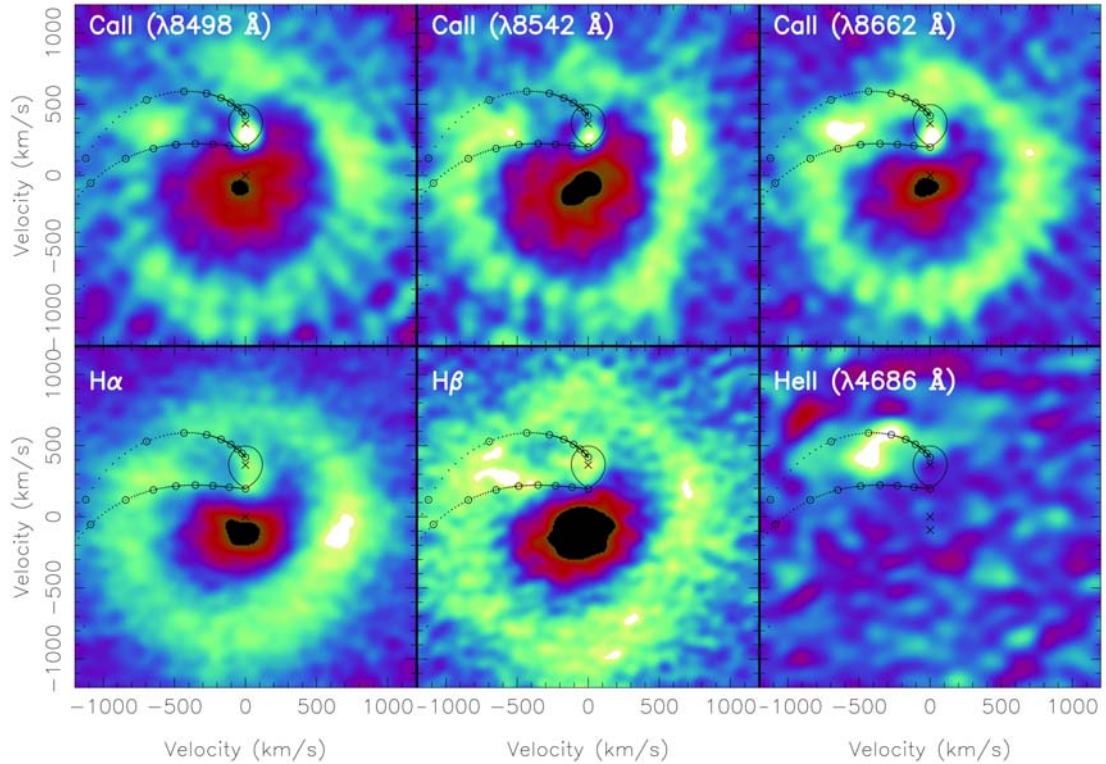


Figure 6.6: Doppler maps of CTCV 1300 in Ca II (8498, 8542, 8662 Å), H α , H β and He II (4686 Å) computed from the trailed spectra in Figures 6.3 and 6.4. Data taken during eclipse have been omitted from the fit. The predicted position of the secondary star and the path of the gas stream are marked. The three crosses on the map are, from top to bottom, the centre of mass of the secondary star, the centre of mass of the system, and the white dwarf. These crosses, the Roche lobe of the secondary star, the Keplerian velocity along the gas stream (top curve), and the predicted trajectory of the gas-stream (bottom curve) have been plotted using the system parameters found in §6.2.7. The series of circles along the gas stream mark the distance from the white dwarf at intervals of $0.1L_1$, where $1.0L_1$ is the secondary star.

emission appears to show emission near both the Keplerian velocity stream and at velocities intermediate to the Keplerian velocity stream and free-fall velocity stream, although it is possible that this is an artifact arising from limited phase coverage (Marsh & Horne, 1988). If this is a genuine feature, its position relative to the Ca II emission suggests that the He II emission is caused by a mixture of gas-stream and disc material. He II bright spot emission at Keplerian disc velocities has been observed in other short period CVs (Marsh et al., 1990; Copperwheat et al., 2012).

6.2.4 Radial velocity of the Secondary Star

The secondary star in CTCV 1300 is visible through weak absorption lines. The strongest of these lines is the Na I doublet at 8189 Å. In order to determine the radial velocity, the individual spectra of CTCV 1300 were cross-correlated against template spectra as described in §3.5.1. The Na I line at 8189 Å was used because it is much stronger and less affected by telluric absorption than the line at 11393 Å.

Fits to the continuum were subtracted from the individual spectra, which were then corrected for the orbital motion of the secondary star with a first guess of K_2 . For each individual spectrum, a template spectrum was created that consisted of an average of all the spectra *minus* the spectrum under study (Marsh et al., 1994). Because these template spectra were made from the CV data, they did not require broadening for orbital smearing or the rotational velocity of the secondary star. These template spectra were then cross-correlated against the uncorrected data. This yielded a new value of K_2 and γ to correct the spectra with. An intrinsic error was summed in quadrature to each error bar to account for systematic error and reach a reduced- χ^2 of 1. This process was repeated until K_2 converged, which corresponded to a value of $K_2 = 379 \pm 6 \text{ km s}^{-1}$, with a systematic error of 22 km s^{-1} added in quadrature to each error bar. The radial velocity curve obtained using this technique is shown in the upper panel of Figure 6.7.

The value of γ obtained via the auto-correlation technique is not representative of the true systemic velocity, which must be determined through cross-correlation with a template star of known radial velocity. Therefore, in order to verify this result and find the true systemic velocity (γ), the normalised spectra of CTCV 1300 were cross-correlated against the M-dwarf template spectra (see §2.1.2) using the same wavelength range. The template spectra were artificially broadened by 46 km s^{-1} (see Equation 3.9) to account for the orbital smearing of CTCV 1300 through the 210-second VIS-arm exposures (see §2.1.2), and then by the best-fitting values for the rotational velocity of the secondary star ($v \sin i$) found in §6.2.6. An intrinsic error of 22 km s^{-1} was added to each error bar from the M2V cross-correlation, and 24 km s^{-1} to M5V data, to account for systematic errors and reach a reduced- χ^2 of 1. The radial velocity curves are shown in the centre panel (M2), and bottom panel (M5) of Figure 6.7. Cross-correlating against the M2 and M5 templates yield values of $K_2 = 373 \pm 6 \text{ km s}^{-1}$ and $K_2 = 376 \pm 7 \text{ km s}^{-1}$, respectively. The M2 template could not be corrected for flexure, and so only the M5 template was used to derive the systemic velocity for CTCV 1300. Using the radial velocities provided by Gizis et al. (2002), a value of $\gamma = -20 \pm 5 \text{ km s}^{-1}$ was found. For K_2 , the value found through the auto-correlation, that is $K_2 = 379 \pm 6 \text{ km s}^{-1}$ is preferred. This is because the average spectra of the data is a better match to the data than the M5 and M2 templates.

The radial velocity curves produced through this technique show some variation from a sine fit between phases 0.4 to 0.6, which is characteristic of irradiation suppressed absorption (e.g. Billington et al., 1996). Marsh & Horne (1988) recommend only fitting the above data between phases 0.8 to 1.2, because at these phases the effects of irradiation are at a minimum. Fitting the auto-correlation data gives a value of $K_2 = 378 \pm 6 \text{ km s}^{-1}$, which is used hereafter. This value is in excellent agreement with the photometric value predicted in §5.2.1, $K_2 = 372.2 \pm 2.5 \text{ km s}^{-1}$.

Fitting the M5 and M2 templates between the same phases gives $K_2 = 372 \pm 7$ km s⁻¹ and $K_2 = 378 \pm 8$ km s⁻¹ respectively, which are in excellent agreement with the auto-correlation data and the photometric method.

6.2.5 Irradiation of the Secondary Star

The Doppler maps of Ca II emission presented in Figure 6.6 suggest a very different value of K_2 to that found from cross-correlating the Na I doublet, which indicates that irradiation may be affecting one, or perhaps both, of these measurements. As discussed in §6.2.4, the radial velocity curves produced via cross-correlation of the sodium doublet (Figure 6.7) show some variation from a sine curve, suggesting that irradiation affects the sodium doublet. Because this line is in absorption, a decrease in line flux at phase 0.5 would be expected. This effect is observed, although the flux is found to vary by less than 5 per cent across an orbital cycle. In contrast, the Ca II emission varies significantly throughout the orbital cycle. The component from the secondary star is only visible during phases ~ 0.25 - 0.75 , when the inner face is along the line of sight. This suggests that irradiation heavily affects the distribution of calcium emission.

The estimates of K_2 measured from the Doppler maps (Figure 6.6), were corrected for the effects of irradiation using Equation 3.14 and the values of q and R_2/a found in §6.2.7. The resulting values are shown in Table 6.1. The estimates of K_2 from the doppler maps, once corrected for irradiation, are consistent with $K_2 = 378 \pm 6$ km s⁻¹ found from fitting the sodium doublet.

For the H α emission, both the uncorrected K_2 and the corrected K_2 ($f = 0.50$) value are consistent with K_2 measured from the sodium lines. The H α emission therefore appears to be consistent with optically thick emission excited by irradiation from the white dwarf and inner disc.

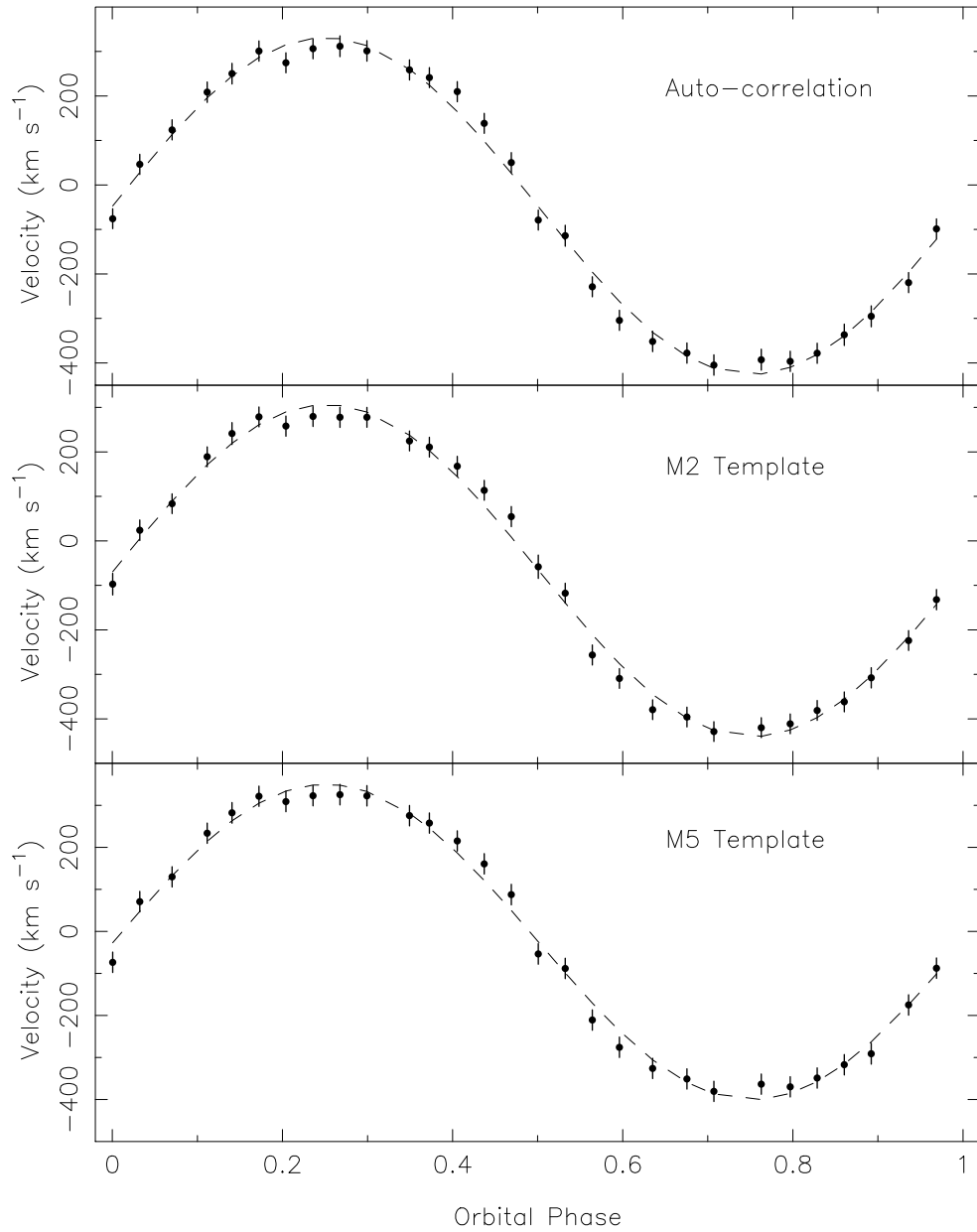


Figure 6.7: The radial velocity curve of CTCV 1300 obtained through auto-correlation (upper panel), cross-correlation against an M2 template (centre panel) and cross-correlation against an M5 template (lower panel).

Table 6.1: Measured and corrected values of K_2 found using optically thick ($f=0.50$) and thin ($f=0.77$) corrections.

Ion	Line (Å)	K_{meas} (km s ⁻¹)	K_{corr} ($f=0.77$) (km s ⁻¹)	K_{corr} ($f=0.50$) (km s ⁻¹)
Na I	8183/8194	378 ± 6	-	-
Ca II	8498	298 ± 5	403 ± 15	359 ± 11
Ca II	8542	298 ± 15	403 ± 29	359 ± 22
Ca II	8662	277 ± 22	370 ± 40	330 ± 30
H α	6562	350 ± 50	470 ± 80	420 ± 70

6.2.6 Rotational Velocity of the Secondary Star

The normalised spectra of CTCV 1300 were corrected for the orbital motion of the secondary star using the value of K_2 obtained in §6.2.4. The spectra were then averaged together in order to maximise the strength of the Na I doublet at 8189 Å. The spectral-type templates were broadened to match the smearing due to the orbital motion of CTCV 1300 through the 210 second VIS-arm exposures and rotationally broadened by a range of velocities (50-200 km s⁻¹) as described in §3.5. In principle, the orbital smearing is a function of orbital phase, and thus varies throughout the orbital cycle. In this study a single value of 46 km s⁻¹ was adopted, which is the average value of the smearing across an orbital cycle. Changing this to the maximum and minimum possible values of orbital smearing required, that is the smearing at conjunction and quadrature, was found to alter the final value of $v \sin i$ obtained by 3 km s⁻¹. This uncertainty is added in quadrature to the uncertainties calculated below.

The value of $v \sin i$ was found using the optimal-subtraction technique described in §3.6. This required an estimate of the limb-darkening coefficient of the secondary star and a smoothing coefficient to smooth the residuals when computing χ^2 . The limb-darkening coefficient is highly uncertain, although Copperwheat et al. (2012) have shown that altering the limb-darkening coefficient has little effect on the value of $v \sin i$ obtained. In this thesis, a limb-darkening coefficient of 0.5 and smoothing

Gaussian of FWHM = 15 km s⁻¹ was adopted. A wavelength range of 8080-8106, 8125-8206, 8226-8245 and 8264-8285 Å was used, which attempted to include as much of the continuum as possible around the Na I doublet, whilst trying to avoid telluric regions.

The values of χ^2 versus $v \sin i$ for both spectral-type templates are shown Figure 6.8. After removing the intrinsic $v \sin i$ of the template stars (M5 \approx 3 km s⁻¹, M2 \approx 9 km s⁻¹), a value of $v \sin i = 129 \pm 3$ km s⁻¹ was obtained for the M2 template and a value of $v \sin i = 125 \pm 4$ km s⁻¹ for the M5 template. The uncertainties on these values come from the formal error estimation of $\Delta\chi^2 = \pm 1$. This does not attempt to include systematic errors. Because of the lack of available templates, the spectral type of the secondary star was estimated using the empirical donor sequence of Knigge et al. (2011). For a system with an orbital period of 128.07 minutes, spectral type of the secondary star is expected to be \sim M4.3. A spectral type of $M4.5 \pm 0.5$ was therefore adopted. Interpolating between the two values of $v \sin i$ above gives a final value of $v \sin i = 125 \pm 7$ km s⁻¹. This error takes into account the uncertainty on finding the minimum $v \sin i$ for each template (± 3 -4 km s⁻¹ for each template), the uncertainty from averaging the orbital smearing (± 3 km s⁻¹), and the uncertainty in spectral type (± 0.5 spectral types).

6.2.7 System Parameters

Using the values of $K_2 = 378 \pm 6$ km s⁻¹ and $v \sin i = 125 \pm 7$ km s⁻¹ found in §6.2.4 and §6.2.6 in conjunction with the orbital period and a measurement of the eclipse full width at half depth ($\Delta\phi_{1/2}$), accurate system parameters for CTCV 1300 can be calculated. The best measurement of the orbital period, P_{orb} , comes from §4.2, where $P_{orb} = 0.088940717(1)$ days. In Figure 5.1a, there are six light curves of CTCV 1300, from which it was determined that $\Delta\phi_{1/2} = 0.0791(5)$.

The system parameters and their errors were calculated using a Monte Carlo

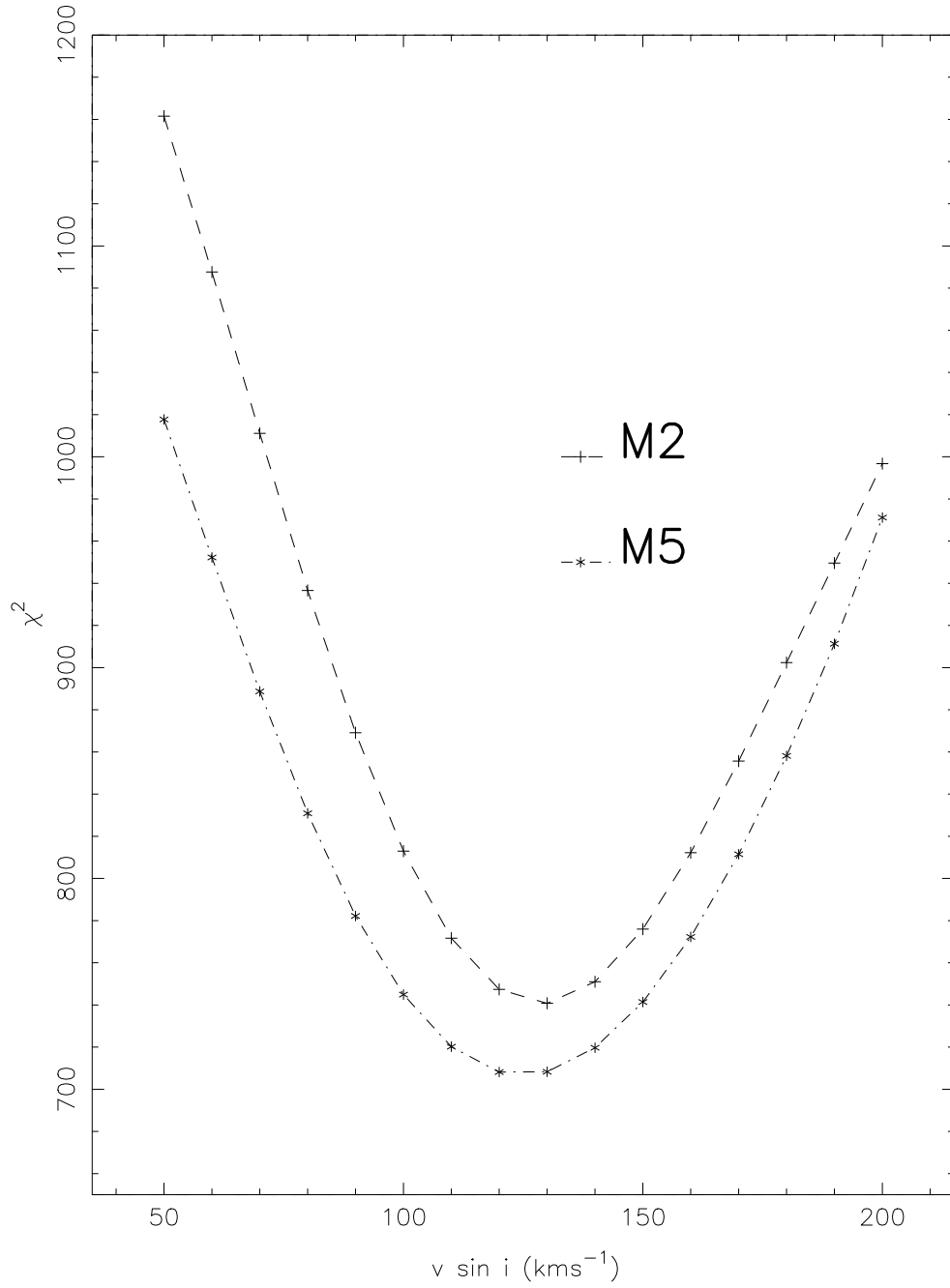


Figure 6.8: χ^2 vs $v \sin i$ from the optimal subtraction technique.

Table 6.2: System parameters for CTCV 1300.

Parameter	Measured Values	Monte Carlo Values	Photometric
P_{orb} (s)	-	-	0.088940717(1)
$\Delta\phi_{1/2}$	0.0791 ± 0.0005	-	<i>not stated</i>
K_2 (km s ⁻¹)	378 ± 6	-	372.2 ± 2.5
$v \sin i$ (km s ⁻¹)	125 ± 7	-	$122 \pm 10^*$
q	-	0.252 ± 0.025	0.240 ± 0.021
i°	-	85.7 ± 1.5	86.3 ± 1.1
M_w/M_\odot	-	0.79 ± 0.05	0.736 ± 0.014
M_2/M_\odot	-	0.198 ± 0.029	0.177 ± 0.021
R_2/R_\odot	-	0.223 ± 0.011	0.215 ± 0.008
a/R_\odot	-	0.834 ± 0.020	0.813 ± 0.011
K_w (km s ⁻¹)	-	95 ± 9	90 ± 8
Distance (pc)	260 ± 50	-	375 ± 13

* Derived using the values in Table 5.1a and Equation 3.12.

approach similar to Horne et al. (1993), Smith et al. (1998), Thoroughgood et al. (2001) and Thoroughgood et al. (2004). The Monte Carlo simulation took 250,000 values of K_2 , $\Delta\phi_{1/2}$, $v \sin i$ and P_{orb} , treating each as being normally distributed about their measured values with standard deviations equal to the errors on the measurements. The mass of each component, the inclination of the system and the radius of the secondary star were then calculated as described in §3.7, omitting (K_2 , $v \sin i$, $\Delta\phi_{1/2}$) triplets that are inconsistent with $\sin i \leq 1$. Each accepted M_1 , M_2 pair is plotted in Figure 6.9, and the masses and their errors are computed from the mean and standard deviation of the distribution of these pairs. The mass of the white dwarf was found to be $M_1 = 0.79 \pm 0.05 M_\odot$, and the mass of the secondary star $M_2 = 0.198 \pm 0.029 M_\odot$. These values are found to be in good agreement with those presented in Table 5.1a. The values of all system parameters found from the Monte Carlo simulation are listed in Table 6.2, along with those presented in Table 5.1a for direct comparison.

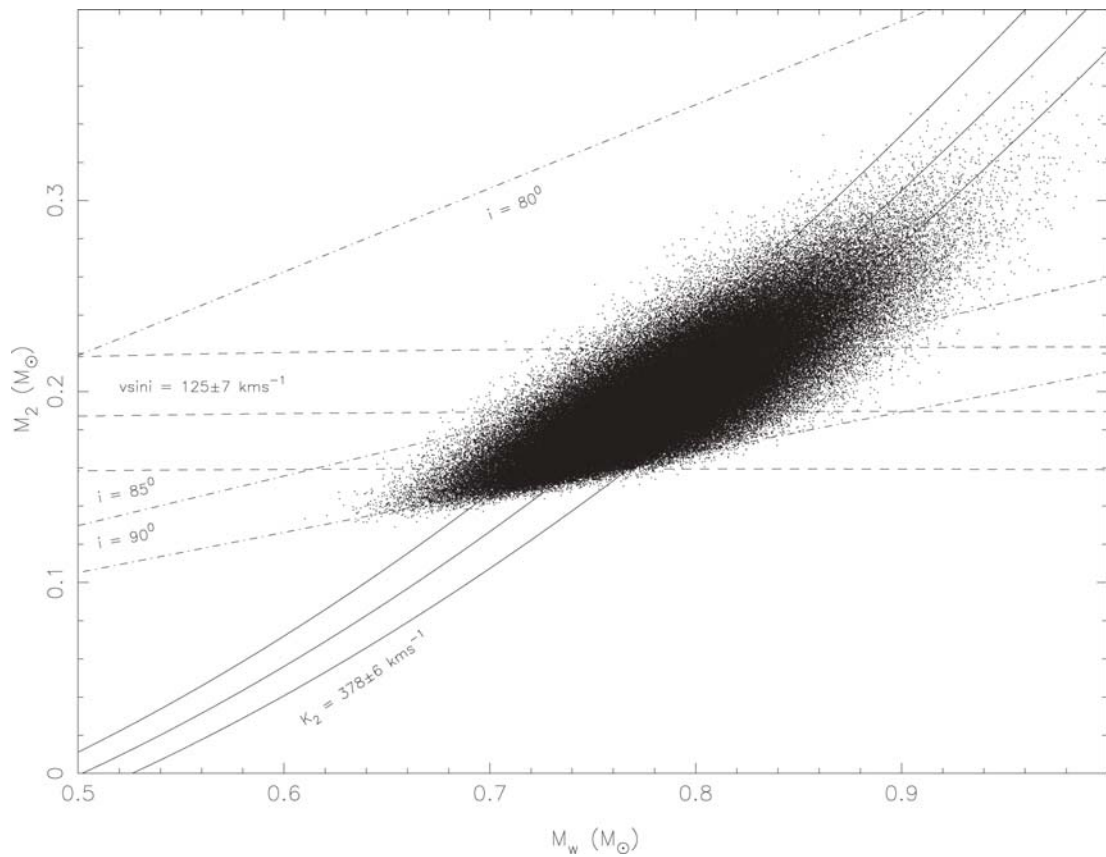


Figure 6.9: Monte Carlo determination of system parameters for CTCV 1300. Each dot represents an (M_1, M_2) pair. Dot-dashed lines are lines of constant inclination, the solid curves satisfy the constraints from the radial velocity of the secondary star, K_2 , and the dashed lines satisfy the constraints of the rotational velocity of the secondary star, $v \sin i$.

6.2.8 Distance

At mid-eclipse ($\phi = 0$), the apparent magnitude of the system is 16.90 ± 0.05 around the Na I doublet, which is approximately the I -band. This value is not corrected for differential slit losses. The secondary star is found to contribute 62 ± 14 per cent at mid-eclipse, which gives an apparent magnitude of $m_I = 17.43 \pm 0.26$. The absolute magnitude can be estimated using the revised empirical donor sequence of Knigge et al. (2011) to obtain $M_I = 10.32 \pm 0.14$. Using Equation 3.15, a distance of $d = 260 \pm 50$ pc was obtained. This distance places the system somewhat closer than the distance of $d = 375 \pm 13$ pc found in Chapter 5, but still consistent to $\sim 2.2\sigma$.

6.3 Discussion

The system parameters listed in Table 6.2 are found to be in good agreement with those found using the photometric method in Chapter 5. Together with Copperwheat et al. (2012), there is confidence that photometric mass determinations such as those of Chapter 5 are reliable across a range of orbital periods, and that the ϵ - q relations of Patterson et al. (2005), Knigge (2006) and Pearson (2006) are well founded across the range of orbital periods tested.

The uncertainties in the system parameters for CTCV 1300 determined in this Chapter, and in Chapter 5, are quite large in comparison to many of the other systems studied in Chapter 5. The reason for the large uncertainties in CTCV 1300 in Chapter 5 is because the eclipse light curves used for model fitting suffer from heavy flickering, which causes difficulties in obtaining an accurate value for the mass ratio, q . The large uncertainties in this Chapter arise because of the interpolation technique used to arrive at a value for $v \sin i$. The error on $v \sin i$ ($\pm 7 \text{ km s}^{-1}$) is the dominant source of uncertainty in the final system parameters. In principle, a wider selection of spectral type templates would allow for further constraining of $v \sin i$ and

the derivation of the spectral type of the secondary star.

Chapter 7

The Brown Dwarf Mass Secondary Star in SDSS J1433+1011

The contents of this Chapter are to be submitted for publication by Savoury & Littlefair in the Monthly Notices of the Royal Astronomical Society (Savoury & Littlefair, 2013). This work was carried out in collaboration with Stuart Littlefair, who was responsible for applying for the use of the GEMINI facilities, and producing a model spectrum of SDSS 1433 (Figure 7.1 of this Chapter). The reduction and analysis of the data and the following text are my own work.

7.1 Introduction

The effective temperatures of the secondary stars in CVs are a useful indicator of the evolutionary status of CVs and their secondary stars (e.g. Smith & Dhillon, 1998; Beuermann et al., 1998; Baraffe & Kolb, 2000; Knigge et al., 2011). Using $T_{eff} - P_{orb}$ relationships, the presence of evolved secondary stars have been inferred (e.g. Thorstensen et al., 2002; Littlefair et al., 2006b; Rodríguez-Gil et al., 2009). These relationships are useful, however they are unconstrained for systems that have

evolved past P_{bounce} due to a lack of direct observational evidence.

Systems that have evolved past P_{bounce} should contain brown dwarf like secondary stars. These objects are a unique type of star; a previously stellar object stripped of mass until it falls below the hydrogen burning limit. Despite the fact that various models (e.g. Kolb, 1993; Willems et al., 2005) predict that between 15 and 70 per cent of the CV population should have evolved to such a point where the secondary star has become degenerate, there is no direct spectroscopic evidence for the existence of these objects (Littlefair et al., 2003). Although several authors have inferred the presence of an L-type secondary star in some CVs (e.g. Mennickent et al., 2004; Unda-Sanzana et al., 2008; Aviles et al., 2010), these objects are not necessarily sub-stellar, as some L-dwarfs may be capable of hydrogen fusion (Kirkpatrick et al., 1999). Sub-stellar status can only be confirmed in these systems with an accurate determination of the secondary star mass. The combination of effective temperature and secondary star mass (and P_{orb}) make a powerful tool for probing the evolutionary status of CVs and their secondary stars. Sadly, there are no CVs that are known to possess a sub-stellar secondary star *and* have an accurate determination of the secondary star's effective temperature.

The light curve modelling technique used in Chapter 5 revealed the presence of three secondary stars with masses below the hydrogen burning limit. Of the objects found in Chapter 5, SDSS 1507 is halo CV (Patterson et al., 2008; Uthas et al., 2011), and so there are two stars that can be considered as 'normal' post-period-bounce systems; SDSS 1035 and SDSS 1433. Of these, SDSS 1433 has the secondary star with the highest mass, and is therefore more likely to have the brightest secondary star.

A model spectrum of SDSS 1433 was produced by fitting white dwarf and accretion disc models to the GALEX UV fluxes (Morrissey et al., 2007) and SDSS optical spectrum (Szkody et al., 2007) simultaneously (e.g. Gänsicke et al., 2006; Little-

fair et al., 2008). This model spectrum was then extrapolated into the infrared, as shown in Figure 7.1. Also shown in Figure 7.1, are UKIDSS photometry data points (Lawrence et al., 2007; Warren et al., 2007), which show the predicted spectrum significantly underestimates the flux. This indicates that the secondary star could make a significant contribution to the total J-band light. Although encouraging, this model spectrum should be treated with caution. The spectrum of the accretion disc and bright spot is highly uncertain at infrared wavelengths, and cyclotron emission from the magnetic field of the white dwarf may also be significant (Littlefair et al., 2005). Nevertheless, the infrared excess indicates that SDSS 1433 represents the best chance of making a direct spectroscopic detection of a brown dwarf like secondary star in an accreting binary. A direct detection of the secondary star would be unique, and determination of the spectral type would provide another independent test of binary evolution models (e.g. Smith & Dhillon, 1998; Patterson et al., 2005; Knigge, 2006; Knigge et al., 2011).

In this Chapter, I attempt to use time-resolved J-band spectroscopy to make a direct detection of the secondary star in SDSS 1433.

7.2 Results

7.2.1 Average Spectrum

Figure 7.2 shows the average J-band spectrum of SDSS 1433 in the rest frame of the binary and the rest frame of the secondary star. M5, L3 and L8 template stars (Cushing et al., 2005) and a telluric spectrum created from an G2V template (see §2.6.2) are also shown for comparison.

The average J-band flux of the system (across all orbital phases) is estimated to be 0.064 ± 0.004 mJy, which gives an apparent J-band magnitude of $m_J = 18.47 \pm$

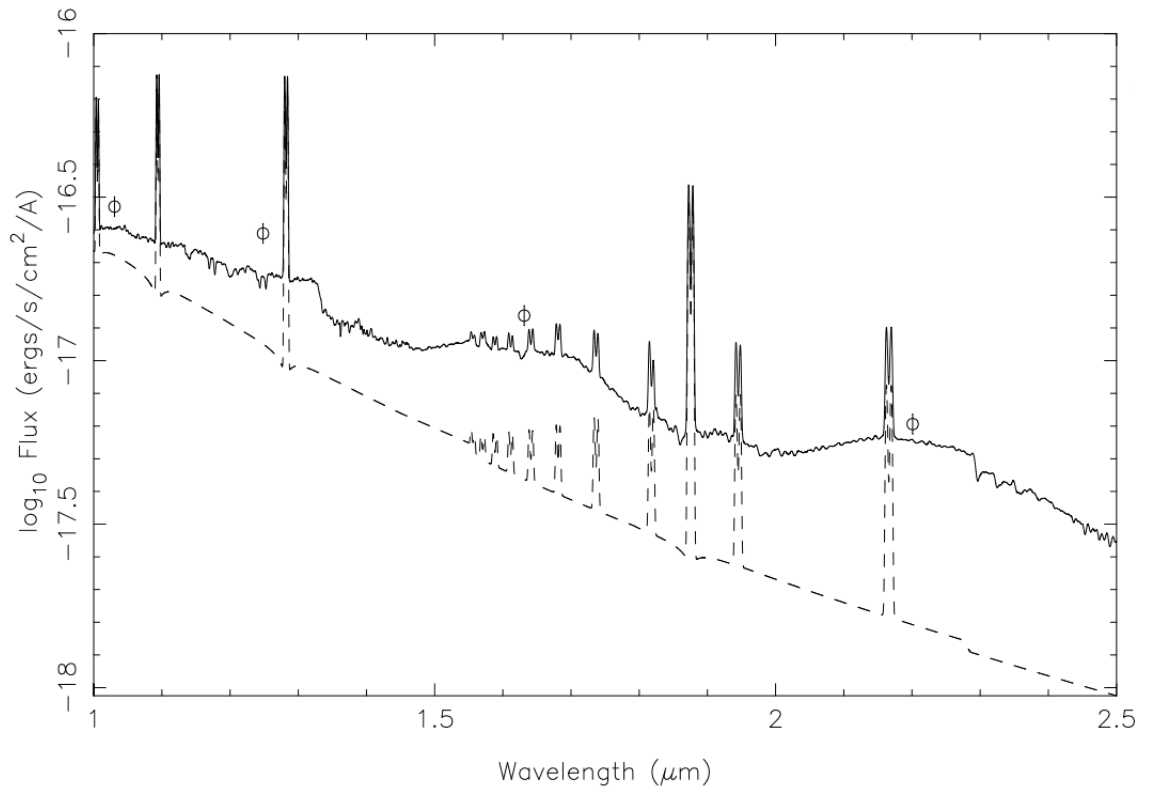


Figure 7.1: Model spectrum of SDSS 1433. The dashed line shows a model of the white dwarf and accretion disc, as determined by simultaneous fits to GALEX UV fluxes and SDSS optical spectrum, and extrapolating into the infrared. The solid line shows the addition of an L2 (Kelu1AB) secondary star, scaled to the distance of the system. The open circles show data points from UKIDSS photometry. Figure by Dr. Stuart Littlefair.

0.09. This value is not corrected for differential slit losses between the target and comparison stars.

Accretion Disc Features

The spectrum is dominated by the strong, double-peaked emission lines of He I, Paschen- γ and Paschen- β . The broad, double-peaked nature of these lines indicate they originate from the accretion disc (e.g. Horne & Marsh, 1986). The full width at half-maxima (FWHM) of the He I, Paschen- γ and Paschen- β lines were found to be $2600 \pm 100 \text{ km s}^{-1}$, $2500 \pm 300 \text{ km s}^{-1}$ and $2300 \pm 100 \text{ km s}^{-1}$ respectively. The peak separations for these lines were found to be $1500 \pm 300 \text{ km s}^{-1}$, $1400 \pm 400 \text{ km s}^{-1}$ and $1500 \pm 300 \text{ km s}^{-1}$ respectively. These values are in excellent agreement with those of Tulloch et al. (2009), who found the FWHM of the H α line to be $2200 \pm 200 \text{ km s}^{-1}$, with a peak separation of $1300 \pm 200 \text{ km s}^{-1}$.

Secondary Star Features

The average spectrum of SDSS 1433 appears to show increasing flux towards the red end of the spectrum. The slope of the continuum was measured at $(3.30 \pm 0.13) \times 10^{-2} \text{ mJy}/\mu\text{m}$. The presence of a red continuum could reasonably be attributed to the secondary star because the white dwarf and accretion disc are expected to have a blue continuum (e.g. Fig 3.2 of Hellier, 2001). However, at short orbital periods it is unknown what impact the accretion flow might have upon the shape of the spectrum. The presence of a red continuum alone is therefore insufficient evidence for the detection of the secondary star.

There is evidence of a secondary star absorption feature around 13300 \AA that is attributed to the headless water band at 13300 \AA . Features observed in other CVs and L-type dwarfs, such as the Na I doublet around 11393 \AA (e.g. Chapter 6) and the K I doublet around 11731 \AA (e.g. Copperwheat et al., 2012) appear weak or absent. It

is possible that these features are lost in the noise of the spectrum (Littlefair et al., 2000). The Na I lines are also located at a region in the spectrum where telluric features are the most prominent, further increasing the uncertainty of any detection. There is some tentative evidence of K I absorption around 12432 Å.

When the spectrum is corrected for the expected orbital motion of the secondary star as found in Chapter 5 (see Figure 7.2), the second component of the potential K I absorption doublet around 12477 Å appears present, which was not previously visible. The water band, which was previously visible, is still clearly present in the average spectrum, however it appears sharper.

There is no evidence of H₂O or CH₄ absorption around 11000 Å in either spectra, which, for mid to late T-dwarfs, should be similar in strength to that of the water band (e.g. Kirkpatrick, 2005; Burgasser, 2007).

7.2.2 Skew Mapping

Given the faintness of the potential secondary star features and the poor signal-to-noise of the data, there is an element of uncertainty as to whether these observed features are genuine absorption features or merely random fluctuations in the noise of the spectrum. However, if these features are real, then a skew map should produce a clear peak, centered on the radial velocity of the secondary star (see §3.5.2). If such a peak is present then it will also provide another independent test of the photometric modelling technique used in Chapter 5.

The data were phase binned into 15 bins according to the ephemeris of Littlefair et al. (2008) and a range of template spectra from M5 to L8 were obtained from the IRTF spectral library (Cushing et al., 2005). The template spectra were broadened to match the rotational velocity of the secondary star predicted from the system parameters found in Chapter 5 ($v \sin i = 99.7 \text{ km s}^{-1}$). The amount of broadening required for each template was calculated by assuming that the intrinsic rotational

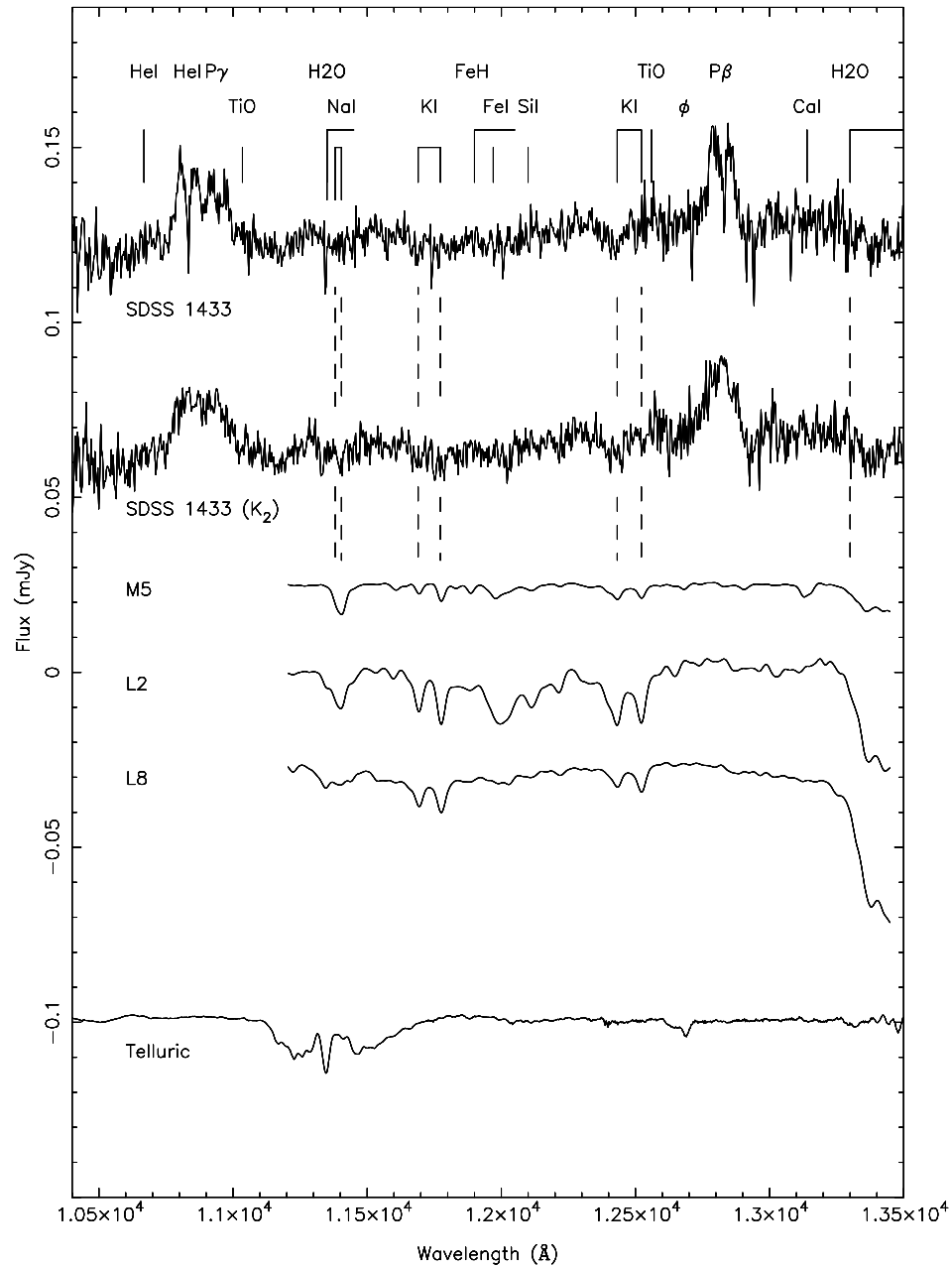


Figure 7.2: The average J-band spectrum of SDSS 1433. The upper spectrum of SDSS 1433 is in the rest frame of the binary, and offset by 0.06 mJy from the absolute flux. The lower spectrum of SDSS 1433 has been corrected for the radial velocity of the secondary star found in Chapter 5 and thus represents an average spectrum in the rest frame of the secondary star. Also shown is an M5, L3 and L8 template star, and the telluric spectrum. The template and telluric spectra are normalised and offset.

velocity of the template stars (Tinney & Reid, 1998; Mohanty & Basri, 2003; Reiners & Basri, 2007, 2008; Morin et al., 2010; Deshpande et al., 2012), and the additional broadening required, are added in quadrature to give the total rotational broadening. The templates and phase binned CV spectra were then normalised by dividing by a first order polynomial, and then subtracting a 2nd order fit to the continuum. This ensured that relative line strength across the spectrum was preserved. Both the CV and template spectra were binned onto the same wavelength scale (11203-13450 Å in 624 pixels), and the template spectrum broadened to match the resolution of the CV data (see §2.1.3). The Pβ emission line was also masked. Skew maps were then produced for SDSS 1433 by cross-correlating the phase-binned spectra of SDSS 1433 against the template stars, and then back-projecting the cross-correlation functions as described in §3.5.2. Figure 7.3 shows the skew map of SDSS 1433 made with the L2 template, which was found in §7.2.3 to be a reasonable estimate of the spectral type of the secondary star.

When the skew maps were first produced, the L2 map showed a significant peak at $K_x = 230 \pm 50 \text{ km s}^{-1}$, $K_y = 470 \pm 70 \text{ km s}^{-1}$. The uncertainties were derived using a bootstrapping technique, where the cross-correlation procedure was repeated, each time with one different phase bin masked. The uncertainties from this technique, σ_{K_x} and σ_{K_y} , were found to be $\sigma_{K_x} = \sim 30 \text{ km s}^{-1}$ and $\sigma_{K_y} = \sim 40 \text{ km s}^{-1}$ (assuming $\gamma = 0 \text{ km s}^{-1}$). The change in position of the peak was then measured by cross-correlating against a range of different template stars to find the uncertainty given by the spectral type. This gave $\sigma_{K_x} = 37 \text{ km s}^{-1}$ and $\sigma_{K_y} = 50 \text{ km s}^{-1}$. These values were then added in quadrature to give the final uncertainty. Because the emission lines were masked, the peak of the skew map can be attributed to the secondary star. However, the peak of the secondary star should lie on the $K_x = 0$ axis. It is possible to shift the peak onto the $K_x = 0$ axis by introducing a non-zero γ , or by applying a phase offset.

Follow up observations made with a 0.5m telescope¹ in March 2012 revealed a phase lag of $\phi = +0.09$ between the observed mid-eclipse time and the mid-eclipse time predicted by the ephemeris of Littlefair et al. (2008). This difference is not consistent with statistical errors. The rate of change in orbital period (\dot{P}) required to create a phase shift of $\phi = +0.09$ is $(5.2 \pm 0.5) \times 10^{-8}$ days yr⁻¹ (see Appendix C). This is several orders of magnitude larger than expected for systems near the period minimum (Knigge et al., 2011). Enhancing the mass transfer rates by including enhanced AML (e.g. Willems et al., 2005; Littlefair et al., 2008) only improves this difference by a factor of 10, and so it is likely that an additional mechanism is responsible for the observed period change. Possible explanations for the observed phase lag could be the presence of a third body affecting the arrival time of the eclipses, or a low sampling rate in the original observations that lead to the uncertainties being underestimated. Further monitoring of SDSS 1433 is thus highly desirable to determine an improved ephemeris. The observed phase lag indicates that the ephemeris used to phase bin the data may not be valid for the spectroscopic observations obtained in 2009 and 2010, and that a phase offset may be appropriate. A phase offset of $\phi = -0.0675$ was found to be sufficient to shift the peak of the skew map onto or close to the $K_x = 0$ axis, without the need to introduce a non-zero γ .

The L2 map in Figure 7.3 shows a significant peak at $K_x = -30 \pm 50$ km s⁻¹, $K_y = 520 \pm 50$ km s⁻¹. This value is in excellent agreement with the radial velocity predicted in Chapter 5 of $K_2 = 511 \pm 1$ km s⁻¹. This provides strong evidence that the photometric model found in Chapter 5 is correct, and that the tentative absorption features visible in Figure 7.2 are real.

¹Eclipse obtained 13th March 2012 by Dr. Stuart Littlefair. For further information see <https://sites.google.com/site/point5metre/>.

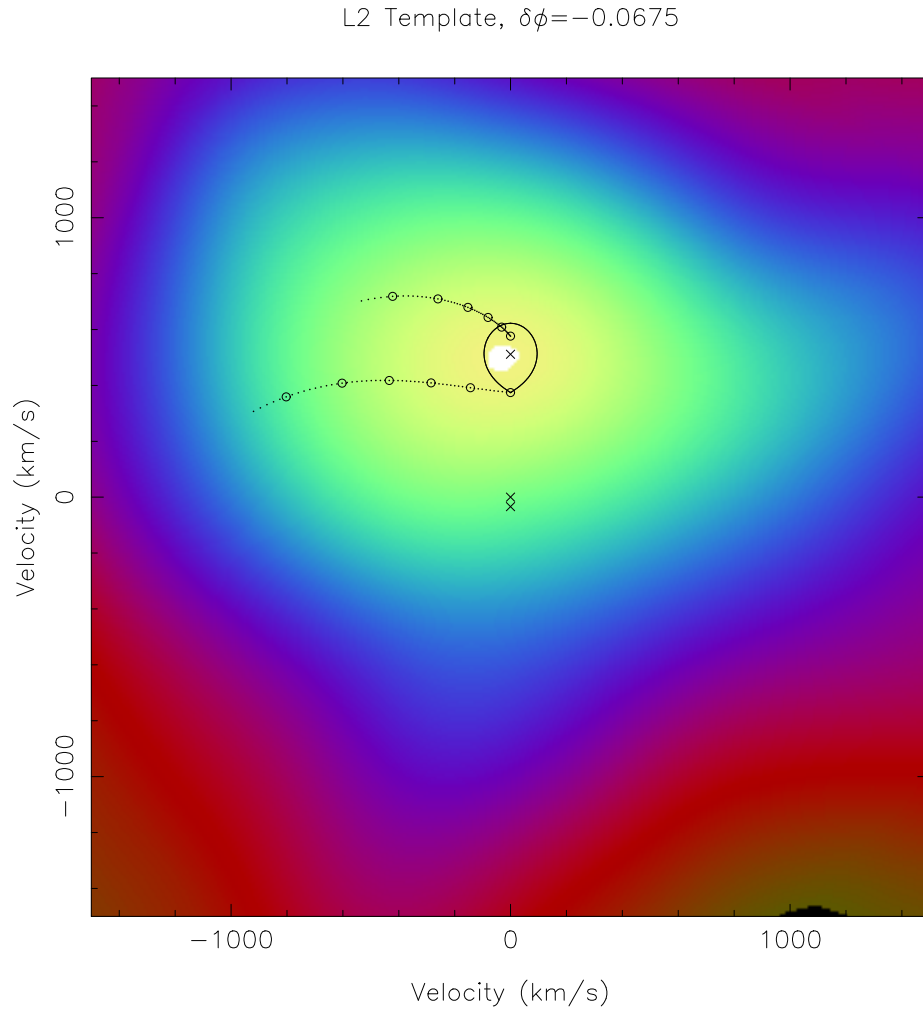


Figure 7.3: Skew map for SDSS 1433 produced using an L2 template. The predicted position of the secondary star and the path of the gas stream are marked. The crosses on the map are, from top to bottom, the centre of mass of the secondary star, the centre of mass of the system, and the centre of mass of the white dwarf. These cross, the Roche lobe of the secondary, the path of the gas stream (lower curve), the Keplerian velocity of the gas stream (upper curve) are plotted using the values of q , K_2 and K_w derived in Chapter 5.

7.2.3 The Spectral Type of the Secondary Star

The normalised spectra of SDSS 1433 were corrected for the orbital motion of the secondary star found in Chapter 5. The spectra were then averaged together in order to maximise the strength of any secondary star features present. The template spectra were broadened to match the rotational velocity of the secondary star, as described in §7.2.2. Both the target spectrum and template spectra were normalised by dividing by a first order polynomial, and then binned onto the same wavelength scale (11203-13450 Å in 624 pixels). The $P\beta$ emission line was masked.

Figure 7.4 shows the resulting plot of χ^2 versus spectral type (SpT), using a limb darkening coefficient of 0.5 and smoothing Gaussian of 70 km s⁻¹ (see §3.6). The points show a clear reduction in χ^2 from M5 to around L2.0. Beyond L2.0, χ^2 begins to increase. A 3rd order polynomial fit to the data indicates a minimum χ^2 corresponding to a spectral type of L2.0. The minimum spectral type was found to vary slightly depending on the level of smoothing used. In order to estimate the uncertainty in spectral type, the optimal subtraction routine was repeated with different levels of smoothing (15 – 200 km s⁻¹) and the resulting change in the minimum spectra type measured. The minimum was found to vary between L1.5 and L3.0, and so the uncertainty in spectral type was estimated to be ± 1.0 SpT.

A similar routine was performed by optimally subtracting the template spectra (M5-L8) from the L2.0 template, as shown in Figure 7.5. The resulting χ^2 -SpT plot has a similar shape to that of Figure 7.4. This indicates that the shapes of the χ^2 -SpT plots is due to differences in the line strengths of each template star.

7.2.4 Secondary Star Contributions

The optimal subtraction technique carried out in §7.2.3 suggested a spectral type of $L2.0 \pm 1.0$ for the secondary star in SDSS 1433. The optimal subtraction routine

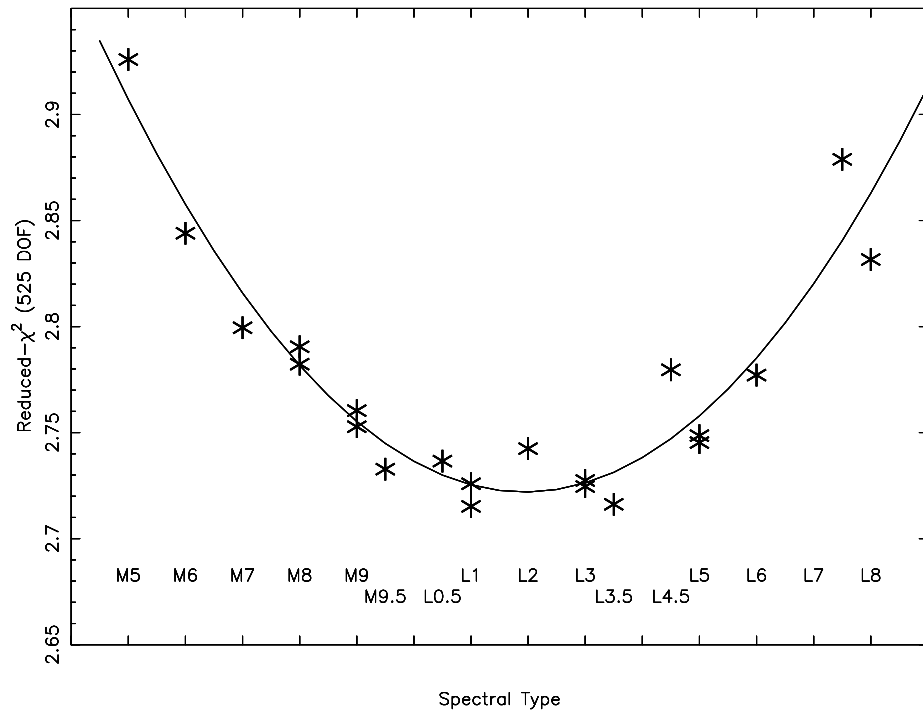


Figure 7.4: Reduced- χ^2 versus spectral type from the optimal subtraction technique.

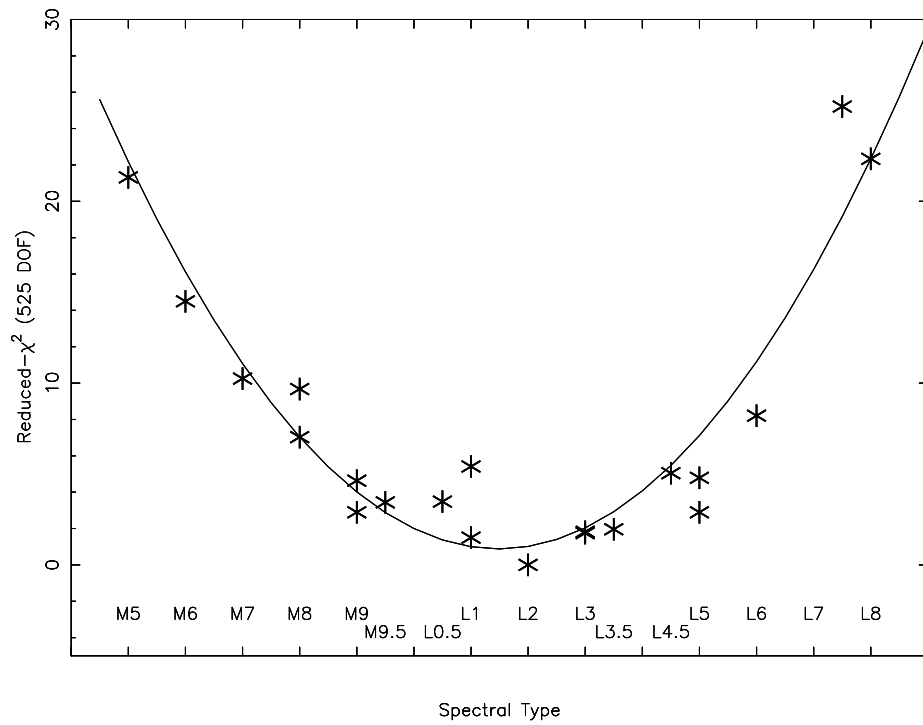


Figure 7.5: The variation in Reduced- χ^2 versus spectral type when optimally subtracting from the L2 template.

also provided an estimate of the fractional contribution of the secondary star to the total light in the system for a given template star (see §3.6). These contributions are based upon the absolute line strengths of the absorption features in each template. Therefore, by taking into account the brightness of the secondary star, it is possible to place an additional constraint on the spectral type as follows. The revised optimal model track of Knigge et al. (2011) provides theoretical absolute magnitudes for a number of Roche-lobe filling secondary stars of different spectral types. Scaling these magnitudes to take into account the size of the Roche-lobe in SDSS 1433 gives the expected absolute J-band magnitude of the secondary star in SDSS 1433 for a given spectral type. If a suitable measurement of the absolute magnitude of the system is available, then the expected fractional contribution of the secondary star, for a number of spectral types, can be calculated. Therefore, by comparing the theoretical fractional contributions to the contributions provided by the optimal subtraction technique, the contributions with the closest match will thus provide a good estimate of the spectral type of the secondary star.

The secondary stars of Knigge et al. (2011) have their surface brightness set by the effective temperature of an equivalent main sequence star, and are then corrected for the surface area of the Roche-lobe. The Roche-lobe depends upon the mass ratio of the system, and the polytropic index of the secondary star (Sirotkin & Kim, 2009). Because the sequence of Knigge et al. (2011) assumes a white dwarf mass of $0.75M_{\odot}$, whereas the modelling process in Chapter 5 suggests $\sim 0.87M_{\odot}$, the magnitudes obtained by Knigge et al. (2011) were adjusted using the mass ratio of $q = 0.0661 \pm 0.0007$ found in Chapter 5. An estimate of the absolute magnitude of the system was obtained using the distance, $d=226 \pm 12$ pc obtained through fitting the white dwarf atmospheres, also in Chapter 5, and the apparent J-band magnitude of the system as estimated from the average spectrum in §7.2.1 ($m_J = 18.47 \pm 0.09$). These figures provided an absolute magnitude of the system of $M_J = 11.70 \pm 0.20$.

This value is not corrected for differential slit losses between the target and the standard star and thus represents a fainter limit to the actual magnitude. Figure 7.6 shows a plot of the fractional contributions obtained for each L-template star from the optimal subtraction routine versus the expected contributions obtained via scaling the magnitudes of Knigge et al. (2011) for late M and L-type dwarfs. The observed contributions are approximately constant across the range of spectral types, whilst the expected contributions decrease rapidly until L0, and then steadily decrease towards later spectral types. Given the large uncertainties, it is not possible to constrain the convergence point. However, it is clear from Figure 7.6 that the two trends converge before L4.5 and later than L0.0. This suggests a spectral type of $L2.0 \pm 2.0$. This is in excellent agreement with the expected spectral type of $L2.0 \pm 1.0$ found in 7.2.3.

It should however be noted that the point of convergence is highly dependent on the absolute magnitude of the system. For example, if the apparent J-band magnitude estimated by UKIDSS photometry of $m_J = 17.698 \pm 0.022$ (Lawrence et al., 2007; Warren et al., 2007) were used, this would provide an absolute magnitude of the system of $M_J = 10.93 \pm 0.14$. This would shift the expected contributions downwards on the plot, resulting in a convergence point around M9.0 to L.0. Likewise, if the magnitude were in fact lower than previously derived, e.g. $M_J \approx 12.5$, the expected contributions would be shifted upwards on the plot, resulting in a convergence point around L6-L7.

7.3 Discussion

The presence of a red continuum, evidence of typical secondary star absorption lines, and the peak in the skew map at the expected radial velocity of the secondary star indicate that a genuine detection of the secondary star in SDSS 1433 has been made.

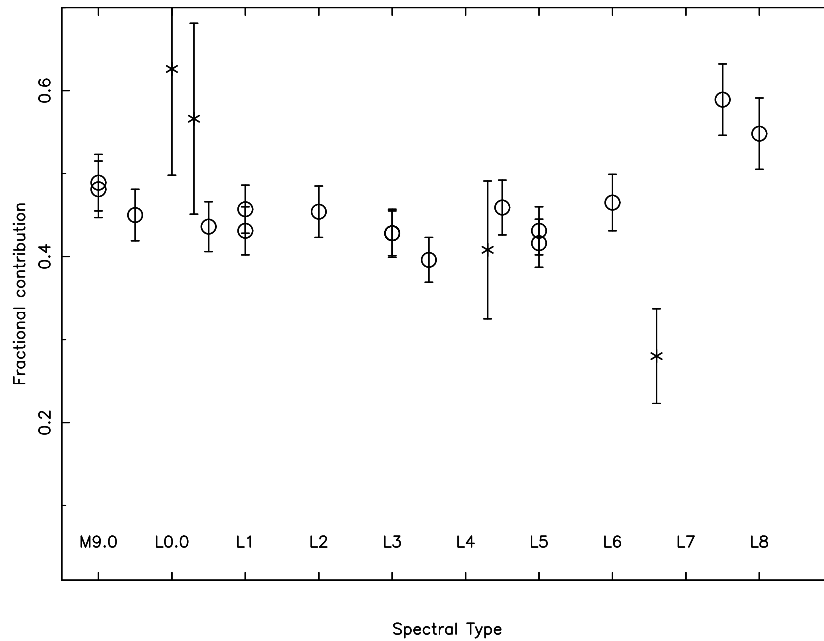


Figure 7.6: The observed fractional contribution (circles) of each template versus the theoretical contribution (crosses).

This is a significant result as this represents the first direct spectroscopic detection of a brown-dwarf like object in an accreting binary.

By using a variety of techniques, it was possible to estimate the spectral type of the secondary star. Visual inspection of the average spectrum reveals no evidence of H_2O or CH_4 absorption, which appears to rule out mid-to late T-types. Performing an optimal subtraction technique suggests a spectral type of $\text{L}2.0 \pm 1.0$, which is supported by the brightness of the secondary star relative to the total light of the system. This indicates that the secondary star in SDSS 1433 has a spectral type of early to mid L. This is slightly later than, but still consistent with, the spectral type predicted by the revised optimal model track of Knigge et al. (2011), which suggests a spectral type of L0 for a secondary star of similar mass to that in SDSS 1433.

Chapter 8

Conclusions and Future Work

8.1 Conclusions

In this thesis I have performed follow-up observations of a number of recently discovered eclipsing dwarf novae using high-speed, three-colour photometry. The primary aim of this was to identify systems that are suitable for light curve modelling and the determination of system parameters. This required the white dwarf and bright spot ingress and egress features to be clearly visible in their eclipse light curves. As shown in Chapter 1, system parameters are crucial to improving our understanding of evolutionary processes that inherent to not only CVs, but also many other areas of astrophysics (e.g. Warner, 1995; Knigge et al., 2011).

In total, eclipse light curves of 20 CVs were obtained, which in most cases, represents the best quality data currently available for these objects. Of the sample of 20 CVs, 6 showed clear white dwarf and bright spot ingress and egress features in their light curves and were therefore deemed suitable for modelling. This sample was supplemented with an additional 11 eclipsing CVs that had previously been analysed by other members of my group, taking the total sample size to 17. Of these CVs, 11 are short period ($P_{orb} \leq 95$ minutes), and one is within the period gap.

For each of these 17 objects the system parameters were determined by fitting a physical model of the binary to the observed light curve by χ^2 -minimisation. Two of the 11 short period systems appear to have evolved past the period minimum, which supports predictions that between 15 and 70 per cent of the CV population has evolved past the orbital period minimum. However, the secondary star masses and radii were found to be inconsistent with model predictions, with the majority of secondary stars being ~ 10 per cent larger than predicted. I show that this can be explained by either enhancing the mass transfer rate, or by modifying the stellar physics of the secondary star to take into account star spot coverage. Unfortunately, more precise secondary star masses for systems with orbital periods between 100 and 130 minutes are needed to choose between these alternatives.

The white dwarfs in this sample were found to show a strong tendency towards high masses. The high mass dominance seems to imply that the white dwarfs in CVs are not significantly eroded by nova outbursts, and may actually increase in mass over several nova cycles. There is no evidence for He-core white dwarfs within this study, despite predictions that between 40 and 80 percent of short period CVs should contain He-core white dwarfs.

Studies in the literature (e.g. Copperwheat et al., 2010) suggest that the photometric fitting technique is robust for systems with orbital periods above the period gap. However, for objects below the period gap, independent tests of the photometric technique are rare. I therefore obtained time-resolved spectroscopy for one of the objects for which system parameters were determined through photometric fitting. The object selected was CTCV 1300, which had an orbital period of 128.1 min.

The double-peaked nature of the Balmer and He I lines present in the average spectrum confirmed the presence of an accretion disc, whilst careful analysis of the Na I doublet absorption lines at 8189 Å revealed the radial velocity of the secondary star to be $K_2 = 378 \pm 6 \text{ km s}^{-1}$, and the rotational velocity of the secondary star

to be $v \sin i = 125 \pm 7 \text{ km s}^{-1}$. Using these measurements, I determined the mass of the white dwarf to be $M_w = 0.79 \pm 0.05 M_\odot$ and the mass of the M-type secondary star to be $M_2 = 0.198 \pm 0.029 M_\odot$. The radius of the secondary star was found to be $R_2 = 0.223 \pm 0.011 R_\odot$.

The system parameters determined through spectroscopic analysis were in good agreement with those previously determined using photometric techniques. This is significant, as these results support the validity and accuracy of the purely photometric mass determination technique in short period cataclysmic variables.

In the final section of this thesis, I attempted to use time-resolved spectroscopy of a period bouncing CV to make the first direct spectroscopic detection of a brown dwarf like secondary star in an accreting binary. The average spectrum of the system shows appears to show faint absorption features that are typical of absorption from the secondary star. A skew mapping technique was performed with an L2 template, which subsequently revealed a significant peak that is attributed to the radial velocity of the secondary star around $K_2 = 520 \pm 70 \text{ km s}^{-1}$. This is in good agreement with the value of K_2 found from photometric fitting, and therefore confirms that the absorption features are genuine. This also provides further verification of the photometric mass determination technique.

The spectral type of the secondary star was estimated using an optimal subtraction routine. This method suggests a spectral type of $L2.0 \pm 1.0$. Additional constraints on the spectral type were placed by visually inspecting the average spectrum for the presence of H_2O or CH_4 absorption. These features were not found, apparently ruling out mid-to late T-types. A final constraint was placed by using the contribution of the secondary star to the total J-band light. This technique appears to rule out mid-to late M-types and late L-types, suggesting a spectral type between L0 and L4.5, thus supporting the $L2.0 \pm 1.0$ found through optimal subtraction. These findings are broadly consistent with predictions, which suggest an expected spectral

type of around L0 for a secondary star of similar mass to SDSS 1433 (Knigge et al., 2011).

It is likely that with better signal-to-noise data it would be possible to constrain the spectral type of the secondary star in SDSS 1433 further. High resolution, time-resolved spectroscopy of SDSS 1433 is therefore highly desirable. With higher quality data, it should be possible to improve the precision of the spectral type estimation and also investigate the effects of irradiation.

8.2 Future Work

In this thesis I have shown how crucial accurate and precise system parameters are to our understanding of CVs. It is therefore important that the work presented in this thesis be continued. In Chapter 4, two objects (SDSS 1325 and SDSS 1524) had visible white dwarf and bright spot features in their light curves. On these occasions the low signal-to-noise of the data meant that it was not possible to constrain the MCMC model used to determine system parameters. However, it is likely that with more eclipses of these objects, and thus a greater signal-to-noise ratio, it would be possible to model the eclipses light curves as I have done for the 17 objects presented in Chapter 5. Likewise, a further 5 objects (SDSS 1250, SDSS 1555, CSS080227, GALEX 0035 and SDSS 1006) showed promising light curves that could yield masses in the future. More systems are also being discovered by Catalina Sky Survey (CSS) (Drake et al., 2009), so there is no shortage of candidate systems.

The highly active nature of the short period CV PHL 1445 warrants further study. The orbital period of the system is close to period minimum and so the high levels of flickering observed in Figure 4.1b are unexpected. Further monitoring with ULTRACAM is desirable for eclipse mapping purposes, so as to determine the source of the flickering and nature of the accretion disc.

Appendix A

Model Fits

The following tables list all of the model parameters found via the light curve modelling process. A detailed description of each parameter, and the modelling process, is given in §3.2.

Object	CTCV 1300	CTCV 1300	CTCV 1300	CTCV 1300	CTCV 1300	CTCV 1300	CTCV 1300
band	$u' 1$	$g' 1$	$r' 1$	$u' 2$	$g' 2$	$i' 2$	
q	0.240(23)	0.228(3)	0.218(4)	0.266(16)	0.259(3)	0.234(7)	
$\Delta\Phi$	0.0785(2)	0.0789(1)	0.0788(1)	0.0795(2)	0.0798(1)	0.0791(2)	
R_d/a	0.515(6)	0.519(1)	0.539(2)	0.469(13)	0.487(4)	0.509(6)	
R_w/a	0.0212(24)	0.0217(10)	0.0214(13)	0.0173(29)	0.0214(6)	0.0206(44)	
S/a	0.010(3)	0.012(1)	0.055(1)	0.014(5)	0.011(1)	0.014(2)	
Y	1.16(0.41)	0.79(0.07)	0.39(0.02)	0.07(0.09)	0.13(0.05)	0.01(0.02)	
Z	0.69(0.08)	0.63(0.02)	1.03(0.01)	0.59(0.09)	0.52(0.02)	0.48(0.02)	
θ_{az}	119(4)	132(1)	125(1)	61(12)	121(3)	131(4)	
θ_{tilt}	171(3)	175(1)	169(2)	172(1)	173(1)	170(4)	
θ_{yaw}	14(5)	-6(1)	4(2)	76(13)	9(3)	8(6)	
f_{iso}	0.31(0.01)	0.26(0.01)	0.26(0.01)	0.44(0.04)	0.30(0.01)	0.35(0.02)	
b	-0.13(0.38)	-0.20(0.25)	-0.35(0.19)	1.02(0.40)	0.85(0.23)	1.47(0.24)	
ϕ_0 ($\times 10^{-5}$)	-3(11)	-17(3)	-25(3)	-49(10)	-44(2)	-40(9)	
White Dwarf (mJy)	0.0246(4)	0.0402(1)	0.338(2)	0.0231(6)	0.0405(2)	0.0051(1)	
Disc (mJy)	0.0158(6)	0.0162(2)	0.0401(4)	0.0178(9)	0.0153(3)	0.0046(2)	
Secondary Star (mJy)	0.0007(3)	0.0032(1)	0.0090(2)	0.0044(3)	0.0063(1)	0.0150(1)	
Bright Spot (mJy)	0.0593(2)	0.0914(1)	0.0913(1)	0.0625(3)	0.0943(1)	0.0158(1)	
U_w	0.409	0.308	0.259	0.409	0.308	0.223	

Table A.1a: The model parameters found for CTCV 1300.

Object	CTCV 2354	CTCV 2354	CTCV 2354	CTCV 2354	SDSS 1152	SDSS 1152	SDSS 1152	SDSS 1152
band	u'	g'	r'	u'	g'	r'	u'	r'
q	0.112(1)	0.107(1)	0.107(2)	—	0.160(9)	0.151(8)	—	—
$\Delta\Phi$	0.0655(2)	0.0645(2)	0.0642(1)	—	0.0574(3)	0.0580(5)	—	—
R_d/a	0.436(6)	0.475(3)	0.462(3)	—	0.448(17)	0.442(11)	—	—
R_w/a	0.0280(31)	0.0163(16)	0.0160(16)	—	0.0324(23)	0.0361(39)	—	—
S/a	0.021(6)	0.029(4)	0.020(2)	—	0.042(8)	0.108(45)	—	—
Y	0.02(0.09)	0.04(0.07)	0.02(0.05)	—	2.46(1.32)	2.73(1.25)	—	—
Z	1.00(F)	1.00(F)	1.00(F)	—	2.27(0.47)	2.87(0.92)	—	—
θ_{az}	82(12)	121(5)	80(2)	—	101(13)	153(15)	—	—
θ_{ilt}	46(78)	146(68)	169(11)	—	116(46)	95(68)	—	—
θ_{yaw}	0(F)	0(F)	0(F)	—	36(14)	-9(21)	—	—
f_{iso}	0.99(0.05)	1.00(0.01)	0.00(0.03)	—	0.28(0.09)	0.37(0.05)	—	—
b	0.04(0.07)	1.47(0.02)	1.41(4)	—	0.55(0.50)	0.28(0.51)	—	—
ϕ_0 ($\times 10^{-5}$)	56(12)	-4(8)	-6(8)	—	16(10)	-19(19)	—	—
White Dwarf (mJy)	0.0103(1)	0.0148(1)	0.0074(3)	0.0189(13)	0.0338(5)	0.0279(7)	—	—
Disc (mJy)	0.0302(1)	0.0251(1)	0.0364(4)	—	0.0005(8)	0.0056(11)	—	—
Secondary Star (mJy)	0(0)	0(0)	0.0031(2)	—	0.0081(4)	0.0120(3)	—	—
Bright Spot (mJy)	0.0028(1)	0.0025(1)	0.0039(1)	—	0.0179(2)	0.0192(3)	—	—
U_w	0.492	0.389	0.326	0.473	0.372	0.313	—	—

Table A.1b: The model parameters found for CTCV 2354 and SDSS 1152.

Object	OU Vir	OU Vir	OU Vir	DV UMa	DV UMa	DV UMa	DV UMa
	u'	g'	r'	u'	g'	i'	
band							
q	0.0163(3)	0.0165(2)	0.0161(3)	0.163(13)	0.180(4)	0.174(9)	
$\Delta\Phi$	0.0416(3)	0.0427(1)	0.0422(3)	0.0635(2)	0.0634(1)	0.0629(2)	
R_d/a	0.384(9)	0.372(4)	0.372(5)	0.465(8)	0.465(8)	0.456(4)	
R_w/a	0.0282(30)	0.0253(6)	0.0212(28)	0.0125(23)	0.0125(6)	0.0083(26)	
S/a	0.108(27)	0.130(21)	0.200(20)	0.007(15)	0.010(3)	0.009(2)	
Y	1.87(1.23)	1.50(0.92)	3.95(0.90)	2.11(1.30)	0.43(0.17)	1.13(0.49)	
Z	2.76(0.49)	2.35(0.30)	2.74(0.16)	0.85(0.41)	0.67(0.05)	0.67(0.05)	
θ_{az}	166(4)	169(1)	173(2)	110(11)	115(2)	130(5)	
θ_{tilt}	160(4)	44(3)	161(4)	60(49)	137(6)	12(3)	
θ_{yaw}	-88(14)	11(1)	-3(14)	30(14)	14(3)	33(9)	
f_{iso}	0.42(0.40)	0.41(0.01)	0.51(0.06)	0.14(0.02)	0.20(0.01)	0.11(0.06)	
b	1.50(0.07)	1.50(0.03)	1.38(0.10)	1.48(0.25)	1.48(0.08)	1.47(0.13)	
$\phi_0 (\times 10^{-5})$	-10(12)	-33(4)	76(10)	-32(9)	-27(5)	4(13)	
White Dwarf (mJy)	0.1588(45)	0.0901(8)	0.0258(9)	0.0136(4)	0.0152(2)	0.0099(4)	
Disc (mJy)	0.1694(74)	0.0483(12)	0.1043(15)	0.0047(6)	0.0044(2)	0.0107(5)	
Secondary Star (mJy)	0.0724(36)	0.0442(6)	0.0382(4)	0.0020(3)	0.0023(1)	0.0506(2)	
Bright Spot (mJy)	0.0693(15)	0.0918(3)	0.0693(6)	0.0263(2)	0.0339(1)	0.0474(2)	
U_w	0.316	0.233	0.197	0.341	0.248	0.183	

Table A.1c: The model parameters found for OU Vir and DV UMa.

Object	XZ Eri	XZ Eri	XZ Eri	SDSS 1433	SDSS 1433	SDSS 1433	SDSS 1433
band	u'	g'	r'	u'	g'	r'	r'
q	0.113(16)	0.120(8)	0.122(8)	0.069(8)	0.067(1)	0.064(2)	0.064(2)
$\Delta\Phi$	0.0344(1)	0.0337(2)	0.0334(4)	0.0452(1)	0.0453(1)	0.0452(1)	0.0452(1)
R_d/a	0.449(39)	0.412(8)	0.427(8)	0.465(12)	0.462(2)	0.465(3)	0.465(3)
R_w/a	0.0277(40)	0.0239(8)	0.0268(12)	0.0218(17)	0.0217(3)	0.0221(4)	0.0221(4)
S/a	0.029(14)	0.014(5)	0.027(1)	0.101(27)	0.085(12)	0.073(20)	0.073(20)
Y	0.12(1.56)	1.86(1.48)	0.05(0.49)	0.28(1.49)	3.39(0.74)	2.80(1.04)	2.80(1.04)
Z	1.00(F)	1.00(F)	1.00(F)	2.73(0.62)	2.33(0.41)	1.76(0.35)	1.76(0.35)
θ_{az}	142(8)	136(6)	138(5)	97(17)	136(2)	135(4)	135(4)
θ_{ilt}	132(46)	150(10)	156(9)	86(63)	26(40)	160(24)	160(24)
θ_{yaw}	0(F)	9(F)	0(F)	53(21)	40(6)	1(12)	1(12)
f_{iso}	0.21(0.04)	0.17(0.01)	0.21(0.01)	0.42(0.06)	0.37(0.02)	0.52(0.03)	0.52(0.03)
b	0.38(0.54)	0.09(0.59)	1.04(0.48)	1.42(0.17)	1.23(0.10)	1.14(0.08)	1.14(0.08)
$\phi_0 (\times 10^{-5})$	-179(37)	-168(10)	-169(13)	-56(7)	-46(2)	-48(3)	-48(3)
White Dwarf (mJy)	0.0545(1)	0.0610(4)	0.0540(8)	0.0738(1)	0.1022(2)	0.0818(3)	0.0818(3)
Disc (mJy)	0.0000(0)	0.0024(14)	0.0062(17)	0.0407(1)	0.0221(4)	0.0448(6)	0.0448(6)
Secondary Star (mJy)	0.0047(1)	0.0065(13)	0.0052(13)	0.0000(0)	0.0038(3)	0.0094(5)	0.0094(5)
Bright Spot (mJy)	0.0314(1)	0.0424(3)	0.0413(3)	0.0434(1)	0.0386(2)	0.0353(2)	0.0353(2)
U_w	0.384	0.275	0.236	0.436	0.319	0.274	0.274

Table A.1d: The model parameters found for XZ Eri and SDSS 1433.

Object	SDSS 1035	SDSS 1035	SDSS 1035	SDSS 1507	SDSS 1507	SDSS 1507
band	u'	g'	r'	u'	g'	r'
q	0.050(5)	0.059(4)	0.054(2)	0.069(9)	0.066(2)	0.075(5)
$\Delta\Phi$	0.0404(2)	0.0404(4)	0.0404(1)	0.0405(3)	0.0406(1)	0.0406(1)
R_d/a	0.483(30)	0.458(9)	0.465(8)	0.421(17)	0.420(2)	0.415(3)
R_w/a	0.0211(16)	0.0215(4)	0.0226(6)	0.0234(22)	0.0233(4)	0.0222(6)
S/a	0.073(34)	0.143(29)	0.080(45)	0.051(25)	0.017(14)	0.055(18)
Y	2.06(1.64)	2.56(1.43)	2.83(1.32)	0.17(1.48)	1.33(1.41)	0.10(0.29)
Z	1.00(F)	2.98(0.94)	1.48(0.72)	1.87(0.86)	1.13(0.57)	1.32(0.36)
θ_{az}	158(3)	159(21)	159(2)	89(26)	125(7)	132(4)
θ_{tilt}	88(41)	172(1)	169(6)	19(52)	171(1)	164(6)
θ_{yaw}	1(F)	-30(20)	-21(7)	85(21)	-1(7)	4(9)
f_{iso}	0.48(0.02)	0.49(0.01)	0.47(0.02)	0.31(0.09)	0.34(0.01)	0.35(0.01)
b	0.15(0.49)	1.03(0.68)	-1.43(0.31)	0.01(0.50)	1.44(0.26)	0.51(0.42)
ϕ_0 ($\times 10^{-5}$)	8(21)	-13(3)	-16(5)	-93(14)	-76(2)	-72(5)
White Dwarf (mJy)	0.0667(1)	0.0886(1)	0.0835(3)	0.0859(1)	0.1269(4)	0.1079(4)
Disc (mJy)	0.0050(1)	0.0000(0)	0.0081(8)	0.0100(1)	0.0072(7)	0.0194(9)
Secondary Star (mJy)	0.0000(0)	0.0089(1)	0.0042(9)	0.0000(0)	0.0056(4)	0.0056(3)
Bright Spot (mJy)	0.0305(1)	0.0197(1)	0.0255(2)	0.0624(1)	0.0557(2)	0.0654(3)
U_w	0.531	0.426	0.350	0.497	0.388	0.326

Table A.1e: The model parameters found for SDSS 1035 and SDSS 1507.

Object	SDSS 1227	SDSS 1227	SDSS 1227	SDSS 1502	SDSS 1502	SDSS 1502
band	u'	g'	r'	u'	g'	r'
q	0.125(14)	0.110(3)	0.112(3)	0.122(13)	0.109(1)	0.112(1)
$\Delta\Phi$	0.0565(5)	0.0567(1)	0.0564(2)	0.0644(2)	0.0645(1)	0.0645(1)
R_d/a	0.370(23)	0.388(8)	0.394(8)	0.346(35)	0.402(3)	0.364(2)
R_w/a	0.0226(47)	0.0232(9)	0.0220(24)	0.0218(30)	0.0276(3)	0.0279(4)
S/a	0.078(44)	0.190(35)	0.079(55)	0.037(15)	0.073(3)	0.028(2)
Y	0.62(1.53)	3.84(1.00)	2.67(1.44)	0.69(0.43)	0.69(0.06)	0.91(0.18)
Z	2.74(0.95)	2.87(0.29)	1.69(0.58)	1.00(F)	1.09(0.03)	1.00(F)
θ_{az}	147(35)	164(2)	162(5)	111(5)	163(1)	115(1)
θ_{tilt}	172(3)	117(43)	19(20)	176(2)	178(1)	178(1)
θ_{yaw}	24(49)	-2(6)	18(9)	0(F)	-45(2)	0(F)
f_{iso}	0.24(0.04)	0.16(0.01)	0.16(0.01)	0.42(0.04)	0.31(0.01)	0.36(0.01)
b	0.89(0.54)	1.18(0.85)	0.33(0.82)	0.77(0.18)	0.77(0.04)	0.31(0.07)
ϕ_0 ($\times 10^{-5}$)	9(18)	5(4)	13(8)	-26(9)	-11(1)	-13(2)
White Dwarf (mJy)	0.0495(1)	0.0597(6)	0.0438(7)	0.1227(22)	0.2205(1)	0.1762(5)
Disc (mJy)	0.0000(0)	0.0052(8)	0.0151(11)	0.1632(31)	0.0851(1)	0.1534(8)
Secondary Star (mJy)	0.0100(1)	0.0041(4)	0.0036(7)	0.0041(11)	0.0000(0)	0.0022(4)
Bright Spot (mJy)	0.0445(1)	0.0763(3)	0.0775(5)	0.1056(10)	0.1179(1)	0.1214(3)
U_w	0.367	0.267	0.227	0.449	0.335	0.287

Table A.1f: The model parameters found for SDSS 1227 and SDSS 1502.

Object	SDSS 1702	SDSS 1702	SDSS 1702	SDSS 0903	SDSS 0903	SDSS 0903	SDSS 0903
band	u'	g'	r'	u'	g'	r'	r'
q	0.267(17)	0.242(8)	0.252(10)	0.109(7)	0.106(9)	0.121(7)	0.121(7)
$\Delta\Phi$	0.0710(3)	0.0712(1)	0.0710(2)	0.0475(1)	0.0475(1)	0.0473(1)	0.0473(1)
R_d/a	0.405(10)	0.410(11)	0.413(5)	0.406(11)	0.409(11)	0.414(14)	0.414(14)
R_w/a	0.0146(39)	0.0149(12)	0.0150(21)	0.0217(9)	0.0222(6)	0.0190(9)	0.0190(9)
S/a	0.010(13)	0.013(5)	0.014(6)	0.030(13)	0.030(15)	0.050(28)	0.050(28)
Y	2.73(1.67)	1.63(0.50)	1.01(0.44)	1.01(1.72)	0.70(1.87)	0.79(0.80)	0.79(0.80)
Z	0.86(0.24)	0.92(0.10)	0.79(0.12)	1.00(F)	1.00(F)	1.00(F)	1.00(F)
θ_{az}	114(12)	117(14)	125(7)	161(6)	163(8)	160(3)	160(3)
θ_{tilt}	64(48)	59(55)	85(45)	155(27)	154(32)	140(42)	140(42)
θ_{yaw}	25(16)	52(17)	52(12)	0(F)	0(F)	0(F)	0(F)
f_{iso}	0.36(0.15)	0.31(0.05)	0.29(0.04)	0.50(0.04)	0.50(0.05)	0.44(0.06)	0.44(0.06)
b	1.20(0.22)	1.15(0.08)	0.98(0.08)	1.29(0.24)	1.28(0.22)	0.46(0.35)	0.46(0.35)
ϕ_0 ($\times 10^{-5}$)	-51(13)	-61(6)	-53(8)	-6(4)	-6(4)	0(5)	0(5)
White Dwarf (mJy)	0.0677(16)	0.0925(9)	0.0633(12)	0.0465(12)	0.0576(4)	0.0487(4)	0.0487(4)
Disc (mJy)	0.1102(22)	0.0869(12)	0.1407(16)	0.0254(20)	0.0134(7)	0.0231(7)	0.0231(7)
Secondary Star (mJy)	0.0153(5)	0.0159(2)	0.0631(4)	0.0090(8)	0.0047(4)	0.0058(5)	0.0058(5)
Bright Spot (mJy)	0.0969(8)	0.1577(8)	0.2014(13)	0.0177(6)	0.0092(2)	0.0123(3)	0.0123(3)
U_w	0.378	0.267	0.227	0.348	0.312	0.269	0.269

Table A.1g: The model parameters found for SDSS 1702 and SDSS 0903.

Object	SDSS 1501	SDSS 1501	SDSS 1501	SDSS 1501	CSS080623	CSS080623	CSS080623
band	u'	g'	r'	u'	g'	r'	r'
q	—	0.132(32)	0.114(27)	0.114(14)	0.143(4)	0.135(11)	0.135(11)
$\Delta\Phi$	—	0.0488(1)	0.0486(3)	0.0384(7)	0.0384(2)	0.0386(3)	0.0386(3)
R_d/a	—	0.477(50)	0.457(34)	0.490(29)	0.457(3)	0.459(6)	0.459(6)
R_w/a	—	0.0243(21)	0.0246(27)	0.0251(48)	0.0272(13)	0.0287(27)	0.0287(27)
S/a	—	0.086(45)	0.131(81)	0.046(9)	0.010(1)	0.015(26)	0.015(26)
Y	—	0.25(1.18)	1.17(1.61)	2.00(F)	0.02(0.14)	0.23(0.31)	0.23(0.31)
Z	—	2.24(0.76)	1.99(0.92)	1.00(F)	0.43(0.10)	0.58(0.28)	0.58(0.28)
θ_{az}	—	108(33)	150(39)	139(3)	130(3)	127(4)	127(4)
θ_{tilt}	—	25(57)	81(52)	90(F)	85(13)	72(14)	72(14)
θ_{yaw}	—	47(36)	25(39)	0(F)	11(3)	16(6)	16(6)
f_{iso}	—	0.43(0.20)	0.38(0.07)	0.23(0.06)	0.25(0.01)	0.27(0.01)	0.27(0.01)
b	—	0.62(0.62)	1.16(0.67)	1.35(0.44)	1.34(0.67)	0.14(0.24)	0.14(0.24)
$\phi_0 (\times 10^{-5})$	—	18(7)	30(13)	-58(33)	-37(8)	-63(15)	-63(15)
White Dwarf (mJy)	0.0346(23)	0.0487(5)	0.0436(9)	0.0237(13)	0.0339(1)	0.0332(4)	0.0332(4)
Disc (mJy)	—	0.0057(10)	0.0056(16)	0.0078(26)	0.0051(1)	0.0080(10)	0.0080(10)
Secondary Star (mJy)	—	0.0070(5)	0.0052(7)	0.0003(21)	0.0000(1)	0.0022(9)	0.0022(9)
Bright Spot (mJy)	—	0.0076(3)	0.0131(6)	0.0268(5)	0.0362(1)	0.0391(2)	0.0391(2)
U_w	0.443	0.329	0.281	0.536	0.447	0.364	0.364

Table A.1h: The model parameters found for SDSS 1501 and CSS080623.

Object	SDSS 0901		SDSS 0901		PHL 1445		PHL 1445		PHL 1445	
band	u'	g'	r'	u'	g'	r'	u'	g'	r'	r'
q	—	0.200(6)	0.202(14)	—	—	—	—	0.091(10)	0.088(8)	0.088(8)
$\Delta\Phi$	—	0.0574(2)	0.0577(2)	—	—	—	—	0.0542(2)	0.0548(4)	0.0548(4)
R_d/a	—	0.455(4)	0.444(0.05)	—	—	—	—	0.350(13)	0.339(20)	0.339(20)
R_w/a	—	0.0216(19)	0.0211(16)	—	—	—	—	0.0241(23)	0.0232(48)	0.0232(48)
S/a	—	0.009(4)	0.008(12)	—	—	—	—	0.036(31)	0.053(55)	0.053(55)
Y	—	0.11(0.17)	0.77(0.39)	—	—	—	—	1.18(1.25)	0.86(1.74)	0.86(1.74)
Z	—	0.65(0.14)	0.68(0.24)	—	—	—	—	1.60(0.62)	1.68(0.76)	1.68(0.76)
θ_{az}	—	117(7)	119(7)	—	—	—	—	126(23)	129(24)	129(24)
θ_{tilt}	—	126(6)	133(9)	—	—	—	—	170(43)	38(73)	38(73)
θ_{yaw}	—	18(8)	14(9)	—	—	—	—	-6(24)	-25(25)	-25(25)
f_{iso}	—	0.21(0.01)	0.21(0.01)	—	—	—	—	0.56(0.05)	0.02(0.17)	0.02(0.17)
b	—	0.69(0.41)	0.13(0.19)	—	—	—	—	1.40(0.09)	1.17(0.23)	1.17(0.23)
$\phi_0 (\times 10^{-5})$	—	-10(6)	13(8)	—	—	—	—	27(10)	8(25)	8(25)
White Dwarf (mJy)	0.0260(12)	0.0246(2)	0.0205(3)	0.0625(81)	0.1213(21)	0.1213(21)	0.0124(20)	0.1213(21)	0.0124(20)	0.0124(20)
Disc (mJy)	—	0.0084(4)	0.0135(5)	—	—	—	—	0.0891(27)	0.0942(3)	0.0942(3)
Secondary Star (mJy)	—	0.0013(2)	0.0057(3)	—	—	—	—	0.0082(9)	0.0053(12)	0.0053(12)
Bright Spot (mJy)	—	0.0251(1)	0.0250(1)	—	—	—	—	0.0363(7)	0.0359(6)	0.0359(6)
U_w	0.333	0.245	0.208	0.479	0.371	0.371	0.479	0.371	0.313	0.313

Table A.1i: The model parameters found for SDSS 0901 and PHL 1445.

Appendix B

CTCV 1300 Double Solution

The following table lists the final system parameters for CTCV 1300, derived using both model solutions in Table A.1a. The parameters obtained via spectroscopic methods are also shown for comparison.

	Night 1 MCMC	Night 2 MCMC	X-Shooter Monte Carlo
q	0.224(2)	0.255(3)	0.252(25)
M_w/M_\odot	0.73(1)	0.75(2)	0.79(5)
R_w/R_\odot	0.0112(1)	0.0110(2)	—
M_2/M_\odot	0.163(3)	0.192(5)	0.198(29)
R_2/R_\odot	0.209(1)	0.221(2)	0.223(11)
a/R_\odot	0.806(4)	0.821(6)	0.834(20)
K_w (kms $^{-1}$)	84(1)	95(1)	95(9)
K_2 (kms $^{-1}$)	374(2)	370(2)	378(6)
i°	87.1(2)	85.5(2)	85.7(1.5)

Table B.1: The system parameters of CTCV 1300, found by fitting the photometric model to both nights individually, and via X-Shooter spectroscopy.

Appendix C

Calculating the Required Rate of Change of Orbital Period

In Chapter 7, it was found that a phase lag of $\phi = 0.09$ had arisen between the time of mid-eclipse predicted by the linear ephemeris of Littlefair et al. (2008), and a lone observation obtained 13th March 2012. The mid-eclipse time for this new observation was measured by eye to be HMJD 56000.2169(5). The best matching cycle number using the ephemeris of Littlefair et al. (2008) was 39488. The eclipse times published in Szkody et al. (2007) and Littlefair et al. (2008) were combined with this new eclipse time and fit with a quadratic ephemeris in the form of

$$T_{mid}(HJD) = T_0(HJD) + P_{orb}E + CE^2, \quad (\text{C.1})$$

where T_{mid} , E , P_{orb} and T_0 are the same as for Equation 3.1, and C is the change in orbital period per cycle. This yielded values of $T_0(HJD) = 53858.356166(18)$, $P_{orb} = 0.054240648(4)\text{d}$ and $C = (3.9 \pm 0.4) \times 10^{-12}\text{d hr}^{-2}$. From this, \dot{P} was calculated as follows.

From Equation C.1, the instantaneous orbital period at cycle E, P_E , is given by

$$P_E = \frac{dT}{dE} = P_{orb} + 2CE, \quad (\text{C.2})$$

which in turn gives

$$\frac{dP_E}{dT} = \dot{P} = \frac{dE}{dT} \times \frac{dP_E}{dE} = \frac{2C}{P_E}. \quad (\text{C.3})$$

From Equation C.2, it can be seen that for the values of P_{orb} and C obtained for SDSS 1433, $P_{orb} \approx P_E$. Substituting P_{orb} and C into Equation C.3 therefore gives $\dot{P} = (5.2 \pm 0.5) \times 10^{-8}$ days yr⁻¹.

Bibliography

Andronov N., Pinsonneault M., Sills A., 2003, *ApJ*, 582, 358

Aviles A., Zharikov S., Tovmassian G., Michel R., Tapia M., Roth M., Neustroev V., Zurita C., Andreev M., Sergeev A., Pavlenko E., Tsymbal V., Anupama G. C., Kamath U. S., Sahu D. K., 2010, *ApJ*, 711, 389

Bailey J., 1979, *MNRAS*, 187, 645

Balbus S. A., Hawley J. F., 1991, *ApJ*, 376, 214

Baraffe I., Kolb U., 2000, *MNRAS*, 318, 354

Barnes S. A., 2003, *ApJ*, 586, 464

Bergeron P., Wesemael F., Beauchamp A., 1995, *PASP*, 107, 1047

Beuermann K., Baraffe I., Kolb U., Weichhold M., 1998, *A&A*, 339, 518

Billington I., Marsh T. R., Dhillon V. S., 1996, *MNRAS*, 278, 673

Binney J., Merrifield M., 1998, *Galactic Astronomy*

Bohlin R. C., Colina L., Finley D. S., 1995, *AJ*, 110, 1316

Bristow P., Kerber F., Rosa M. R., Vernet J., Goldoni P., Spanò P., Modigliani A., 2008, in *Society of Photo-Optical Instrumentation Engineers (SPIE) Conference*

- Series Vol. 7014 of Society of Photo-Optical Instrumentation Engineers (SPIE)
Conference Series, X-shooter physical model
- Burgasser A. J., 2007, *ApJ*, 659, 655
- Carroll B. W., Ostlie D. A., 1996, *An Introduction to Modern Astrophysics*
- Casella G., George E., 1992, *The American Statistician*, 46, 167
- Chabrier G., Baraffe I., 1997, *A&A*, 327, 1039
- Chabrier G., Gallardo J., Baraffe I., 2007, *A&A*, 472, L17
- Charbonneau P., MacGregor K. B., 1997, *ApJ*, 486, 502
- Cook M. C., Warner B., 1984, *MNRAS*, 207, 705
- Copperwheat C. M., Marsh T. R., Dhillon V. S., Littlefair S. P., Hickman R.,
Gänsicke B. T., Southworth J., 2010, *MNRAS*, 402, 1824
- Copperwheat C. M., Marsh T. R., Parsons S. G., Hickman R., Steeghs D., Breedt
E., Dhillon V. S., Littlefair S. P., Savoury C., 2012, *MNRAS*, 421, 149
- Cushing M. C., Rayner J. T., Vacca W. D., 2005, *ApJ*, 623, 1115
- Cutri R. et al., 2003, *VizieR Online Data Catalog*, 2246, 0
- Davis P. J., Kolb U., Willems B., Gänsicke B. T., 2008, *MNRAS*, 389, 1563
- D’Cruz N. L., Dorman B., Rood R. T., O’Connell R. W., 1996, *ApJ*, 466, 359
- della Valle M., Duerbeck H. W., 1993, *A&A*, 271, 175
- Deshpande R. et al., 2012, *AJ*, 144, 99
- Denisenko D. V., Kryachko T. V., Satovskiy B. L., 2008, *The Astronomer’s Telegram*,
1640, 1

- Dhillon V. S., 1996, in Evans A., Wood J. H., eds, IAU Colloq. 158: Cataclysmic Variables and Related Objects Vol. 208 of Astrophysics and Space Science Library, The Nova-like variables. p. 3
- Dhillon V. S., Marsh T. R., 1993, in Regev O., Shaviv G., eds, Cataclysmic Variables and Related Physics Vol. 10 of Annals of the Israel Physical Society, Infrared Spectra of Cataclysmic Variables. p. 34
- Dhillon V. S., Marsh T. R., Copperwheat C., Bezawada N., Ives D., Vick A., O'Brien K., 2008, in Phelan D., Ryan O., Shearer A., eds, High Time Resolution Astrophysics: The Universe at Sub-Second Timescales Vol. 984 of American Institute of Physics Conference Series, ULTRASPEC: High-speed spectroscopy with zero readout noise. pp 132–139
- Dhillon V. S., Marsh T. R., Stevenson M. J., Atkinson D. C., Kerry P., Peacocke P. T., Vick A. J. A., Beard S. M., Ives D. J., Lunney D. W., McLay S. A., Tierney C. J., Kelly J., Littlefair S. P., Nicholson R., Pashley R., Harlaftis E. T., O'Brien K., 2007, MNRAS, 378, 825
- Dhillon V. S., Smith D. A., Marsh T. R., 2012, ArXiv e-prints
- Dillon M., Gänsicke B. T., Aungwerojwit A., Rodríguez-Gil P., Marsh T. R., Barros S. C. C., Szkody P., Brady S., Krajci T., Oksanen A., 2008, MNRAS, 386, 1568
- Drake A. J., Djorgovski S. G., Mahabal A., Beshore E., Larson S., Graham M. J., Williams R., Christensen E., Catelan M., Boattini A., Gibbs A., Hill R., Kowalski R., 2009, ApJ, 696, 870
- Duquennoy A., Mayor M., 1991, A&A, 248, 485
- Eggleton P. P., 1983, ApJ, 268, 368

- Epelstain N., Yaron O., Kovetz A., Prialnik D., 2007, MNRAS, 374, 1449
- Feline W., 2005, PhD thesis, The University of Sheffield
- Feline W. J., Dhillon V. S., Marsh T. R., Brinkworth C. S., 2004, MNRAS, 355, 1
- Feline W. J., Dhillon V. S., Marsh T. R., Stevenson M. J., Watson C. A., Brinkworth C. S., 2004, MNRAS, 347, 1173
- Ford E. B., 2005, AJ, 129, 1706
- Ford E. B., 2006, ApJ, 642, 505
- Friend M. T., Smith R. C., Martin J. S., Jones D. H. P., 1988, MNRAS, 233, 451
- Fukugita M., Ichikawa T., Gunn J. E., Doi M., Shimasaku K., Schneider D. P., 1996, AJ, 111, 1748
- Gänsicke B. et al., 2006, MNRAS, 365, 969
- Gänsicke B. et al., 2009, MNRAS, 397, 2170
- Gänsicke B. T., Beuermann K., de Martino D., 1995, A&A, 303, 127
- Gariety M. J., Ringwald F. A., 2012, NA, 17, 154
- Gilks W., Richardson S., Spiegelhalter D., 1995, Markov Chain Monte Carlo in Practice. Chapman & Hall/CRC, London
- Gizis J. E., Reid I. N., Hawley S. L., 2002, AJ, 123, 3356
- Gregory P. C., 2007, MNRAS, 381, 1607
- Grether D., Lineweaver C. H., 2006, ApJ, 640, 1051
- Hamada T., Salpeter E. E., 1961, ApJ, 134, 683

- Hamuy M., Suntzeff N. B., Heathcote S. R., Walker A. R., Gigoux P., Phillips M. M., 1994, *PASP*, 106, 566
- Hanuschik R. W., 2003, *A&A*, 407, 1157
- Hastings W., 1970, *Biometrika*, 57, 97
- Hawley J. F., Balbus S. A., 1998, in Howell S., Kuulkers E., Woodward C., eds, *Wild Stars in the Old West Vol. 137 of Astronomical Society of the Pacific Conference Series, Anomalous Viscosity in Accretion Disks*. p. 273
- Hekker S. et al., 2011, *A&A*, 530, A100
- Hellier C., 2001, *Cataclysmic Variable Stars*
- Hickman R., 2011, PhD thesis, The University of Warwick
- Hjellming M. S., Webbink R. F., 1987, *ApJ*, 318, 794
- Hodapp K. W., Jensen J. B., Irwin E. M., Yamada H., Chung R., Fletcher K., Robertson L., Hora J. L., Simons D. A., Mays W., Nolan R., Bec M., Merrill M., Fowler A. M., 2003, *PASP*, 115, 1388
- Homer L., Szkody P., Chen B., Henden A., Schmidt G., Anderson S. F., Silvestri N. M., Brinkmann J., 2006, *AJ*, 131, 562
- Horne K., 1986, *PASP*, 98, 609
- Horne K., Marsh T. R., 1986, *MNRAS*, 218, 761
- Horne K., Marsh T. R., Cheng F. H., Hubeny I., Lanz T., 1994, *ApJ*, 426, 294
- Horne K., Welsh W. F., Wade R. A., 1993, *ApJ*, 410, 357
- Howell S. B., Nelson L. A., Rappaport S., 2001, *ApJ*, 550, 897

- Kahabka P., van den Heuvel E. P. J., 1997, *ARA&A*, 35, 69
- Kalirai J. S., Bergeron P., Hansen B. M. S., Kelson D. D., Reitzel D. B., Rich R. M., Richer H. B., 2007, *ApJ*, 671, 748
- Kalirai J. S., Hansen B. M. S., Kelson D. D., Reitzel D. B., Rich R. M., Richer H. B., 2008, *ApJ*, 676, 594
- Kelson D. D., 2003, *PASP*, 115, 688
- Kepler S. O., Kleinman S. J., Nitta A., Koester D., Castanheira B. G., Giovannini O., Althaus L., 2007, in Napiwotzki R., Burleigh M. R., eds, 15th European Workshop on White Dwarfs Vol. 372 of *Astronomical Society of the Pacific Conference Series*, The White Dwarf Mass Distribution. p. 35
- Kirkpatrick J. D., 2005, *ARA&A*, 43, 195
- Kirkpatrick J. D., 2008, in van Belle G., ed., 14th Cambridge Workshop on Cool Stars, Stellar Systems, and the Sun Vol. 384 of *Astronomical Society of the Pacific Conference Series*, Outstanding Issues in Our Understanding of L, T, and Y Dwarfs. p. 85
- Kirkpatrick J. D., Reid I. N., Liebert J., Cutri R. M., Nelson B., Beichman C. A., Dahn C. C., Monet D. G., Gizis J. E., Skrutskie M. F., 1999, *ApJ*, 519, 802
- Knigge C., 2006, *MNRAS*, 373, 484
- Knigge C., Baraffe I., Patterson J., 2011, *ApJS*, 194, 28
- Kolb U., 1993, *A&A*, 271, 149
- Kolb U., Baraffe I., 1999, *MNRAS*, 309, 1034
- Kopal Z., 1959, *Close binary systems*

- Kraft R. P., Mathews J., Greenstein J. L., 1962, *ApJ*, 136, 312
- Lasota J.-P., 2001, *NAR*, 45, 449
- Lawrence A. et al., 2007, *MNRAS*, 379, 1599
- Liebert J., Bergeron P., Holberg J. B., 2005, *ApJS*, 156, 47
- Littlefair S., 2002, PhD thesis, The University of Sheffield
- Littlefair S. P., Dhillon V. S., Howell S. B., Ciardi D. R., 2000, *MNRAS*, 313, 117
- Littlefair S. P., Dhillon V. S., Marsh T. R., Gänsicke B. T., 2006a, *MNRAS*, 371, 1435
- Littlefair S. P., Dhillon V. S., Marsh T. R., Gänsicke B. T., Baraffe I., Watson C. A., 2007, *MNRAS*, 381, 827
- Littlefair S. P., Dhillon V. S., Marsh T. R., Gänsicke B. T., Southworth J., Baraffe I., Watson C. A., Copperwheat C., 2008, *MNRAS*, 388, 1582
- Littlefair S. P., Dhillon V. S., Marsh T. R., Gänsicke B. T., Southworth J., Watson C. A., 2006b, *Science*, 314, 1578
- Littlefair S. P., Dhillon V. S., Martín E. L., 2003, *MNRAS*, 340, 264
- Littlefair S. P., Dhillon V. S., Martín E. L., 2005, *A&A*, 437, 637
- MacGregor K. B., Charbonneau P., 1997, *ApJ*, 486, 484
- Marsh T. R., 1987, *MNRAS*, 228, 779
- Marsh T. R., 1988, *MNRAS*, 231, 1117
- Marsh T. R., 1989, *PASP*, 101, 1032

- Marsh T. R., 2001, in Boffin H. M. J., Steeghs D., Cuypers J., eds, *Astrotomography, Indirect Imaging Methods in Observational Astronomy* Vol. 573 of *Lecture Notes in Physics*, Berlin Springer Verlag, *Doppler Tomography*. p. 1
- Marsh T. R., Dhillon V. S., 1997, *MNRAS*, 292, 385
- Marsh T. R., Dhillon V. S., Duck S. R., 1995, *MNRAS*, 275, 828
- Marsh T. R., Horne K., 1988, *MNRAS*, 235, 269
- Marsh T. R., Horne K., Schlegel E. M., Honeycutt R. K., Kaitchuck R. H., 1990, *ApJ*, 364, 637
- Marsh T. R., Robinson E. L., Wood J. H., 1994, *MNRAS*, 266, 137
- Martin C. et al., 2005, *ApJL*, 619, L1
- Maxted P. F. L., Napiwotzki R., Dobbie P. D., Burleigh M. R., 2006, *Nature*, 442, 543
- Mennickent R. E., Diaz M. P., Tappert C., 2004, *MNRAS*, 347, 1180
- Metropolis N., Rosenbluth A., Rosenbluth M., Teller A., Teller E., 1953, *JCP*, 21, 1087
- Meyer F., Meyer-Hofmeister E., 1979, *A&A*, 78, 167
- Modigliani A., Goldoni P., Royer F., Haigron R., Guglielmi L., François P., Horrobin M., Bristow P., Vernet J., Moehler S., Kerber F., Ballester P., Mason E., Christensen L., 2010, in *Society of Photo-Optical Instrumentation Engineers (SPIE) Conference Series* Vol. 7737 of *Society of Photo-Optical Instrumentation Engineers (SPIE) Conference Series*, *The X-shooter pipeline*
- Moffat A. F. J., 1969, *A&A*, 3, 455

- Mohanty S., Basri G., 2003, in Brown A., Harper G. M., Ayres T. R., eds, The Future of Cool-Star Astrophysics: 12th Cambridge Workshop on Cool Stars, Stellar Systems, and the Sun, Rotation & Activity in Mid-M to L Dwarfs p. 683
- Monet D. et al., 2003, AJ, 125, 984
- Morin J. et al., 2010, MNRAS, 407, 2269
- Morrissey P. et al., 2007, ApJS, 173, 682
- Naylor T., 1998, MNRAS, 296, 339
- Nelemans G., 2005, in Hameury J.-M., Lasota J.-P., eds, The Astrophysics of Cataclysmic Variables and Related Objects Vol. 330 of Astronomical Society of the Pacific Conference Series, AM CVn stars. p. 27
- Oke J. B., Gunn J. E., 1983, ApJ, 266, 713
- Osaki Y., 1974, PASJ, 26, 429
- Osaki Y., 1985, A&A, 144, 369
- Paczynski B., 1965, AcA, 15, 89
- Paczynski B., 1967, AcA, 17, 287
- Paczynski B., 1971, ARA&A, 9, 183
- Paczynski B., 1976, in Eggleton P., Mitton S., Whelan J., eds, Structure and Evolution of Close Binary Systems Vol. 73 of IAU Symposium, Common Envelope Binaries. p. 75
- Paczynski B., Sienkiewicz R., 1981, ApJL, 248, L27
- Panei J. A., Althaus L. G., Benvenuto O. G., 2000, A&A, 353, 970

- Parsons S., Marsh T., Gänsicke B., Dhillon V., Copperwheat C., Littlefair S., Pyrzas S., Drake A., Koester D., Schreiber M., Rebassa-Mansergas A., 2012a, MNRAS, 419, 304
- Parsons S. et al., 2012b, MNRAS, 420, 3281
- Parsons S. G., Marsh T. R., Copperwheat C. M., Dhillon V. S., Littlefair S. P., Gänsicke B. T., Hickman R., 2010, MNRAS, 402, 2591
- Passy J.-C., De Marco O., Fryer C. L., Herwig F., Diehl S., Oishi J. S., Mac Low M.-M., Bryan G. L., Rockefeller G., 2012, ApJ, 744, 52
- Patat F. et al., 2011, A&A, 527, A91
- Patterson J., 1984, ApJS, 54, 443
- Patterson J., 1998, PASP, 110, 1132
- Patterson J., 2011, MNRAS, 411, 2695
- Patterson J. et al., 2005, PASP, 117, 1204
- Patterson J., Thorstensen J. R., Knigge C., 2008, PASP, 120, 510
- Pearson K. J., 2006, MNRAS, 371, 235
- Pickles A. J., 1998, PASP, 110, 863
- Politano M., 1996, ApJ, 465, 338
- Politano M., 2004, ApJ, 604, 817
- Politano M., Weiler K. P., 2007, ApJ, 665, 663
- Press W., Teukolsky S., Vetterling W., Flannery B., 1992, Numerical recipes in C. The art of scientific computing. Cambridge: University Press, —c1992, 2nd ed.,

- Pretorius M. L., Knigge C., Kolb U., 2007, MNRAS, 374, 1495
- Prialnik D., 2000, *An Introduction to Stellar Structure and Evolution*. Cambridge University Press, Cambridge
- Ramsay-Howat S. K., Harris J. W., Bennett R. J., 1997, in Ardeberg A. L., ed., *Society of Photo-Optical Instrumentation Engineers (SPIE) Conference Series Vol. 2871 of Society of Photo-Optical Instrumentation Engineers (SPIE) Conference Series, Dedicated calibration facility for the Gemini Telescopes*. pp 1171–1178
- Rappaport S., Joss P. C., Webbink R. F., 1982, ApJ, 254, 616
- Rappaport S., Verbunt F., Joss P. C., 1983, ApJ, 275, 713
- Reiners A., Basri G., 2007, ApJ, 656, 1121
- Reiners A., Basri G., 2008, ApJ, 684, 1390
- Renvoizé V., Baraffe I., Kolb U., Ritter H., 2002, A&A, 389, 485
- Ricker P. M., Taam R. E., 2012, ApJ, 746, 74
- Ritter H., 1976, MNRAS, 175, 279
- Ritter H., 1985, A&A, 148, 207
- Ritter H., Burkert A., 1986, A&A, 158, 161
- Ritter H., Kolb U., 2003, A&A, 404, 301
- Roberts G., Gelman A., Gilks W., 1997, *Annals of Applied Probability*, 7, 110
- Robinson E. L., 1976, ApJ, 203, 485
- Robinson E. L., Barker E. S., Cochran A. L., Cochran W. D., Nather R. E., 1981, ApJ, 251, 611

- Rodríguez-Gil P., Torres M. A. P., Gänsicke B. T., Muñoz-Darias T., Steeghs D., Schwarz R., Rau A., Hagen H.-J., 2009, *A&A*, 496, 805
- Salaris M., Cassisi S., 2005, *Evolution of Stars and Stellar Populations*
- Savoury C. D. J., Littlefair S. P., Dhillon V. S., Marsh T. R., Gänsicke B. T., Copperwheat C. M., Kerry P., Hickman R. D. G., Parsons S. G., 2011, *MNRAS*, 415, 2025
- Savoury C. D. J., Littlefair S. P., Marsh T. R., Dhillon V. S., Copperwheat C. M., Parsons S. G., Steeghs D., 2012, *MNRAS*, 422, 469
- Savoury C. D. J., Littlefair S. P., 2013, *MNRAS*, *in prep*
- Schenker K., 2001, in Podsiadlowski P., Rappaport S., King A. R., D'Antona F., Burderi L., eds, *Evolution of Binary and Multiple Star Systems Vol. 229 of Astronomical Society of the Pacific Conference Series, Thermal-Timescale Mass Transfer and CV Evolution*. p. 321
- Schreiber M. R., Hameury J.-M., Lasota J.-P., 2003, *A&A*, 410, 239
- Schröder K.-P., Cannon Smith R., 2008, *MNRAS*, 386, 155
- Schwarz R., Schwöpe A. D., Vogel J., Dhillon V. S., Marsh T. R., Copperwheat C., Littlefair S. P., Kanbach G., 2009, *A&A*, 496, 833
- Shakura N. I., Sunyaev R. A., 1973, *A&A*, 24, 337
- Shara M. M., 1989, *PASP*, 101, 5
- Shara M. M., Livio M., Moffat A. F. J., Orio M., 1986, *ApJ*, 311, 163
- Shara M. M., Martin C. D., Seibert M., Rich R. M., Salim S., Reitzel D., Schiminovich D., Deliyannis C. P., Sarrazine A. R., Kulkarni S. R., Ofek E. O., Brosch N., Lépine S., Zurek D., De Marco O., Jacoby G., 2007, *Nature*, 446, 159

- Sirotkin F. V., Kim W.-T., 2009, *ApJ*, 698, 715
- Sirotkin F. V., Kim W.-T., 2010, *ApJ*, 721, 1356
- Smak J., 1979, *AcA*, 29, 309
- Smith A., Roberts G., 1993, *J. Roy. Stat. Soc. Series B*, 51, 2
- Smith A. J., Haswell C. A., Murray J. R., Truss M. R., Foulkes S. B., 2007, *MNRAS*, 378, 785
- Smith D. A., Dhillon V. S., 1998, *MNRAS*, 301, 767
- Smith D. A., Dhillon V. S., Marsh T. R., 1998, *MNRAS*, 296, 465
- Smith J. et al., 2002, *AJ*, 123, 2121
- Smith R. C., Collier Cameron A., Tucknott D. S., 1993, in Regev O., Shaviv G., eds, *Cataclysmic Variables and Related Physics Vol. 10 of Annals of the Israel Physical Society, Skew-Mapping: a New Way to Detect Secondary Stars in Cataclysmic Variables*. p. 70
- Southworth J., Copperwheat C. M., 2011, *The Observatory*, 131, 66
- Southworth J., Copperwheat C. M., Gänsicke B. T., Pyrzas S., 2010, *A&A*, 510, A100
- Southworth J., Gänsicke B. T., Breedt E., 2012, in *IAU Symposium Vol. 282 of IAU Symposium, The Orbital Period Distribution of Cataclysmic Variables Found by the SDSS*. pp 123–124
- Southworth J., Hickman R. D. G., Marsh T. R., Rebassa-Mansergas A., Gänsicke B. T., Copperwheat C. M., Rodríguez-Gil P., 2009, *A&A*, 507, 929

- Southworth J., Marsh T. R., Gänsicke B. T., Aungwerojwit A., Hakala P., de Martino D., Lehto H., 2007, MNRAS, 382, 1145
- Spruit H. C., Ritter H., 1983, A&A, 124, 267
- Steeghs D., 1999, PhD thesis, University of St. Andrews
- Stehle R., Ritter H., Kolb U., 1996, MNRAS, 279, 581
- Szkody P. et al., 2002, AJ, 123, 430
- Szkody P. et al., 2003, AJ, 126, 1499
- Szkody P. et al., 2004, AJ, 128, 1882
- Szkody P. et al., 2005, AJ, 129, 2386
- Szkody P. et al., 2006, AJ, 131, 973
- Szkody P. et al., 2007, AJ, 134, 185
- Szkody P. et al., 2009, AJ, 137, 4011
- Taam R. E., Sandquist E. L., 2000, ARA&A, 38, 113
- Tappert C., Augusteijn T., Maza J., 2004, MNRAS, 354, 321
- Thoroughgood T. D., Dhillon V. S., Littlefair S. P., Marsh T. R., Smith D. A., 2001, MNRAS, 327, 1323
- Thoroughgood T. D., Dhillon V. S., Watson C. A., Buckley D. A. H., Steeghs D., Stevenson M. J., 2004, MNRAS, 353, 1135
- Thorstensen J. R., Fenton W. H., Patterson J., Kemp J., Halpern J., Baraffe I., 2002, PASP, 114, 1117
- Tinney C. G., Reid I. N., 1998, MNRAS, 301, 1031

- Tokunaga A. T., Vacca W. D., 2005, *PASP*, 117, 421
- Tonry J., Davis M., 1979, *AJ*, 84, 1511
- Townsley D. M., Gänsicke B. T., 2009, *ApJ*, 693, 1007
- Tulloch S. M., Rodríguez-Gil P., Dhillon V. S., 2009, *MNRAS*, 397, L82
- Unda-Sanzana E., Marsh T. R., Gänsicke B. T., Maxted P. F. L., Morales-Rueda L., Dhillon V. S., Thoroughgood T. D., Tremou E., Watson C. A., Hinojosa-Goñi R., 2008, *MNRAS*, 388, 889
- Uthas H., Knigge C., Long K. S., Patterson J., Thorstensen J., 2011, *MNRAS*, 414, L85
- van Dokkum P. G., 2001, *PASP*, 113, 1420
- van Spaandonk L., Steeghs D., Marsh T. R., Torres M. A. P., 2010, *MNRAS*, 401, 1857
- Vande Putte D., Smith R. C., Hawkins N. A., Martin J. S., 2003, *MNRAS*, 342, 151
- Verbunt F., Zwaan C., 1981, *A&A*, 100, L7
- Vernet J. et al., 2010, *Highlights of Astronomy*, 15, 535
- Vernet J. et al., 2011, *A&A*, 536, A105
- Vogt N., 1982, *ApJ*, 252, 653
- Wade R. A., Horne K., 1988, *ApJ*, 324, 411
- Warner B., 1973, *MNRAS*, 162, 189
- Warner B., 1976, in Eggleton P., Mitton S., Whelan J., eds, *Structure and Evolution of Close Binary Systems Vol. 73 of IAU Symposium, Observations of Dwarf Novae*. p. 85

- Warner B., 1995, Cataclysmic variable stars.. Vol. 28
- Warner B., Woudt P. A., 2010, in Kologera V., van der Sluys M., eds, American Institute of Physics Conference Series Vol. 1314 of American Institute of Physics Conference Series, High-Speed Photometry of Catalina Sources. pp 185–189
- Warren S. et al., 2007, MNRAS, 375, 213
- Watson C. A., Dhillon V. S., 2001, MNRAS, 326, 67
- Watson C. A., Dhillon V. S., Rutten R. G. M., Schwobe A. D., 2003, MNRAS, 341, 129
- Webbink R. F., 1976, ApJ, 209, 829
- Weidemann V., 2000, A&A, 363, 647
- Willems B., Kolb U., Sandquist E. L., Taam R. E., Dubus G., 2005, ApJ, 635, 1263
- Wils P., 2009, Information Bulletin on Variable Stars, 5916, 1
- Wils P., Krajci T., Hamsch F.-J., Muylaert E., 2011, Information Bulletin on Variable Stars, 5982, 1
- Wood J., Horne K., Berriman G., Wade R., O'Donoghue D., Warner B., 1986, MNRAS, 219, 629
- Wood J. H., Horne K., 1990, MNRAS, 242, 606
- Wood J. H., Irwin M. J., Pringle J. E., 1985, MNRAS, 214, 475
- Wood M. A., 1995, in Koester D., Werner K., eds, White Dwarfs Vol. 443 of Lecture Notes in Physics, Berlin Springer Verlag, Theoretical White Dwarf Luminosity Functions: DA Models. p. 41

Yakin D. G., Suleimanov V. F., Borisov N. V., Shimanskii V. V., Bikmaev I. F.,
2011, *Astronomy Letters*, 37, 845

Yaron O., Prialnik D., Shara M. M., Kovetz A., 2005, *ApJ*, 623, 398

Zahn J.-P., 1977, *A&A*, 57, 383

Zorotovic M., Schreiber M. R., Gänsicke B. T., 2011, *A&A*, 536, A42

VE LCEG JG >HJGV CCF JEE >HO CTVH